Taylor, B., Fujioka, K., et al., 1990
Proceedings of the Ocean Drilling Program, Initial Reports, Vol. 126

9. SITE 793[1]

Shipboard Scientific Party[2]

HOLE 793A

Date occupied: 26 May 1989

Date departed: 27 May 1989

Time on hole: 21 hr, 20 min

Position: 31°06.35′N, 140°53.26′E

Bottom felt (rig floor; m, drill pipe measurement): 2975.3

Distance between rig floor and sea level (m): 10.50

Water depth (drill pipe measurement from sea level, m): 2964.8

Total depth (rig floor; m): 3075.0

Penetration (m): 99.70

Number of cores (including cores with no recovery): 11

Total length of cored section (m): 99.70

Total core recovered (m): 78.96

Core recovery (%): 79.2

Oldest sediment cored:
Depth (mbsf): 99.70
Nature: vitric sand and vitric silt
Age: Pliocene-Pleistocene
Measured velocity (km/s): 1.64

HOLE 793B

Date occupied: 27 May 1989

Date departed: 17 June 1989

Time on hole: 21 days, 5 hr, 20 min

Position: 31°06.33′N, 140°53.27′E

Bottom felt (rig floor; m, drill pipe measurement): 2975.3

Distance between rig floor and sea level (m): 10.50

Water depth (drill pipe measurement from sea level, m): 2964.8

Total depth (rig floor; m): 4657.3

Penetration (m): 1682.0

Number of cores (including cores with no recovery): 114

Total length of cored section (m): 1095.50

Total core recovered (m): 697.94

Core recovery (%): 63.7

Oldest sediment cored:
Depth (mbsf): 1403.9
Nature: volcanic breccia and microbreccia
Age: early Oligocene (Core 126-793B-81R)
Measured velocity (km/s): 2.55

Basement:
Depth (mbsf): 1403.90
Nature: volcanic to hyaloclastite breccia
Measured velocity (km/s): 3.1

Comments: Deepest hole reaching basement in Deep Sea Drilling Project (DSDP) or Ocean Drilling Program (ODP) history (longest occupation of any ODP or DSDP hole on a single leg).

Principal results: Site 793 is located in the center of the Izu-Bonin forearc sedimentary basin, about 75 km east of the volcanic front between the islands of Sumisu Jima and Tori Shima, and 125 km west of the axis of the Izu-Bonin Trench. It is located in an interchannel area on the southern side of the broad Sumisu Jima Canyon. The principal objectives of this site were to determine (1) the stratigraphy of the forearc basin and, hence, both the temporal variations in sedimentation, depositional environment, and paleoceanography, and the history of the intensity and chemistry of the arc volcanism; (2) the uplift and subsidence history across the forearc; (3) the nature of the igneous basement and the formation of the 200-km-wide forearc crust; and (4) the microstructural deformation and the large-scale rotation and translation of the forearc terrane since the Eocene. We selected the site on the basis of multichannel seismic records; the site chosen lies on *Fred Moore* 3505, Line 12, at 0109:30Z. Site 793 was occupied from 0745 hr (UTC, or Universal Time Coordinate), 26 May, to 1230 hr, 17 June 1989.

We spudded Hole 793A with the advanced hydraulic piston corer (APC) at 1745 hr on 26 May 1989 and cored 99.7 m with 79% recovery until an overpull and resulting severed piston rod ended operations at the hole. A reentry cone was spudded into the sediment at 0930 hr on 28 May, and Hole 793B was begun by drilling a 14-3/4-in. hole to 586.5 mbsf, which was then lined with 46 joints (562.66 m) of 11-3/4-in. casing. We obtained special permission not to core this section so that we could meet the deep stratigraphic and basement objectives in the time available. We took 114 rotary core barrel (RCB) cores during the next 12 days, with a pipe trip and subsequent reentry after Core 126-793B-87R (1422.9 mbsf) to change the drill bit. At 0320 hr on 14 June, Hole 793B reached a total penetration of 1682 mbsf, with 74% recovery in the sediments above 1403.9 mbsf and 33% recovery in the basement below.

Following a pipe trip to release the bit and add a casing landing tool, a full suite of geophysical and geochemical logs, including the formation microscanner (FMS) and vertical seismic profiling (VSP), was planned. Several bridges were encountered, which required clearing with the pipe, so the hole was logged in stages. The density tool failed. The other physical property and temperature tools logged the intervals 1565.6–1034, 947.8–775.9, and 708.2–586.5 mbsf. The FMS was run from 1539 to 1034 mbsf and from 764.1 to 586.5 mbsf. The geochemistry combination was used in the open hole from 1531 to 1034 mbsf, and through the pipe from 917 to 586.5 mbsf. Poor clamping, a result of formation conditions, limited an attempted VSP to only a few good recording levels.

We defined seven lithostratigraphic units at Site 793:

Unit I (0–98.9 mbsf): Quaternary pumiceous gravel, sandy gravel, and vitric sand; nannofossil clay, clayey silt, and silty clay; and nannofossil-rich clayey silt and clay, with rare vitric sand and silt.

Unit II (586.5–591 mbsf): olivine-clinopyroxene diabase.

Unit III (591–735.7 mbsf): lower to middle Miocene nannofossil-rich silty claystone, silty claystone, nannofossil-rich and nannofossil claystone, vitric siltstone and sandstone, clayey siltstone, and nannofossil-rich clayey siltstone.

Unit IV (735.7–759 mbsf): lower Miocene claystone, nannofossil and nannofossil-rich claystone, and vitric siltstone.

[1] Taylor, B., Fujioka, K., et al., 1990. *Proc. ODP, Init. Repts.*, 126: College Station, TX (Ocean Drilling Program).

[2] Shipboard Scientific Party is as given in the list of participants preceding the contents.

Unit V (759–1373.1 mbsf): lower to upper Oligocene vitric sandstone, pumiceous sandstone, granule- to fine-pebble conglomerate, siltstone, clayey siltstone, and silty claystone.

Unit VI (1373.1–1403.9 mbsf): upper–lower Oligocene(?) very poorly sorted volcanic breccia with sandy matrix, and mixed fresh to altered clasts of mainly plagioclase-rich andesite.

Unit VII (1403.9–1678.4 mbsf): upper–lower Oligocene(?) breccias and massive to pillowed flows of porphyritic and aphyric clinopyroxene-orthopyroxene basaltic andesites and andesites. Note that this unit is subdivided into 17 igneous rock units in the "Igneous Petrology" section (this chapter).

We dated Units I and III–V by means of nannofossils, radiolarians (Units I and III), foraminifers, and paleomagnetics; Units VI–VII were dated by paleomagnetics. Sedimentation rates in Units V and VI are 250 m/m.y. (31–29 Ma) and in the upper part of Unit V are 80 m/m.y. (29–27 Ma). Unit IV was deposited very slowly (~7 m/m.y.) with a probable lacuna at 18–21 Ma. Sedimentation rates are 70 m/m.y. in Unit III, 40 m/m.y. in the uncored interval, and 105 m/m.y. in Unit I (<0.83 Ma). Benthic foraminifers indicate that depositional water depths shallowed from 4–5 km in the late–early Oligocene to 2–4 km at present.

Unit VI represents a debris or talus apron, eroded from local basement topography. Several of the clasts are geochemically similar to the basement calcalkaline andesites at Site 792. Unit V, >600 m thick, records the rapid filling of the forearc basin by turbiditic sandstones, conglomeratic debris flows, and finer interbeds. These sediments were produced by concurrent volcanism as well as by erosion of surrounding highs. Hemipelagic Unit IV was deposited in oxygenated bottom waters during a time of regional volcanic quiescence. Unit III represents an alternation of fine-grained turbidites fed by renewed arc volcanism and hemipelagic sediments. Unit II is a high-Mg series tholeiitic diabase, intruded in the middle Miocene or younger. Unit I records the continuation in the late Pleistocene of the infilling, begun in the early Pliocene, of a broad canyon that was probably incised during the latest Miocene. The increased pumiceous input to the upper part of Unit I records a late Quaternary increase in explosive arc volcanism.

Units III–VI contain numerous normal microfaults and locally abundant subvertical dewatering veinlets, indicative of an extensional regime throughout the basin history. The minimum horizontal compressive stress direction determined from hole ellipticity is N65°E. Paleomagnetic inclination data from the sediments and lavas show that the forearc has been translated about 15° north since 30 Ma.

Volcanism without epiclastic sedimentation accompanied the initial mid-Oligocene forearc basin subsidence, as the formerly contiguous Eocene frontal- and outer-arc highs were separated. This separation probably resulted from rifting rather than spreading at a well-defined axis, given the scale of the basin (40–70 km wide) and multichannel seismic data that imply the presence of half grabens and low-angle detachments in the basement. Most of the Site 793 basement lavas and breccias belong to a high-Mg series of basaltic andesites and andesites that have boninitic affinities. The aphyric lavas and clasts belong to a low-Mg series that has tholeiitic affinities. Both series have <5% vesicles. They are less enriched in Ti, P, Y, Zr, and Ba than most arc lavas. Their high-field-strength element ratios indicate a depleted mantle source.

The pore waters below 787 mbsf broke the record of the previous site for the most extensively altered pore water of seawater origin ever sampled by the DSDP/ODP. Characteristic concentrations include sulfate = 12–16, magnesium = ~0, calcium = 290–300, and silica = 0.14–0.23 (all in mM). Unlike values at Site 792, even the concentration of chloride has been shifted relative to seawater, to stable levels of around 715 mM below 1000 mbsf. These highly altered interstitial Ca-Cl-type waters result from the low-temperature alteration of volcanogenic sedimentary components into smectites, zeolites, and gypsum, in a virtually closed system, as indicated by the high formation factors.

Physical property measurements indicate that

1. the sedimentary section is characterized by generally decreasing porosity, from an average of 68% in Unit I to 31% in Unit VI;
2. wet-bulk density increases concurrently from a mean of 1.68 g/cm^3 (Unit I) to 2.53 g/cm^3 (Unit VI);
3. superimposed on these general trends are cyclic fluctuations, similar to those observed at Site 792;
4. carbonate contents average 25%, 10%, and 21% in Units I, III, and IV, respectively, and values are consistently low throughout Units V and VI, generally <4%;
5. sonic velocity data in Units I, II, and IV display relatively low values with little variability, averaging 1.6, 2.0, and 2.0 km/s, respectively;
6. the diabase intrusion (Unit II) is characterized by extremes in all the physical properties, with averages of 10.4% (porosity), 2.76 g/cm^3 (bulk density), and 5.04 km/s (velocity); and
7. the sediment/basement contact is not well defined by the physical property data (or *in-situ* measurements) because of the gradual transition through the breccias.

However, the volcanic breccia and lava flows within the basement are clearly different with regard to their physical properties. Deeper layers, containing a greater abundance of flow units, are characterized by generally lower porosity values (average of 23.3%) and higher bulk density (2.62 g/cm^3) and velocity values (3.84 km/s), compared with values in breccia units (averages of 28%, 2.5 g/cm^3, and 3.4 km/s, respectively).

The principal results of this site, which made the deepest penetration reaching basement in the history of the DSDP/ODP, are

1. documentation of the absence of pre-mid-Oligocene sediments in the forearc basin depocenter;
2. benthic foraminiferal evidence that depositional water depths shallowed from 4–5 km in the mid-Oligocene to 2–4 km at present;
3. interpretation that the forearc basin formed by mid-Oligocene rifting that separated the formerly contiguous Eocene frontal- and outer-arc highs;
4. recovery of the igneous basement beneath the center of the forearc basin, which includes high-Mg series basaltic andesites and andesites with boninitic affinities as well as a low-Mg series with tholeiitic affinities;
5. confirmation of varying volcanogenic input to the forearc, including volcanic quiescence during the early Miocene and a dramatic increase in volcanic activity in the late Quaternary;
6. documentation of a Neogene intrusion 70 km in front of the "volcanic front";
7. microstructural evidence of an extensional regime throughout the forearc basin history;
8. paleomagnetic evidence that the forearc has been translated about 15° northward since 30 Ma;
9. pore-water indications of low-temperature alteration of the volcanogenic sediments, producing Ca-Cl-type waters; and
10. establishment of a deep, open, reentry site for future investigators.

BACKGROUND AND OBJECTIVES

Site 793 is located at 31°06.33′N, 140°53.27′E, at 2965 m below sea level (mbsl) in the center of the Izu-Bonin forearc sedimentary basin, about 75 km east of the volcanic front between the islands of Sumisu Jima and Tori Shima, and 125 km west of the axis of the Izu-Bonin Trench (Fig. 1). It is located on the southern side of the broad Sumisu Jima Canyon (Fig. 2).

By drilling at this site we sought to determine the following:

1. the stratigraphy of the forearc and, hence, both the temporal variations in sedimentation, depositional environment, and paleoceanography, and the history of the intensity and chemistry of arc volcanism;
2. the uplift/subsidence history across the forearc to obtain information on forearc flexure and basin development;
3. the nature of the forearc igneous basement to answer questions concerning the nature of volcanism in the initial stages of subduction and the formation of the 200-km-wide forearc crust, including the possibility of later forearc volcanism; and
4. the microstructural deformation and the large-scale rotation and translation of the forearc terrane since the Eocene.

The first of these objectives was addressed partly through detailed studies of sediments retrieved at Site 793. The type of sed-

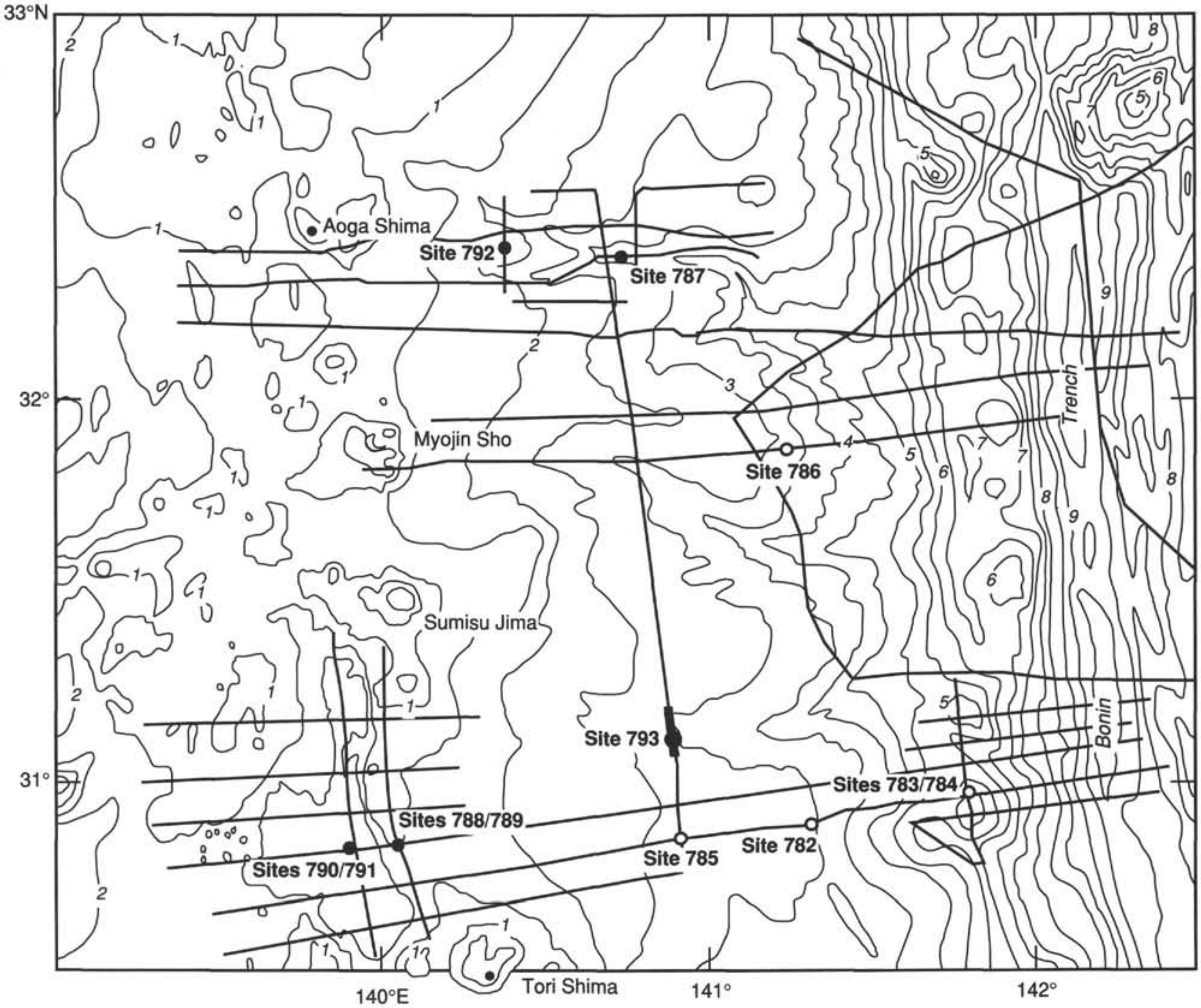

Figure 1. Bathymetric map (500-m-contour interval) of the Izu-Bonin arc-trench system between 30.5° and 33°N. The locations of sites drilled on ODP Legs 125 (open circles) and 126 (filled circles) are shown on the map, as are the locations of site survey multichannel seismic (MCS) lines. The segment of MCS Line 12 (shown in Fig. 2) is delineated by the thicker line segment.

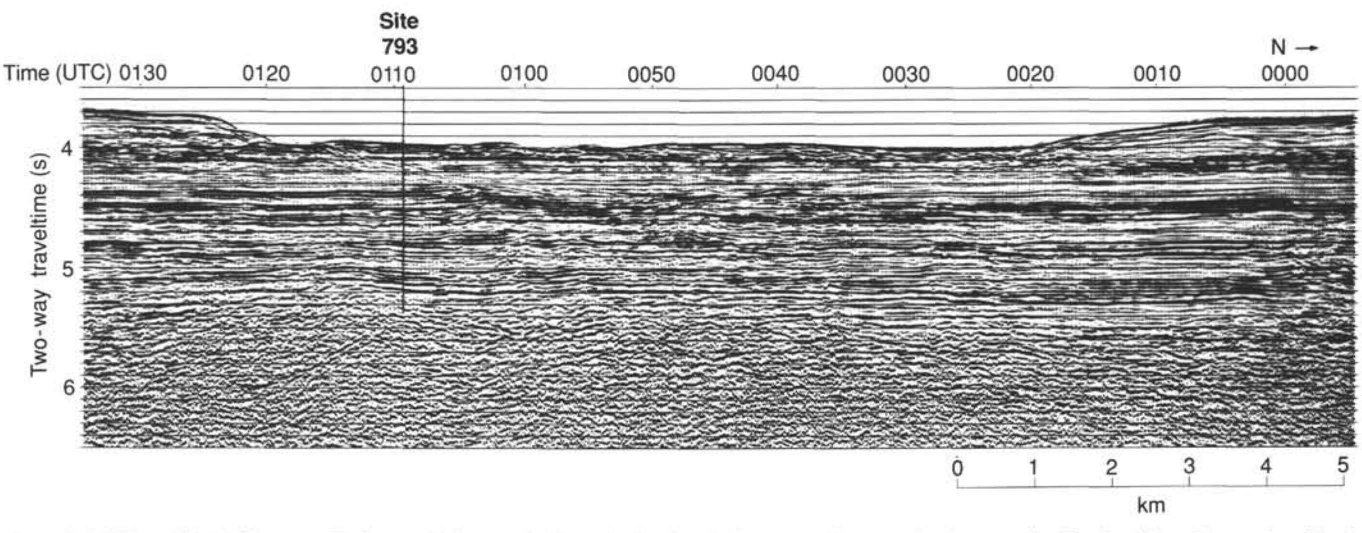

Figure 2. MCS profile 12 (Systrom, Taylor, et al., in prep.) along the Izu-Bonin forearc sedimentary basin, crossing Sumisu Jima Canyon (see Fig. 1 for location).

imentation and style of deposition in the forearc basin was expected to change with time as the proximity to arc volcanoes changed, as the volume and eruptive style of arc products varied, as the basin filled, and as the development of submarine canyons eroded and redistributed sedimentary material. Geostrophic currents, such as the paleo-Kuroshio, and changes in global sea level also may have affected the pattern of sedimentation and their effects may be deciphered from the stratigraphic record.

These sediments also contain a temporal record of the variations in the intensity and composition of arc volcanism. Studies of the chronology and nature of tephras at this site will test various conflicting models concerning the complex relationships between tectonic and volcanic phenomena in island arcs, such as changes in subduction rate, periodicity in backarc rifting and spreading, pulses of arc volcanism, and variations in arc geochemistry (see "Introduction" chapter, this volume, for elaboration).

The second objective was investigated through a combination of paleontological estimates of paleobathymetry, backstripping of the sedimentation history using the physical property and logging data, and seismic stratigraphic analyses of interconnecting multichannel seismic (MCS) profiles. Determination of the forearc vertical displacement history provided some of the information necessary to decide (1) whether fairly stable conditions have prevailed since the mid-Tertiary, as suggested by the well-developed submarine canyon system and lower-slope terrace of serpentinite seamounts; (2) whether the frontal- and outer-arc high resulted from igneous construction or from differential uplift; (3) whether the upper-slope basin between them is caused by forearc spreading or differential subsidence; and (4) whether flexural loading of the forearc by arc volcanoes or by coupling with the subducting plate is an important process.

The third objective was investigated by studies of the basement rocks retrieved at this site. Basement beneath the thickly sedimented upper-slope basin between the frontal- and outer-arc highs had never been sampled in this or any other intraoceanic arc-trench system. From the available data, it appears that the present 150–230-km-wide Bonin-Mariana forearc formed, in large part, by volcanism during the initial stages of arc development in the Eocene and early Oligocene, (see "Introduction" chapter, this volume, for elaboration). Similar volcanism has not occurred since and cannot be studied as an active phenomenon anywhere on Earth at present. Studies of the basement rocks permitted evaluation of the three main alternative hypotheses for the origin and evolution of this forearc terrane, namely: (1) the frontal- and outer-arc highs could have originally been continuous and subsequently separated by forearc spreading; (2) the frontal- and outer-arc highs could have been built separately but nearly synchronously on former West Philippine Plate crust; or (3) the terrane could form part of a continuous Eocene arc volcanic province, possibly with overprints of later forearc volcanism. Each scenario of forearc basement development implies a different crustal structure for the forearc.

The fourth objective of the site, the study of microstructures and plate rotations, was addressed through a study of FMS images as well as the structural and paleomagnetic properties of the cored materials. Microstructures in the drill cores and on the FMS images of the drill-hole wall helped us to determine the intensity of faulting in space and time across the forearc terrane and to define the syndepositional structures. Measurements of the paleomagnetic properties of subaerial portions of the Izu-Bonin and Mariana forearcs have shown at least 20° of northward drift and from 30° to >90° of clockwise rotation since the Eocene (see "Introduction" chapter, this volume, for more details). Studies of the paleomagnetism of the cores constrained the numerous different models for the nature and timing of these motions, and their relationship to the overall structural evolution of the forearc. The FMS data helped orient the rotary cores so that declinations, and hence rotations, could be determined.

Given the previous drilling in the Izu-Bonin forearc on this leg and on Leg 125, the remaining primary objectives were to recover the mid-Oligocene and older stratigraphy and basement of the forearc basin. To meet these objectives required a deep penetrating reentry hole, but the estimated site time was 3 days more than that available. To save this time, a request was made and approved to drill without coring the interval below APC refusal to 600 mbsf.

SEISMIC STRATIGRAPHY

Site 793 lies on *Fred Moore* 3505, Line 12, at 0109:30Z. We correlated the MCS reflection data with recovered core material (Fig. 3) by using velocity data obtained from physical properties measurements, averaged over each lithologic unit (see "Physical Properties" section, this chapter), to convert depths (mbsf) into two-way traveltimes. For the uncored interval between 99.7 and 586.5 mbsf, we used stacked velocity values derived from the reflection data to make the conversion. Physical properties and stacking velocities are in close agreement for the cored intervals at this site.

Two of the active channels within the broad submarine valley can be seen at 0053–0100Z and 0116–0121Z on Line 12 (Fig. 3). Site 793 is located in the interchannel area. Unit I recovered Quaternary material filling a paleo-canyon, the base of which can be seen at 4.46 s and 0053Z in Figure 3. Because of the canyon fill and the uncored interval between 99.7 and 586.5 mbsf, the uppermost seismic stratigraphic units adjacent to the site were not sampled. These include a unit of discontinuous, high-amplitude reflectors down to 4.1 s, which overlies a unit of subparallel, weak reflectors down to 4.36 s. Unit II, a diabase sill, corresponds to the strong reflector at 4.62 s that is at the base of an uncored interval of subparallel, continuous, mainly strong reflectors, typical of turbidites. Lower amplitude, less continuous reflectors between 4.63 and 4.79 s correlate with Units III and IV. Unit V is seismically expressed as a series of subparallel reflectors, laterally varying in amplitude, that are offset by several normal faults. High-amplitude reflectors at 5.03 to 5.18 s correlate with the coarse sediments in the lower half of this unit. There is a gradual transition in physical properties data from the basal sediments, including the volcanic-clast breccia of Unit VI, to the andesitic basement (see "Physical Properties" section, this chapter). Acoustic basement (>5.25 s) is characterized by chaotic and discontinuous reflectors underlying the stratified sedimentary sequences.

OPERATIONS

Site 792 to Site 793 (BON 6D)

The transit from Sites 792 to 793 (proposed Site BON 6D) took 8.6 hr to traverse 82 nmi at an average speed of 9.5 kt. At 0715 hr (all times in UTC) on 26 May 1989, the first of two beacons was dropped. As the bottom-hole assembly (BHA) for the first hole was being made up, the first beacon died and the backup beacon had to be deployed at 0813 hr.

The drilling program for this site called for coring 1700 mbsf into mid-Oligocene forearc sediments. To complete operations within the remaining 22 days, some changes in scientific objectives were needed, and a plan of action was established that included blind drilling, spot coring, and the setting of a reentry cone with 11-3/4-in. casing. A summary of drilling operations at this site is presented in Table 1.

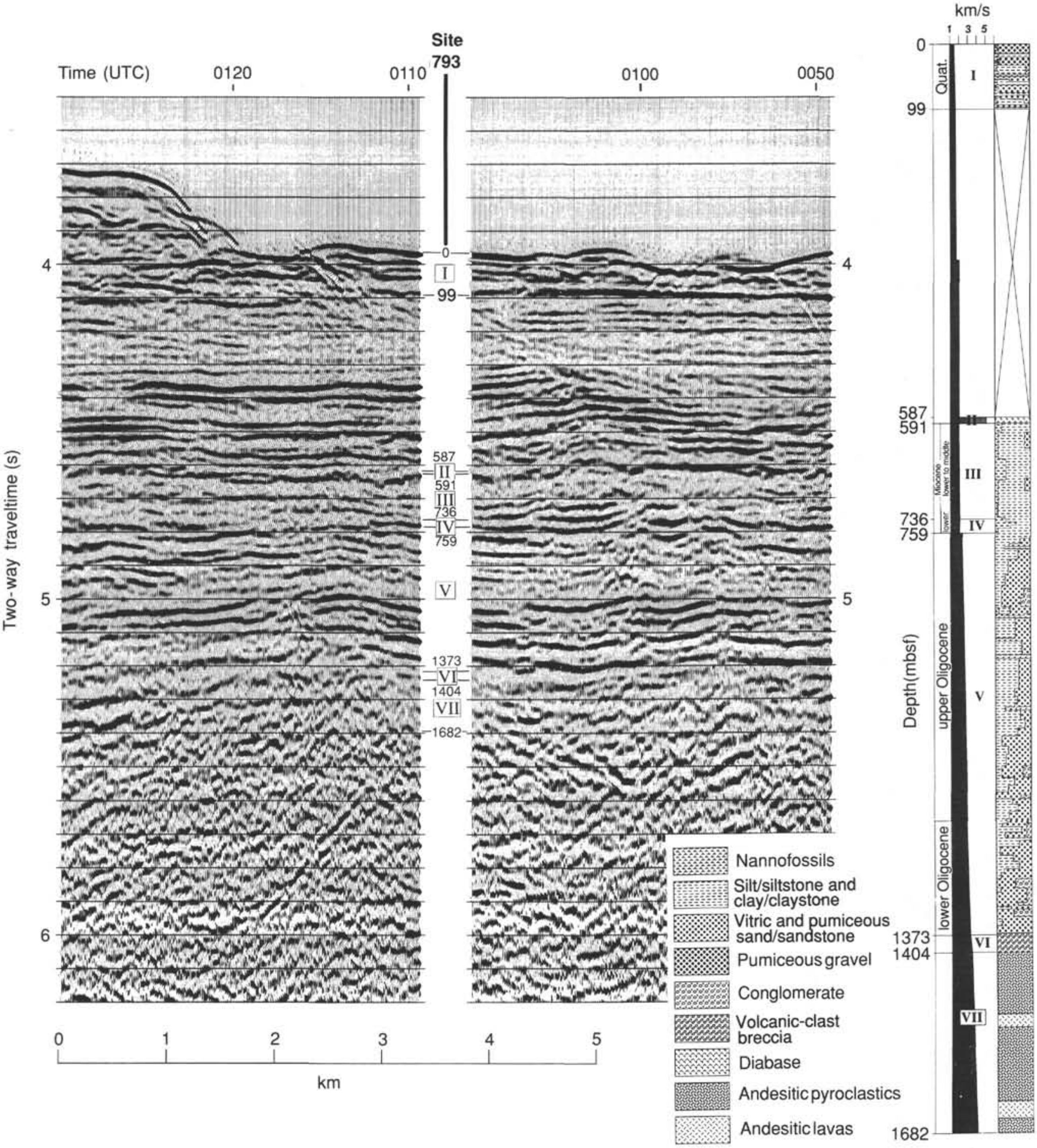

Figure 3. Correlation of Site 793 lithostratigraphy with site survey multichannel seismic reflection data. Lithologic units are identified on the seismic section, unit boundaries are given in meters below seafloor (mbsf), and the lithologic column (see "Lithostratigraphy and Accumulation Rates" section, this chapter) is presented on the right side of the figure. The location of the *Fred Moore* seismic line is shown in Figures 1 and 2. The seismic section has been stacked (48 fold), deconvolved, migrated, and filtered 10–60 Hz. Vertical exaggeration is about 4×.

Hole 793A

Prior to spudding Hole 793A, a jet-in test was conducted to examine the capabilities of the sediment to support a reentry cone and to determine what length to make the 16-in. casing shoe. At 1735 hr on 26 May, the jet-in test concluded with a final penetration of 22 m.

The bit was lifted off bottom, the ship offset 10 m south, and the first APC core was shot at 2970 mbsf at 1745 hr on 26 May. The first core established the mud line at 2975.3 mbsf. We routinely obtained Cores 126-793A-2H through -10H encountering overpulls as much as 60,000 lb. Orientation of the cores commenced with Core 126-793B-6H. The percentage recovery of the first 11 cores was 79%.

Table 1. Coring summary, Site 793.

Core no.	Date (1989)	Time (UTC)	Interval (mbsf)	Cored (m)	Recovered (m)	Recovery (%)
126-793A-						
1H	May 26	1845	0.0-4.2	4.2	4.21	100.0
2H	26	1935	4.2-13.5	9.3	7.08	76.1
3H	26	2010	13.5-23.0	9.5	9.35	98.4
4H	26	2055	23.0-32.5	9.5	9.56	100.0
5H	26	2130	32.5-42.0	9.5	9.76	103.0
6H	26	2220	42.0-51.6	9.6	8.82	91.9
7H	26	2310	51.6-61.2	9.6	4.42	46.0
8H	26	2355	61.2-70.9	9.7	7.19	74.1
9H	27	0040	70.9-80.5	9.6	7.78	81.0
10H	27	0130	80.5-90.1	9.6	1.99	20.7
11H	27	0215	90.1-99.7	9.6	8.80	91.6
Coring totals				99.7	78.96	79.2
126-793B-						
1R	June 2	0250	586.5-594.7	8.2	3.79	46.2
2R	2	0415	594.7-604.3	9.6	0.47	4.9
3R	2	0525	604.3-614.0	9.7	4.97	51.2
4R	2	0630	614.0-623.6	9.6	5.88	61.2
5R	2	0730	623.6-633.3	9.7	6.63	68.3
6R	2	0830	633.3-642.8	9.5	3.41	35.9
7R	2	0935	642.8-652.4	9.6	0.63	6.6
8R	2	1030	652.4-662.1	9.7	2.00	20.6
9R	2	1155	662.1-671.8	9.7	3.91	40.3
10R	2	1300	671.8-681.4	9.6	4.25	44.3
11R	2	1405	681.4-691.1	9.7	8.07	83.2
12R	2	1500	691.1-700.8	9.7	2.20	22.7
13R	2	1600	700.8-710.4	9.6	5.56	57.9
14R	2	1645	710.4-720.1	9.7	2.07	21.3
15R	2	1740	720.1-729.7	9.6	5.58	58.1
16R	2	1910	729.7-739.1	9.4	8.89	94.6
17R	2	2120	739.1-748.8	9.7	8.25	85.0
18R	2	2250	748.8-758.4	9.6	9.83	102.0
19R	3	0020	758.4-768.0	9.6	5.05	52.6
20R	3	0150	768.0-777.7	9.7	9.84	101.0
21R	3	0310	777.7-787.3	9.6	8.97	93.4
22R	3	0435	787.3-797.0	9.7	4.63	47.7
23R	3	0620	797.0-806.7	9.7	6.53	67.3
24R	3	0810	806.7-816.4	9.7	8.87	91.4
25R	3	0945	816.4-825.7	9.3	9.03	97.1
26R	3	1150	825.7-835.4	9.7	9.88	102.0
27R	3	1330	835.4-845.1	9.7	9.31	96.0
28R	3	1510	845.1-854.7	9.6	9.91	103.0
29R	3	1650	854.7-864.4	9.7	7.22	74.4
30R	3	1835	864.4-874.0	9.6	8.50	88.5
31R	3	2025	874.0-883.7	9.7	9.14	94.2
32R	3	2235	883.7-893.3	9.6	6.45	67.2
33R	4	0020	893.3-903.0	9.7	9.83	101.0
34R	4	0200	903.0-912.6	9.6	8.28	86.2
35R	4	0335	912.6-922.3	9.7	9.35	96.4
36R	4	0520	922.3-932.0	9.7	8.09	83.4
37R	4	0705	932.0-941.6	9.6	9.89	103.0
38R	4	0905	941.6-951.3	9.7	7.44	76.7
39R	4	1115	951.3-961.0	9.7	0.69	7.1
40R	4	1310	961.0-970.6	9.6	10.01	104.3
41R	4	1505	970.6-980.3	9.7	9.57	98.6
42R	4	1710	980.3-989.7	9.4	7.11	75.6
43R	4	1905	989.7-999.4	9.7	8.61	88.7
44R	4	2115	999.4-1009.1	9.7	9.95	102.0
45R	4	2240	1009.1-1018.7	9.6	1.30	13.5
46R	5	0025	1018.7-1028.0	9.3	10.49	112.8
47R	5	0200	1028.0-1037.6	9.6	6.62	68.9
48R	5	0345	1037.6-1047.3	9.7	8.58	88.4
49R	5	0545	1047.3-1057.0	9.7	4.11	42.4
50R	5	0745	1057.0-1066.7	9.7	8.92	91.9
51R	5	1035	1066.7-1076.4	9.7	9.76	100.0
52R	5	1345	1076.4-1086.1	9.7	6.11	63.0
53R	5	1540	1086.1-1095.7	9.6	5.63	58.6
54R	5	1735	1095.7-1105.4	9.7	5.91	60.9
55R	5	1950	1105.4-1115.0	9.6	3.96	41.2
56R	5	2150	1115.0-1124.7	9.7	7.22	74.4
57R	5	2340	1124.7-1134.0	9.3	4.20	45.1
58R	6	0225	1134.0-1143.6	9.6	9.78	102.0
59R	6	0425	1143.6-1153.2	9.6	9.92	103.0
60R	6	0640	1153.2-1162.9	9.7	9.62	99.2
61R	6	0830	1162.9-1172.6	9.7	4.18	43.1
62R	6	1040	1172.6-1182.2	9.6	4.80	50.0
63R	6	1235	1182.2-1191.9	9.7	5.23	53.9
64R	6	1500	1191.9-1201.5	9.6	9.82	102.0
65R	6	1710	1201.5-1211.1	9.6	9.38	97.7
66R	6	1915	1211.1-1220.8	9.7	9.29	95.8

Table 1 (Continued).

Core no.	Date (1989)	Time (UTC)	Interval (mbsf)	Cored (m)	Recovered (m)	Recovery (%)
126-793B- (cont.)						
67R	6	2110	1220.8-1230.5	9.7	9.27	95.5
68R	6	2300	1230.5-1240.2	9.7	8.69	89.6
69R	7	0110	1240.2-1249.8	9.6	9.58	99.8
70R	7	0330	1249.8-1259.4	9.6	9.85	102.0
71R	7	0600	1259.4-1268.7	9.3	9.30	100.0
72R	7	0825	1268.7-1278.4	9.7	9.71	100.0
73R	7	1045	1278.4-1288.0	9.6	6.35	66.1
74R	7	1450	1288.0-1297.7	9.7	9.36	96.5
75R	7	1735	1297.7-1307.3	9.6	9.56	99.6
76R	7	2050	1307.3-1317.0	9.7	9.51	98.0
77R	8	0040	1317.0-1326.7	9.7	8.71	89.8
78R	8	0335	1326.7-1336.4	9.7	9.78	101.0
79R	8	0615	1336.4-1346.0	9.6	7.65	79.7
80R	8	0945	1346.0-1355.7	9.7	8.78	90.5
81R	8	1155	1355.7-1365.3	9.6	8.31	86.5
82R	8	1450	1365.3-1374.9	9.6	9.54	99.4
83R	8	1745	1374.9-1384.5	9.6	2.51	26.1
84R	8	2035	1384.5-1394.2	9.7	3.02	31.1
85R	9	0040	1394.2-1403.9	9.7	3.35	34.5
86R	9	0450	1403.9-1413.6	9.7	2.78	28.6
87R	9	0900	1413.6-1422.9	9.3	5.02	54.0
88R	9	1115	1422.9-1431.4	8.5	2.15	25.3
89R	10	1520	1431.4-1441.1	9.7	4.88	50.3
90R	10	1840	1441.1-1450.4	9.3	0.05	0.5
91R	10	2155	1450.4-1460.1	9.7	0.00	0.0
92R	11	0520	1460.1-1469.7	9.6	4.08	42.5
93R	11	0910	1469.7-1479.4	9.7	3.01	31.0
94R	11	1320	1479.4-1489.0	9.6	2.59	27.0
95R	11	1635	1489.0-1498.7	9.7	3.08	31.7
96R	11	1855	1498.7-1508.3	9.6	1.41	14.7
97R	11	2205	1508.3-1518.0	9.7	1.08	11.1
98R	12	0050	1518.0-1527.6	9.6	5.74	59.8
99R	12	0325	1527.6-1537.3	9.7	1.90	19.6
100R	12	0630	1537.3-1546.9	9.6	2.06	21.4
101R	12	0920	1546.9-1556.6	9.7	1.31	13.5
102R	12	1245	1556.6-1566.3	9.7	2.14	22.0
103R	12	1530	1566.3-1575.9	9.6	3.45	35.9
104R	12	1820	1575.9-1585.5	9.6	5.30	55.2
105R	12	2120	1585.5-1595.2	9.7	4.42	45.5
106R	13	0010	1595.2-1604.8	9.6	1.69	17.6
107R	13	0350	1604.8-1614.4	9.6	5.52	57.5
108R	13	0645	1614.4-1624.1	9.7	3.55	36.6
109R	13	1005	1624.1-1633.8	9.7	3.71	38.2
110R	13	1230	1633.8-1643.4	9.6	5.88	61.2
111R	13	1535	1643.4-1653.1	9.7	2.49	25.7
112R	13	1900	1653.1-1662.7	9.6	2.34	24.4
113R	13	2225	1662.7-1672.4	9.7	4.09	42.1
114R	13	0320	1672.4-1682.0	9.6	6.02	62.7
Coring totals				1095.5	697.94	63.7

After Core 125-793A-12H was shot, the core barrel became firmly imbedded in the sediment and required 120,000-lb overpull to be extracted. The excessive overpull was too much for the piston rod connection and it sheared, leaving part of the piston rod and the core barrel in the hole. Having completed the scientific objectives of this hole, the drill pipe was tripped to the surface and broke the plane of the rotary table at 0435 hr on 27 May, thereby officially ending Hole 793A.

Hole 793B

As soon as the advanced-hydraulic-piston-core/extended-core-barrel (APC/XCB) bottom-hole assembly (BHA) was laid down, work began on configuring the reentry cone running assembly. The cone was skidded over the center of the moonpool, a commandable beacon permanently attached to the upper lip of the cone, and the 16-in. casing shoe spaced out. The BHA was lowered through the rotary table and latched to the reentry cone. The reentry cone and BHA were lowered through the moonpool doors at 0300 hr on 28 May.

There were two short stops on the way to the seafloor to reduce the buoyancy of the drill pipe, and at 0933 hr the casing shoe was spudded in at the mud line. The jet-in procedure was finished and the reentry cone released by 1130 hr.

The drilling phase of this hole began at 1130 hr on 28 May and continued until 0745 hr on 29 May, when a total depth of 586.5 mbsf was attained. The hole was stopped short of the original target depth of 600 mbsf when a formation change at 535 mbsf indicated harder material that would be suitable for anchoring the bottom of the casing string. The hole was then swept twice and displaced with potassium chloride-treated mud. The top drive was racked, and at 1415 hr we began to pull the drillstring out of the hole.

The bit cleared the seafloor at 1610 hr and was on deck at 2200 hr. The casing running tools were made up and 46 joints (562.66 m) of 11-3/4-in. casing were run to the bottom. When the end of the casing reached a depth corresponding to 9 m above the reentry cone, we conducted a 2-hr television (TV) search for the cone starting at 1800 hr on 30 May. At 2015 hr, the casing string was stabbed into the reentry cone.

The casing string encountered resistance almost immediately upon entering the 16-in. casing hanger. After pumping mud and repositioning the vessel, the casing started to feed into the hole. The casing was worked while maintaining circulation to advance down the bore slowly. At 0425 hr on 31 May, the casing hanger was successfully landed in the reentry cone. The casing was then secured in place with a cement slurry, after which the pipe began its trip to the surface at 1145 hr.

First Reentry

A 6-collar RCB BHA was made up without a bit release because the only mechanical bit release (MBR) on board had sustained numerous cracks in the box connection during Leg 125 and was considered a total loss. The BHA was run in the hole to 2961.5 mbsl with the vibration-isolated television (VIT) system. At 0630 hr on 1 June, a TV search for the reentry cone commenced and found its target within 10 min. Reentry of the cone with the RCB occurred at 0650 hr.

At 1115 hr, the tedious process of drilling out the cement plug began; after cleaning up the rat hole, RCB coring commenced at 2330 hr on June 1, at a depth of 3561.8 mbsl (586.5 mbsf). The first core taken in Hole 793B took 115 min to cut 8.2 m, which corresponds to a rate of penetration of 4 m/hr. We discovered that the casing had been anchored in a diabase sill. This zone virtually ended with Core 126-793B-1R.

The remaining cores for the day took a more "reasonable" time (on the order of 40 m/hr) to penetrate the sediment. By the end of the first day, 114.3 m had been cored with 40% recovery.

By the end of the June 3, the material had compacted, the rate of penetration (ROP) slowed to a more stable level, and recovery improved to 79%. We continued RCB coring into upper Oligocene vitric sandstone and claystone. Hole surveys conducted at 1000, 1105, and 1201.5 mbsf found the hole angle at 1° or less.

On the morning of 8 June, one of the two heave compensator hoses ruptured. There were no spares on board, so coring continued with one hose and with limited performance potential on the heave compensator. Fortunately, the seas remained fairly calm for the rest of the leg. The penetration rate slowly but relentlessly continued to decrease with depth so that by the end of June 8, the ROP had dropped to 10 m/hr.

As the morning of 9 June approached, the ROP had slowed to 3.5 m/hr. Although there were no visible signs of bit distress such as erratic torque and undergauged core diameter, the high number of rotating hours (74 hr), the hardness of bottom, the light BHA (only six drill collars), and nearly 5 days remaining on site dictated that a bit change would be a prudent course of action. The progress up to that time had been 836.4 m cored with 73.4% recovery (613.9 m).

Starting at 0930 hr on 9 June, the drill bit began to be pulled to the surface. The drill bit broke the plane of the rotary table at 1830 hr on 9 June. Examination of the bit showed it to be in fair condition with about 25 inserts missing.

Second Reentry

A nine-collar BHA was rapidly made up and the new bit was run in the hole to 2170 mbsl at 2330 hr. The cone was reentered at 0210 hr on 10 June, and the drillstring was run to the bottom.

Cores 126-793B-88R through -90R (1442.3–1450.4 mbsf) recovered lower Oligocene volcanic breccia. While pumping down the core barrel for Core 126-793B-90R, an increase in pump pressure was observed. This was ascribed initially to a plugged jet, and Core 126-793B-90R was cut and retrieved. Recovery for this core was 5 cm of breccia.

The core barrel for Core 126-793B-91R was then pumped down with the slightly higher pressure still in evidence. When this core was retrieved with no recovery, it was assumed that the problem of the abnormally higher pressure was caused by an obstruction in the core throat or a partially jammed flapper, not a clogged jet orifice. A core barrel with a "deplugger" was pumped down and the pump pressure monitored for a drop to normal operating pressure. A couple of taps with the wireline jars were needed to unseat the deplugger, which was then tripped to the surface. There was no drop in pressure.

We dropped a center bit in hopes that this would clear the obstruction. Still the pressure remained high. The center bit was tripped out and the deplugger run in for a second time, this time with success. The pressure dropped, the deplugger was withdrawn, and a standard core barrel was run in the hole.

Normal coring operations resumed at 0145 hr on 11 June with Core 126-793B-92R, which yielded 4 m of volcanic breccia. The average rate of penetration for the day was 4 m/hr. Surveys were run at Cores 126-793B-96R and -106R, which found the hole at 1.75° and 2.0° from vertical, respectively.

Early in the morning of 14 June, Hole 793B reached total depth at 1682 mbsf and became the deepest hole ever cored into basement during DSDP or ODP operations. The drill string was pulled out of the hole, and the bit reached the rotary table at 1300 hr on 14 June.

Third Reentry

The logging BHA was assembled and run into the hole in the late hours of 14 June. The bit reentered the cone at 2214 hr. The first log attempted was a geophysical combination (DIL/LSS/NGT/TEMP). Several bridges were encountered, which required clearing with the pipe, so the hole was logged in stages. The density tool failed. Other physical properties and temperature tools logged the intervals 1565.6–2034, 947.8–775.9, and 708.2–586.5 mbsf. The FMS was run from 1539 to 1034 mbsf and from 764.1 to 586.5 mbsf. The geochemistry combination was used in the open hole from 1531 to 1034 mbsf, and through the pipe from 917 to 586.5 mbsf. Poor clamping, a result of formation conditions, limited an attempted VSP to only a few good recording levels. Logging was completed in Hole 793B at 0415 hr on 17 June.

Site 793 to Tokyo

JOIDES Resolution was underway for Tokyo by 2130 hr on 17 June. Leg 126 ended officially when the first anchor was dropped in Tokyo harbor at 0700 hr on 19 June 1989.

LITHOSTRATIGRAPHY AND ACCUMULATION RATES

Site 793 is located in the central part of the forearc basin of the Izu-Bonin Arc. The drill site is near the southern side of the east-west-trending Sumisu Jima Canyon, which heads east of the arc volcanoes, passes through structural lows at the outer-arc high, and ends at a mid-slope terrace on the inner wall of the Izu-Bonin Trench (Taylor and Smoot, 1984). Near the drill site, Sumisu Jima Canyon is a broad, flat-floored depression that contains three active, leveed, thalweg channels; it does not, therefore, possess the features of a true submarine canyon, such as a V-shaped profile and steep walls with rock outcrops (Shepard, 1963); instead, in the following discussion, we refer to this feature as a submarine valley. Site 793 is located in an interchannel setting between the southern two leveed channels. Seismic data (Fig. 2) indicate an older (probably Pliocene) erosional surface of similar width beneath the modern submarine valley; to the north, the paleo-valley fill is up to 400 m thick.

We drilled Hole 793A to a depth of 99.7 mbsf and recovered part of the Quaternary section that infills the paleo-valley. We then set a reentry cone and casing and recommenced coring at 586.5 mbsf, so that we bypassed the lower part of the paleo-valley fill, including its erosional contact with underlying sediments, and a considerable thickness of probable Pliocene and possibly upper Miocene deposits. The successions recovered in Holes 793A and 793B are separated by a long uncored interval, and so the sediments in these two holes are described and interpreted separately. The characteristics and depths of all units recognized at Site 793 are summarized in Table 2, and in Figures 4 and 5.

Hole 793A

The recovery in Hole 793A was 79%. The predominant sediment types recovered are pumiceous gravel, pumiceous pebbly sand, pumiceous sand, black vitric sand and silt, nannofossil clay, nannofossil clayey silt, and nannofossil-rich clayey silt. The pumiceous gravel is concentrated in the upper 32.5 m (Cores 126-793A-1H through -3H). The carbonate content of the fine-grained sediments (Fig. 4) is higher than in any other Pleistocene section drilled during Leg 126, with values as high as 60%.

We recognized only one lithologic unit in Hole 793A. Contrasts in the abundance of pumiceous gravel are sufficient to justify division of the succession into two subunits, with the base of Subunit IA placed at 32.5 mbsf (Fig. 4).

Unit I

Interval: Cores 126-793A-1H through -11H
Age: Quaternary
Depth: 0–98.9 mbsf

Subunit IA

Subunit IA (0–32.5 mbsf; Cores 126-793A-1H through -4H) consists of 71% pumiceous gravel and sandy gravel, 15% nan-

Table 2. Lithostratigraphic units, Site 793.

Unit/ subunit	Lithology	Sedimentary structures	Interval (mbsf)	Age	Occurrence
IA	Intermediate to felsic pumiceous gravel and sandy gravel, nannofossil clay, nannofossil clayey silt, nannofossil-rich clayey silt, and nannofossil-rich clay. Rare vitric sand and vitric silt.	Gravel; structureless, poorly sorted, maximum clast size = 5 cm. Fine-grained sediments are burrowed and contain scattered granules and pebbles of pumice.	0–32.5	Quaternary	126-793A-1H through -4H
IB	Pumiceous and vitric sand, nannofossil-rich clayey silt, nannofossil-rich clay, nannofossil silty clay, vitric silt, and pumiceous gravel.	Sand and gravel beds; graded, parallel laminated to locally ripple laminated; maximum pebble size = 5 cm. Fine-grained sediments are burrowed and contain scattered pumice granules and pebbles. Includes a very thick, gravel-matrix debris-flow deposit with cobbles and boulders of fine-grained sediments.	32.5–98.9	Quaternary	126-793A-5H through -11H
II	Olivine-clinopyroxene diabase sill.		586.5–591.0	post-middle Miocene	126-793B-1R
III	Nannofossil-rich silty claystone, silty claystone, nannofossil-rich claystone, nannofossil claystone, vitric siltstone, vitric sandstone, clayey siltstone, and nannofossil-rich clayey siltstone.	Graded beds; lower division parallel- to ripple-laminated vitric sandstone/siltstone; middle division parallel-laminated silty claystone/clayey claystone; fine-grained burrowed top, rich in nannofossils, contains scattered grains of mafic glass or felsic pumice. Dip is 3°–4°. Sub-vertical veinlets and normal microfaults.	591.0–735.7	early to middle Miocene	126-793B-2R through -16R-4, 0 cm
IV	Claystone, nannofossil claystone, nannofossil-rich claystone, and vitric siltstone. Maximum $CaCO_3$ is 60%. Uppermost rocks are pale red and contain todorokite (MnO_2) and gypsum. Carbonate content is negligible near base. Scattered large benthic foraminifers.	Top of unit strongly burrowed and contains abundant dewatering veinlets and slickensided microfaults. The base contains few burrows and is fissile. Dip is 8°–10°.	735.7–759.0	early Miocene	126-793B-16R-5, 0 cm, through -19R-1, 60 cm
V	Vitric sandstone, pumiceous sandstone, granule to fine-pebble conglomerate, siltstone, clayey siltstone, and silty claystone.	Graded sandstone beds with Bouma sequences and erosional bases. Thick to very thick sandstones, pebbly sandstones, and conglomerates contain fluid-escape pillars, dish structures, decimeter-scale intraclasts, large reworked benthic foraminifers, fragments of calcareous red algae, and pumice. Fine-grained lithologies are parallel-laminated upper divisions of turbidites. Some ungraded conglomerates and pebbly sandstones. Dip is $<10°$. Fractures, microfaults, and gypsum-filled veins occur. Entire unit fines upward.	759.0–1373.1	early to late Oligocene	126-793B-19R-1, 60 cm, through -82R-6, 78 cm
VI	Very poorly sorted volcanic breccia with sandy matrix, and mixed fresh to altered clasts of plagioclase-rich andesite	Chaotic	1373.1–1403.9	early(?) Oligocene	126-793B-82R-6, 78 cm, through -85R
VII	Breccias and massive to pillowed lava flows of porphyritic and aphyric clinopyroxene-orthopyroxene basic andesite.	Local clast-supported breccia with zeolite cements and internal sediments in cavities.	1403.9–1678.4	early(?) Oligocene	126-793B-86R to -114R

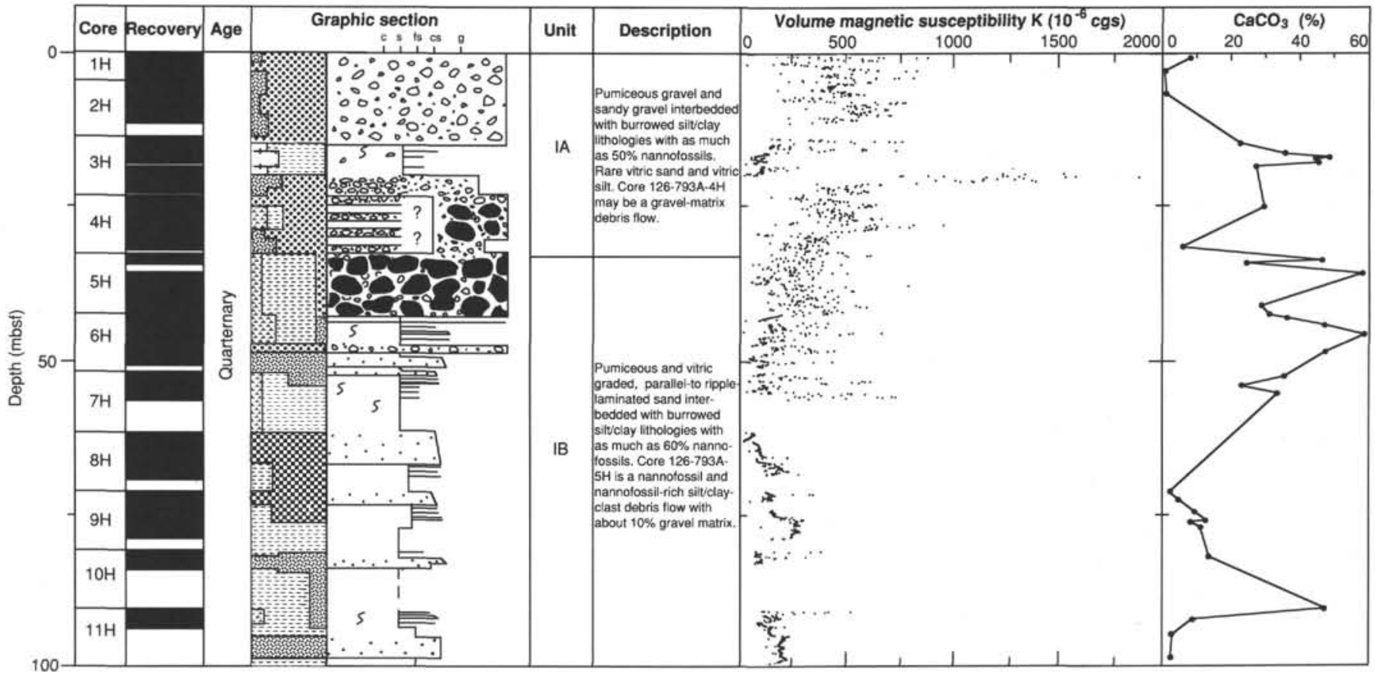

Figure 4. Lithostratigraphic summary for Hole 793A, including a graphic display of core recovery and the downhole distributions of carbonate minerals and magnetic susceptibility. The carbonate curve is primarily a function of the distribution of nannofossils throughout the section, whereas the magnetic susceptibility data reflect the distribution of coarse mafic volcanic lithics and crystals or their dilution by carbonate. The proportions of rock types are shown in the lithology column (see Fig. 3 for legend); the format is more generalized than in core descriptions in that it reflects the percent of groups of rock types observed within a given cored section (i.e., carbonate, gravel, sand, and silt plus clay), and does not show mixed biogenic/siliciclastic lithologies. The graphic column is a simplified sedimentological log displaying relative grain size on the horizontal axis (c = clay, s = silt, fs = fine-grained sand, cs = coarse-grained sand, and g = gravel); on this column, sedimentary structures (see Fig. 4, "Explanatory Notes" chapter, this volume) and bedding within the cored units are schematically displayed; in addition, clast types are illustrated as follows: black ovals = sedimentary intraclasts; unfilled, sharp-edged shapes = volcanic pebbles and cobbles; and dark, sharp-edged shapes = angular fragments of andesite. We cannot determine whether disturbance in Core 126-793A-4H is a result of drilling or presence of a debris flow with gravel matrix.

nofossil clay and nannofossil clayey silt, 10% nannofossil-rich clay and nannofossil-rich clayey silt, and <1% each of vitric sand, vitric silt, and vitric silty sand. The upper 6 cm of Core 126-793A-1H is a sample of the surface sediment just below the mud line and consists of grayish brown (10YR 5/2) nannofossil-rich vitric clayey silt and nannofossil-rich vitric silty clay.

The pumiceous gravel is generally structureless and poorly sorted (Fig. 6). Maximum clast diameter is about 5 cm. Pumice composition is variable, including rhyolite and andesite. The pumice is highly vesicular (Fig. 7).

The fine-grained sediment types differ from one another in color, nannofossil content, and in the relative proportions of silt and clay. They are generally burrowed and contain scattered granules and pebbles of pumice as large as 3 cm in diameter (Fig. 8). In Core 126-793A-4H, nannofossil clay is very disturbed and consists of masses of this material surrounded by pumiceous gravel. The original relationship of the gravel to the fine-grained sediments is not clear, but local apparent stratigraphic continuity suggests that the pumice layers may have formed thin (<5-cm-thick) beds in the fine-grained sequence (Fig. 9). Conversely, the mixture of fine-grained sediment types and pumice gravel may be analogous to features in Core 126-793A-5H (see the following discussion) that are not believed to reflect drilling disturbance.

There are a few, thin, graded beds of light gray to black vitric sand in Subunit IA (Fig. 10). These may have erosional bases and are parallel laminated.

Subunit IB

Subunit IB (32.5–98.9 mbsf; Cores 126-793A-5H through -11H) consists of 39% pumiceous and vitric sand, 21% nannofossil-rich clay and nannofossil-rich clayey silt, 16% nannofossil clay and nannofossil silty clay, 11% vitric silt, 6% pumiceous gravel, and 4% nannofossil-rich silt. The fine-grained sediment types are generally bioturbated and may contain isolated clasts of pumice as large as 2–3 cm in diameter.

A significant proportion of the pumiceous gravel occurs as matrix around stiff fragments of fine-grained sediments in Core 126-793A-5H (see whole-core photograph in Section 3, this volume). Individual fragments are up to 30 cm thick. The arrangement of sediment types in this core does not appear to be a result of drilling disturbance because long intervals of fine-grained lithologies are tilted, we recorded a full stroke of the APC, recovery was 100%, and no apparent suction and flow-in occurred.

Sections 126-793A-6H-4 and -6H-5 contain an undisturbed bed of sandy pumiceous gravel 140 cm thick. Maximum clast size is 5 cm at the top of this bed. This gravel bed contains crude horizontal stratification (Fig. 11) and appears to be amalgamated, with a sharp grain-size break in Section 126-793A-6H-4 at 139 cm. Immediately above this contact, the upper gravel layer is normally graded, although it has a sharp top.

The beds of pumiceous and vitric sand are variable in thickness and composition, with the two end members being thick horizons of black fine sand in Core 126-793A-8H, and thin to

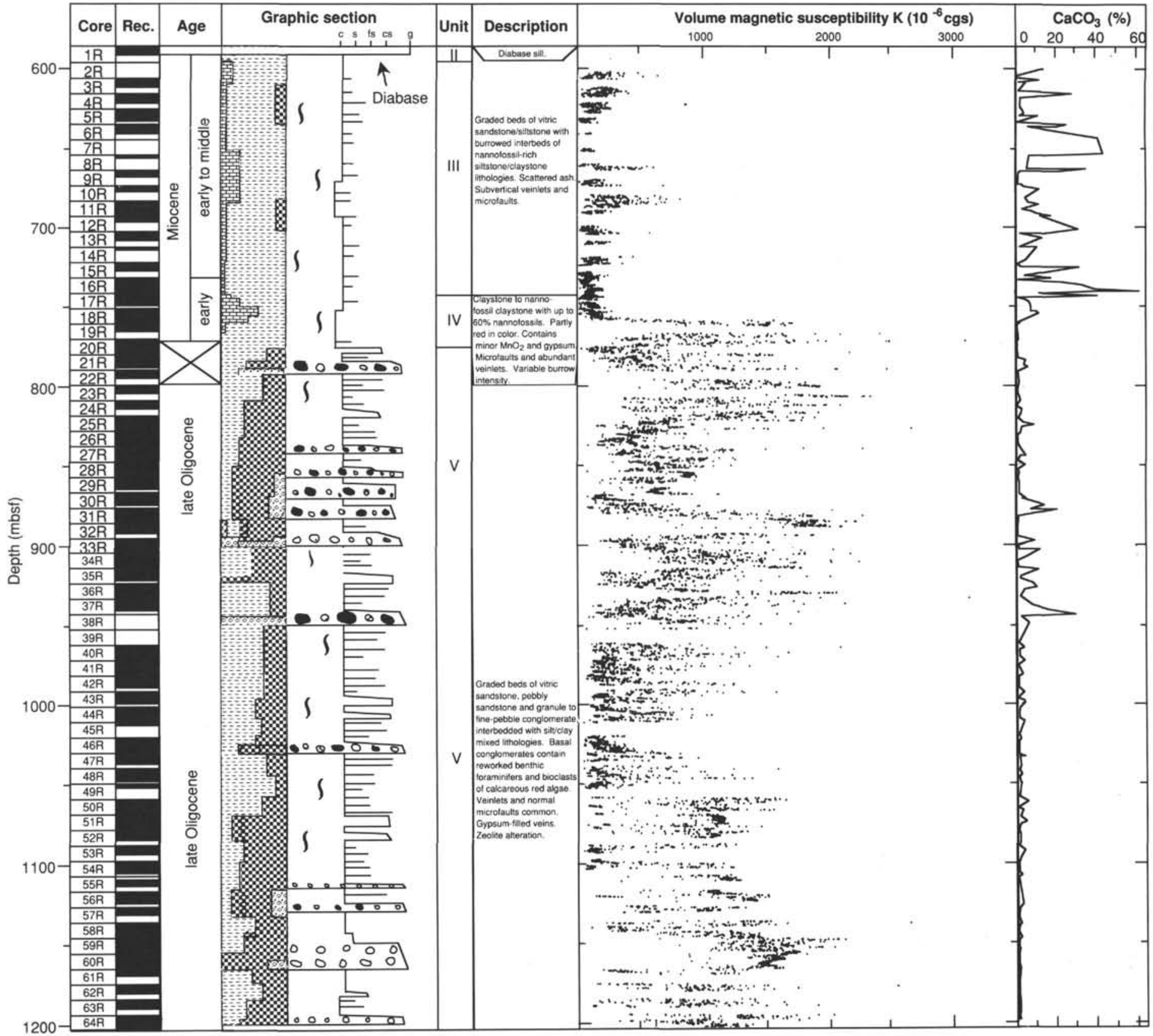

Figure 5. Lithostratigraphic summary for Hole 793B, to the base of Unit VI, including a graphic display of core recovery and the downhole distributions of carbonate minerals and magnetic susceptibility. Symbols are th same as in Figure 4 except that c = claystone, s = siltstone, fs = finegrained sandstone, cs = coarse-grained sandstone, and g = conglomerate.

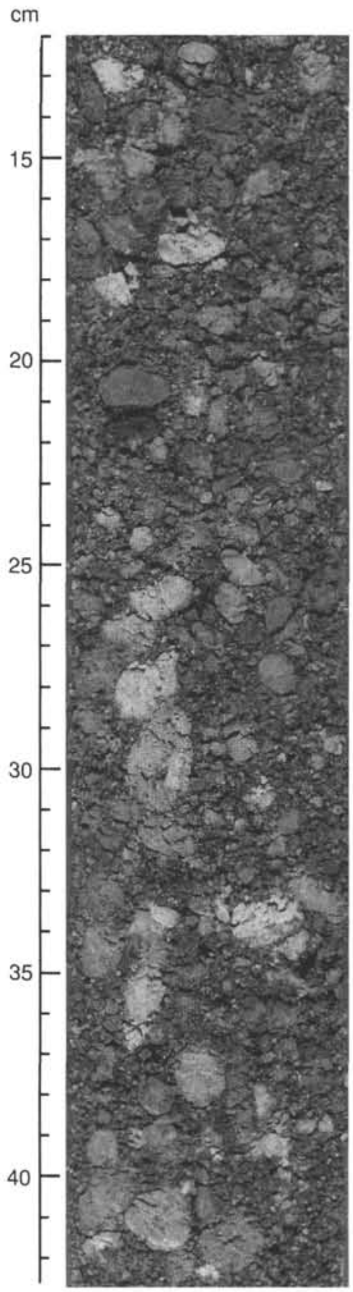

Figure 6. Poorly sorted pumiceous sandy gravel of Unit IA (Interval 126-793A-2H-5, 12–42 cm).

very thin beds of black or white sand throughout (Fig. 12). Thin to medium beds tend to have sharp bases, normal grading (Fig. 13), parallel lamination (Fig. 14), and local cross lamination (Fig. 15). Parallel laminae are defined by grain size fluctuations and by compositional variation (Fig. 16). The tops of the thinner sand beds grade upward into vitric silt. In two cases, this upper silt division is enriched in dusky green (5G 3/2) celadonite (Fig. 15).

The beds of vitric silt tend to be <10 cm thick, dark gray to black, and graded. Some beds contain delicate parallel lamination (Fig. 17). One thin bed of graded vitric silt is overlain by an inversely graded mixture of nannofossil silty clay and sand- to pebble-size pumice clasts (Fig. 18).

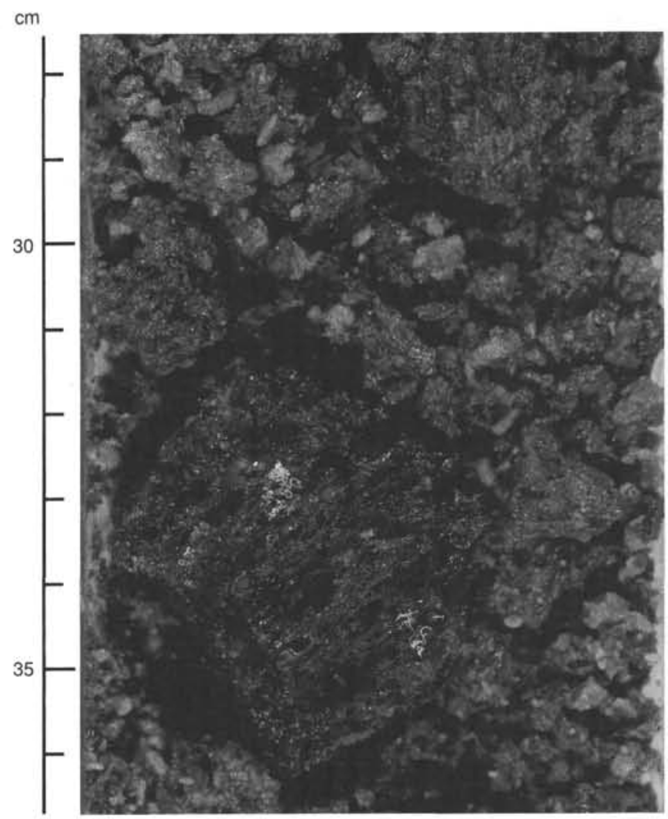

Figure 7. Vesicular pumice clasts in Subunit IA (Interval 126-793A-4H-1, 28–36 cm).

Interpretation of Hole 793A

The pumiceous gravels of Subunit IA are structureless and probably represent the accumulation of waterlogged ejecta from silicic to intermediate caldera eruptions along the nearby Izu-Bonin Arc. Many of the minor vitric sand beds in this subunit contain scour marks and sedimentary structures like those of turbidites (Bouma, 1962), although the turbidity currents in this case may have been generated directly by submarine or subaerial volcanic eruptions feeding large amounts of sandy ash to the water column and to submarine slopes around the arc volcanoes. The burrowed fine-grained sediments in Subunit IA, containing variable amounts of biogenic carbonate as great as 50%, represent quiescent periods between eruptive phases. At these times, the seafloor received pelagic carbonate via settling from the sea surface as well as arc-derived siliciclastic material that was transported by weak bottom currents and/or by surface or mid-water plumes.

Some of the pumiceous gravel in the upper part of Subunit IB may represent primary ejecta that settled to form thin layers in an otherwise fine-grained succession. The disturbed mixture of these materials in Core 126-793A-5H, however, probably represents older deposits that were remobilized into a debris flow, which was probably triggered by a sediment failure along the margin of the paleo-valley (Fig. 2). The failure involved somewhat compacted nannofossil clay, nannofossil silty clay, nannofossil-rich clayey silt, and interbeds of fairly cohesionless pumiceous gravel. The high percentage of fine-grained clasts would have impeded the upward escape of pore fluids, creating elevated pore-fluid pressures in the flow. These elevated pore-fluid pressures account for mobility of the flow in spite of little clay-size matrix (Pierson, 1981).

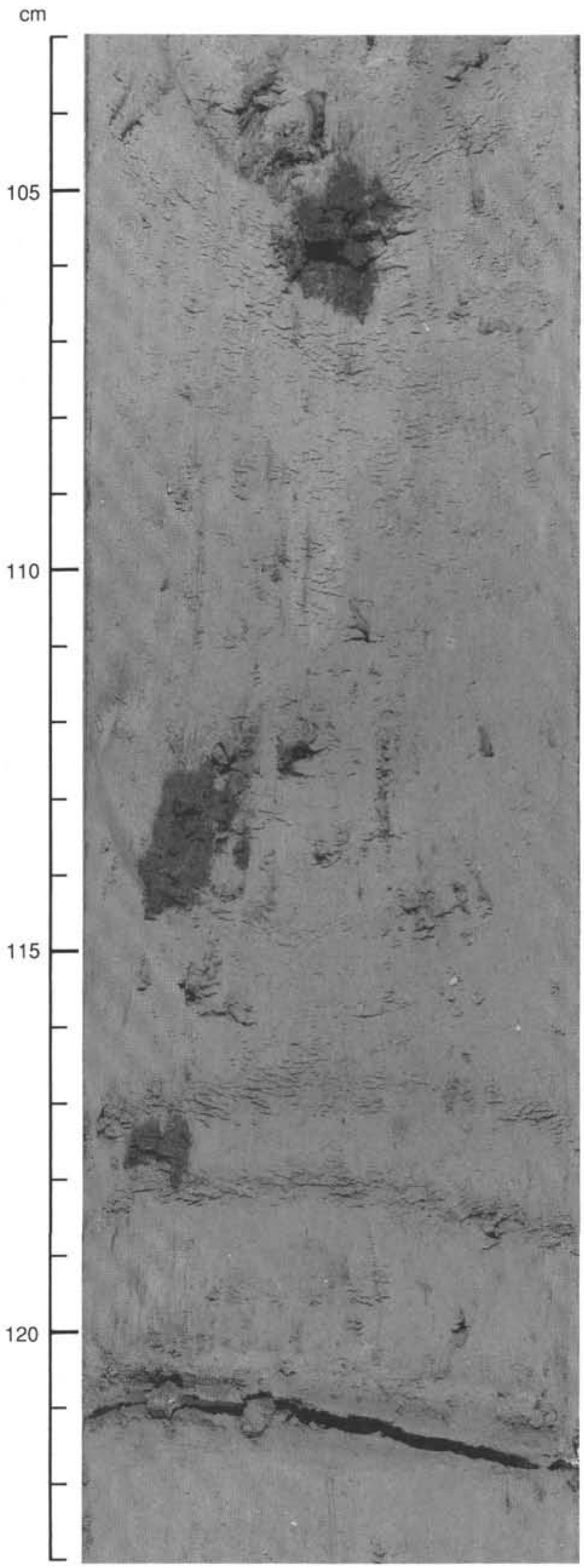

Figure 8. Fine pebbles of dark gray pumice at 104, 105–106, 113–114, and 117–118 cm, partially smeared during the core-splitting process. The surrounding sediment is nannofossil-rich silty clay (Interval 126-793A-3H-2, 103–123 cm).

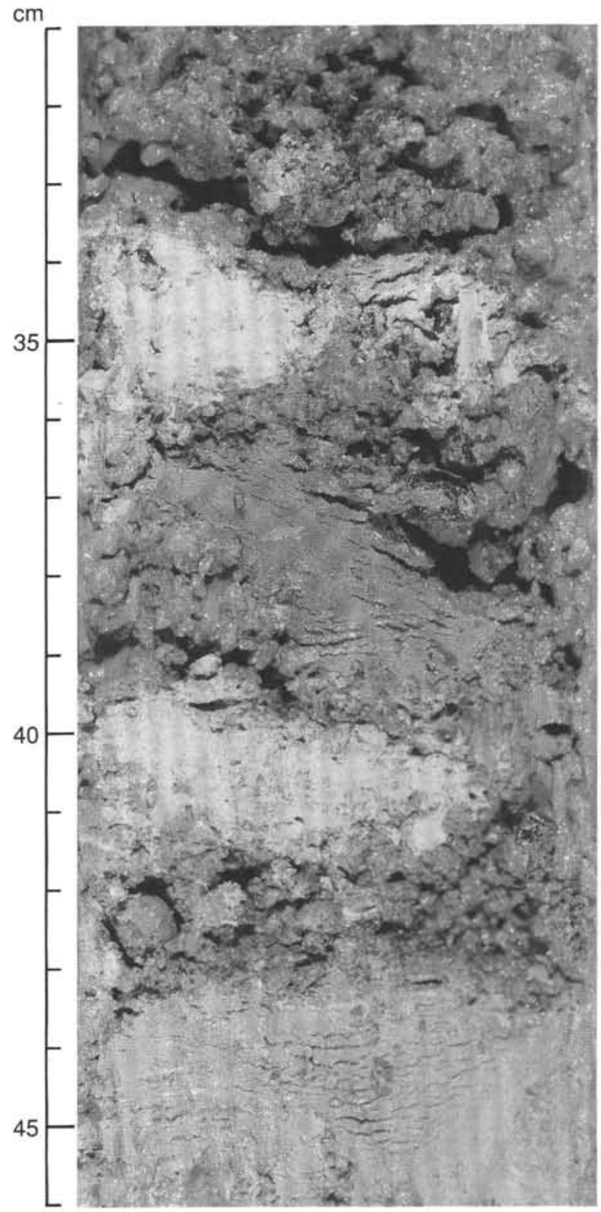

Figure 9. Disturbed nannofossil clay (white), nannofossil-rich clay (gray) and interstitial pumiceous gravel (Interval 126-793A-4H-3, 31–46 cm). The interval from 41 to 44 cm suggests that the pumiceous gravel forms thin interbeds in the fine-grained sediments but this sediment may have been disturbed before coring.

Some graded beds with homogeneous and distinctive composition (e.g., Fig. 12) probably represent primary accumulations of volcanic ash. Most of the pumiceous and vitric sand beds, however, contain tractional structures like those characteristic of turbidite facies. Mixed compositions in some sand beds (e.g., Fig. 16) require some degree of mixing of different source materials before final deposition, a typical feature of resedimented deposits. The thick vitric sand beds in Cores 126-793A-8H through -11H were probably emplaced by high-concentration turbidity currents, although the extent of drilling disturbance prevents recognition of diagnostic primary structures. Such high-concentration flows would have been maintained by turbulence, elevated pore pressures, and grain interaction (dispersive pressure).

Some of the vitric silt beds are probably fine-grained turbidites, and others likely consist of primary ejecta from subma-

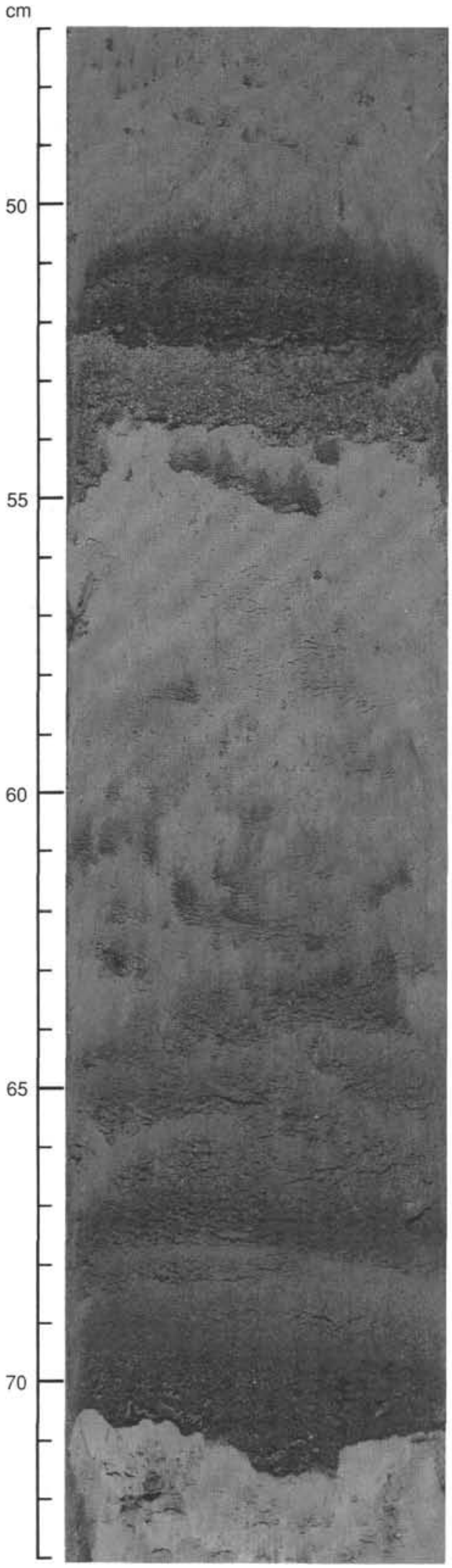

Figure 10. Graded beds of parallel-laminated, fine-grained, black vitric sand, overlain gradationally by burrowed nannofossil-rich silty clay (Interval 126-793A-3H-2, 47–73 cm): The lower sand bed has an erosional base.

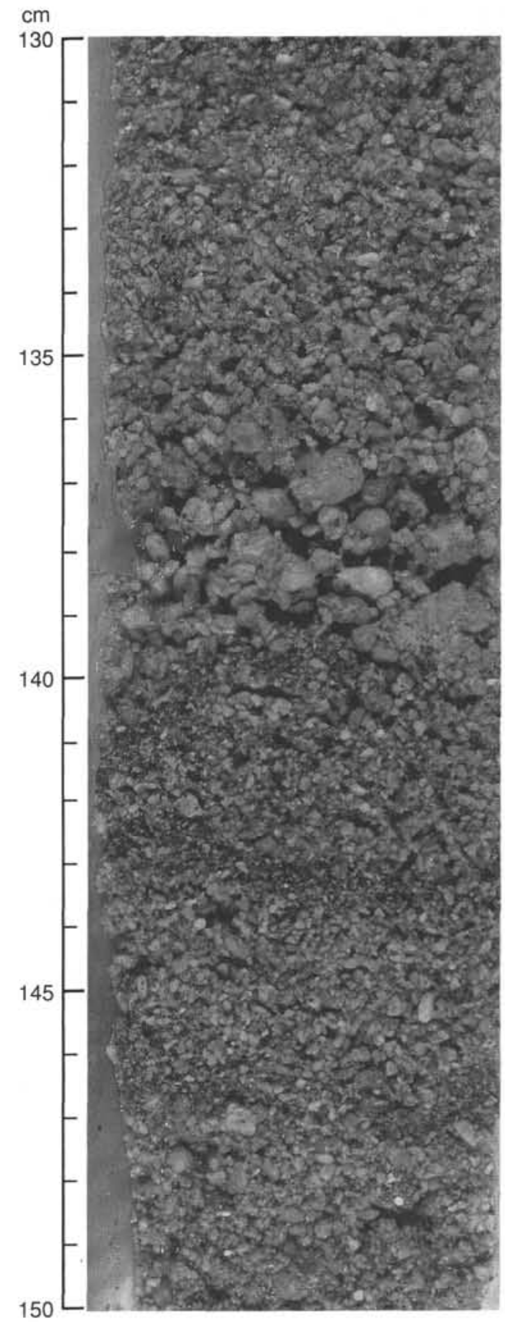

Figure 11. Horizontally stratified, pumiceous pebble and granule gravel in Subunit IB (Interval 126-793A-6H-4, 130–150 cm).

rine or subaerial eruptions. One striking example of a primary volcanic deposit is shown in Figure 18, in which a thin, graded, vitric silt bed is immediately overlain by an inversely graded accumulation of pumice sand and pebbles. A plausible scenario for deposition of these volcaniclastic materials begins with a volcanic eruption, producing high-density black sand and silt grains, probably andesitic glass, and low-density pumice ash. The black sand and silt settled rapidly to form a graded bed. Next, the pumice ash was progressively saturated by water, the smallest grains becoming waterlogged and settling first, followed by increasingly coarser grains.

Biogenic carbonate content in the fine-grained sediments of Subunit IB is commonly 30%–60%, corresponding to times of

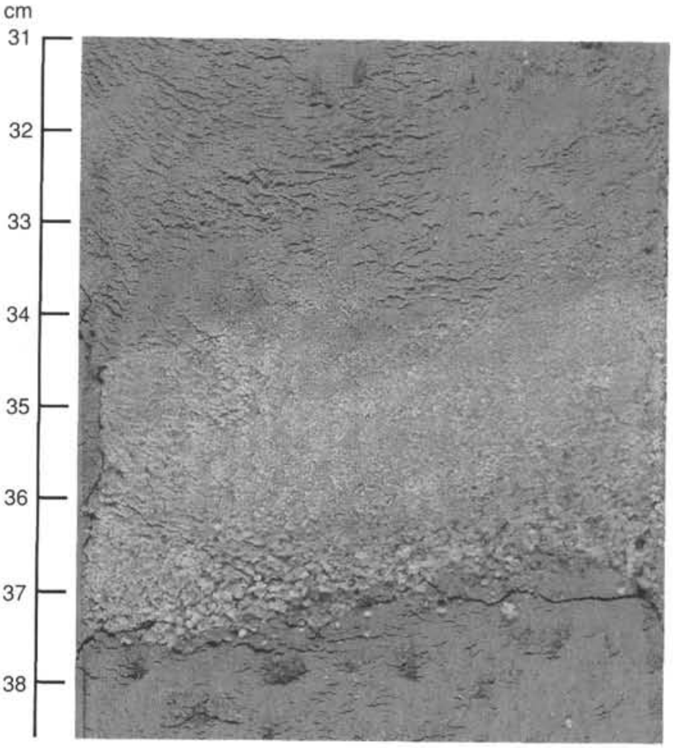

Figure 12. White, graded, pumiceous ash bed, interbedded with nannofossil-rich clayey silt (Interval 126-793A-7H-3, 31–38 cm).

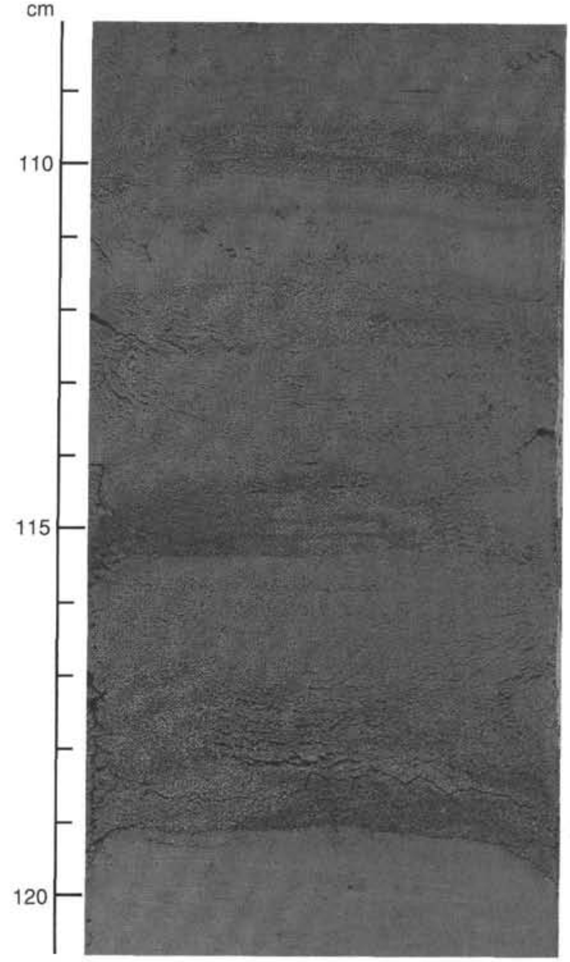

Figure 13. Sharp-based, parallel-laminated, graded beds of vitric sand in Subunit IB (Interval 126-793A-7H-2, 109–120 cm).

slow supplies of volcanogenic materials, either by direct air fall or as a result of resedimentation.

All sediments of Unit I were deposited in an erosional valley that extended into the forearc basin from the landward slope of the trench. The erosional surface has been onlapped and smoothed by the accumulation of carbonate-rich, fine-grained sediments ("hemipelagites"), air-fall/suspension deposits of pumice, thin ash beds, and thinly bedded sand/silt turbidites. Most of the succession in Unit I was deposited between two active, leveed channels on the floor of the valley; the predominance of fine-grained sediments may reflect this interchannel setting. The only facies that reflects deposition in a major submarine valley is the chaotic debris flow in Core 126-793A-5H.

Hole 793B

Hole 793B was cored from a depth of 586.5 mbsf. Units II–VI are described below. Igneous Unit II and the basement Unit VII are described and discussed in detail in the "Igneous Geochemistry" section (this chapter). The other units are sedimentary.

Unit II

Interval: Core 126-793B-1R
Age: younger than middle Miocene
Depth: 586.5–591.0 mbsf

Unit II, consisting of olivine-clinopyroxene diabase, is described in detail in the "Igneous Petrology" section (this chapter). The base of Unit II was determined from drilling records. The top includes 10 cm of epidote-carbonate-rich silicified sediment that is the baked upper contact of the diabase.

Unit III

Interval: Core 126-793B-2R through Section 126-793B-16R-4
Age: early to middle Miocene
Depth: 591.0–735.7 mbsf

The contact of Unit III with the diabase sill was not recovered. The lower contact of Unit III is placed at a sharp change in lithology and color at the top of burrowed nannofossil claystones of Unit IV. The color change is striking, with the drab gray colors of Unit III being replaced downward by light reddish brown (5YR 6/4) sediment at the top of Unit IV. Recovery in Unit III was 43%.

Unit III consists of 24% nannofossil-rich silty claystone, 24% silty claystone, 13% nannofossil-rich claystone, 8% nannofossil claystone, 8% vitric siltstone, 7% vitric sandstone, 4% clayey siltstone, 4% nannofossil-rich clayey siltstone, 3% sandy siltstone, and 2% sandy mudstone. Much of the section consists of graded beds with a lower division of parallel- to ripple-laminated vitric siltstone or vitric sandstone, a middle division of parallel-laminated clayey siltstone to silty claystone, and a cap of strongly burrowed, fine-grained sedimentary rock containing variable amounts of nannofossils (Fig. 19). Carbonate contents in some of the burrowed facies are as high as 40% (Fig. 5). The burrowed rock locally contains disseminated sand-size grains of mafic volcanic glass and/or felsic pumice (Fig. 20). Isolated pebbles of pumice also occur in the burrowed, fine-grained sedimentary rock.

Interval 126-793B-3R-1, 73–107 cm, consists of a bed of very poorly sorted, pebbly, very coarse-grained muddy sandstone, containing large tilted intraclasts of nannofossil-rich clayey siltstone and a cobble of vesicular, intersertal, clinopyroxene-plagioclase basalt 7 cm in diameter (Fig. 21). Chemical analysis of

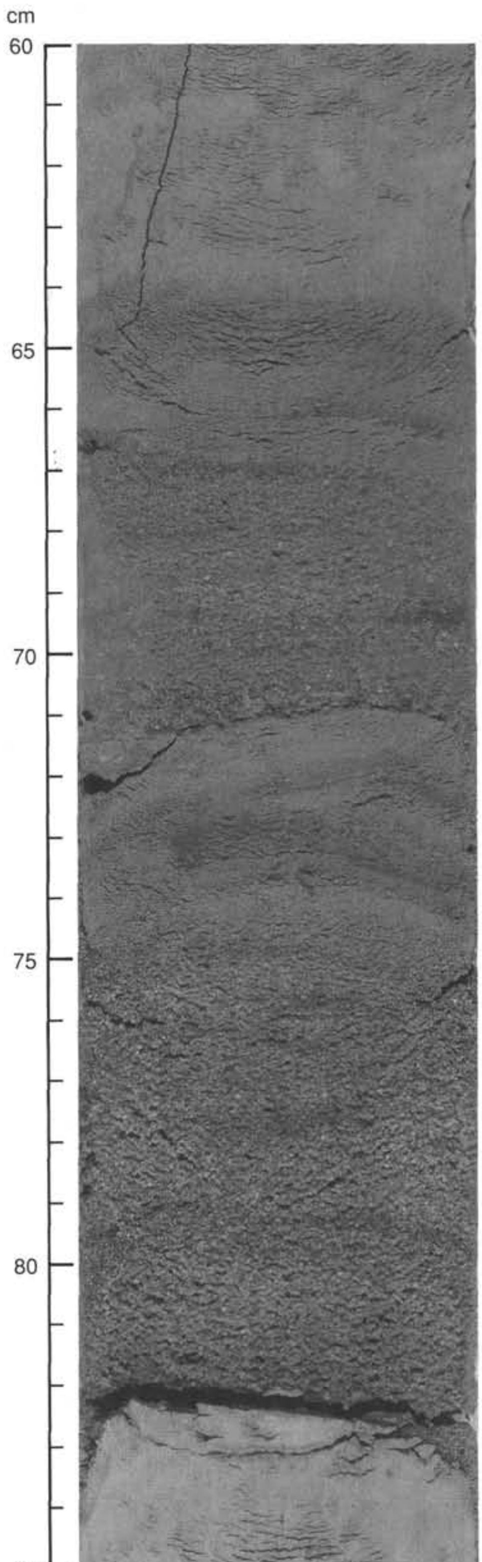

Figure 14. Two beds of parallel-laminated, medium- to fine-grained, pumiceous sand in Subunit IB (Interval 126-793A-6H-2, 60–85 cm). The bases of the beds are at 71 and 82 cm.

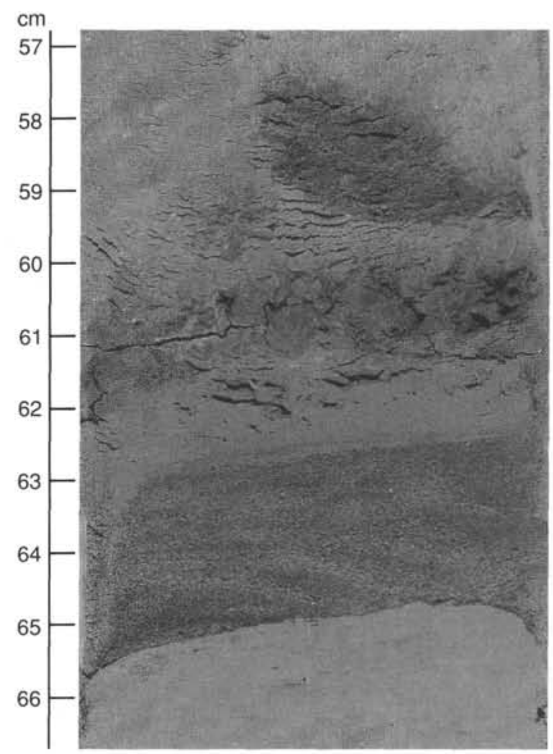

Figure 15. Sharp-based, cross-laminated, graded bed of vitric sand (63–65 cm), overlain by a band of celadonite-rich sediment (60–61 cm). The underlying and overlying sediment is nannofossil clayey silt (Interval 126-793A-7H-2, 57–66 cm).

the basalt is presented in Table 2 (see "Igneous Geochemistry" section, this chapter).

The beds in Unit III dip at 3°–4°. Between 610 and 660 mbsf, there are several occurrences of subvertical veinlets (Fig. 22) like those described from Sites 787 and 792 (see site chapters, this volume), from the Middle America Trench slope by Ogawa and Miyata (1985) and from the Japan Trench by Arthur et al. (1980) and Lundberg and Leggett (1986). Below a depth of 625 mbsf, steeply dipping microfaults and fractures are present (Fig. 23).

Unit IV

Interval: Sections 126-793B-16R-5 through -19R-1 at 60 cm
Age: early Miocene
Depth: 735.7–759.0 mbsf

Recovery of Unit IV was 92%. The most significant lithologic difference between Unit IV and the surrounding sedimentary rocks is the uniformly fine grain size of the material. The unit consists of 47% claystone, 43% nannofossil claystone, 5% nannofossil-rich claystone, 3% vitric siltstone, and 1% each of vitric sandstone and silty claystone. Maximum contents of calcium carbonate (60%) occur in Section 126-793B-17R-1. From the top to the base of Core 126-793B-17R, the color changes downward from light reddish brown (5YR 6/4), through pale red and weak red (10R 6/4, 10R 5/4), through pale yellowish brown (10YR 6/2), to light olive gray (5Y 5/2). Core 126-793B-18R contains intervals with the following colors: light olive gray (5Y 5/2), pale yellowish brown (10YR 6/2), dark gray (5GY 4/1), grayish green (10GY 5/2), olive gray (5Y 3/2), and reddish brown (5YR 4/4). The lower contact of Unit IV, in Section 126-793B-19R-1 at 60 cm, is a rapid downward change from pale yellowish brown (10YR 6/2), slightly burrowed, fissile claystone to

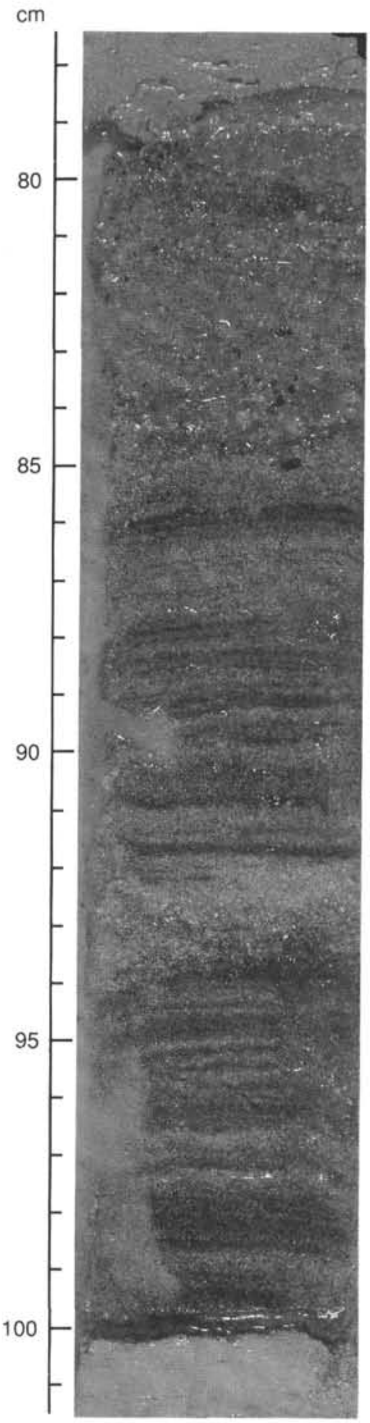

Figure 16. Parallel-laminated sand bed with dark laminae composed of mafic glass and light laminae composed of felsic pumice (Interval 126-793A-7H-1, 78-101 cm). The granules at the top of the bed are low-density pumice clasts. The core is partially obscured by water in the liner.

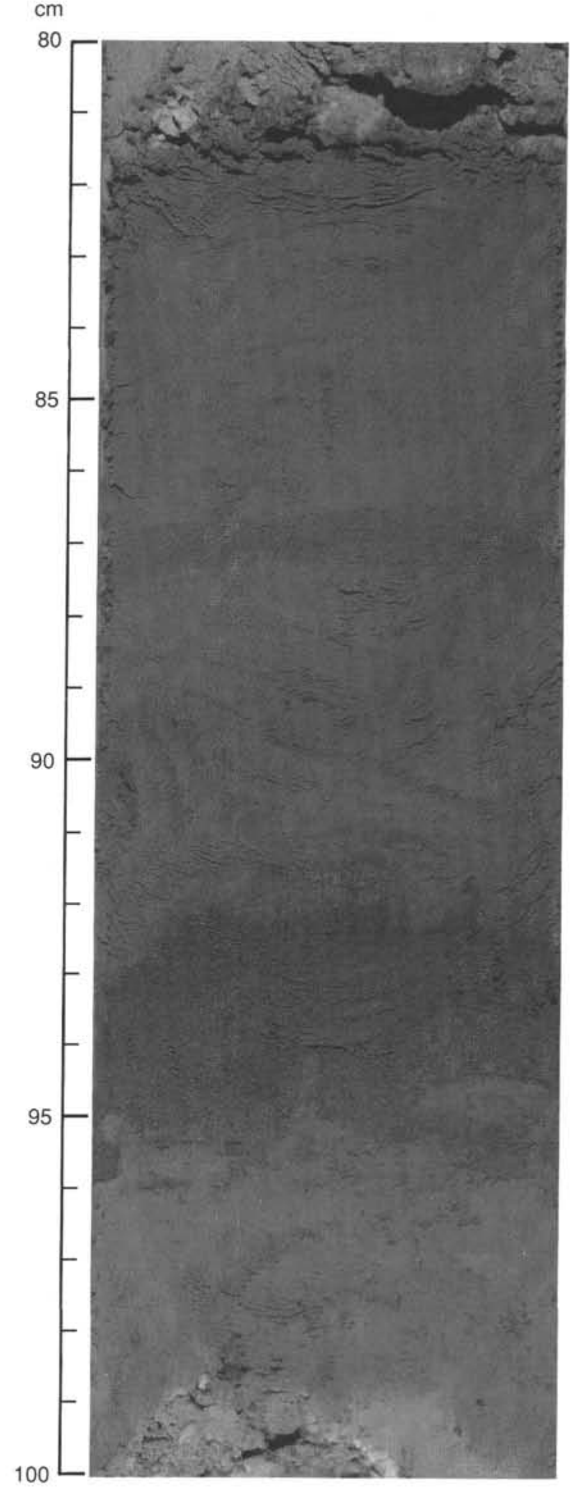

Figure 17. Two probable ash beds that grade from coarse to fine vitric silt. The upper bed (82–87 cm) has delicate parallel laminae in its upper part (Interval 126-793A-5H-4, 80–100 cm).

the typical, slightly calcareous, grayish green (5GY 5/1), strongly burrowed silty claystone of Unit V. This lithologic change is most easily explained by a modification of the surface current pattern and consequent reduction in nannofossil production. A less likely alternative explanation is a change in bottom-water chemistry, causing dissolution of calcareous nannofossils. The 88 cm of silty claystone and claystone between the highest sandstone bed and the contact are much more like the fine-grained rocks of Unit V than the mudrocks of Unit IV.

The main primary structure in these sedimentary rocks is variable degrees of bioturbation. The intensity of burrowing varies directly with the carbonate content, so that the noncalcareous claystones near the base of the unit generally lack bur-

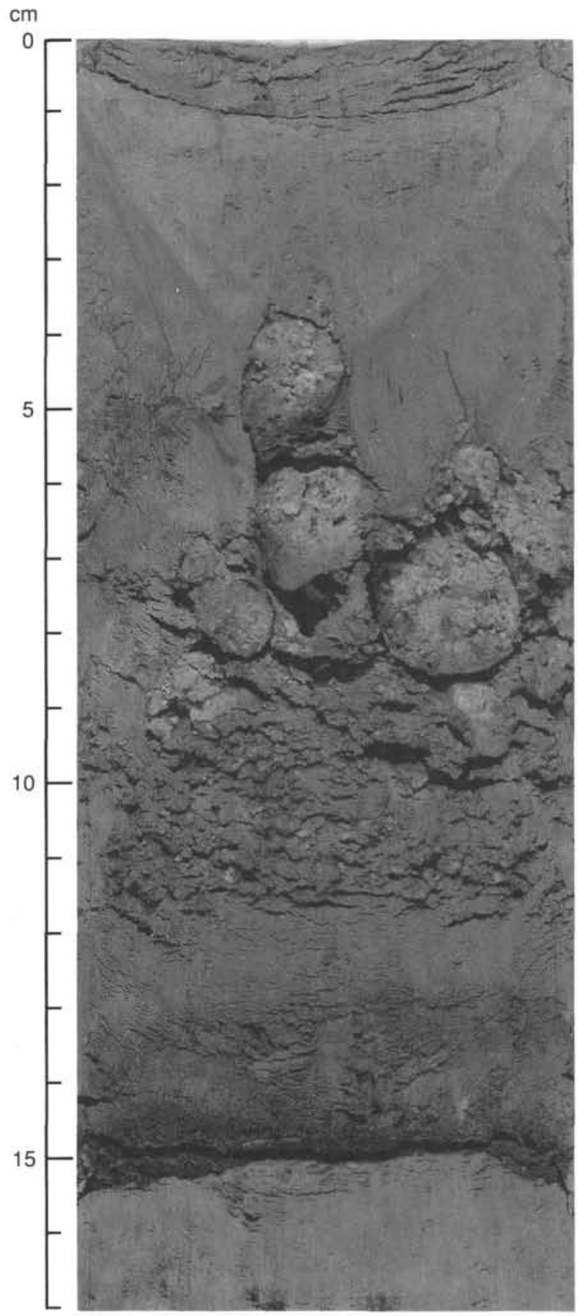

Figure 18. Graded bed of vitric silty ash, overlain by an inversely graded layer of sand- to pebble-sized pumice clasts (Interval 126-793A-6H-2, 0–17 cm). See text for discussion.

rows. These claystones contain only a few very thin (1–3 cm) interbeds of parallel- to ripple-laminated vitric siltstone. Scattered benthic foraminifers are visible in the core.

Unit IV is characterized by a suite of mineralogical and structural features. Sample 126-793B-17R-1, 85 cm, contains a 2 × 4 cm nodule of gypsum. Just below this (Interval 126-793B-17R-2, 10–70 cm), there are black smears and poorly developed dendrites of todorokite (manganese oxide). Much of the rock is cut by subvertical, wavy, dewatering veinlets along which the core is strongly fractured (Fig. 24). There are several, irregular, slickensided microfaults that dip at about 45°–60°. From Section 126-793B-18R-6 to the base of the unit, the claystone is fis-

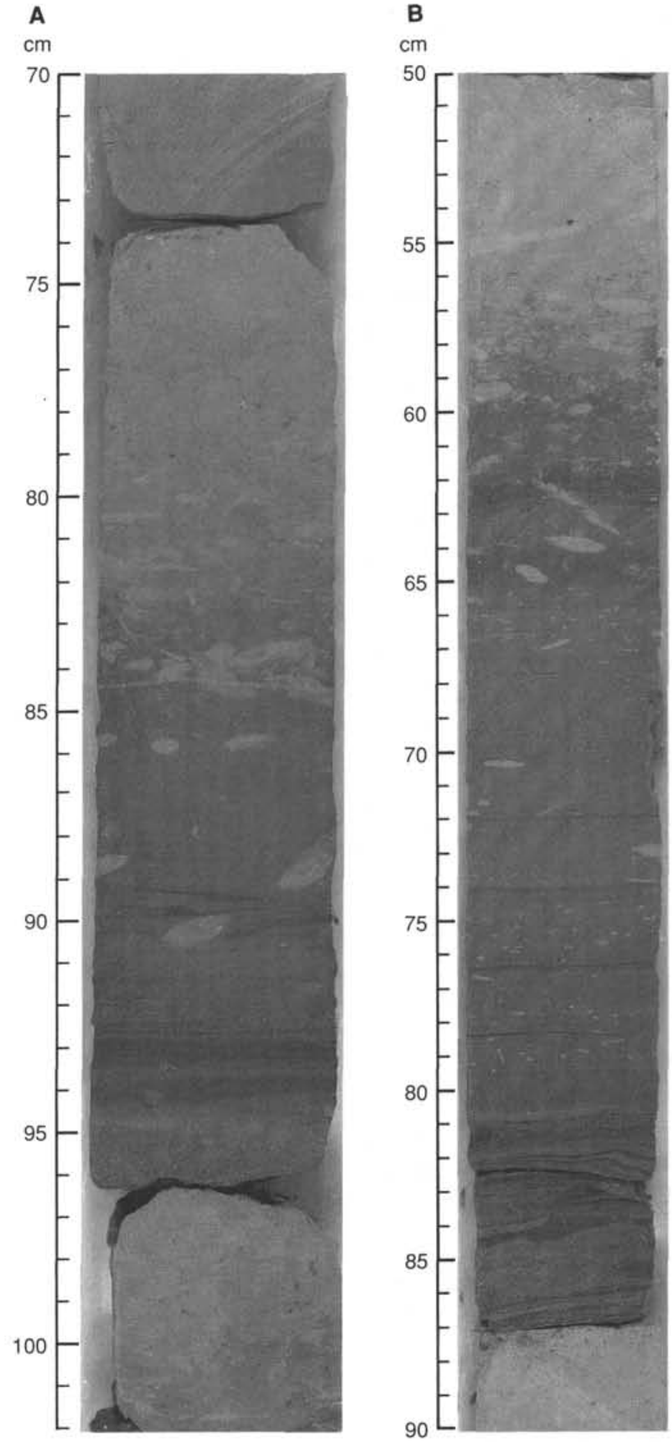

Figure 19. Two examples of graded beds of vitric siltstone, overlain first by parallel-laminated clayey siltstone and silty claystone and then by strongly burrowed nannofossil silty claystone or nannofossil claystone. **A.** A bed with a basal division of cross lamination, overlain by parallel-laminated siltstone cut by a few deep burrows; trace fossils include flattened *Planolites, Zoophycos,* and *Chondrites* (Interval 126-793B-4R-4, 70–102 cm). **B.** A bed with a basal division of parallel lamination, partly modified by soft-sediment deformation, overlain by finely laminated clayey siltstone, and then by nannofossil claystone (Interval 126-793B-6R-2, 50–90 cm).

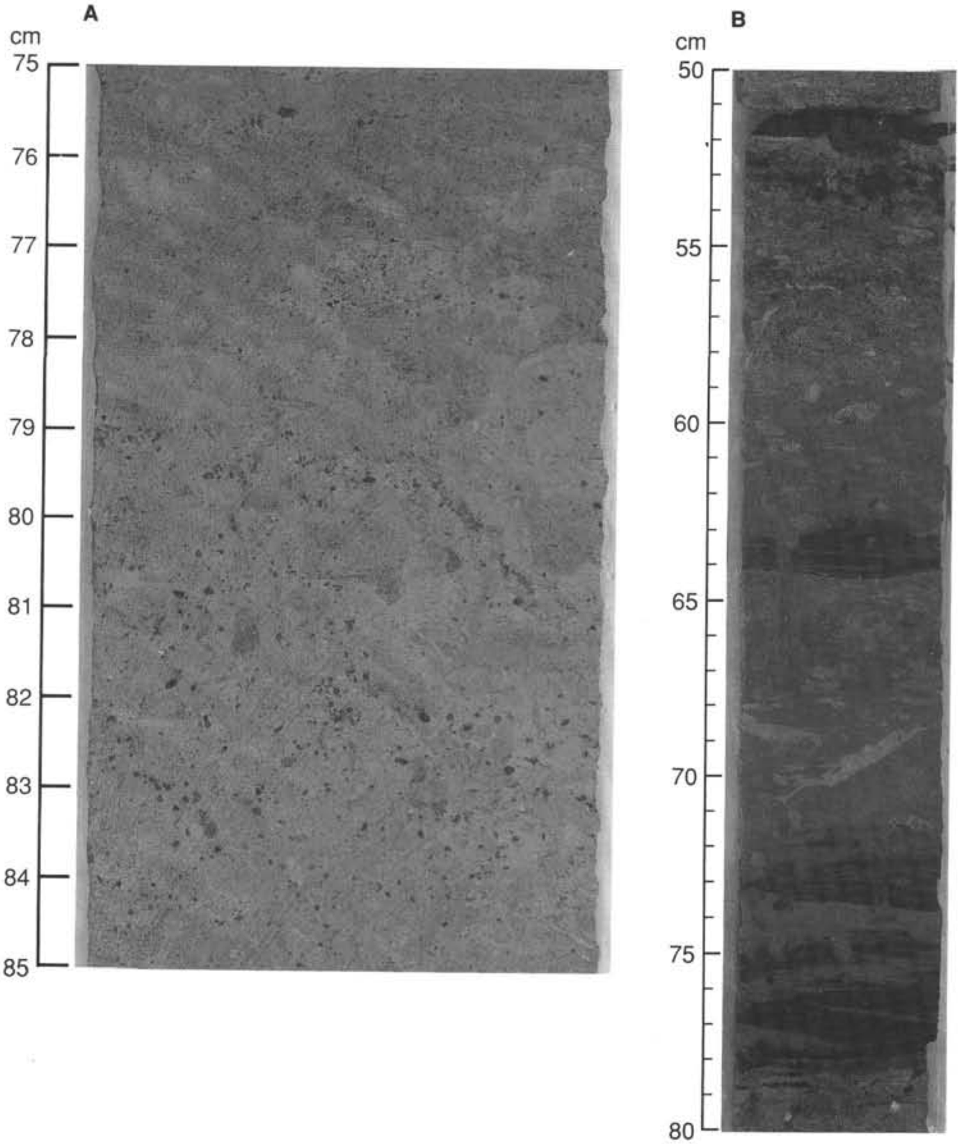

Figure 20. **A.** Sandy mudstone formed by biogenic mixing of fine-grained sediment and mafic ash. (Interval 126-793B-15R-2, 75–85 cm). **B.** Interbedded very thin, graded, parallel- and cross-laminated beds of black vitric siltstone and very fine sandstone, and burrowed silty claystone. From 49–58 cm, the burrowed material contains abundant, dispersed, black sand (Interval 126-793B-11R-1, 50–80 cm).

sile, with a well-developed, bedding-parallel parting. Bedding dips at 8°–10° in this unit.

Unit V

Interval: Sections 126-793B-19R-1 at 60 cm through -82R-6 at 78 cm
Age: early to late Oligocene
Depth: 759.0–1373.1 mbsf

The sharp lithologic change from Unit IV to Unit V is described above. This contact may mark a hiatus. The base of Unit V is a fault that separates the graded sandstone beds of this unit from the volcanic breccia of Unit VI. Recovery of Unit V was 83%.

Unit V is characterized by thin to very thick graded beds of vitric sandstone (Fig. 25) and, in some intervals, pumiceous sandstone (Fig. 26); together, these constitute 50% of the unit. The bases of these beds are sharp, and basal scour marks (e.g., flutes) are present on a few beds (Fig. 27). Fine-grained, carbonate-poor rocks, typically with <5% calcium carbonate, collectively constitute 42% of the unit (claystone, 3%; silty claystone and clayey siltstone, 22%; siltstone, 17%); whereas nannofossil-rich, fine-grained rocks containing about 20% calcium carbonate constitute only 1.5%. Much of the fine-grained sedimentary rock is either the upper, parallel-laminated to slightly burrowed parts of graded sandstone beds, or consists of graded beds of clayey siltstone to silty claystone that are parallel to ripple laminated. Some fine-grained facies in Unit V contain features attributed to wet-sediment deformation of water-rich sediments (Fig. 28). A fine-grained sandstone bed in Interval 126-793B-59R-3, 74–146 cm, contains a small quantity of plant debris.

The sandstones, siltstones, and finer grained sedimentary rocks of Unit V are associated in some parts of the section with thick to very thick beds of pebbly sandstone or granule to fine-pebble conglomerate, some apparently as thick as 5–10 m. The conglomerates constitute 8% of Unit V. The coarsest and thickest beds are concentrated in the lower part of the unit (Figs. 5 and 29). Higher in the section, thick and very thick sandstone

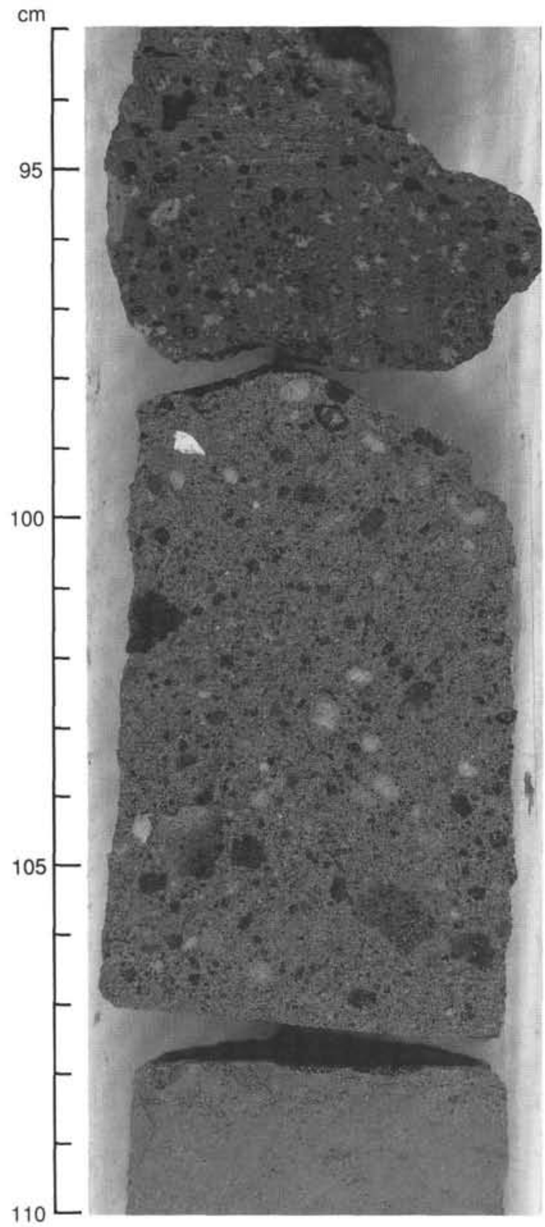

Figure 21. The lower part of a sharp-based, very poorly sorted bed of very coarse-grained gravel-rich muddy sandstone (98–107 cm). Above the sediment shown in this photograph (73–93 cm), the bed contains large, tilted intraclasts of nannofossil-rich clayey siltstone that are a minimum of 15 cm across. A cobble-sized clast of basalt, 7 cm across, is shown in the upper part of the photograph (93–98 cm; Interval 126-793B-3R-1, 93–110 cm).

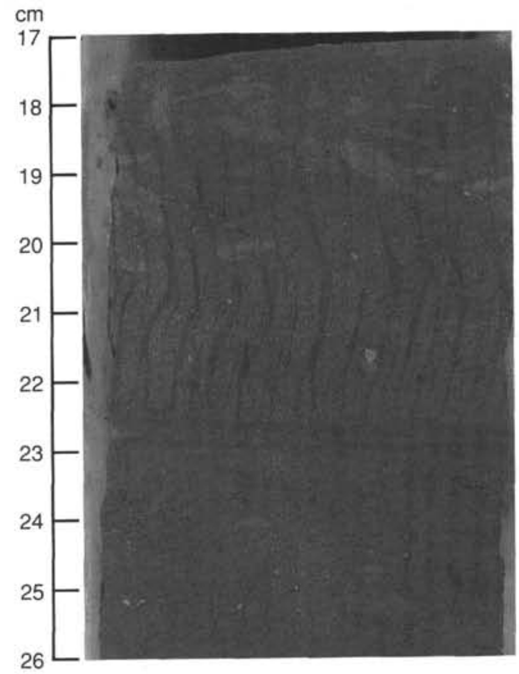

Figure 22. S-shaped, subvertical, locally bifurcated dewatering veinlets in silty claystone of Unit III (Interval 126-793B-12R-1, 17–26 cm).

beds appear to be randomly distributed and are absent in the uppermost part of the unit. This distribution defines an overall upward-fining trend throughout Unit V.

Examples of five of the very thick beds are sketched in Figure 30. Examples A, B, and C are characterized by very poor sorting, poorly developed clast fabric and grading (the latter, if present, is restricted to the top of the bed in divisions of parallel or ripple lamination), and concentrations of cobble- to boulder-size intraclasts well above the base of the bed. Example C contains fluid-escape pillars in its upper part (Fig. 31A); Examples D and E contain intraclasts that are tens of centimeters in diameter, but these tend to be confined to the lower part of the bed. Thick divisions of parallel- and ripple-laminated sandstone form the upper parts of these beds, and step-wise normal grading is well developed. Some beds are inversely graded at the base (Fig. 32).

Some of the intraclasts in the conglomerates are composed of more than one lithology. These clasts were probably partly consolidated before incorporation into the flows; otherwise, they would have been quickly disaggregated by shear during transport.

The very thick sandstone beds in Unit V are also poorly organized and lack tractional structures except at the top of the bed. A 6-m-thick sandstone bed in Core 126-793B-51R contains dish structures in its lower part (Fig. 31B) and broad fluid-escape pillars and injections of sandstone near its top.

Volcanic clasts in the conglomerates of Unit V are mainly clinopyroxene-orthopyroxene-plagioclase andesite + opaques ± quartz. There are minor clasts of hornblende-augite dacite; intersertal, quenched basalt; brick-red rhyolite with quartz phenocrysts, orthopyroxene and magnetite; white and red pumice; and basaltic scoria.

Smear-slide estimates of Unit V sandstone and siltstone compositions were hampered by intense diagenetic alteration of constituent grains and an abundance of authigenic cements. The vitric and crystal components of these rocks have been altered (possibly by dissolution-precipitation reactions) to clay minerals and zeolites that are often indistinguishable from pore-filling cements; thus, smear-slide descriptions are an unsatisfactory way to recognize original framework detrital modes. Additional problems are related to sandstone induration, which required that sediment be forcefully scraped to make the smear slide, breaking up grains and artificially increasing the amount of silt- to clay-size material. Often silt-size, clay-mineral vesicle fillings could be seen in smear slides, implying that vesicular altered glass had been crushed during sample preparation. Thin sections were prepared to help resolve these problems.

We examined 14 sandstone thin sections. This sample set spans the entire Unit V, from the top (Sample 126-793B-20R-4, 96 cm; 773.5 mbsf) to the base (Sample 126-793B-82R-CC, 11

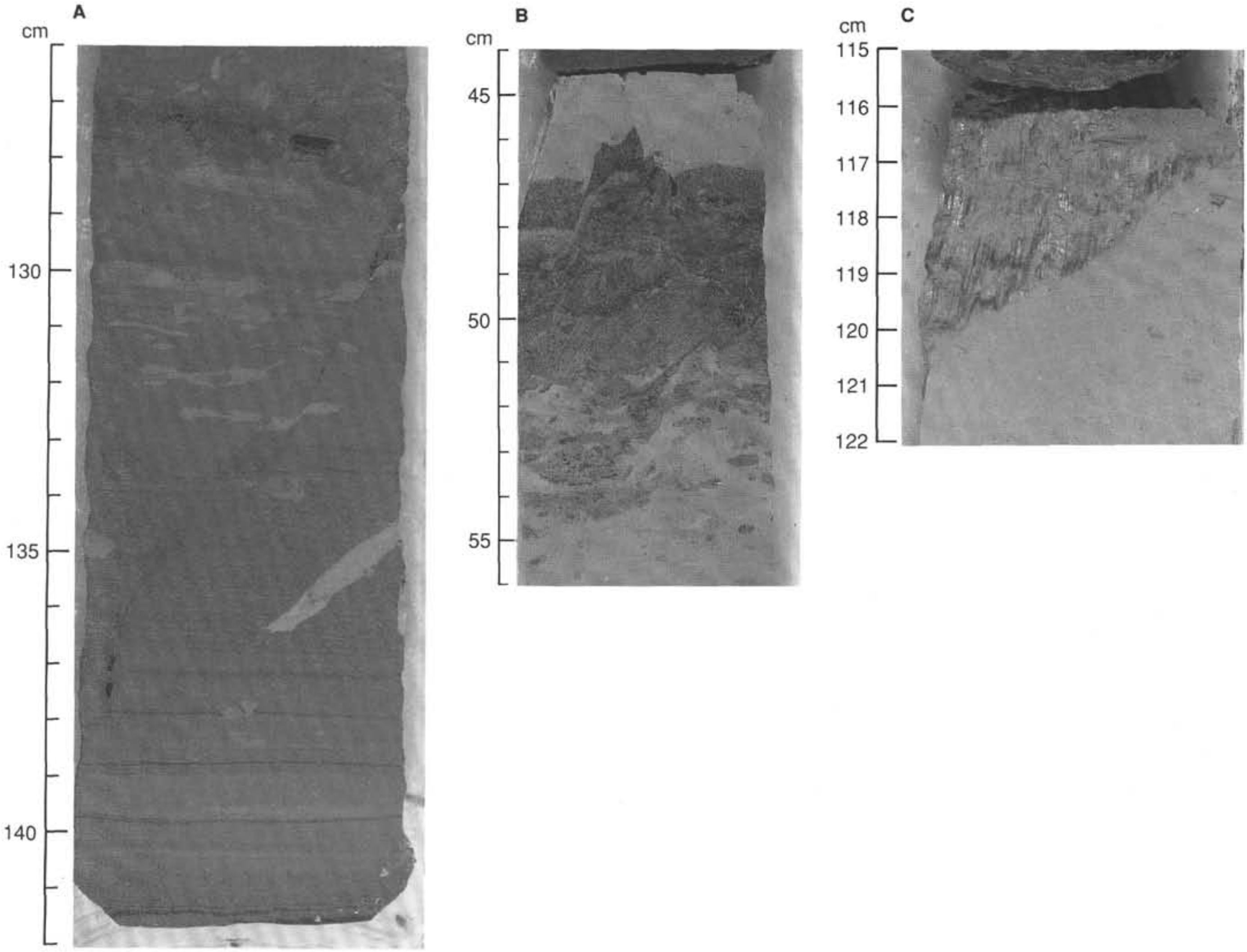

Figure 23. Normal microfaults in Unit III. **A.** Steeply dipping, curved fault with a few millimeters of displacement in parallel-laminated silty claystone (Interval 126-793B-5R-4, 126–142 cm). **B.** Steeply dipping, conjugate faults with displacements of about 1 cm in nannofossil-rich silty claystone (light gray), and burrowed sandy mudstone (Interval 126-793B-14R-1, 44–56 cm). **C.** Slickensides on a fault surface that cuts across nannofossil-rich claystone (Interval 126-793B-8R-1, 115–122 cm).

cm; 1375.3 mbsf). Visual estimates of grain and cement percentages show no distinct trends with depth. The sandstones are generally rich in vitric components, with less abundant crystals and lithic grains; hence, they are best described as crystal-vitric or lithic-crystal-vitric sandstones. Mean estimates of the proportion of the various framework grain types is as follows: 71% volcanic glass, 15% plagioclase feldspar, 4% lithics, and 9% heavy minerals. Included in the volcanic glass category are vitric grains exhibiting a wide range of vesicularity (nonvesicular to pumiceous) and containing variable percentages of plagioclase microlites and phenocrysts. The majority of the vitric material, except for opaque, dark brown to black glass, appears to be altered to zeolites and/or green to brownish green clay minerals. The major crystal component, plagioclase feldspar, is moderately to completely replaced by zeolites throughout the unit. Accessory minerals are predominantly pyroxene and opaques with rare hornblende. Rock fragments include (1) holocrystalline, polymineralic, hypabyssal volcanic or intrusive grains consisting of plagioclase in various combinations with hornblende, opaques, and clinopyroxene; and (2) metavolcanic grains altered by hydrothermal or low-grade metamorphic processes. Microfossils/bioclasts include planktonic foraminifers, reworked benthic foraminifers, fragments of calcareous red algae, bryozoans, and very rare coral. The reworked bioclastic debris is predominantly in the lower part of the unit, mainly in Cores 126-793B-74R through -80R.

Interparticle porosity appears to be minor because two major phases of cementation permeate sandstones within Unit V. The first type is a green to greenish brown, clay-mineral rim to pore-fill cementation, which is followed by stage(s) of zeolite rim to pore-fill cementation. Zeolite crystals are fibroradiating to lath-shaped to blocky. These cements are ubiquitous throughout Unit V except for the lowermost sample studied (Sample 126-793B-82R-CC, 11 cm). Whole-rock X-ray diffraction (XRD) results indicate the presence of a wide range of authigenic minerals: heulandite, clinoptilolite, analcime, phillipsite, mixed-layer mica-smectite, pyrophyllite, and chabazite (Table 3).

A common diagenetic feature noted during visual core description of sandstones was "snowflake" alteration, consisting of closely spaced, 1–2-mm-scale, delicate, white, lacelike spots. A thin-section of this material displays localized centers of low-birefringent, fibroradiating zeolite (heulandite or chabazite) as

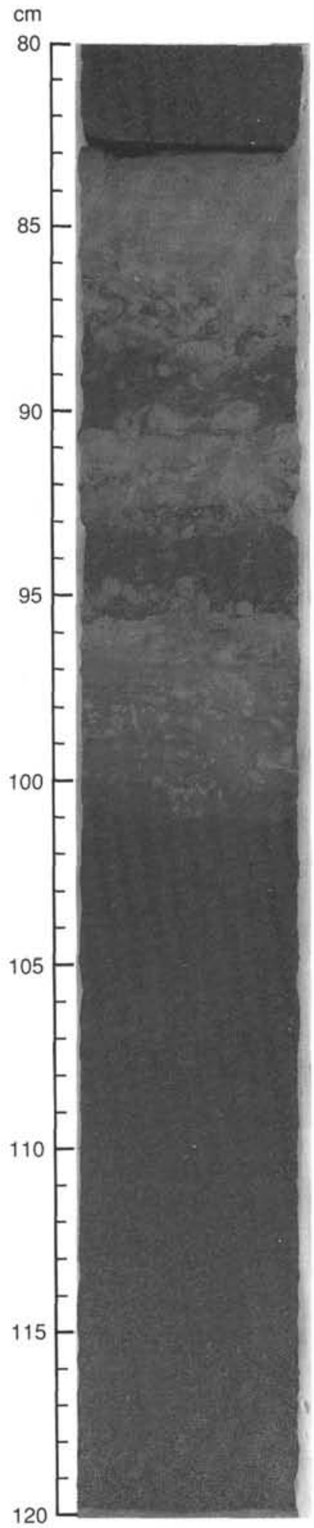

Figure 24. Strongly burrowed nannofossil claystone of Unit IV, cut by abundant subvertical dewatering veinlets (Interval 126-793B-16R-5, 80–120 cm). In places, the core is fractured along the length of the veinlets.

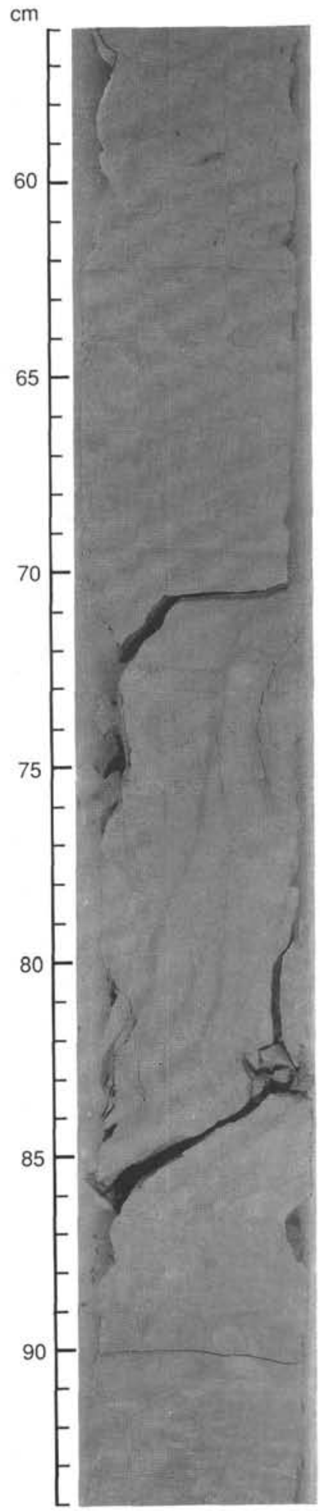

Figure 25. Very thin to medium graded beds of fine-grained vitric sandstone, separated by burrowed horizons of clayey siltstone, in the upper part of Unit V (Interval 126-793B-19R-3, 56–94 cm).

both grain alteration and cement (Sample 126-793B-60R-3, 128 cm).

Where cementation/alteration is minor, smear-slide estimates are similar to thin-section percentages. For example, smear-slide Sample 126-793B-21R-1, 80 cm, had the following framework composition: 10% feldspar, 3% lithics, 82% vitric grains, and 5% accessory minerals. A thin section from an adjacent interval (Sample 126-793B-21R-1, 83 cm) contains 11% feldspar, a trace of lithics, 84% vitric grains, and 5% accessory minerals (same operator).

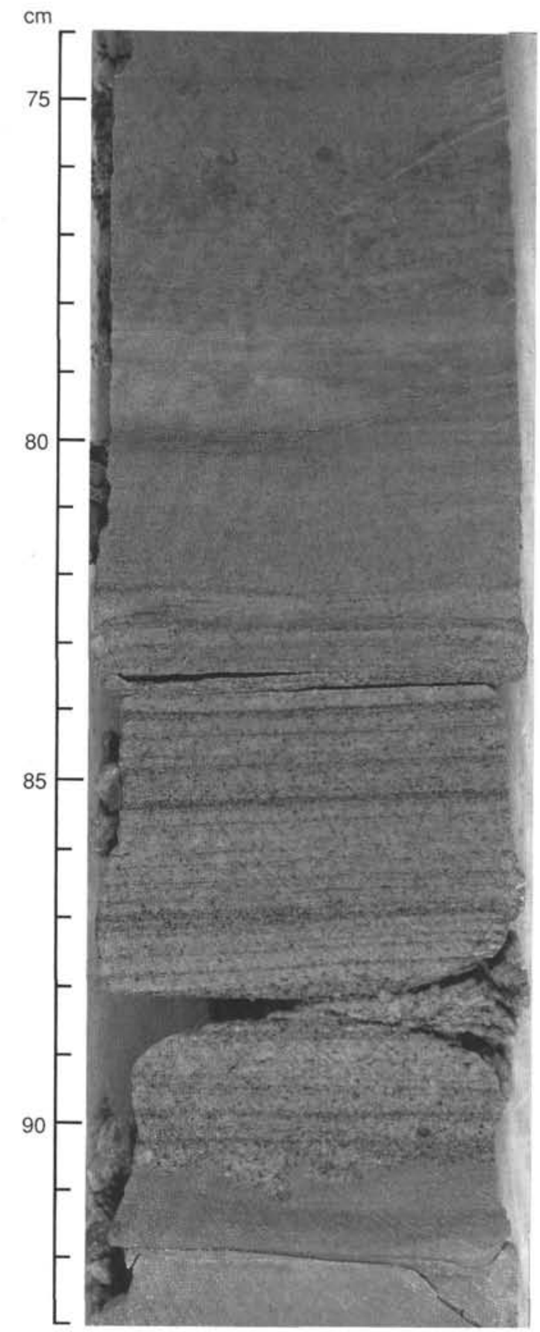

Figure 26. Sharp-based, graded, parallel-laminated bed of pumiceous medium-grained sandstone. There is a thin ripple-laminated division at 82–83 cm, beneath the upper parallel-laminated division of very fine-grained sandstone. The base of this bed is irregular as a result of erosion, possibly modified by loading. The underlying lithology is vitric siltstone (Interval 126-793B-20R-7, 74–93 cm).

Unit V is just over 600 m thick, and parts of this section are characterized by distinctive bedding styles or grain compositions. Rather than describing all parts of the unit in detail, two examples of the facies associations that occur in this unit are highlighted (Fig. 29).

The first of these associations (Fig. 29A) is characterized by an alternation of very thin- to medium-bedded, graded sandstone with thick to very thick beds of pebbly sandstone or granule to fine-pebble conglomerate. The conglomeratic beds contain intraclasts of silty claystone as large as 70 cm across, some of which are internally folded (Fig. 33).

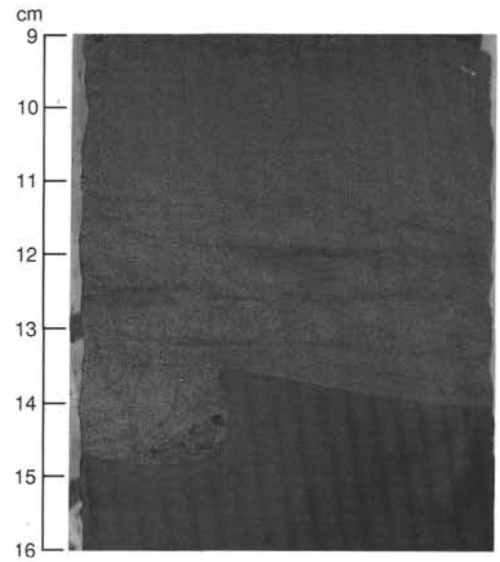

Figure 27. Example of a nose of a flute cast on the base of a graded, fine-grained sandstone bed (Interval 126-793B-47R-3, 9–16 cm). Note the accumulation of coarse and very coarse sand grains in the former zone of flow separation at the upstream end of the flute cast. Ripple laminations in the sandstone bed confirm that flow was from right to left.

An interval from ~900 to 1020 mbsf, partly shown in Figure 29A, is characterized by large quantities of pumice in sandstone beds (Fig. 34). This partly overlaps with an interval of anomalously low sediment bulk density from 950 to 1050 mbsf (see "Physical Properties" section, this chapter). Alteration of much of the pumice to celadonite (see the following discussion of XRD analysis) results in a dusky blue-green (5BG 3/2) color for this rock. The pumice tends to occur well above the base of the beds, as concentrated bands in parallel-laminated sandstone. In many beds, the increase in pumice size and abundance away from the base of the bed produces inverse grading. Low-density pumice granules and fine pebbles appear to have been transported by flows that also carried more sand-size dense crystals and glass grains. Laminae rich in pumice may have formed as a result of subtle changes in flow velocity and concentration.

The second facies association that we use as an example of Unit V is typified by very thick beds of pebbly sandstone and volcanic-lithic conglomerate (Fig. 29B). The thickest beds with no evidence for internal amalgamation are 10–15 m thick (e.g., Fig. 30A). These conglomerates and pebbly sandstones, as in the overlying section to a depth of about 1180 mbsf, contain scattered, resedimented benthic foraminifers up to ~5 mm in diameter (Fig. 35). Beds in Cores 126-793B-72R through -80R also contain pebble-size bioclasts, up to 2 cm in diameter, of calcareous red algae and coral-bearing limestone (Fig. 36).

Bedding in Unit V dips at a maximum of about 10°. Structural features include steeply dipping fractures, mineral-filled fractures and faults, and microfaults (Fig. 37), as well as more significant faults that juxtapose different rock types (Fig. 38). Most faults dip at about 45°–60°, and many have slickensided surfaces. Gypsum is the most common mineral along fault planes and in veins or fractures (Fig. 39).

The lower part of Unit V contains steeply dipping (about 60°) or cross-cutting (Fig. 40), light-colored, 1–3-mm-thick bands or zones in sandstone beds that appear to differ from the surrounding rock only in clay content. The dip of these features is

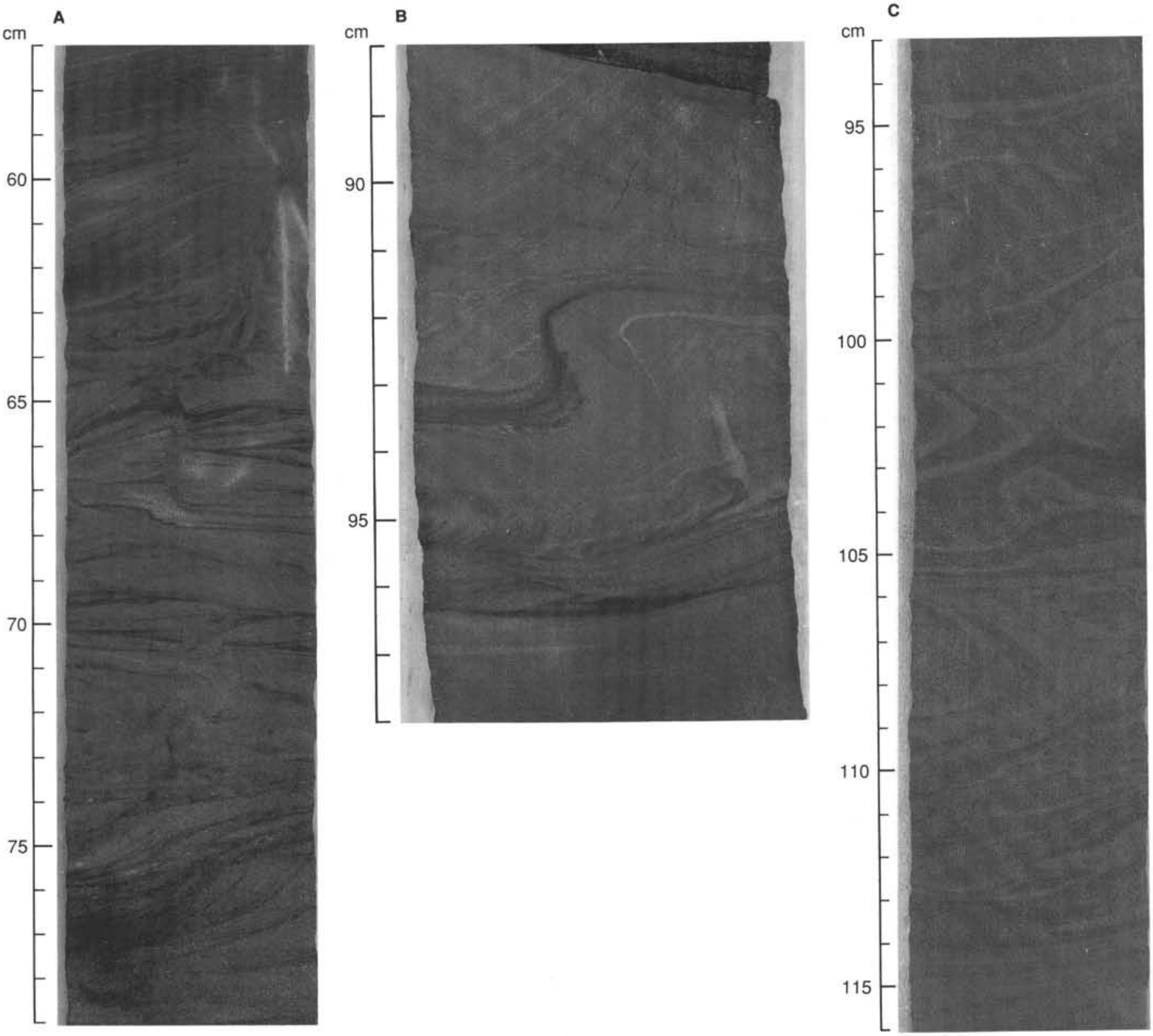

Figure 28. Examples of wet-sediment deformation in Unit V. **A.** The upper, predominantly ripple-laminated division of a bed that grades from coarse-grained to very fine-grained sandstone. The base of the bed is at 107 cm in this section. There is a liquefied, partly homogenized zone from 69 to 74 cm, and synsedimentary faults and clastic injections from 60 to 67 cm (Interval 126-793B-40R-3, 57–79 cm). **B.** Plastically folded parallel laminae and oversteepened cross laminae in a graded siltstone bed with base at 96 cm (Interval 126-793B-42R-1, 88–98 cm). **C.** Plastically folded fine-grained sandstone and siltstone interbeds (Interval 126-793B-72R-3, 93–116).

similar to the dip of associated microfaults in the fine-grained sediments.

Unit VI

Interval: Section 126-793B-82R-6 at 78 cm through Core 126-793B-85R
Age: early(?) Oligocene
Depth: 1373.1–1403.9 mbsf

The top of Unit VI is a fault of unknown displacement. The base is also a sheared fault zone (see "Downhole Measurements" section, this chapter), but it is defined as well by the shipboard petrologists as the place where volcanic clasts that are identical in composition to lava flows in the basement form essentially 100% of the coarser material in the rock. The composition of these flows is clinopyroxene-orthopyroxene-plagioclase andesite, with pyroxene more abundant than plagioclase (see thorough discussion of the definition of this contact in the "Igneous Geochemistry" section, this chapter). Recovery was 34%. The only lithology in this unit is grayish green (5G 5/2), very poorly sorted volcanic breccia and microbreccia. Most clasts are angular (Fig. 41), although some are subangular to subrounded. In Section 126-793B-83R-1, this material has a matrix of zeolitic claystone that forms about 10% of the rock. Below this level, there is little claystone matrix between sand- and granule-size volcanic grains and crystals.

Clasts, up to 30 cm in diameter, are fragments (with chilled margins) of vesicular, clinopyroxene-orthopyroxene-plagioclase

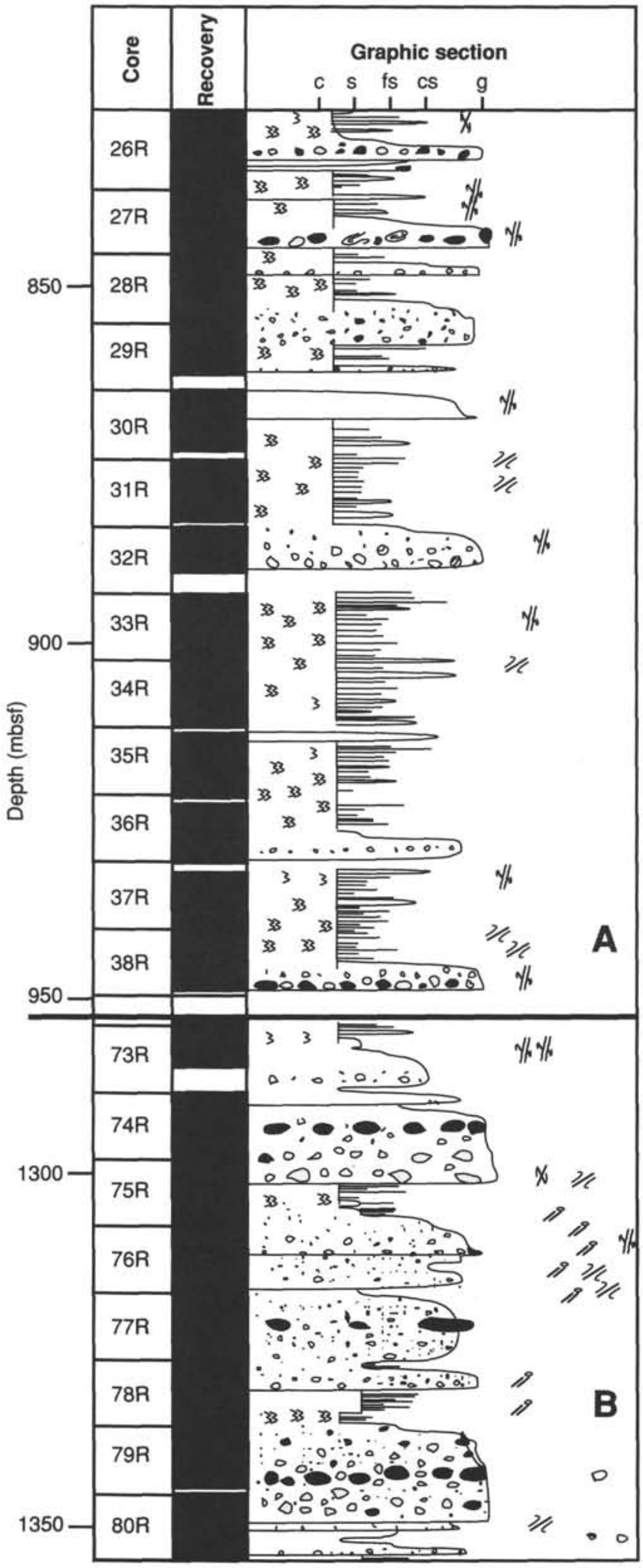

Figure 29. Examples of facies associations in Unit V. See text for discussion. The width of the column varies with grain size. Symbols are the same as those used on barrel sheets and explained in the caption to Figure 5. **A** and **B** indicate separate examples.

andesite + opaques ± quartz. Plagioclase is more abundant than pyroxene. The chemistry of these clasts is similar to the chemistry of the basement at Site 792 (see "Igneous Geochemistry" section, "Site 792" chapter), but different from the chemistry of the immediately underlying basement (see Table 3 and "Igneous Petrology" section, this chapter). Smectite occurs in the vesicles of these clasts. In Cores 126-793B-84R and -85R, there are also clasts of andesitic tuff and clinopyroxene-phyric basaltic andesite. Some other clasts resemble hyaloclastites.

X-Ray Diffraction Analysis

The results from XRD analysis of 97 samples from Units I through VI are summarized in Table 3. The main processes that these data record are replacement of volcanic glass by clay minerals and zeolites, alteration of feldspar, and cementation in coarse-grained sediments. Presentation of mineralogical data for Unit V is divided into six parts, each corresponding to a particular depth, because of the great thickness of this unit, and because diagenetic alteration varies considerably from the top to the bottom of the unit.

Unit I

The XRD data confirm that the nannofossil-rich silty clays of Unit I contain abundant calcite. Vitric silts and sands contain little calcite. Quartz, feldspar, smectite, and chlorite are common in all samples. Chlorite reflects the high Mg concentration of interstitial water (see "Sediment/Fluid Geochemistry" section, this chapter). Mica-group minerals are present in silts and clayey silts. Pyrolusite (MnO_2) and maghemite (τ-Fe_2O_3) occur in a black vitric silt (ash) bed (Sample 126-793A-5H-6, 70 cm). Volcanic glass is partially altered to palagonite and smectite. Most glass, however, is still amorphous, producing a high background around 0.33 nm; this glass is clear and colorless in smear slides. Pyrite (FeS_2) is present in nannofossil-rich silty clay near the base of the unit (Sample 126-793A-11H-1, 36 cm).

Unit III

The XRD analyses show abundant calcite in the fine-grained, burrowed sediment types of Unit III. Calcite abundance decreases below 705 mbsf, a feature also shown by bulk calcium carbonate analysis (Fig. 5). Quartz, feldspar, and smectite are common in all samples, whereas mica-group minerals and chlorite are rare or present in only trace amounts. This latter feature distinguishes these sedimentary rocks from the sediments of Unit I. In detail, the minor chlorite decreases rapidly from the top of Unit III, reflecting a sharp decline in the concentration of Mg in interstitial waters from 600 to 800 mbsf (see "Sediment/Fluid Geochemistry" section, this chapter).

Unit IV

The XRD data show a sharp increase in the proportions of calcite, chlorite, quartz, Ca-feldspar, and smectite at the top of Unit IV, coincident with a sharp increase in Ca concentration and a sharp decrease in Mg concentration in the interstitial waters (see "Sediment/Fluid Geochemistry" section, this chapter). The lithology here is nannofossil claystone. Gypsum and todorokite (manganese oxide) are also present in the upper part of Unit IV.

The distinctive clay-mineral assemblage of Unit IV may reflect intense alteration of fine-grained volcanic components in the sediments, leading to uptake of Mg and release of Ca.

Unit V

Sediments in the depth interval from 780 to 870 mbsf are characterized by relatively high abundances of smectite, in association with analcime, gypsum, ankerite, and smectite-mica

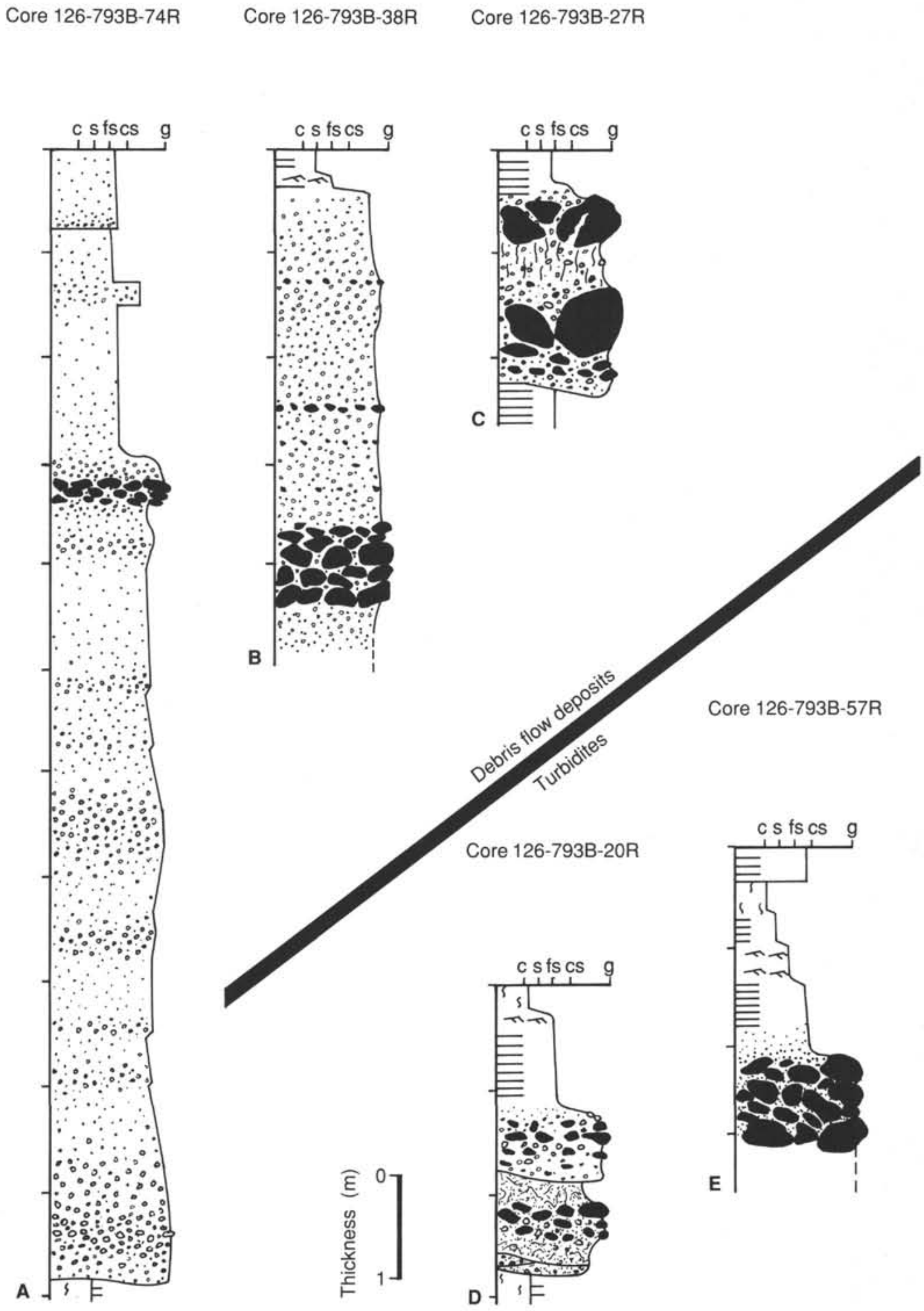

Figure 30. Sketches of five thick beds with basal divisions of pebbly sandstone and granule-pebble conglomerate. In two of the beds (D and E), the pebbly sediment grades upward into parallel- and ripple-laminated sandstone and siltstone. The other three beds (A, B, and C) show no systematic grading, except at the top. All of these beds contain cobble- and boulder-sized intraclasts of fine-grained sediment (e.g., silty claystone). All beds are drawn to the same scale; the width of the column varies with grain size. Symbols are the same as those used on barrel sheets and in Figure 5, except for the vertical fluid-escape pillars in C.

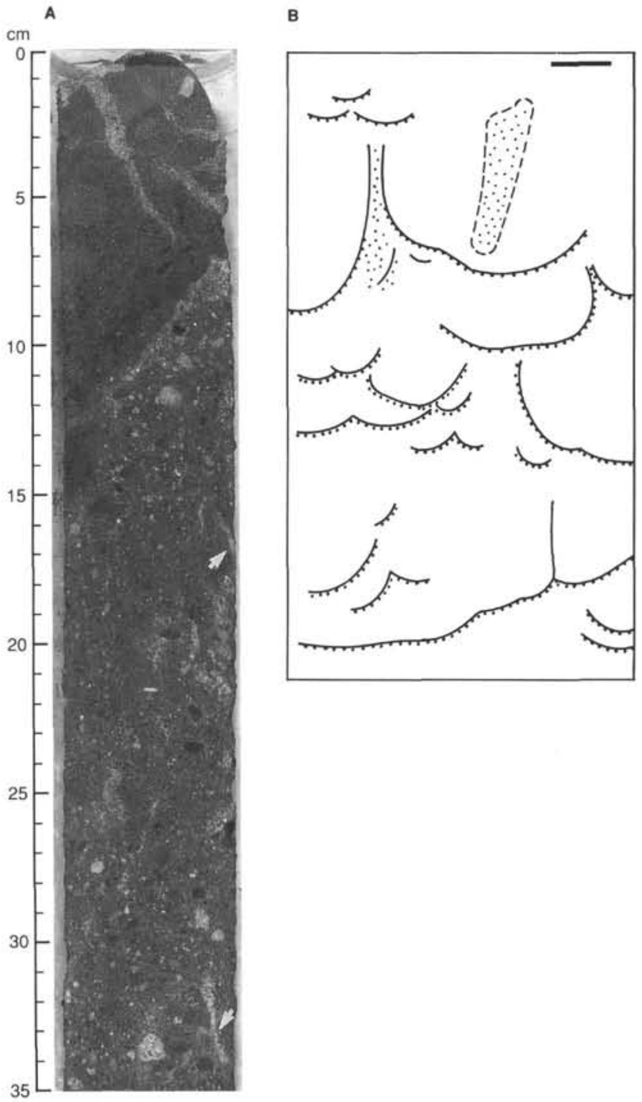

Figure 31. Examples of fluid-escape structures. **A.** Two-to-three-cm-long subvertical fluid-escape pillars (see arrows) in the upper part of graded bed of pebbly sandstone (Interval 126-793B-27R-5, 0–35 cm). The pillars are light in color because fine-grained matrix has been washed away by escaping pore fluids. Features in this bed are also illustrated in Figures 30 and 33. The clast of silty claystone at the top of the photograph is cut by injections rooted in the adjacent pebbly sandstone. **B.** Tracing of dish structures on the surface of a polished slab taken from a 6-m-thick bed of sandstone (Interval 126-793B-51R-4, 53–63 cm). Scale bar is 1 cm long. Cross sections of fluid-escape pillars are stippled. One pillar cuts upward between the edges of two dishes in the upper left-hand part of the sketch. The unpatterned sediment is medium-grained sandstone.

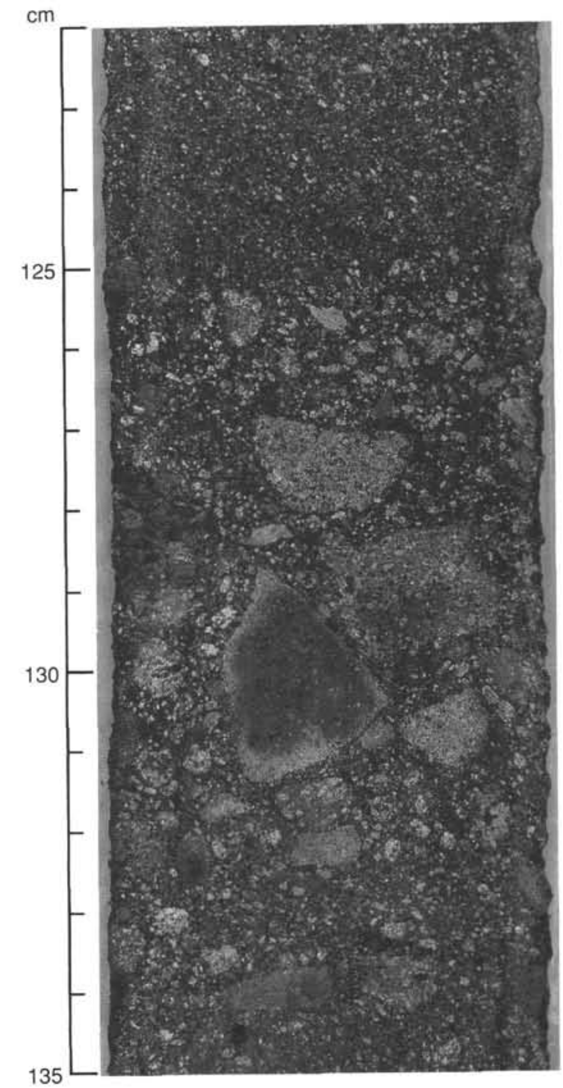

Figure 32. Inverse grading at the base of a pebbly granule conglomerate in Unit V (Interval Interval 126-793B-30R-3, 122–135 cm). There is also an inversely graded division of coarse- to very coarse-grained sandstone from 121 to 125 cm. All of this coarse-grained sediment is interpreted as the deposit of a single sediment gravity flow having sharp-based, inversely graded intervals that represent the lower parts of traction carpets generated by intense shear at the base of a high-concentration flow (Hiscott and Middleton, 1979, 1980; Lowe, 1982).

mixed-layer clays. The Na and Mg required for formation of analcime and smectite were derived from modified seawater that constitutes the pore water. From 800 to 870 mbsf, analcime and smectite are associated with albite.

Relative to overlying sediments, there is an increase in the interval from 870 to 895 mbsf in the amounts of chlorite, quartz, smectite, and smectite-mica mixed-layer clays. The zeolite phase changes from analcime to heulandite. Pyrophyllite and Ca-feldspar are also present. The smectite shows a ⟨060⟩ reflection at 0.153–0.154 ηm, indicating that this is a trioctahedral smectite, rich in Mg and Ca. Sample 126-793B-30R-5, 45 cm, contains a small amount of phillipsite in association with smectite. Phillipsite is a common submarine alteration product of volcanic glass.

The interval from 920 to 1060 mbsf is characterized by a lack of chlorite, perhaps because of severe depletion of Mg in pore waters at this depth (see "Sediment/Fluid Geochemistry" section, this chapter). The main minerals in the sedimentary rocks are smectite, calcite, quartz, Na-feldspar, and heulandite. Analcime is not present. A mineral-filled vein in this interval (Sample 126-793B-44R-3, 16 cm) consists of heulandite-clinoptilolite.

Very fine-grained sandstones in the part of the section from 1130 to 1150 mbsf contain abundant smectite, local celadonite, chabazite ($Ca[Al_2Si_4]O_{12} \cdot 6H_2O$), and Ca-feldspar. Chlorite, calcite, and quartz are rare. The smectite has a ⟨060⟩ reflection at 0.15388 nm (Sample 126-793B-58R-5, 20 cm) and is, therefore, a trioctahedral, Mg- and Ca-rich variety. This is consistent

Table 3. X-ray diffraction data for Holes 793A and 793B.

Core, section, interval (cm)	Depth (mbsf)	Unit	Color	Texture	Clay minerals			Minerals
					1.4 nm	1.0 nm	0.7 nm	
126-793A-								
1H-1, 126	1.3	I	2.5Y 6/2	Pumiceous gravel	Trace	—	—	Calcite, quartz, feldspar
3H-2, 121	16.2	I	5G 5/2	Silt	Present	Present	Present	Calcite, quartz, feldspar
3H-4, 26	18.3	I	5G 2/1	Silt	Present	—	Present	Calcite, quartz, feldspar
4H-3, 90	26.9	I	5Y 6/1	Nannofossil clay	Present	Trace	Present	Calcite, quartz, feldspar
5H-1, 93	33.4	I	5Y 6/1	Nannofossil-rich silty clay	Present	Present	Present	Calcite, quartz, feldspar
5H-6, 70	40.7	I	5G 2/1	Vitric silt	Present	—	Trace	Calcite, quartz, feldspar, pyrolusite, maghemite
5H-7, 120	42.7	I	5Y 6/1	Nannofossil-rich silty clay	Present	Present	Present	Calcite, quartz, feldspar
7H-2, 60	53.7	I	5G 3/2	Silt	Present	—	Present	Calcite, quartz, feldspar, palagonite, glauconite
8H-1, 50	61.7	I	N1	Vitric very fine-grained sand	Trace	—	—	Calcite, feldspar
9H-4, 12	74.0	I	5Y 2/1	Vitric silt	Present	Present	Present	Calcite, quartz, feldspar
11H-1, 36	90.5	I	5GY 2/1	Nannofossil-rich silty clay	Present	—	Trace	Calcite, quartz, feldspar, pyrite
126-793B-								
2R-1, 8	594.8	III	5GY 6/1	Claystone	Present	Trace	Trace	Calcite, quartz, feldspar
2R-1, 10	594.8	III	5GY 6/1	Pebble	Present	Trace	Trace	Calcite, quartz, feldspar
2R-1, 40	595.1	III	5GY 6/1	Nannofossil claystone	Present	—	Trace	Calcite, quartz, feldspar
3R-1, 10	604.4	III	N4	Very fine-grained sandstone	Present	—	—	Quartz, feldspar, palagonite
3R-1, 40	604.7	III	5GY 4/1	Silty claystone	Present	—	—	Calcite, quartz, feldspar
3R-2, 10	605.8	III	5GY 4/1	Very fine-grained sandstone	Present	Trace	—	Calcite, quartz, feldspar
3R-2, 44	606.2	III	5GY 4/1	Siltstone	Present	—	—	Calcite, quartz, feldspar, hematite, magnetite
3R-2, 100	606.8	III	5GY 4/1	Coarse-grained sandstone	Present	—	—	Calcite, quartz, feldspar, palagonite
3R-3, 50	607.8	III	5GY 4/1	Siltstone	Present	—	—	Calcite, quartz, feldspar
3R-4, 10	608.9	III	5GY 4/1	Siltstone	Present	—	—	Calcite, quartz, feldspar
4R-1, 50	614.5	III	5GY 4/1	Vitric silty claystone	Present	—	Trace	Calcite, quartz, feldspar
4R-2, 80	616.3	III	5GY 4/1	Vitric sandstone	Present	Trace	—	Calcite, quartz, feldspar
4R-3, 130	618.3	III	5GY 6/1	Vitric silty claystone	Present	—	—	Calcite, quartz, feldspar
4R-4, 50	619.0	III	5GY 4/1	Vitric silty claystone	Present	Present	Present	Calcite, quartz, feldspar, glauconite
6R-1, 38	633.7	III	N7	Silty sandstone	Trace	—	—	Calcite, quartz, feldspar
6R-1, 50	633.8	III	5G 3/1	Siltstone	Present	—	Trace	Quartz, feldspar
6R-2, 47	635.3	III	N6	Siltstone	Trace	—	—	Quartz, feldspar
6R-2, 70	635.5	III	5G 3/1	Siltstone	Present	—	Present	Calcite, quartz, feldspar
6R-2, 85	635.6	III	5Y 4/1	Siltstone	Present	—	—	Calcite, quartz, feldspar
6R-2, 19	635.0	III	5Y 4/1	Siltstone	Present	—	—	Calcite, quartz, feldspar
8R-1, 92	653.3	III	5Y 3/1	Siltstone	Trace	—	—	Calcite, quartz, feldspar
11R-1, 31	681.7	III	5Y 2/1	Claystone	Present	—	—	Calcite, quartz, feldspar, glauconite
14R-1, 10	710.5	III	5GY 5/1	Nannofossil-rich silty claystone	Present	—	—	Calcite, quartz, feldspar, glauconite
15R-2, 95	722.6	III	5GY 4/1	Sandy claystone	Present	—	Present	Calcite, quartz, feldspar
16R-3, 40	733.1	III	5YR 4/1	Vitric siltstone	Present	—	—	Calcite, quartz, feldspar
16R-5, 50	736.2	IV	5YR 6/1	Nannofossil-rich claystone	Abundant	Present	Present	Calcite, quartz, feldspar, glauconite
17R-1, 85	740.0	IV		Gypsum nodule	Common	—	—	Gypsum
17R-2, 15	740.8	IV	10R 6/4	Nannofossil claystone	Abundant	Present	Present	Calcite, quartz, feldspar, palagonite
17R-2, 63	741.2	IV	10R 6/4	Black manganese blotches	Present	—	—	Calcite, quartz, feldspar, todorokite
17R-5, 100	746.1	IV	5Y 5/2	Claystone	Abundant	Present	Present	Calcite, quartz, feldspar, palagonite
18R-5, 98	755.8	IV	10Y 6/2	Vitric claystone	Abundant	Present	Common	Calcite, quartz, feldspar, palagonite
20R-5, 90	774.9	V	5GY 6/1	Clayey siltstone clasts	Common	Present	—	Quartz, feldspar, palagonite heulandite-clinoptilolite
21R-6, 40	785.6	V	5G 2/1	Crystal-vitric nannofossil sandstone	Abundant	—	Present	Calcite, quartz, heulandite-clinoptilolite
22R-2, 79	789.6	V	5GY 2/1	Crystal-vitric siltstone	Abundant	—	Present	Calcite, quartz, feldspar, heulandite-clinoptilolite, smectite-mica mixed
23R-CC, 31	797.3	V	5G 6/1	Very fine-grained sandstone	Trace	—	—	Gypsum, analcime
23R-CC, 36	797.4	V	5G 6/1	Very fine-grained sandstone-vein	Present	—	—	Gypsum
25R-4, 22	821.1	V	5YR 2/1	Very fine-grained sandstone	Common	—	—	Analcime
27R-3, 69	839.1	V	5GY 4/1	Fine-grained sandstone-vein	Trace	Present	—	Gypsum, feldspar
27R-3, 130	839.7	V	5GY 4/1	Clayey siltstone	Abundant	Trace	Common	Calcite, quartz, feldspar, analcime
29R-4, 60	859.8	V	5GY 4/1	Fine-grained sandstone	Abundant	—	Trace	Feldspar, analcime
30R-5, 45	870.9	V	5GY 4/1	Very fine-grained siltstone	Abundant	—	Common	Quartz, feldspar, heulandite-clinoptilolite, analcime, phillipsite
31R-7, 10	883.1	V	5GY 4/1	Very fine-grained sandstone	Abundant	—	Present	Calcite
32R-1, 3	883.7	V	5G 2/1	Very fine-grained sandstone	Abundant	Trace	Common	Quartz, feldspar, smectite-mica mixed
33R-2, 35	895.2	V	N1	Vitric fine-grained sandstone	Abundant	—	Present	Calcite, quartz, feldspar, pyrophyllite, analcime heulandite, heulandite-clinoptilolite
33R-6, 120	902.0	V	5BG 3/2	Pumiceous sandstone	Common	—	—	Calcite, quartz, heulandite
34R-6, 128	911.8	V	N2	Fine-grained sandstone	Abundant	—	Trace	Calcite, feldspar, heulandite, analcime, heulandite-clinoptilolite
35R-2, 89	915.0	V	5G 2/1	Crystal-vitric fine grained sandstone	Common	—	—	Calcite, feldspar, heulandite, analcime, heulandite-clinoptilolite
40R-8, 44	971.9	V	5G 6/1	Silty claystone	Common	—	—	Calcite, feldspar, heulandite
42R-2, 40	982.2	V	5B 5/1	Siltstone	Abundant	—	—	Calcite, quartz, feldspar, heulandite
44R-3, 16	1002.6	V	5GY 2/1	Silty claystone	Trace	—	—	Calcite, quartz, feldspar, heulandite-clinoptilolite
46R-2, 100	1021.2	V	5G 3/1	Vitric siltstone	Common	—	—	Calcite, quartz, feldspar, heulandite
48R-2, 34	1039.4	V	5GY 2/1	Clayey siltstone	Abundant	—	—	Calcite, quartz, feldspar, heulandite
49R-4, 23	1052.0	V	5GY 2/1	Fine-grained sandstone	Common	—	—	Calcite, quartz, feldspar, heulandite
50R-5, 83	1063.8	V	5YR 2/1	Very fine-grained sandstone	Common	—	—	Calcite, feldspar, heulandite, analcime, heulandite-clinoptilolite
53R-5, 45	1089.6	V	5Y 4/1	Very fine-grained sandstone	Abundant	—	—	Calcite, feldspar, heulandite-clinoptilolite
54R-3, 55	1099.3	V	5Y 2/1	Clayey sandstone	Anundant	—	—	Calcite, quartz, feldspar, heulandite-clinoptilolite
55R-3, 100	1109.4	V	N2	Very fine-grained crystal-vitric sandstone	Abundant	—	—	Calcite, quartz, feldspar, heulandite, heulandite-clinoptilolite
56R-3, 100	1119.0	V	5BG 5/2	Very fine-grained sandstone	Abundant	—	—	Calcite, quartz, feldspar, heulandite
57R-3, 85	1128.6	V	5Y 2/1	Silty claystone-vein	Abundant	—	—	Calcite, quartz, feldspar, heulandite, heulandite-clinoptilolite, analcime
58R-2, 96	1136.5	V	5BG 4/6	Sandstone	—	Common (celadonite)	—	Dolomite, analcime
58R-5, 20	1140.2	V	5GY 4/1	Very fine-grained sandstone	Abundant	Trace	—	Quartz, feldspar, analcime, chabazite
59R-7, 20	1152.8	V	5YR 2/1	Very fine-grained sandstone	Abundant	—	—	Quartz, feldspar, analcime, heulandite, chabazite
60R-1, 107	1154.3	V	N2	Crystal-vitric sandstone	Abundant	—	—	Feldspar, analcime, heulandite, chabazite
62R-1, 59	1173.2	V	5GY 2/1	Siltstone	Abundant	—	—	Quartz, feldspar, heulandite
64R-6, 10	1201.0	V	5GY 2/1	Medium-grained sandstone	Abundant	—	—	Calcite, feldspar, analcime, heulandite
65R-3, 50	1205.0	V	5G 2/1	Conglomerate	Abundant	—	—	Calcite, feldspar, analcime, heulandite-clinoptilolite
66R-2, 130	1213.9	V	5G 3/2	Very fine grained sandstone	Abundant	—	—	Quartz, feldspar, analcime, heulandite-clinoptilolite
67R-6, 80	1229.1	V	5GY 2/1	Siltstone	Abundant	Present	—	Calcite, quartz, feldspar, analcime, heulandite-clinoptilolite
68R-2, 60	1232.6	V	5GY 2/1	Sandy siltstone	Abundant	Trace	Present	Quartz, feldspar, analcime
69R-1, 28	1240.5	V	5GY 4/1	Medium-grained crystal-vitric sandstone	Abundant	—	—	Calcite, quartz, feldspar, heulandite, heulandite-clinoptilolite
70R-3, 63	1253.4	V	N1	Very fine-grained sandstone with slickensides	Abundant	—	—	Heulandite
72R-5, 62	1275.3	V	5G 5/2	Very fine-grained sandstone	Abundant	—	—	Calcite, dolomite, quartz, feldspar, heulandite-clinoptilolite
73R-3, 30	1281.7	V	5G 4/1	Siltstone	Abundant	—	—	Dolomite, quartz, feldspar, heulandite
74R-1, 15	1288.2	V	5G 2/1	Silty claystone	Abundant	—	—	Calcite, feldspar, heulandite-clinoptilolite
75R-2, 50	1309.3	V	5GY 2/1	Conglomerate	Abundant	—	—	Calcite, dolomite, quartz, feldspar, heulandite-clinoptilolite
76R-4, 45	1312.3	V	5GY 2/1	Pebbly sandstone	Common	Present	—	Quartz, feldspar, heulandite, heulandite-clinoptilolite
77R-1, 25	1317.3	V	5GY 2/1	Fine-grained sandstone	Abundant	—	—	Calcite, dolomite, quartz, feldspar, heulandite, heulandite-clinoptilolite
78R-2, 50	1328.7	V	5G 2/1	Volcanic sandy granule conglomerate	Abundant	—	—	Feldspar, analcime, heulandite-clinoptilolite
78R-5, 105	1333.8	V	5GY 4/1	Fine-grained crystal-vitric sandstone	Abundant	Trace	—	Calcite, quartz, feldspar, heulandite-clinoptilolite, analcime
80R-1, 102	1347.0	V	5GY 2/1	Granule-rich coarse-grained sandstone	Abundant	—	—	Calcite, feldspar, heulandite-clinoptilolite, analcime
81R-4, 98	1361.2	V	2YR 2/1	Siltstone	Common	Trace	—	Quartz, feldspar, heulandite-clinoptilolite, palagonite
82R-3, 20	1368.5	V	5G 2/1	Granule-rich medium-grained sandstone	Abundant	—	—	Quartz, feldspar, heulandite-clinoptilolite, palagonite
82R-6, 78	1373.6	V/VI	5GY 2/1	Fault shear zone	Present	Present	—	Feldspar, palagonite
83R-CC, 15	1375.0	VI	5G 5/2	Microbreccia	Present	—	—	Quartz, feldspar, analcime, palagonite
84R-1, 23	1384.7	VI	5G 5/2	Volcanic breccia	Present	Trace	Present	Analcime
85R-1, 58	1394.8	VI	5G 5/2	Volcanic breccia	Abundant	—	Present	Feldspar

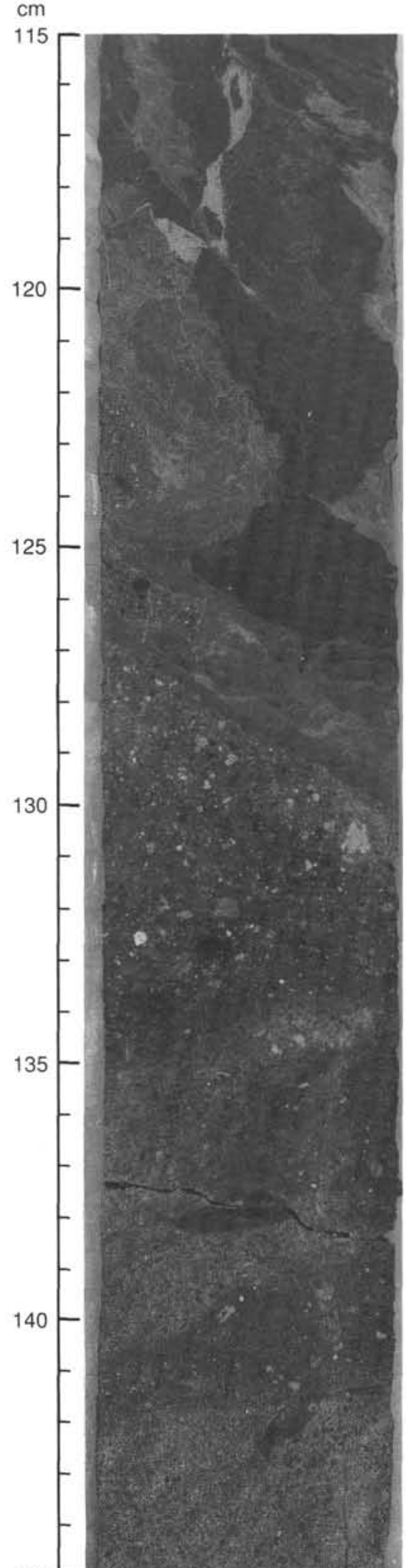

Figure 33. The lower part of a deformed sedimentary clast, at least 70 cm across, that occurs 35 cm above the base of a 2.3-m-thick graded bed of pebbly sandstone (Interval 126-793B-27R-5, 115-145 cm). The sedimentary structures and grain size of this bed are shown in Figure 30.

with the fact that interstitial waters are almost saturated with respect to Ca at this depth (see "Sediment/Fluid Geochemistry" section, this chapter).

Cobalt-blue celadonite is present in a sandstone bed (Sample 126-793B-58R-2, 96 cm) in this interval, associated with dolomite and analcime. Both celadonite and trioctahedral (magnesian) smectite suggest low-temperature, nonoxidative alteration of volcanic glass.

Siltstone to conglomerate beds in the interval from 1200 to 1230 mbsf contain abundant smectite, analcime, and heulandite-clinoptilolite. Chlorite, quartz, and feldspar are rare. Calcite concentration is elevated in beds containing tests and broken tests of benthic foraminifers.

In the interval from 1250 to 1373 mbsf, a slickensided fault surface at 1253 mbsf (Sample 126-793B-70R-3, 63 cm) contains a high concentration of heulandite and smectite. Dolomite is present from 1275 to 1320 mbsf. Analcime is present below 1330 mbsf in fine-grained crystal-vitric sandstone and coarse-grained sandstone, in association with abundant smectite. The surface of the fault that separates Units V and VI (1373 mbsf) contains abundant palagonite with a small amount of smectite-mica mixed-layer clay.

Unit VI

The volcanic breccia at the base of the sedimentary succession contains significantly more feldspar than the overlying section, in association with smectite and palagonite. The feldspar is albite.

Sediment Accumulation Rates

Sedimentation rates for Site 793 were established from calcareous nannofossil datums and paleomagnetic reversals (Table 4), which were used to construct the age-depth curve shown in Figure 42. The interval between 98.9 and 586.5 mbsf was drilled without taking any cores; thus, age-depth information for the sedimentary section between those depths is not available.

Sedimentation rates in Unit V (late early to early late Oligocene; 30.33–29.21 Ma) are >250 m/m.y., similar in magnitude to rates in equivalent sedimentary sections of early late Oligocene age at Sites 787 and 792 (see "Lithostratigraphy and Accumulation Rates" section, "Site 787" and "Site 792" chapters, this volume). Toward the top of Unit V (29.21–26.86 Ma), sedimentation rates decline to about 80 m/m.y. The high rates throughout Unit V reflect the influx of volcaniclastic material to the forearc basin at this time.

The early Miocene sediments were deposited very slowly (~7 m/m.y.). These low sedimentation rates occur in Unit IV and the lower part of Unit III, which are characterized by nannofossil claystones and nannofossil-rich claystones that slowly accumulated in the absence of significant volcanic input. These low sedimentation rates may also reflect a stratigraphic discontinuity at or near the Unit III/IV contact. Sedimentation rates rise sharply to 70 m/m.y. in the middle Miocene (Unit III) and average 40 m/m.y. in the uncored interval.

Pleistocene sedimentation rates (Unit I) are over 100 m/m.y., similar to rates seen at Sites 792 (see "Lithostratigraphy and Accumulation Rates" section, "Site 792" chapter, this volume) for the same time interval. This rate reflects renewed volcaniclastic input to the forearc basin.

Interpretation of Sedimentary Units in Hole 793B

Unit III

The sharp-based, graded beds in this unit are typical fine-grained turbidites, except that their parallel- to ripple-laminated

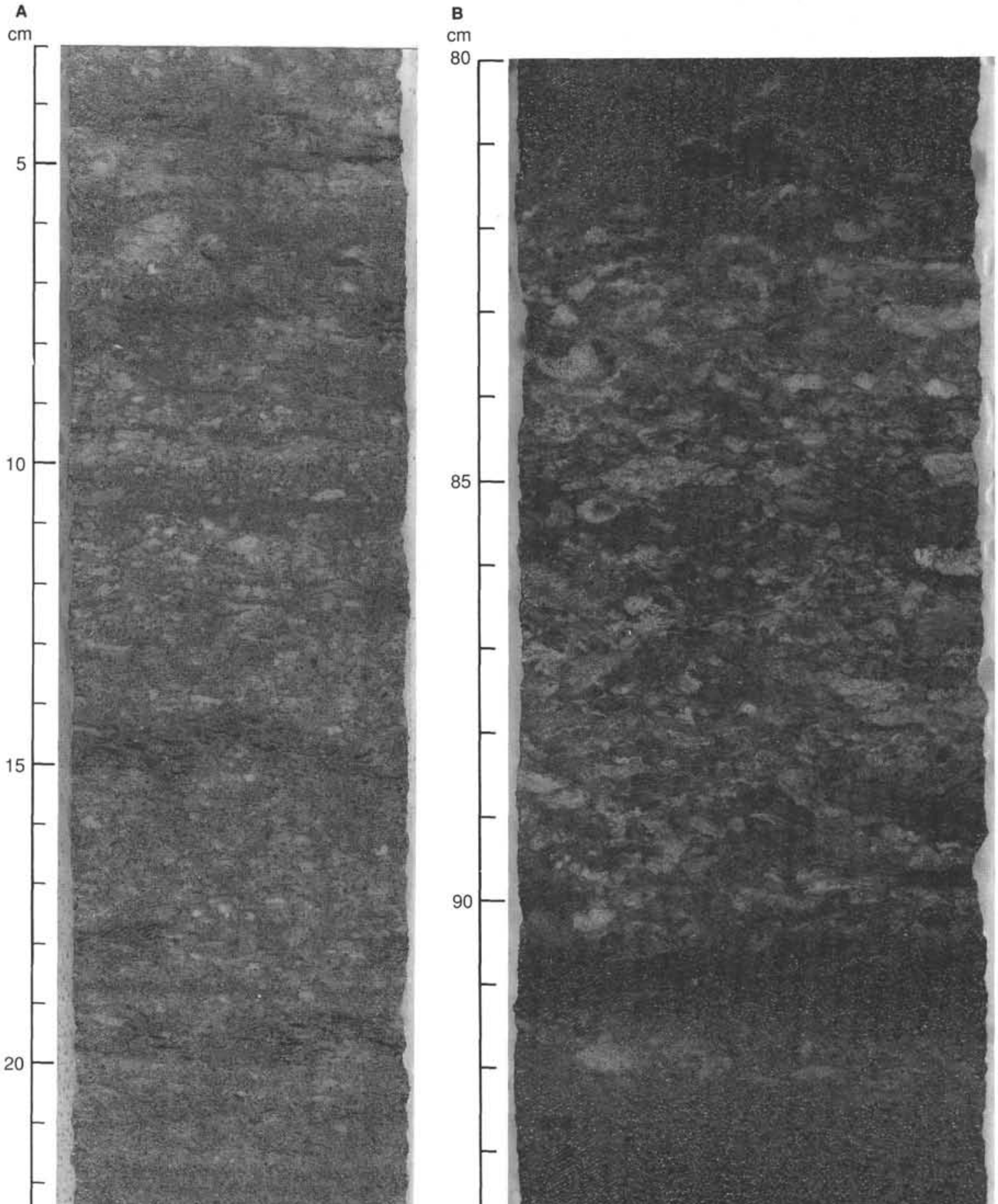

Figure 34. Examples of pumiceous, granule-rich, and pebbly sandstones in Unit V. **A.** Part of a parallel-laminated sandstone bed with light-colored, low-density pumice grains concentrated in bands within the finer grained sandstone. There are dark-colored clasts of pumice, altered to clay minerals, concentrated in bands at 14–15 and 19–20 cm (Interval 126-793B-37R-4, 3–23 cm). **B.** A high concentration of pumice granules and pebbles in a matrix of fine-grained sandstone (Interval 126-793B-43R-5, 80–94 cm).

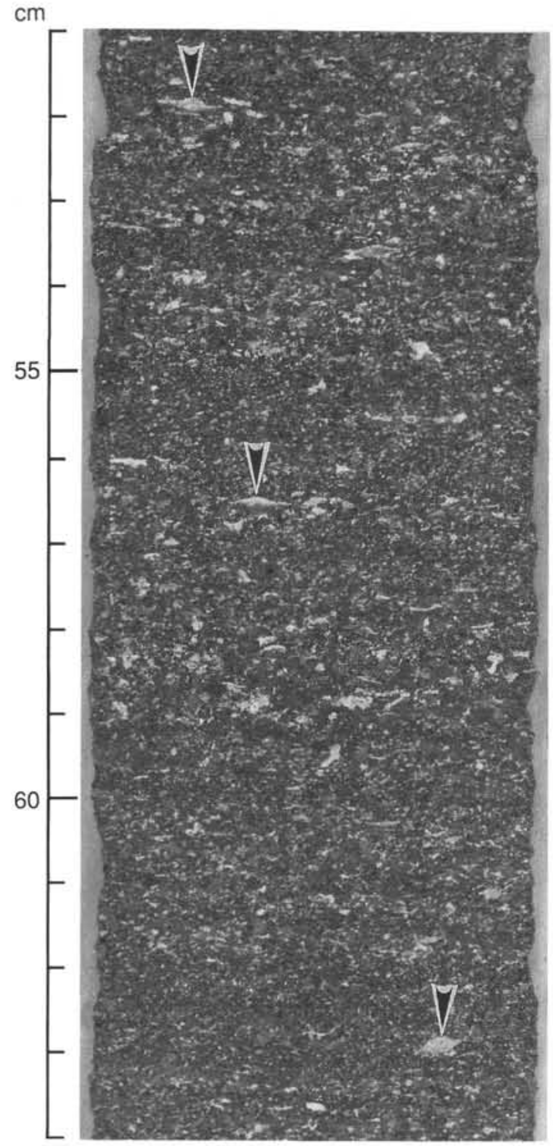

Figure 35. Medium-grained, parallel-laminated sandstone rich in tests of *Discocyclina* and other larger benthic foraminifers (Interval 126-793B-63R-3, 51–64 cm). The foraminifers (at 52, 56, and 63 cm; see arrows) have a discoid shape.

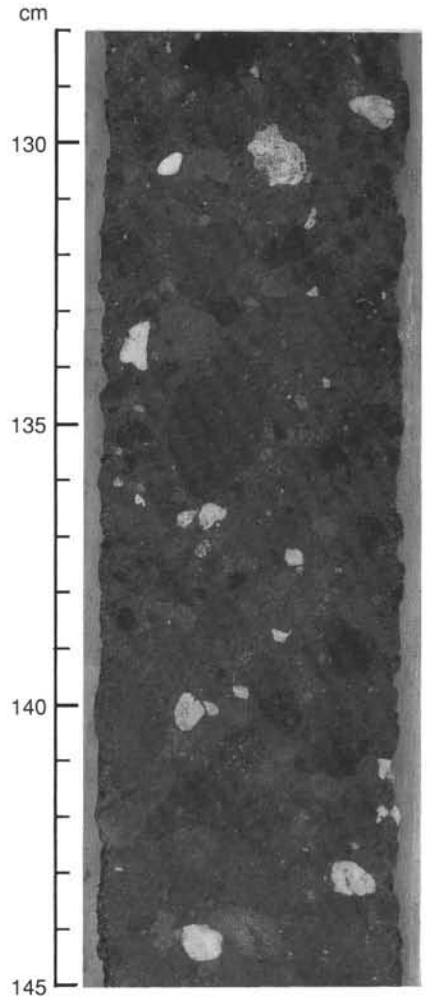

Figure 36. Volcanic-lithic conglomerate with large white bioclasts of calcareous red algae (Interval 126-793B-75R-2, 128–145 cm).

siltstone and silty claystone divisions (T_d division of Bouma, 1962) are several times thicker than the basal sandstone/siltstone division. Some of these fine-grained turbidites are on the order of 50 cm thick. Given the lack of thick-bedded, coarse-grained beds in Unit III, and sheetlike geometry of the basin fill on seismic profiles, we interpret the depositional setting to have been a rather featureless basin plain over which dilute, unconfined turbidity currents spread out to form sheetlike deposits. The interbedded facies are strongly burrowed siltstone-claystone sediment types with high contents of biogenic carbonate and scattered sand- to granule-size grains of mafic volcanic glass, and felsic pumice. These are interpreted as hemipelagic deposits produced by the settling of biogenic and volcanogenic fractions, as well as mixing by burrowers. In some cases, the fallout of volcanic ash formed very thin layers of coarse silt to granules. The grain size and total volume of volcanic ejecta in this unit is much less than in Unit I, suggesting limited activity of the nearby arc volcanoes at this time. As at Sites 787 and 792 (see "Site 787" and "Site 792" chapters, this volume), the volcanogenic input to the basin was compositionally bimodal.

The 35-cm-thick bed of muddy sandstone, with large intraclasts and basalt cobbles, is interpreted as a thin debris-flow deposit. This is the only such bed in Unit III and probably represents an unusual event like a seismically triggered failure on the margin of the forearc basin. Only a thin feather-edge of what was probably a thicker flow reached this part of the basin.

As at Sites 787 and 792, subvertical veinlets are the expression of a fracture cleavage that formed during early dewatering of unlithified, wet, muddy sediments (Ogawa and Miyata, 1985). The extensional regime inferred from these veinlets is consistent with numerous extensional microfaults noted in cores from Unit III.

Unit IV

Unit IV consists entirely of variable mixtures of biogenic carbonate, both nannofossils and foraminifers, and siliciclastic claystone, except for rare, thin, graded siltstone beds (turbidites). We interpret these rocks as hemipelagic deposits that accumulated in a low-energy environment. The clay fraction was probably advected from the vicinity of the volcanic front by storm waves and fairly weak marine currents; there is no evidence for bottom-current reworking. Slow depositional rates, and an almost complete absence of direct volcanogenic input, indicate

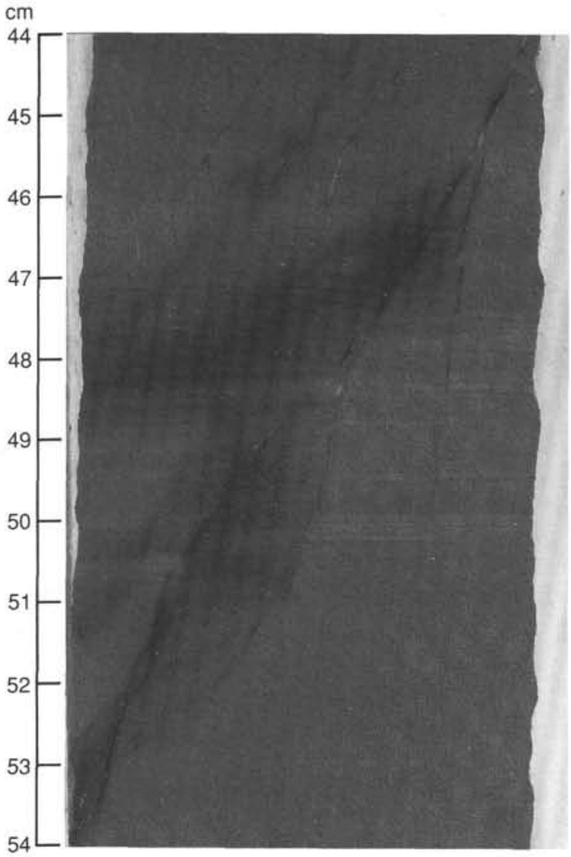

Figure 37. Steeply dipping, curved, anastomosing microfaults, with the total displacement of 8 mm partitioned between two of the faults from 48 to 53 cm (Interval 126-793B-54R-2, 44–54 cm).

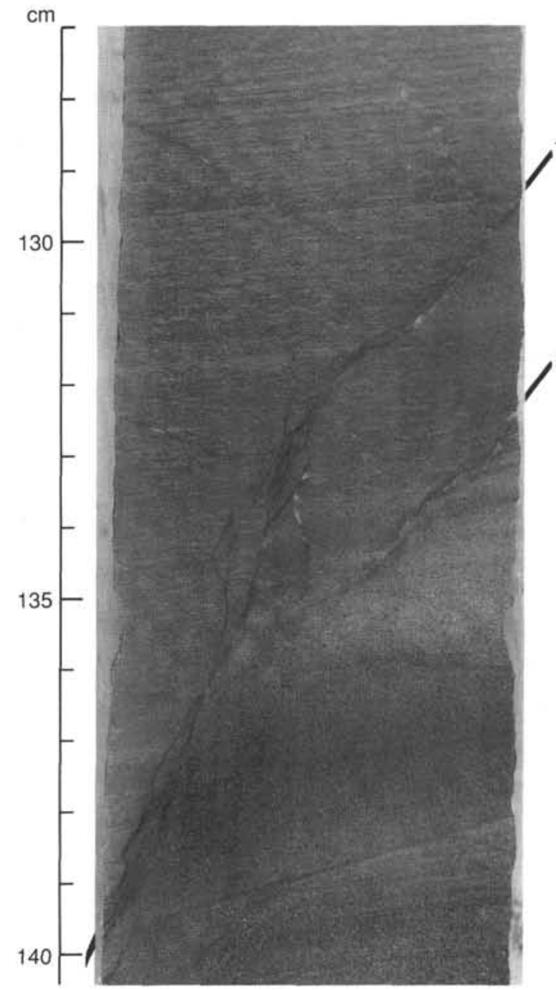

Figure 38. Complex set of braided faults, with different lithologies on the opposite sides of fault plane 2. The sediments above and below this fault are, respectively, very fine-grained and fine-grained pumiceous sandstone. Fault surfaces 1 and 2 merge below 135 cm (Interval 126-793B-54R-4, 127–140 cm).

that the Izu-Bonin Arc was largely inactive during this part of the early Miocene. This suggestion is corroborated by results from Site 792 (see "Lithostratigraphy and Accumulation Rates" section, "Site 792" chapter, this volume), where lower Miocene nannofossil chalk marks a period of very slow deposition without significant volcanic input. As at Site 792, the lower epiclastic input in Unit IV of Site 793, relative to that of the underlying Unit V, may partly be a response to the significant rise in global sea level from the mid-Oligocene into the Miocene (Haq et al., 1987).

The upper part of Unit IV is characterized by strongly burrowed, red-colored (oxidized) sedimentary rock, diagenetic manganese oxide (todorokite), and biogenic carbonate contents of about 40%–60%. We interpret these features to be the product of a very slow delivery of siliciclastic detritus. Oxygenated bottom waters were in contact with the surface sediment long enough to oxidize the organic fraction and any iron-rich minerals completely.

In the rocks of the lower part of Unit IV, the color is drabber, burrow density is drastically reduced, and carbonate content is low. Fissility, a product of recrystallization of clay minerals parallel to the bedding, is probably better developed in the claystone in this part of the section because of a primary, undisturbed alignment of phyllosilicate grains in the unburrowed sediments. On the basis of the lack of bioturbation, we interpret this part of the unit to have been deposited beneath poorly oxygenated bottom waters. The changes in lithology and burrow intensity from the top to the base of Unit IV may either reflect higher rates of accumulation in the older strata or temporal differences in the character of bottom waters. Benthic foraminifers are rare in the lower part of Unit IV, and no samples were processed from the fissile interval to aid in our assessment of the bottom-water character. Organic carbon content in this sedimentary rock is low, about 0.2% (see "Sediment/Fluid Geochemistry" section, this chapter).

A striking feature of Unit IV is the abundance of dewatering veinlets. Veinlets are also present in Unit III, but they are absent from the upper part of the more sandy Unit V. The claystones of Unit IV are impermeable, and it is possible that the large quantities of pore water that must have been expelled from the more permeable Unit V generated and maintained a dense network of veinlets to accommodate the high flow volumes. The veinlets contain a greater proportion of zeolite precipitates than at other Leg 126 sites, consistent with greater net transport of pore fluids through the veinlet network. The kinked geometry of the veinlets is attributed to compaction, perhaps with a component of directed shear, after the early phase of dewatering.

The gypsum nodule in Unit IV reflects the Ca-rich, pore-water chemistry of this site (see "Sediment/Fluid Geochemistry" section, this chapter).

Unit V

All sediments in Unit V were deposited by sediment gravity flows, ranging in character from debris flows to turbidity currents of both high and low concentration, that diluted the pe-

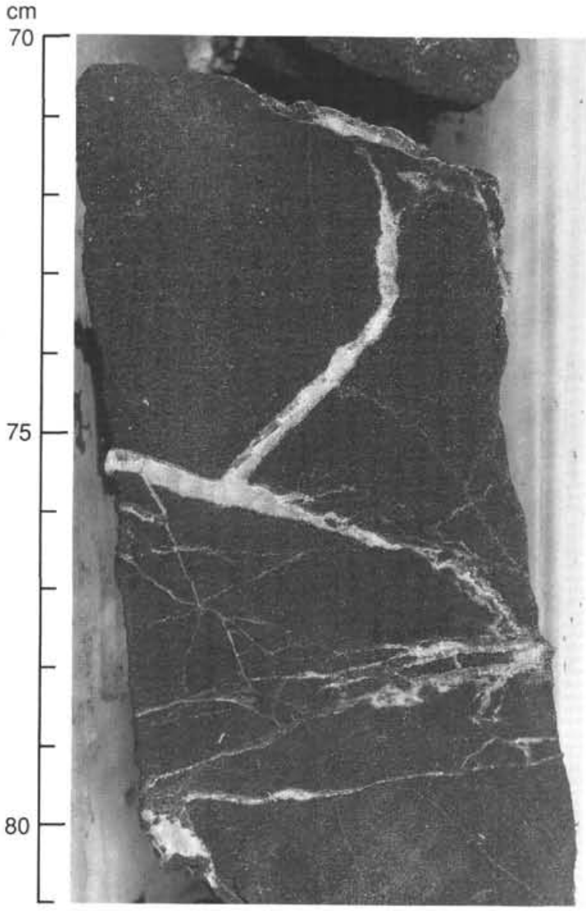

Figure 39. Gypsum-filled fractures in very fine-grained sandstone of Unit V (Interval 126-793B-27R-3, 70–81 cm).

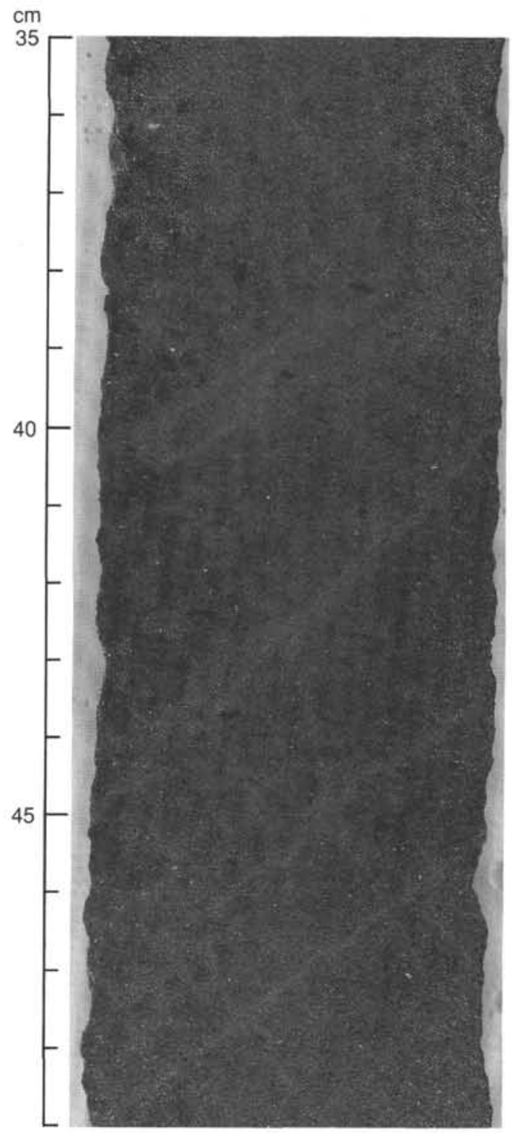

Figure 40. Orthogonal sets of light-colored bands or zones in fine-grained sandstone. There is no sharp fracture in the middle of these zones. Examination of a thin section indicates that the lighter areas contain more clay minerals than the darker areas. The set that dips from right to left has the same orientation as microfaults at this general depth in Unit V (Interval 126-793B-77R-1, 35–49 cm).

lagic input to this part of the section to insignificant levels. The debris-flow deposits are structureless and are characterized by poorly developed fabric and grading. Large silty claystone intraclasts are commonly present well above the base of the bed (Fig. 30). Gravel-size material in some of these beds consists only of such intraclasts, whereas in other beds there is a polymictic assemblage of volcanic pebbles, including clasts of andesite flows. In the lower part of Unit V, the conglomeratic beds also contain large benthic foraminifers, bioclasts of calcareous red algae, bryozoans, rare coral, and lithified algal micrite clasts.

Many of the pebble-size volcanic clasts were derived by subaerial or coastal/nearshore erosion of arc volcanoes. The bioclastic debris was derived from shallow-marine areas around the same volcanoes. These larger clasts were mixed, in shallow water or during resedimentation, with finer grained erosional products, and with primary volcanic ejecta (vitric sand) on the seafloor around the volcanic edifices.

The graded sandstones and pebbly sandstones of Unit V were deposited by turbidity currents during a period of rapid sediment supply that diluted pelagic and primary pyroclastic input to the forearc basin. Much of the detritus in these beds, however, may have been produced along the arc by nonexplosive volcanic activity, with the abundant primary material being contributed directly, or quickly resedimented, into the forearc basin. The necessity to derive a large fraction of the coarser siliciclastic material from active volcanoes is a consequence of the great volumetric difference between the sedimentary fill of the forearc basin, and the probable area of emergent arc volcanoes that could have acted as sources for epiclastic material.

In part of Unit V, there is direct evidence for contemporaneous, explosive, and acidic volcanic activity. In the interval from 900 to 1020 mbsf (28.3–29.5 Ma; Fig. 32), most sandstone beds contain abundant pumice clasts that were probably transported into the basin as a part of the load of the turbidity currents. There is no evidence for the direct accumulation of pumice by air fall to the sea surface and settling. For other parts of Unit V, there are apparently no macroscopic criteria to distinguish resedimented volcanogenic material from detritus supplied directly by submarine eruptions, followed by flow as a density current into the basin.

There is no evidence that the conglomerates in the lower part of Unit V were deposited in channels, although similar sediments in ancient successions commonly reside in shallow channels or large scours. Conglomerates of this type are known from the inner to middle parts of ancient submarine fans, both within

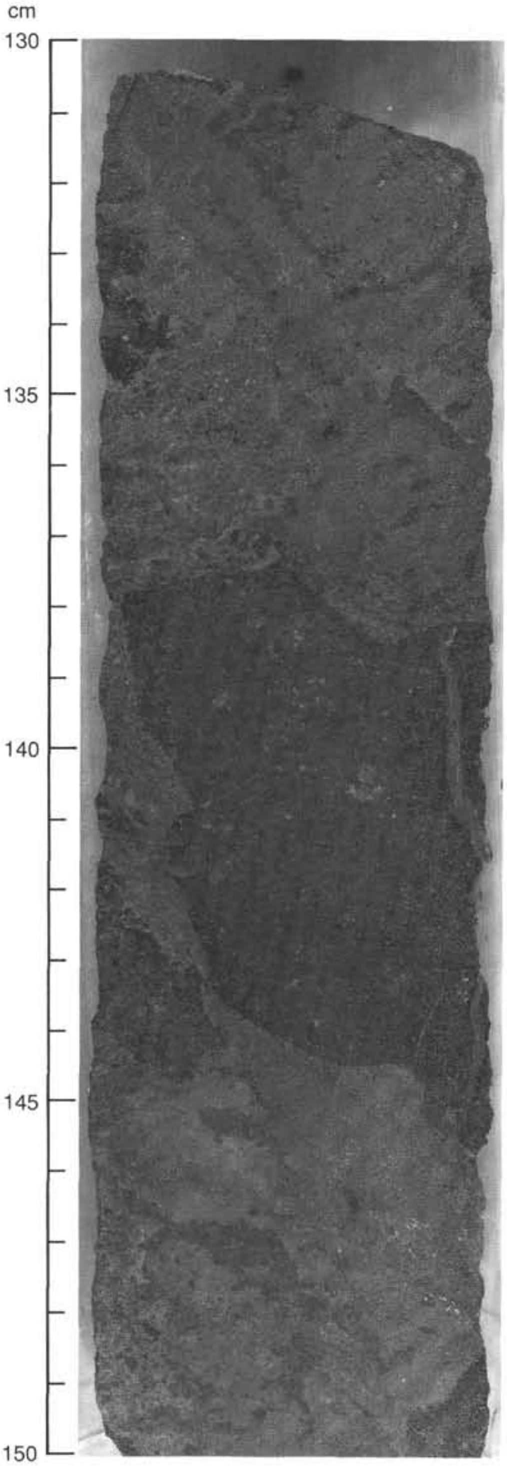

Figure 41. Angular cobbles of porphyritic lava in a matrix of sandstone of the same composition. Much of the field of view consists of clasts (Interval 126-793B-83R-1, 130–150 cm).

and beyond fan channels, and from coarse-grained slope aprons (Nelson and Maldonado, 1988). Conglomeratic beds higher in the section (825–900 mbsf; Figs. 5 and 29A) are interbedded with thin- to medium-bedded turbidites and seem to represent unique, high-volume events rather than channel-fill deposits. Some of these events were debris flows that may have been generated by catastrophic failure of parts of the coarse-grained apron surrounding the arc volcanoes, perhaps associated with tectonic rejuvenation of the flanks of the basin. The global sea level was fairly low at this time (Haq et al., 1987), which may have also aided the delivery of coarser grained material to the basin (Mutti, 1985). Within error limits for biostratigraphic and paleomagnetic datums, this upper conglomeratic interval (28 ± 0.5 Ma; Fig. 42) is broadly contemporaneous with conglomerates at the base of the sedimentary section at Site 792 (see "Lithostratigraphy and Accumulation Rates" section, "Site 792" chapter, this volume).

The overall upward fining in Unit V from the basal conglomerates and pebbly sandstones to the uppermost thin- to medium-bedded turbidites is probably controlled by tectonic evolution of the forearc basin. The basin was apparently formed by rifting of a wide Eocene arc terrane, with the western and eastern flanks now exposed at the frontal- and outer-arc highs, respectively (see "Principal Results" section, this chapter). Uplift of the flanks of this rift, deepening of the basin, steepening of bottom slopes, increased seismic activity, and perhaps augmented volcanicity would have all contributed to the coarse-grained and very thickly bedded interval at the base of the unit. The upward fining above the conglomeratic interval may have been produced

Table 4. Calcareous nannofossil datums and paleomagnetic reversal events used to construct the Site 793 age-depth curve.

Chronostratigraphic event	Core	Depth (mbsf)	Age (Ma)
Nannofossils:			
	Hole 793A		
FO *E. huxleyi*	2H-CC	11.28–23.0	0.275
LO *P. lacunosa*	5H-1, 141 cm	32.56–33.91	0.460
younger than LO acme of *Reticulofenestra* sp A.	11H-CC	98.9–99.7	<0.830
	Hole 793B		
FO *S. heteromorphus*	14R-CC	706.36–720.10	17.2–18.6
FO *D. druggi*	18R-4, 23–25 cm	753.55–758.40	23.2
LO *S. ciperoensis*	23R-CC	791.93–806.7	25.2
LO *S. distensus*	30R-CC	861.92–874.0	28.2
FO *S. ciperoensis*	57R-CC	1128.9–1143.4	30.2
Paleomagnetics:			
	Hole 793A		
Brunhes/Matuyama	9H-3 to -9H-4	75.4–77.2	0.73
Top of Jaramillo	9H/11H	78.68–90.9	0.91
	Hole 793B		
Base of second normal in Anomaly 5B	1R/2R	590.29–603.83	15.27
Base of third normal in Anomaly 5C	9R, 20 cm	662.3–668.09	16.22
Base of second normal in Anomaly 6A	16R-5, 130 cm	737.0–737.5	21.71
Top of first normal in Anomaly 6AA	17R-2, 70 cm	741.3–742.7	21.90
Top of first normal in Anomaly 8	20R-6, 110 cm	776.6	26.86
Base of second normal in Anomaly 8	25R-5, 20 cm	824.1–824.4	27.74
Top of first normal in Anomaly 9	31R-3, 110 cm	878.1–878.7	28.15
Base of second normal in Anomaly 9	40R-5, 90 cm	967.9	29.21
Top of first normal in Anomaly 10	53R/54R	1091.73–1099.5	29.73
Top of second normal in Anomaly 10	63R-1, 30 cm	1182.5–1187.0	30.09
Top of second normal in Anomaly 10	70R-4, 120 cm	1255.5	30.33

Note: Site 793 age-depth plot appears in Figure 42; FO = first occurrence; LO = last occurrence.

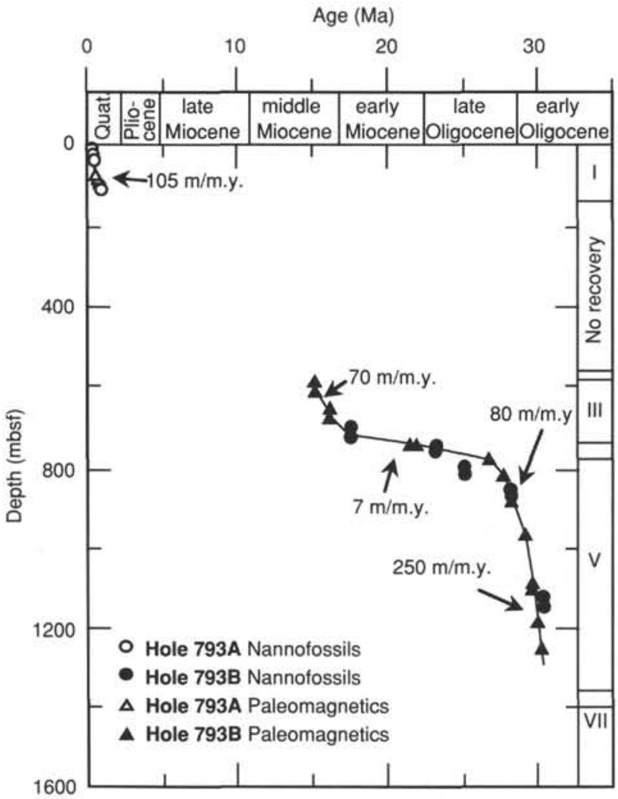

Figure 42. Age-depth curve for Site 793 constructed from data in Table 4. Lithologic unit boundaries are located along the right-hand side of the figure.

by a combination of effects: (1) a decreasing rate of extension; (2) a decline in the elevation and extent of the source area; and (3) a decrease in seafloor gradients along the basin-margin slopes caused by the infilling of the basin.

Unit VI

The lack of organization, very poor sorting, and clast angularity of the volcanic breccias of Unit VI suggest a very local source area. The features of the sediment are like those of rockfall or talus deposits, although there is sufficient mud matrix in the upper part of the unit to have permitted downslope transport by debris flow. We interpret this material to be a debris or talus apron along the flanks of a volcanic edifice or intrabasinal fault scarp. Petrologic differences between the clasts in Unit VI and the basement (see "Igneous Petrology" section, this chapter) indicate that this volcanic breccia was derived from a separate volcano or flow field.

History of Volcanic Activity

The lower to upper Oligocene turbidite succession contains little direct air fall of pumice or other ejecta except for a pumice-rich interval from 900 to 1020 mbsf. Nevertheless, it is difficult to account for the enormous volume of sediment deposited in the forearc basin, at rates of about 80-250 m/m.y., without invoking contemporaneous production of large quantities of volcanogenic material. Continuous volcanic activity, combined with relentless subaerial and coastal erosion, maintained a constant flux of detritus to the steep flanks of the arc volcanoes. From this position, the materials were periodically carried out onto the forearc basin plain.

There is a general upward fining toward the top of Unit V (759–825 mbsf), signaling a decline in the rate of production and input of volcanic products, perhaps caused in part by drowning of the source area as a result of a significant rise in global sea level from the mid-Oligocene into the Miocene (Haq et al., 1987). The presence of only a few percent of volcanic ash in Unit IV (present as vitric siltstone and vitric sandstone) combined with slow rate of deposition (7–13 m/m.y.) point to a period of volcanic quiescence in the early Miocene.

Unit III contains significant quantities of volcanic ejecta, both as disseminated grains in burrowed sediments, and as primary or resedimented volcanic glass of sand and silt size. The rate of input of volcanogenic material is less than in Unit V, but much more than in Unit IV. After an early Miocene hiatus, therefore, volcanic activity resumed at a moderate level from the late early Miocene into the middle Miocene.

Unit I is separated from Unit III by about 500 m for which no sedimentary record was recovered. We cannot comment, therefore, about trends in volcanic activity between the middle Miocene and the Quaternary. In the Quaternary (Unit I), there are large amounts of volcanogenic gravel, sand, and silt, all indicating important input from volcanoes of the Izu-Bonin Arc. Subunit IA, in particular, consists mainly of pumiceous gravel and sandy gravel produced by large caldera eruptions along the arc. Pumice from the same phase of intense volcanic activity was recovered at several other Leg 126 sites, particularly in the backarc.

BIOSTRATIGRAPHY

Calcareous Nannofossils

Hole 793A

We placed Samples 126-793A-1H-CC and -2H-CC, which contain *Emiliania huxleyi,* in Zone CN15. Samples 126-793A-3H-4, 0 cm, -3H-CC, and -4H-CC contain neither *E. huxleyi* nor *Pseudoemiliania lacunosa* and thus belong in Zone CN14b. We assigned Samples 126-793A-5H-1, 141 cm, through -11H-CC, which contain *P. lacunosa* and *Gephyrocapsa oceanica,* to Zone CN14a. Sample 126-793A-11H-CC does not contain the acme of *Reticulofenestra* sp. A, which implies that this sample is younger than that datum (0.83 Ma; Takayama and Sato, 1987). Other species recovered from Hole 793A include *G. oceanica, Calcidiscus leptoporus, Umbilicosphaera sibogae,* and *Coccolithus pelagicus.*

Hole 793B

Core 126-793B-1R was drilled through a diabase sill and is barren of calcareous nannofossils. We placed the interval from Sample 126-793B-2R-CC through -10R-CC in Zone CN4, given that *Sphenolithus heteromorphus* and *Calcidiscus macintyrei* are present. Samples 126-793B-11R-5, 85–87 cm, through -14R-CC occur below the first occurrence (FO) of *C. macintyrei* and above the FO of *S. heteromorphus,* and were assigned to Zone CN3. Other species present in these two zones are *Cyclicargolithus floridanus, Discoaster deflandrei,* and *Coccolithus pelagicus. Sphenolithus belemnos* occurs with *S. heteromorphus* in Sample 126-793B-14R-1, 42–44 cm, which is evidence that this sample is near the base of Zones CN3–CN4.

Samples 126-793B-15R-3, 1–2 cm, through -18R-4, 23–25 cm, do not contain *S. heteromorphus* or *S. belemnos,* and lie above the FO of *Discoaster druggii* in Sample 126-793B-18R-4, 23–25 cm. Therefore, we assigned this interval to Zone CN1c. The absence of *S. belemnos* in this section implies that Zone CN2 is missing and that a hiatus occurs between Samples 126-793B-14R-CC and -15R-3, 1–2 cm. Other species present in Zone CN1c are *C. floridanus, D. deflandrei,* and *Reticulofenestra bisecta. R. bisecta* may be reworked in this interval.

Samples 126-793B-18R-CC through -20R-CC are barren. Samples 126-793B-21R-CC and below contain typical Oligocene assemblages, including *R. bisecta, C. floridanus* and *D. deflan-*

drei; in the absence of exclusively Miocene species, we consider these assemblages to be of Oligocene age. Because of the rare and sporadic occurrences of the index species *Sphenolithus ciperoensis* and *Sphenolithus distentus* in the Oligocene interval, the zonal boundaries are tentative. We placed Samples 126-793B-21R-CC through -30R-CC, which lie above the last occurrence (LO) of *S. distentus,* in Zone CP19b. The LO of *S. ciperoensis* is in Sample 126-793B-23R-CC. We assigned Samples 126-793B-31R-CC through -54R-CC to Zone CP19a, given the co-occurrence of *S. ciperoensis* and *S. distentus.* Samples 126-793B-55R-CC and -56R-CC are barren. The interval from Samples 126-793B-57R-3, 82–83 cm, through -81R-1, 86 cm, contains sporadic occurrences of *R. bisecta, C. floridanus, D. deflandrei, S. distentus,* and *Sphenolithus predistentus* and does not contain *S. ciperoensis.* Therefore, we tentatively placed this interval in Zones CP17–CP18. The occurrence of one questionable specimen of *Reticulofenestra umbilica* in Sample 126-793B-81R-1, 86 cm, may be a result of reworking. All samples examined below Sample 126-793B-81R-1, 86 cm, are barren of calcareous nannofossils.

Planktonic Foraminifers

Hole 793A

Minute juvenile planktonic foraminifers and specimens of *Globigerina quinqueloba* are present in Samples 126-793A-1H-1, 0–2 cm, and -1H-1, 2–5 cm, which consist predominantly of volcanic ash. Zonal markers were not observed in these samples. Sample 126-793A-1H-1, 6–8 cm, is similar to the previous samples, but several additional adult planktonic foraminifers are present, including *Globorotalia inflata, Globigerinoides ruber, Globigerinoides trilobus,* dextral and sinistral *Globigerina pachyderma, Globigerinoides tenellus, Globigerinita glutinata,* and *Orbulina universa.* Zonal markers are not present in this sample. *Globorotalia truncatulinoides* is abundant in Sample 126-793A-3H-4, 0 cm, in addition to the species present in the samples above. Rare specimens of *Globorotalia tosaensis* are also present in this core. The overlap of these two species ranges between 0.2 and 1.8 Ma in the subtropical Northwest Pacific (Keller, 1979). Other Pleistocene species present in Sample 126-793A-3H-4, 0 cm, are sinistral *Globorotalia menardii,* sinistral *Globorotalia tumida,* and *Globigerina calida,* placing this sample in Zone N23 (sensu Blow, 1969).

Samples 126A-793A-5H-3, 2–4 cm, and -5H-CC contain *G. inflata, G. tosaensis, Globigerina hexagona,* and other long-ranging taxa. The absence of *G. truncatulinoides* assigns these samples to the zonal range of *G. tosaensis* (>0.2 Ma and <2 Ma; Keller, 1979). Sample 126-793A-7H-3, 60–65 cm, contains *G. inflata* and *G. tosaensis-truncatulinoides.* The absence of *G. truncatulinoides* s.s. places this sample in the zonal range of *G. tosaensis* (Keller, 1979). Sample 126-793A-7H-CC consists mainly of volcanic ash. Zonal markers were not observed in this sample. Sample 126-793A-9H-CC contains *G. tosaensis, Globorotalia crassaformis hessi,* and a primitive form of *G. tumida*; we assigned this core to the zonal range of *G. crassaformis hessi* (Keller, 1979; Fig. 43). Samples 126-793A-10H-2, 102–104 cm, and -11H-CC contain mainly volcanic ash. Planktonic foraminifers are similar to those found in Sample 126-793A-9H-CC. We placed these samples in the zonal range of *Globorotalia crassaformis hessi.*

The abundance and preservation of foraminifers ranges from very abundant to rare and good to moderate, respectively.

Hole 793B

Samples 126-793B-2R-1, 36–38 cm, -2R-1, 64–65 cm, and -2R-CC, are dominated by *Globoquadrina venezuelana, Globoquadrina dehiscens, Globigerinoides immaturus, Globorotalia scitula, Sphaeroidinellopsis disjuncta, Globorotalia peripheronda,* and *Catapsydrax parvula.* They were placed in Zone N10. Samples 126-793B-8R-1, 60–62 cm, and -8R-CC contain *Globigerina continuosa* and *Globigerina drury,* in addition to the species mentioned above, and were assigned to Zone N10.

Globoquadrina venezuelana, G. dehiscens, G. scitula, Globorotalia praescitula, and *S. disjuncta* are present in Samples 123-793B-9R-2, 64–65 cm, and -9R-3, 61–62 cm. The overlap of *G. scitula* with *G. praescitula* places this sample in Zone N9 (Bolli et al., 1985). One specimen of *Globorotalia foshi lobata* was found in Sample 126-793B-9R-1, 60–65 cm. The stratigraphic range of this species spans the N11/12 boundary (Berggren et al., 1985), and its presence in this sample remains anomalous.

Samples 126-793B-12R-2, 46–49 cm, and -12R-2-CC, contain *S. disjuncta, Globigerina continuosa, Globoquadrina altispira, Catapsydrax parvula,* and others, and were assigned to Zone N9.

Sample 126-793B-16R-CC contains a few broken, flattened, and deformed specimens, tentatively identified as *Catpsydrax* sp., a minute globorotalid, and two specimens of *Chiloguembelina cubensis,* the range of which is late Eocene–mid-Oligocene. This sample may contain reworked faunas.

Minute benthonic calcareous and planktonic foraminifers, including juvenile specimens of *Catapsydrax* sp., are present in Sample 126-793-17R-4, 59–60 cm. These sediments may have been redeposited by a turbidity current. We cound not assign an age to this sample. Sample 126-793B-31R-2, 93–95 cm, contains specimens of *C. cubensis, Globigerina praebulloides,* and *Globigerina* sp. cf. *G. venezuelana,* and was tentatively placed in Zone "N4" (sensu Berggren et al., 1985). Sample 126-793B-52R-2, 33–35 cm, contains a recrystallized specimen of *Globigerina ampliapertura* and one specimen of *Globoquadrina pseudovenezuelana.* The ranges of both these species is late Eocene to early Oligocene. This sample is tentatively assigned to Zones "N4"/P21 (Berggren et al., 1985). Sample 126-793B-74R-1, 5–7 cm, contains one large broken globigerinid that we could not identify at the species level.

The abundance and preservation of specimens ranges from barren to abundant and from poor to good, respectively.

Benthic Foraminifers

Tertiary strata at Site 793 may be subdivided biostratigraphically into seven zonules on the basis of benthic foraminifers (Fig. 43). We estimated depositional water depths mainly on the basis of a comparison of (1) Holocene and Quaternary benthic foraminifer data from Holes 792B (1798 mbsl), 790A (2222 mbsl), 790B (2223 mbsl), 791A (2268 mbsl), 793A (2975 mbsl), and 787B (3254 mbsl) (see "Biostratigraphy" sections in other site chapters, this volume); (2) Pleistocene strata from offshore Shizuoka and Shikoku, Japan (Akimoto, 1989; Yasuda, 1989); and (3) Cenozoic benthic foraminifer data (Ingle, 1980; Woodruff, 1985; van Morkhoven et al., 1986) for the Miocene and Oligocene strata. We determined the age of each zonule on the basis of calcareous nannofossil zonations in this chapter.

The seven assemblage-zonules are as follows:

1. *Rhabdammina* spp.-*Thalmannammina*? sp. Assemblage Zonule

Characteristic species: deep-water agglutinated foraminifers such as *Rhabdammina* spp., *Thalmannammina*? sp., and *Haplophragmoides* sp. from mudstones and reworked larger inner neritic benthic foraminifers from coarse sandstone

Abundance: few agglutinated foraminifers; larger foraminifers are rare in Cores 126-793B-72R through -67R and common in Cores 126-793B-66R through -64R

Samples: 126-793B-67R-1, 2–4 cm, -73R-CC, and -74R-1, 5–7 cm, from mudstones

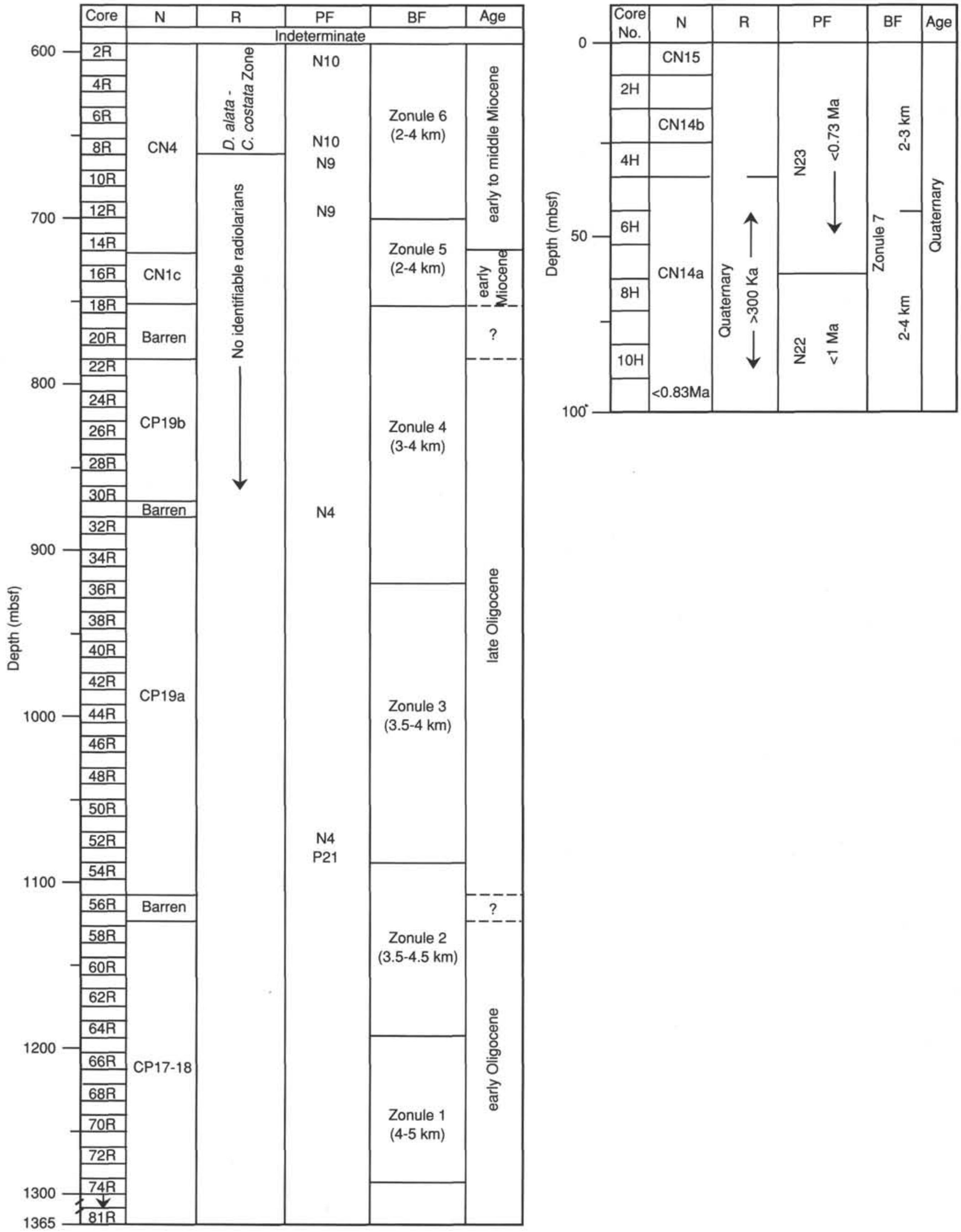

Figure 43. Biostratigraphic results from Site 793. N = calcareous nannofossils, R = radiolarians, PF = planktonic foraminifers, BF = benthic foraminifers.

Age: late early Oligocene
Depositional water depth: between 4 and 5 km
Remarks: This zonule is characterized by primitive agglutinated foraminifers and the absence of calcareous foraminifers. These benthic foraminifers show depositional water depths below the CCD. Larger foraminifers from sandstones may be reworked from an inner neritic zone to abyssal depths.

2. *Rhizammina* sp.-*Marginulina*? sp. Assemblage Zonule
Characteristic species: *Rhizammina* sp., *Marginulina*? sp., *Rhabdammina* sp., *Thalmannammina*? sp., *Haplophragmoides* sp., and *Nodosaria* sp. A
Abundance: few
Samples: from 126-793B-53R-CC through -61R-CC
Age: late early-early late Oligocene
Depositional water depth: between 3.5 and 4.5 km
Remarks: This assemblage zonule is composed of primitive agglutinated foraminifers and primitive calcareous foraminifers. This assemblage indicates depositional water depths near the carbonate compensation depth (CCD).

3. *Stilostomella* sp.-*Nodosaria* sp. A Assemblage Zonule
Characteristic species: *Rhizammina* sp., *Stilostomella* sp., *Nodosaria* sp. A., *Glomospira gordialis, Reophanus oviculus, Rhabdammina* sp., *Labrospira* sp., *Trochammina* sp. and *Pleurostomella* spp.
Abundance: few
Samples: 126-793B-36R-2, 108–111 cm, through -52R-2, 33–35 cm
Age: early late Oligocene
Depositional water depth: between 3.5 and 4 km
Remarks: This assemblage, which consists of primitive agglutinated foraminifers and primitive calcareous foraminifers plus *Stilostomella* sp. and *Pleurostomella* sp., shows depositional water depths above the CCD.

4. *Rhabdammina* spp.-*Oridorsalis umbonatus* Assemblage Zonule
Characteristic species: R*habdammina* spp., *Rhizammina* sp., *Stilostomella* spp., *Thalmannammina*? sp., *Gyroidinoides* sp., *Oridorsalis umbonatus, Pullenia* spp., *Reophax* spp., and *Glomospira gordialis*
Abundance: few; common in Samples 126-793B-35R-CC and -35R-3, 109–111 cm
Samples: 126-793B-18R-3, 102–104 cm, through -35R-CC
Age: late Oligocene
Depositional water depth: between 3 and 4 km
Remarks: The zonule is marked by the occurrence of primitive agglutinated foraminifers, *Stilostomella* spp., plus deep-sea trochospiral and planispiral calcareous forms such as *Oridorsalis umbonatus, Gyroidinoides* sp., and *Pullenia* spp.

5. *Cibicidoides* spp.-*Rhizammina* sp. Assemblage Zonule
Characteristic species: *Stilostomella* spp., *Cibicidoides* spp., *Globocassidulina subglobosa, Rhizammina* sp., *Oridorsalis umbonatus, Pullenia bulloides, Gyroidinoides* sp., *Pullenia* spp., *Pleurostomella* spp., *Anomalinoides* spp., *Rhabdammina* sp., *Bulimina grata,* and *Eggerella* sp.
Abundance: abundant in Samples 126-793B-17R-4, 59–60 cm, and -16R-CC; few in Samples 126-793B-16R-1, 70–72 cm, and -12R-CC
Samples: 126-793B-12R-CC through -17R-4, 59–60 cm
Age: early Miocene
Depositional water depth: between 2 and 4 km
Remarks: This zonule is characterized by the fauna from the subjacent zonule and the dominance of calcareous foraminifers such as *Pullenia bulloides, Cibicidoides* spp., *Anomalinoides* spp., and *Globocassidulina subglobosa.* Complex agglutinated foraminifers such as *Vulvulina* sp. and *Eggerella* sp. have their FO in this zonule.

6. *Stilostomella* spp.-*Pullenia bulloides* Assemblage Zonule
Characteristic species: *Stilostomella* spp., *Oridorsalis umbonatus, Pullenia bulloides, Globocassidulina subglobosa, Gyroidinoides* spp., *Anomalinoides* spp., *Cibicidoides* spp., *Pullenia* spp., and *Chrysalogonium* sp.
Abundance: common below Sample 126-793B-8R-1, 60–62 cm; few above Sample 126-793B-7R-CC.
Samples: 126-793B-2R-1, 36–38 cm, through -12R-2, 46–49 cm
Age: late early-early middle Miocene
Depositional water depth: between 2 and 4 km.
Remarks: This zonule is characterized by the fauna from the subjacent zonule without primitive agglutinated foraminifers genera such as *Rhizammina, Rhabdammina,* and *Bathysiphon.*

7. *Pullenia bulloides-Melonis barleeanus* Assemblage Zonule
Characteristic species: *Pullenia bulloides, Melonis barleeanus, Epistominella exigua, Melonis pompilioides, Oridorsalis umbonatus, Cibicidoides wellerstorfi, Sphaeroidina bulloides, Pyrgo murrhina, Tosaia hanzawai,* and *Uvigerina probosidea.*
Abundance: abundant
Samples: 126-793A-3H-4, 0–2 cm, through -11H-CC
Age: Pleistocene
Depositional water depth: between 2 and 4 km below Sample 126-793A-7H-3, 60–65 cm; between 2 and 3 km above Sample 126-793A-5H-CC, as determined by presence of *Uvigerina probosidea,* etc.

Radiolarians

Hole 793A

We examined all core-catcher samples from this hole. Quaternary radiolarians are present in all samples except 126-793A-2H-CC and -8H-CC. The occurrence of *Druppatractus aquilonius* in and below Sample 126-793A-3H, 0 cm, indicates an age >300 Ka for samples at and below this level (Foreman, 1981).

Hole 793B

Rare, moderately preserved radiolarians are present in Sample 126-793B-2R-CC and Samples 126-793B-4R-CC through -8R-CC. The presence of *Cyrtocapsella tetrapera* and *Stichocorys wolffii* in these samples suggests assignment to the late early to early middle Miocene *Calocycletta costata* or *Didymocyrtis alata* zones. No identifiable faunas were found in, or below, Sample 126-793B-9R-CC. Radiolarians are present in many samples, but they are typically infilled and have suffered extreme dissolution.

Summary

Radiolarians, calcareous nannofossils, and planktonic foraminifers indicate a Quaternary age for all cores from Hole 793A (Fig. 43). A maximum age of no greater than 0.83 Ma is indicated from nannofossil data. Calcareous nannofossils, radiolarians, and planktonic foraminifers indicate an early middle to late early Miocene age range for samples down to the level of Sample 126-793B-14R-CC in Hole 793B. A possible hiatus occurs between Samples 126-793B-14R-CC and -15R-3, 1–2 cm, below which early Miocene (Zone CN1c) nannofossils occur. The hiatus is equivalent to nannofossil Zone CN2 (approximately 1.9 m.y. duration).

We could not determine an age for the interval between Samples 126-793B-18R-CC and -20R-CC. Biostratigraphic data are insufficient to determine whether or not there is a hiatus at this level. Below Sample 126-793B-21R-CC nannofossils and rare planktonic foraminifers indicate late Oligocene (Zone CP19b) through late early Oligocene ages (Zones CP17–18). Reworked upper Eocene planktonic foraminifers may indicate the age of the source area for detrital sediments.

Benthic foraminifer faunal changes show shallowing water depths from 4–5 km in the early Oligocene to 2–3 km at present. As the present water depth is 3 km, this estimate means that 1–2 km shallowing of the sea floor, and 0.3–0.7 km of total basement uplift has occurred since about 32 Ma.

PALEOMAGNETICS

Introduction

We made magnetic measurements on the archive halves of all but the first two cores (coarse gravels) from Hole 793A and on all sediment cores from Hole 793B. Below Core 126-793B-82R, we measured only selected core sections or cores containing possible lava flows because many of the lower cores consisted of coarse volcanic breccia. We also carried out stepwise alternating field (AF) demagnetizations on selected discrete samples (in the form of 7 cm^3 cubes from Hole 793A and 10-cm^3 minicores) from Hole 793B, employing the fully automatic spinner (FAS) (see "Explanatory Notes" chapter, this volume). In some cases, we used the Schonstedt AF demagnetizer in conjunction with the FAS instrument to extend discrete sample demagnetization beyond 50 mT. The results from discrete sample analysis (Fig. 44) show that a stable magnetization component is dominant in most of the cores and confirm the reliability of the results from archive halves.

Although core sections were not stored in the core rack in the core cutting room, natural remanent magnetization (NRM) declinations below Core 126-793B-24R nevertheless exhibited a strong tendency to cluster at 0° or 360°, whereas in some cases the inclinations systematically became more positive with increasing depth within the core (see "Paleomagnetics" section, "Site 792" chapter, this volume). This was a particular problem for cores from the lower parts of the hole (Fig. 45). During sawing, the cores were deliberately rotated 180° from their normal orientation several times. However, this did not consistently alter the direction of declination clustering. In most cases, AF demagnetization to 15 mT was effective in removing much of this remanence contamination; but, in some instances (e.g., Cores 126-793B-76R through -82R, 1305–1375 mbsf), it had little effect. Only ~30% of the discrete samples from cores with archive half declinations clustered at 0° or 360° exhibited similar biased declinations. The remaining discrete samples had NRM declinations significantly different from their archive halves. This suggests that the precautions taken in storing the cores may have been of some benefit. However, an additional (and as yet unidentified) source of magnetic contamination remains.

Magnetostratigraphy

Hole 793A

Figure 46 shows the declination and inclination data for the archive halves of the cores from Hole 793A. We have filtered highly scattered data from cores severely disturbed by drilling, or consisting of coarse-grained material, out of this plot for the sake of clarity. The <1-Ma paleontologic age determination for all cores from Hole 793A (see "Biostratigraphy" section, this chapter) allows us to label the normal-to-reverse polarity change in Core 126-793A-9H-3 (75.4 mbsf) as the Brunhes-Matuyama reversal. The short normal polarity interval in Core 126-793A-10H (beginning at ~81 mbsf) is tentatively identified as the Jaramillo Polarity Zone. A short reversed zone of magnetization in Core 126-793A-6R-1 (42.4–43.0 mbsf), the existence of which was confirmed by discrete sample AF demagnetization, may correspond to a reversed polarity event at ~0.5 Ma reported in rapidly deposited glacial loess deposits in eastern Europe (Champion et al., 1988).

Hole 793B

Figure 47 summarizes the magnetostratigraphy of the cores from Hole 793B. Below Core 126-793B-25R, core sections composed of coarse-grained sediment types (i.e., sandstones and clastic debris flows) displayed high (~50°) inclinations and normal polarities after AF demagnetization, even for intervals where the finer grained sediment types displayed reversed polarities. Because this probably represents a recently acquired viscous magnetization, we have filtered these core sections out of the composite figure. In addition, we have also deleted cores displaying persistent clustering of declinations at 0° and 360°, or those from which discrete samples exhibited intermediate or contradictory polarities after high AF demagnetization.

Because paleontologic evidence indicates a late early to middle Miocene age for the first 14 cores of Hole 793B (see "Biostratigraphy" section, this chapter), we tentatively assigned the long reversed interval represented by Cores 126-793B-2R through -8R (595–660 mbsf) as reversed Chron C5B (Berggren et al., 1985), with the normal sill in Core 126-793B-1R probably representing the normal part of the same chron. Thus, the following sequences of mostly normal-polarity (660–690 mbsf) and mostly reversed-polarity cores (690–718 mbsf) would correspond to Chron C5C, normal and reversed, respectively. A depositional hiatus or unconformity near the top of Core 126-793B-15R is directly followed by a sequence of tightly spaced, multiple reversed- and normal-polarity zones (720–750 mbsf), probably representing the C6 reversed through C6A or C6B polarity chrons (Fig. 47A). This is consistent with the 20.5–23.2 Ma paleontological age assignment for this interval (see "Biostratigraphy" section, this chapter).

Low sedimentation rates, as indicated by a paucity of volcanic input and a barren interval (see "Lithostratigraphy and Accumulation Rates" section, this chapter) may account for the apparent compressed section represented in Cores 126-793B-19R and -20R, as the succeeding cores are characterized by a late Oligocene paleontologic assemblage (see "Biostratigraphy" section, this chapter).

The long normal and reversed polarity zones distributed over Cores 126-793B-21R through -85R (the last sedimentary core before basement) can be correlated with Chrons C8 through C10 in Figure 47 (B–D), which represent a time period of ~4 m.y. The mixed polarities in the sedimentary cores below 1320 mbsf almost certainly reflect incomplete removal of the present-field normal component of magnetization in the coarser grained rock types, rather than field reversals. The underlying volcanic breccia and flows are predominantly of normal polarity, but with an apparent reversed flow (recognized only after discrete sample analysis) in Core 126-793B-104R. This sequence likely represents the C11 normal polarity chron (assuming that no major hiatus or unconformity exists between the sediment and basement), with the reversed flow at ~1580 mbsf corresponding to the short reversed polarity zone at 31.6 Ma (Fig. 47D).

We correlate the reddish, carbonate-rich claystone in Cores 126-793B-16R and -17R, centered at ~740 mbsf (see "Lithostratigraphy and Accumulation Rates" section, this chapter) with a similar carbonate zone occurring in Core 126-792E-27R, as both encompass a short zone of reversed polarity (Chron C6A?). Unlike the multiple polarity zones that characterize the basement rocks at Site 792, the extrusive units at the base of Site 793 appear to represent a simpler normal-reverse-normal polarity sequence.

Table 5 summarizes the datums derived from the best determined polarity chron boundaries in the preceding discussion.

Paleolatitude

Despite scatter in the data, and a distinct variation between inclinations associated with normally and reversely magnetized

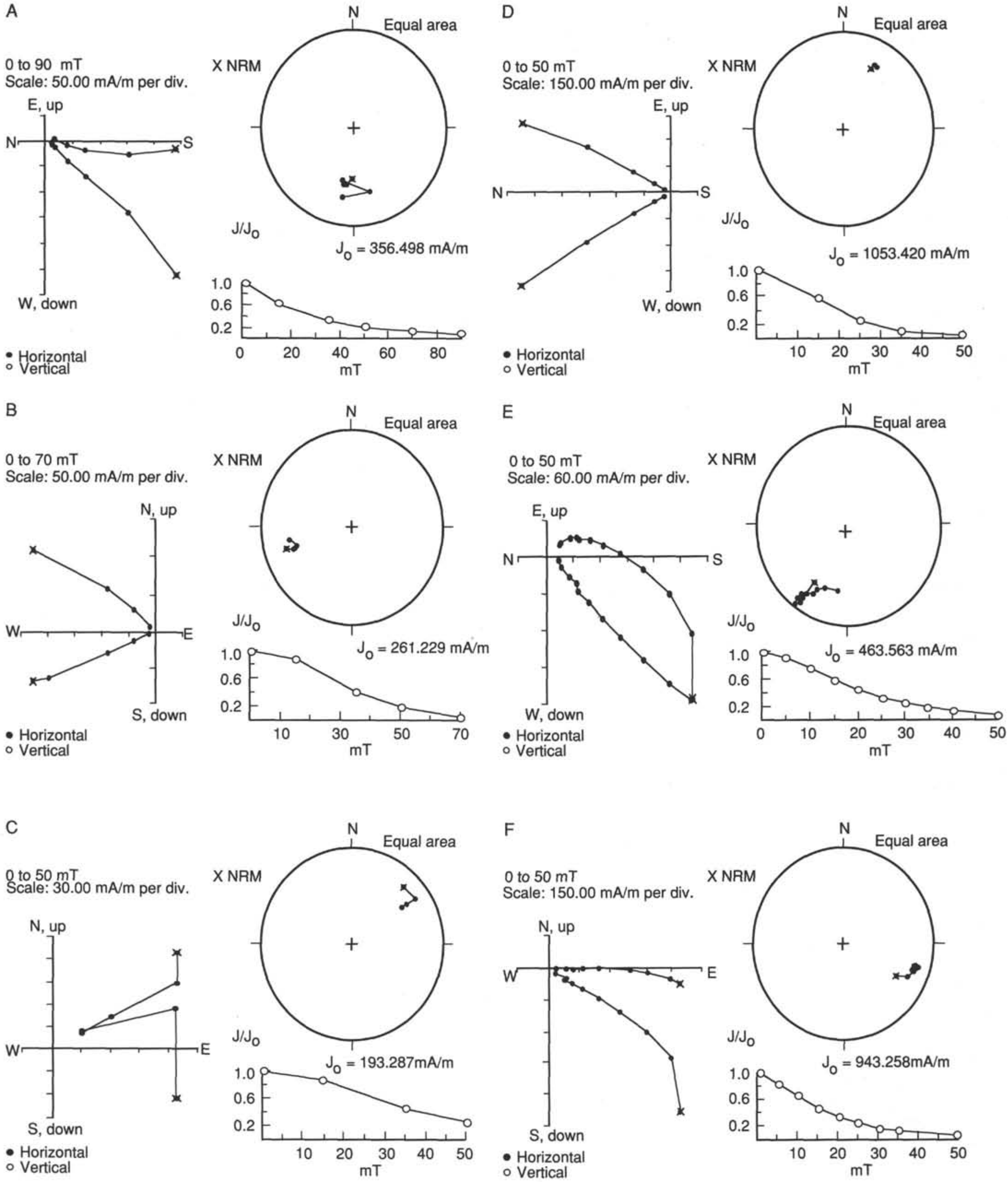

Figure 44. Examples of orthogonal directions, changes of remanence vector direction, and total intensity during stepwise AF demagnetization for discrete sedimentary and igneous rock samples. Numerical values of remanence intensity and inclination for these samples are given in Table 5. **A.** Sample 126-793B-35R-3, 102 cm. **B.** Sample 126-793B-71R-2, 135 cm. **C.** Sample 126-793B-74R-1-15 cm. **D.** Sample 126-793B-92R-3, 11 cm. **E.** Sample 126-793B-104R-1, 118 cm. **F.** Sample 126-793B-110R-2, 68 cm.

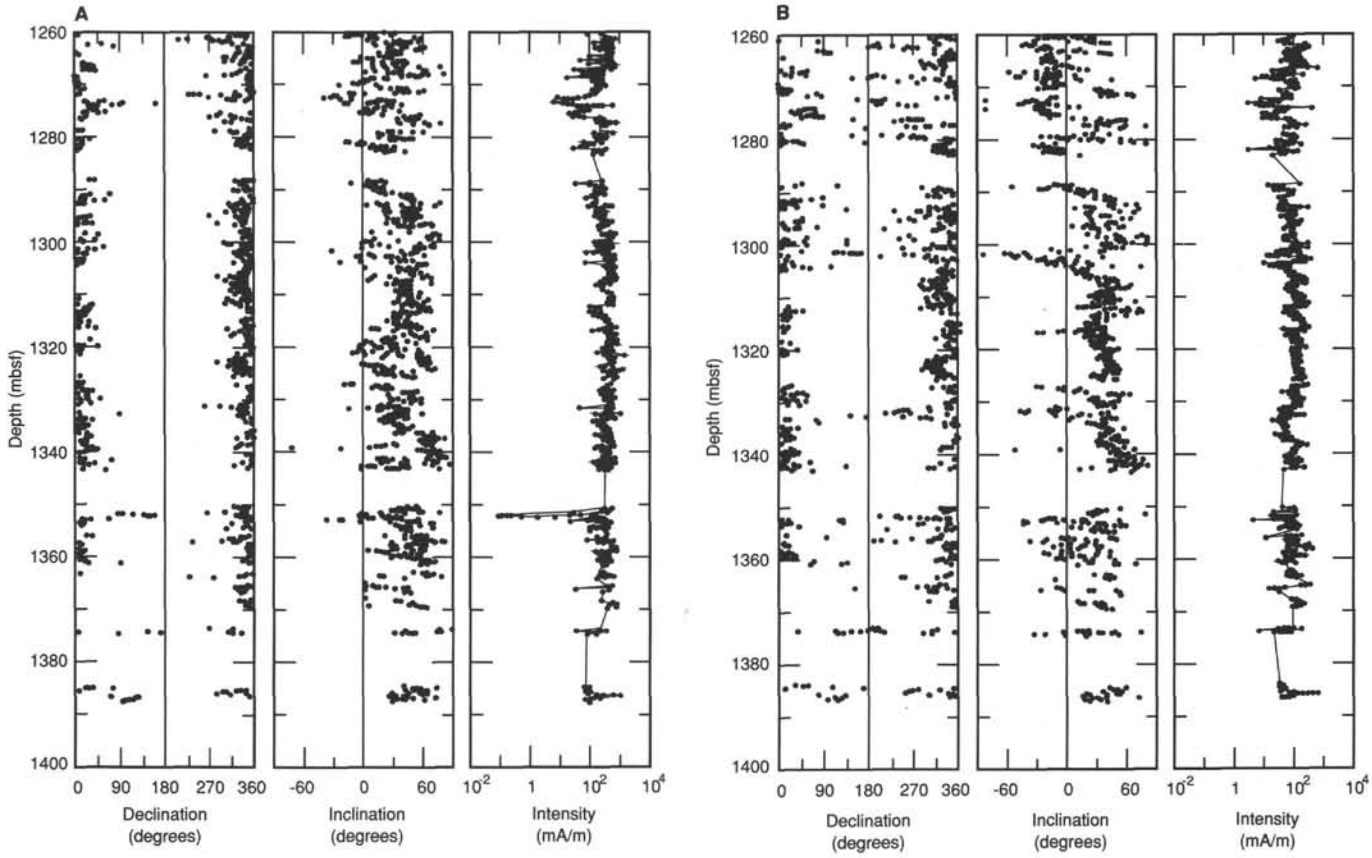

Figure 45. Comparison between paleomagnetic results for Cores 126-793B-71R to -84R. **A.** Before AF demagnetization. **B.** After AF demagnetization.

core intervals, the mean inclinations of the various archive halves and discrete samples suggest a progressive decrease from $\sim 40°$ in the middle Miocene (represented by the top of Hole 793B) to near 30° for the middle Oligocene sediments (directly above basement) (Fig. 48). Inclination data from cores that exhibit low directional scatter near the bottom of Hole 793B, including both sedimentary and igneous rock types (archive halves, Fig. 49; discrete samples, Table 6) support the idea that this site was situated at a significantly lower latitude in mid-Oligocene time. This result is consistent with DSDP results from the West Philippine Basin (as summarized in fig. 3 of Seno and Maruyama, 1984), which also suggests $\sim 15°$ of northward translation since the middle Oligocene.

The directional inconsistency between the data of normal and reversed polarities in the Oligocene (Fig. 48) probably results from incomplete removal of the secondary viscous remanence caused by the present geomagnetic field. Although the maximum field intensity of AF demagnetization of archive halves is limited by ODP policy, this inconsistency may be eliminated by further shore-based demagnetization and measurement of additional discrete samples. Paleomagnetic evidence for or against progressive azimuthal rotation of this site should also be forthcoming, following shore-based paleomagnetic measurement of discrete samples and processing of FMS data.

Reversal Studies

The use of the multishot tool in Hole 793A enabled us to recover an azimuth-corrected reversal record of the Brunhes-Matuyama polarity transition (Fig. 50). Unfortunately, the sediment immediately above and below the reversal interval was watery and highly disturbed by the drilling process. Therefore, the discrete samples taken across this zone did not produce a usable detailed record of the geomagnetic field behavior during the time of the reversal. However, as at the previous sites, the inclination data suggest two rapid polarity reversals, although part of the second inclination reversal is missing between Sections 126-793A-9H-3 and -9H-4 (75.4 mbsf).

IGNEOUS PETROLOGY

This section describes the three main occurrences of igneous rocks in Hole 793B: (1) a diabase that intrudes middle Miocene sedimentary rocks, (2) volcanic clasts throughout the sedimentary sequence, and (3) the basement lava flows and breccias.

Olivine Diabase Intrusion

A total of 3.65 m of an olivine-diabase (lithologic Unit II) was penetrated in the first rotary core (126-793B-1R) of Hole 793B (586.5 mbsf). The approximate thickness of the diabase inferred from the drilling log is 4.5 m (90% recovery; Fig. 51). The diabase is directly overlain by 15 cm of epidote-carbonate-rich silicified sediments (Core 126-793B-1R; Fig. 52) that contain small bubbles and 5-mm pieces of diabase. The epidote and bubbles in the sediment are evidence for baking by the intrusion. The underlying sediments are middle Miocene in age, yielding a maximum age for the intrusion. The basal contact with the sediments was not recovered, but petrographic features of the lowest diabase indicate that its lower chilled margin was recovered. The diabase is of normal polarity, whereas the underlying sediments are reversed (see "Paleomagnetism" section, this chapter). The measured sonic velocity values of the intrusion are in the range of 5.00–5.14 km/s, whereas in the underly-

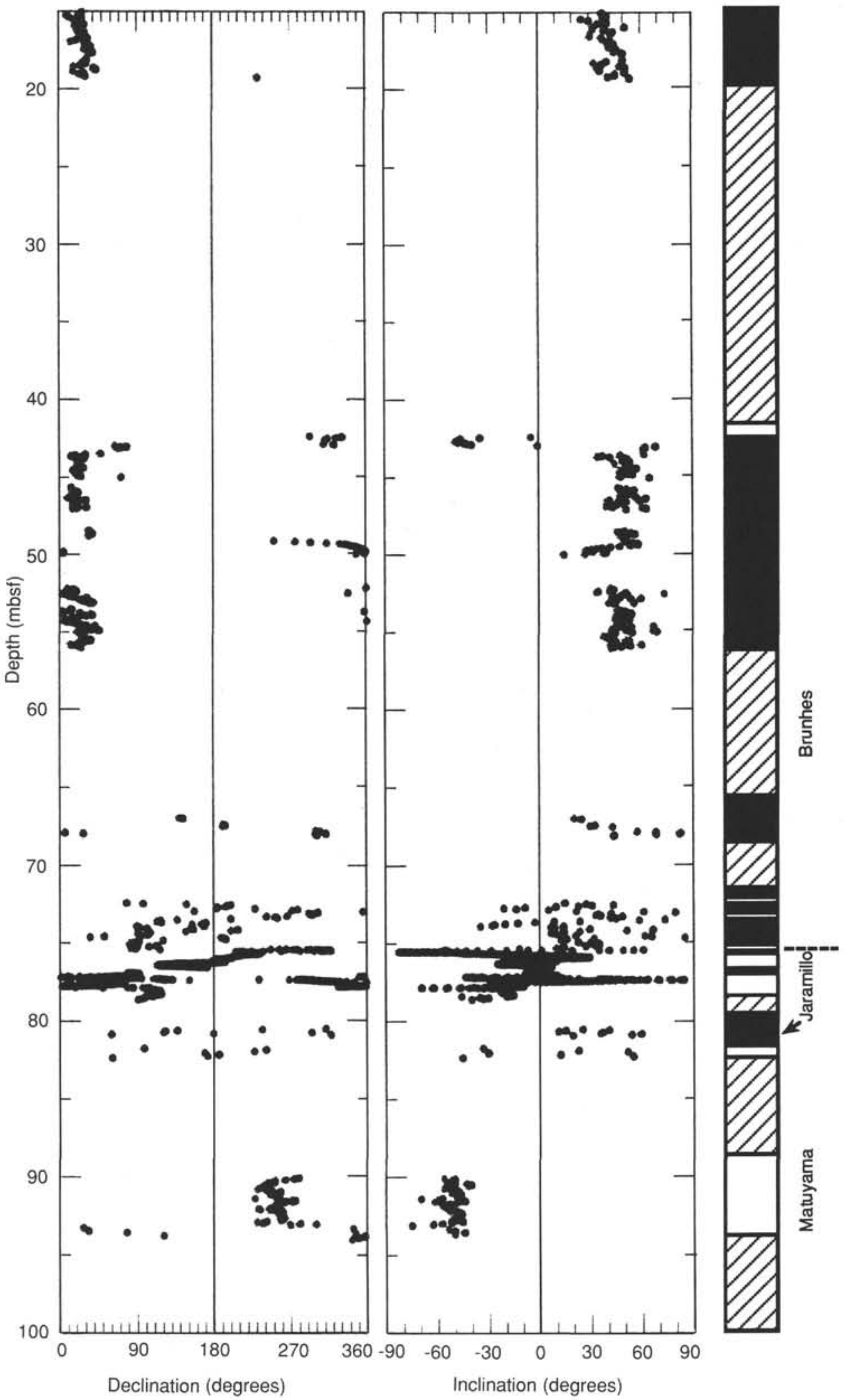

Figure 46. Paleomagnetic data vs. sub-bottom depth (mbsf) for Hole 793A. The data for cores with coarse sediment types and those disturbed by drilling are omitted (indicated by cross-hatching in magnetostratigraphy column, far right).

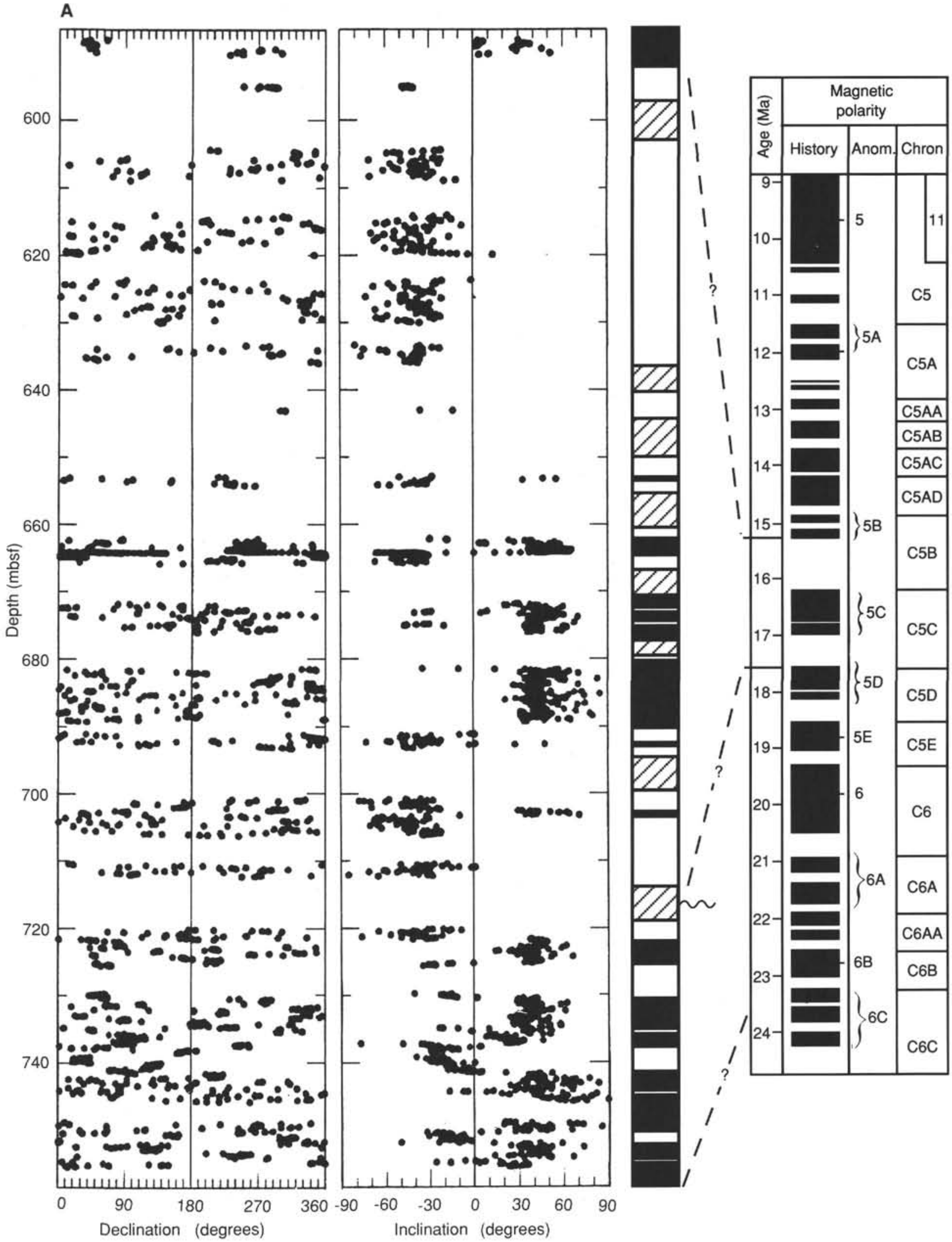

Figure 47. **A.** Paleomagnetic data vs. sub-bottom (mbsf) for Cores 126-793B-1R through -18R and correlation with the standard polarity time scale (Berggren et al., 1985). Cores with coarse sediment types and those disturbed by drilling are omitted (indicated by cross-hatching in magnetostratigraphy column, far right). Wavy lines beside the polarity column indicates hiatus/unconformity horizons estimated from biostratigraphic data (see "Biostratigraphy" section, this chapter). **B.** Data from Cores 126-793B-19R through -39R. **C.** Data from Cores 126-793B-40R through -61R. **D.** Data from Cores 126-793B-62R through -85R.

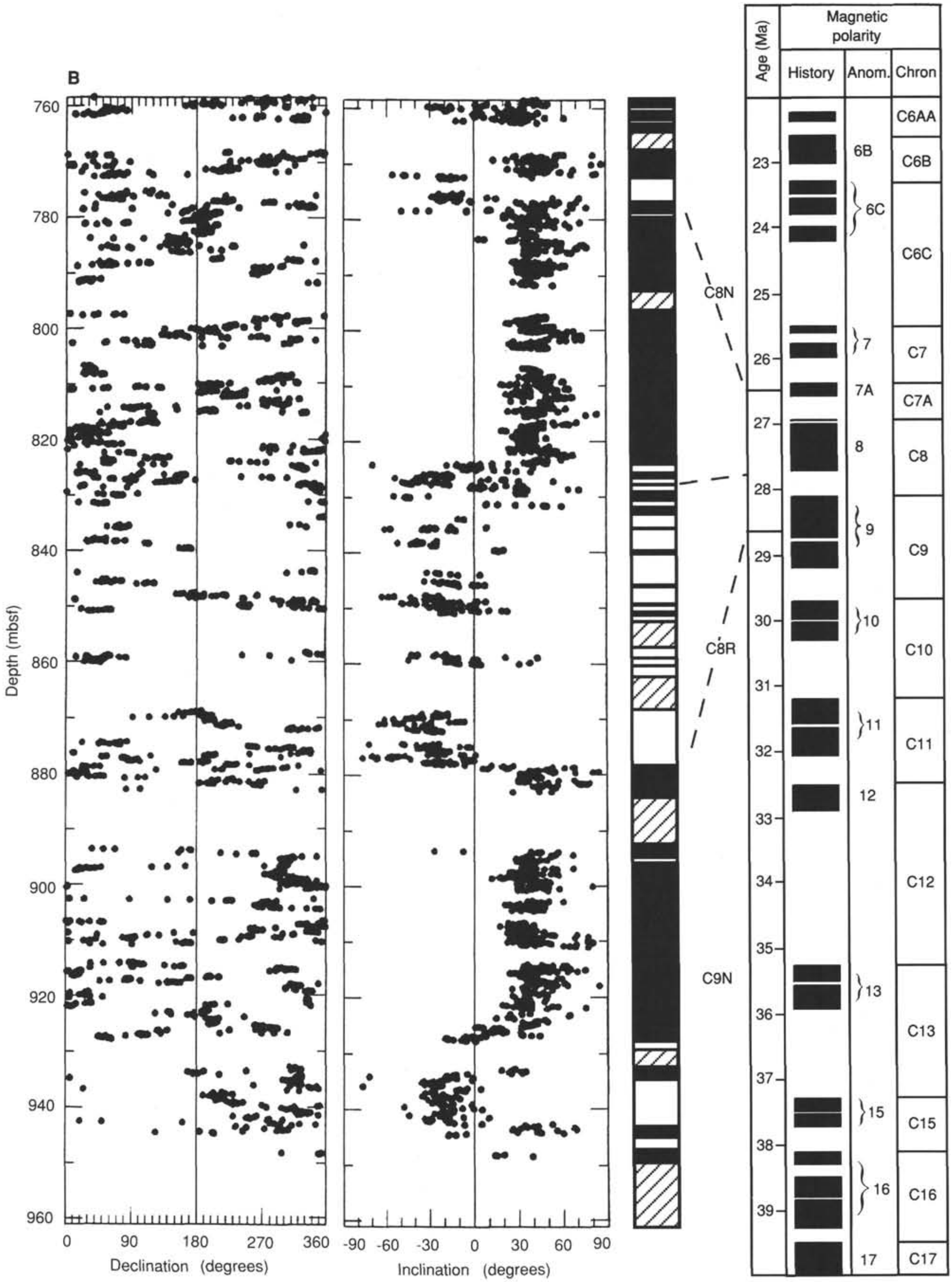

Figure 47 (continued).

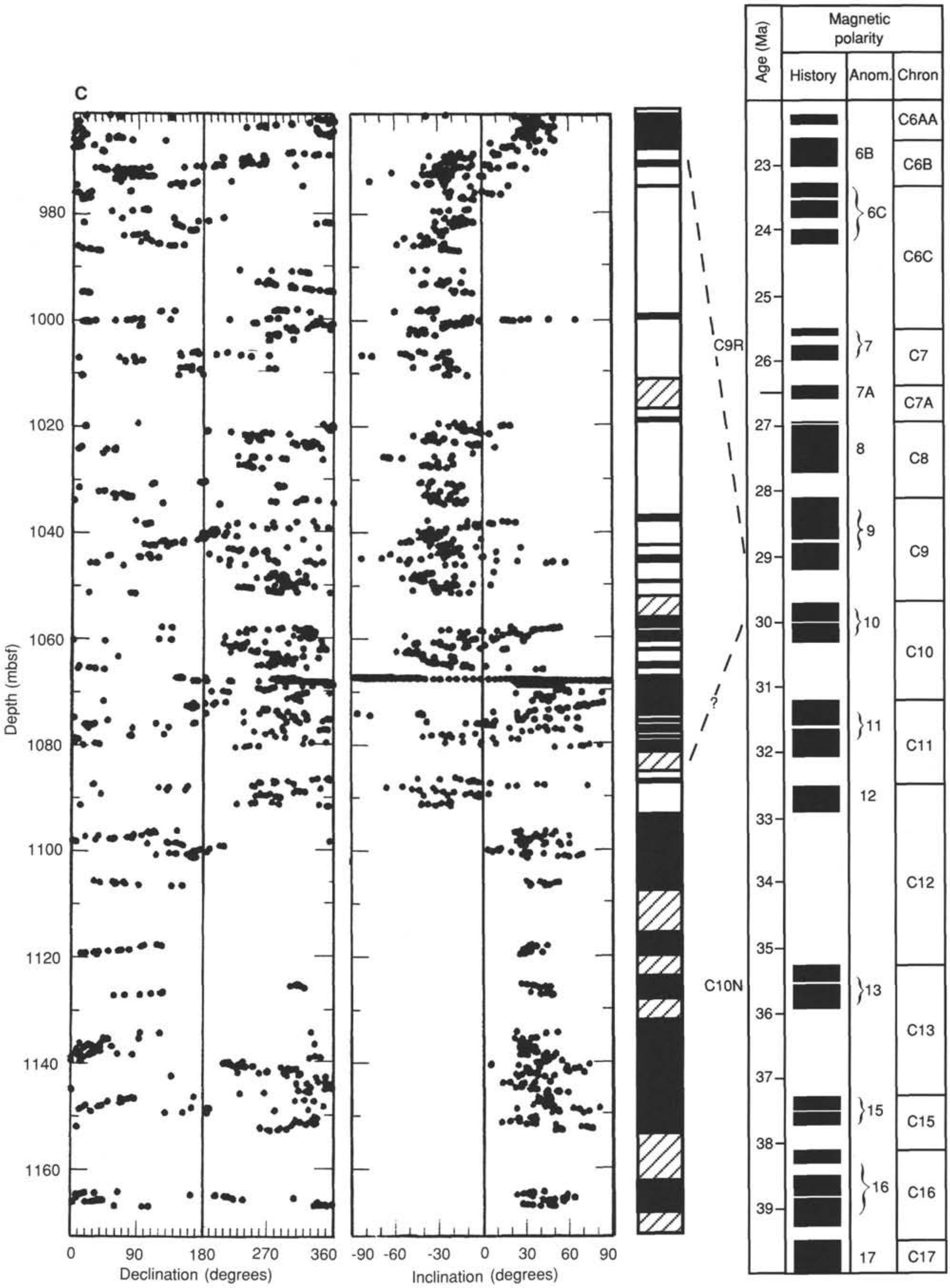

Figure 47 (continued).

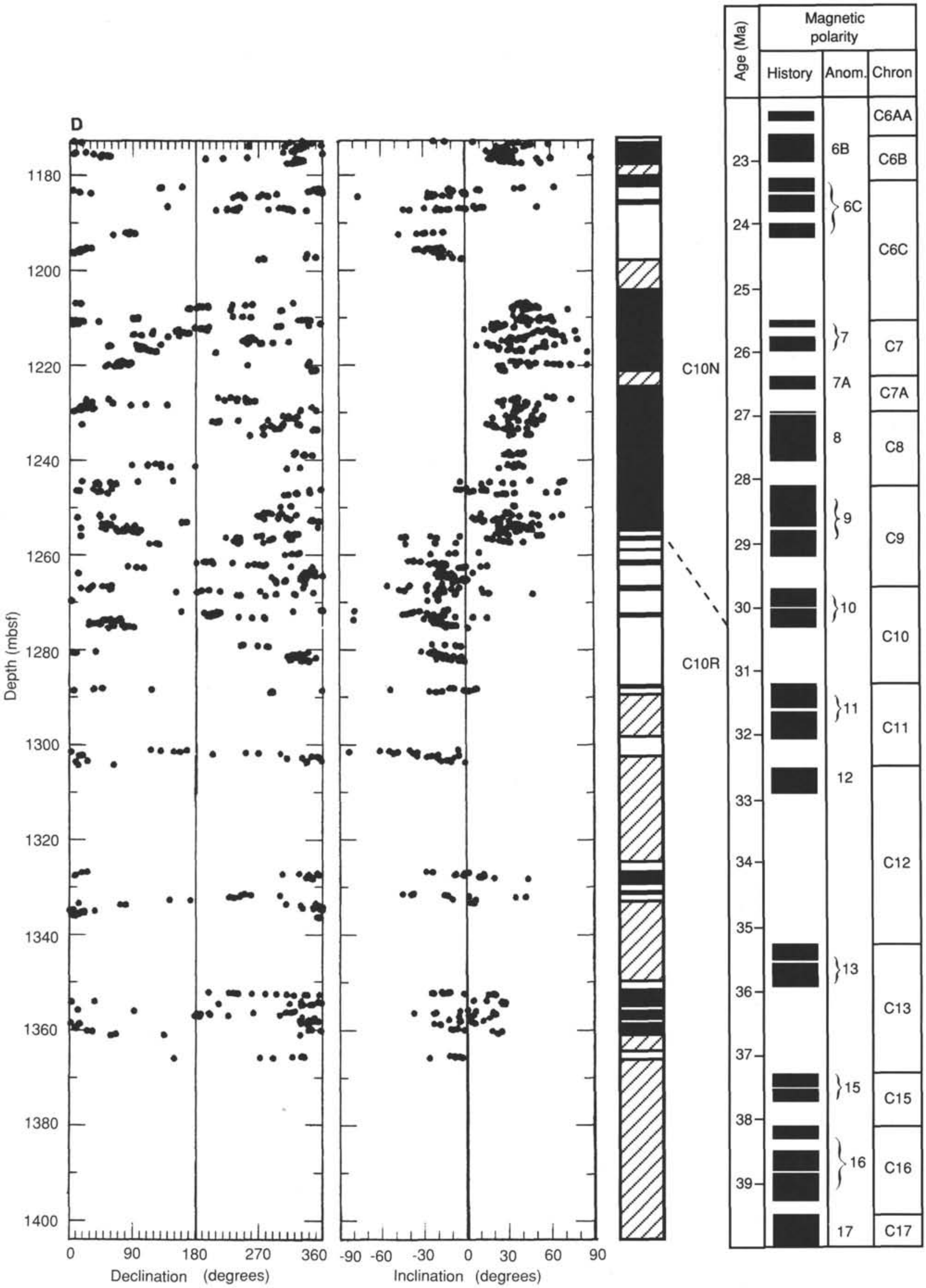

Figure 47 (continued).

Table 5. Datums derived from the polarity chron boundaries judged as most reliable in Site 793.

Age (Ma)	Chron	Depth (mbsf)
0.73	1-2	75.4-77.2
0.91	Jaramillo	80.5-88.1
15.27	C5B	594.7-603.8
16.22	C5C	662.3-668.1
21.71	C6A	737.0-737.5
21.90	C6AA	741.3-742.7
26.86	C8	776.6
27.74	C8	824.1-824.4
28.15	C9	878.1-878.7
29.21	C9	967.9
29.73	C10	1095.7-1099.9
30.09	C10	1182.8-1187.3
30.33	C10	1255.5

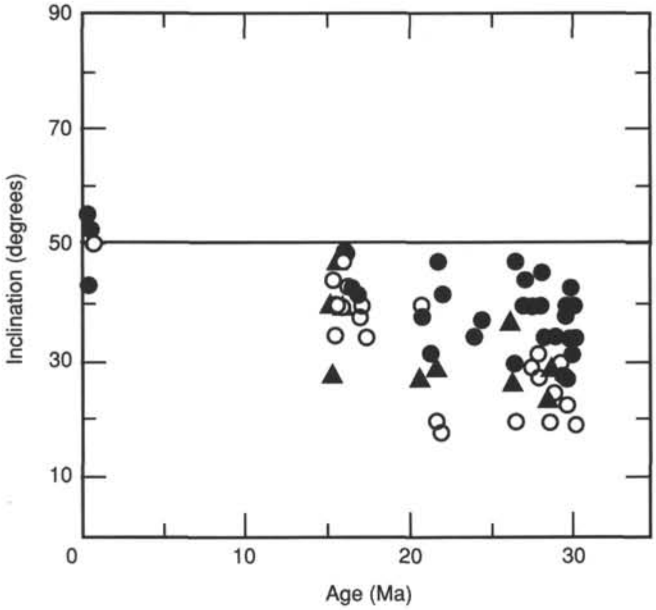

Figure 48. Mean inclinations for archive halves and discrete samples (mean value per core) vs. age for Site 793. Solid and open circles represent normal and reversed intervals, respectively. Triangles represent discrete samples. Horizontal line shows the inclination value of the axial geocentric dipole field for the present latitude of this site.

ing sediments they are much lower, 2.03 km/s; (see "Physical Properties" section, this chapter).

The differences in density and porosity between the intrusion and the underlying sediments are also striking (porosity = 9%-12% vs. 64% in the underlying sediments; density = 2.7 g/cm^3 vs. 1.78 g/cm^3 in the underlying sediments; see "Physical Properties" section, this chapter). The intrusion is too thin to be resolved by MCS profiles, so its lateral extent is unknown. The difference in magnetic polarity between the diabase and the underlying sediments, the contrast of the textures between the upper and lower margins of the unit, and the presence of a thermal contact with the overlying sediments provide evidence that this unit is intrusive. However, on the basis of the textural and structural evidence from the intrusive, we cannot conclude whether it is a concordant or discordant feature.

Petrographic Description

Minerals in the groundmass of the olivine-diabase are fresh, in contrast with the interstitial glass and olivine phenocrysts, which are altered to smectites. The top (Sections 126-793B-1R-1 through -1R-2, 60 cm) of the intrusion is fine grained with few glomeroporphyritic clots, whereas the middle to lower part (Interval 126-793B-1R-2, 60 cm, to -1R-3) has large (5-10 mm) subspherical dark inclusions and larger, more abundant, crystal clots (Fig. 53). The base of the unit is characterized by the presence of large olivine, clinopyroxene, orthopyroxene, and pseudomorphosed olivine phenocrysts in a fine-grained glassy groundmass, implying accumulation at a chilled margin (Fig. 54).

Subparallel, subhorizontal, dark-colored glassy bands (3-10 mm thick) are present at about 10-cm intervals in the intrusion. They are formed, like the subspherical inclusions, of a more vesiculated and finer grained material. These glassy bands or inclusions include quenched clinopyroxene and plagioclase crystals, abundant opaque minerals (up to 10%), and vesicles. The dark color is caused by the presence of smectites that fill the vesicles and replace the glass. These bands and inclusions probably represent more differentiated melts, squeezed during cooling into thermal contraction cracks of the intrusion by a filter-press process. The inclusions sometimes are tadpole shaped, tapering downward, with vesicles at the top. This particular example may have formed from more hydrous magma than mid-ocean ridge basalt (MORB).

Three thin sections from the upper, middle, and lower parts of the sill are representative of the recovered material and show the textural differences within this diabase (Fig. 54). The upper part consists of subhedral olivine phenocrysts altered to smectites in an intersertal to intergranular groundmass of subhedral zoned plagioclase laths, subhedral clinopyroxene, subhedral orthopyroxene, and opaque minerals. Point counting on thin section Sample 126-793B-1R-1, 102-104 cm, produced the following modal proportions: olivine pseudomorphs, 2.9%; plagioclase, 41%; clinopyroxene, 18.3%; orthopyroxene, <0.5%; opaque mineral, 4.2%; and glass, 33.8%.

The central part of the intrusion differs in that it has a greater abundance of olivine-clinopyroxene-orthopyroxene glomeroporphyritic aggregates in an intersertal groundmass containing clinopyroxene-plagioclase-opaque mineral. These clots are formed of olivine pseudomorphs of partly fresh orthopyroxene and fresh clinopyroxene. Also, the fine-grained inclusions are more abundant in this part of the intrusion (Fig. 51).

Finally, at the base of the unit is a 3-cm-thick vitrophyric layer with olivine-clinopyroxene-orthopyroxene glomeroporphyritic aggregates and isolated plagioclase phenocrysts, which represents the chilled margin. Subhedral olivine (~10% of the thin section), altered to smectites and calcite, is present either as isolated corroded phenocrysts (2 mm) or clustered with pyroxenes. In the aggregates, euhedrally zoned clinopyroxene crystals (up to 6 mm) exhibit multiple-style twinning and exsolution lamellae, and the orthopyroxenes are rounded crystals (3 mm) that are often surrounded by clinopyroxene. Tiny plagioclase laths (0.1 mm) are sometimes included in the orthopyroxene. Glass, altered to smectite, is caught in the glomeroporphyritic aggregates. These glomeroporphyritic aggregates (40% of the basal chilled margin) indicate accumulation. Finally, the cryptocrystalline groundmass (60%) includes abundant, small, quenched plagioclase and clinopyroxene microphenocrysts and crystallites. Rounded vesicles, 0.1 mm in diameter, are filled with smectites.

The crystallization sequence within the sill is inferred to be olivine, followed by orthopyroxene + clinopyroxene, followed by plagioclase, followed by the opaque mineral. The lack of the opaque mineral in the chilled margin and its abundance in the dark-colored inclusions and bands indicate that this is a late

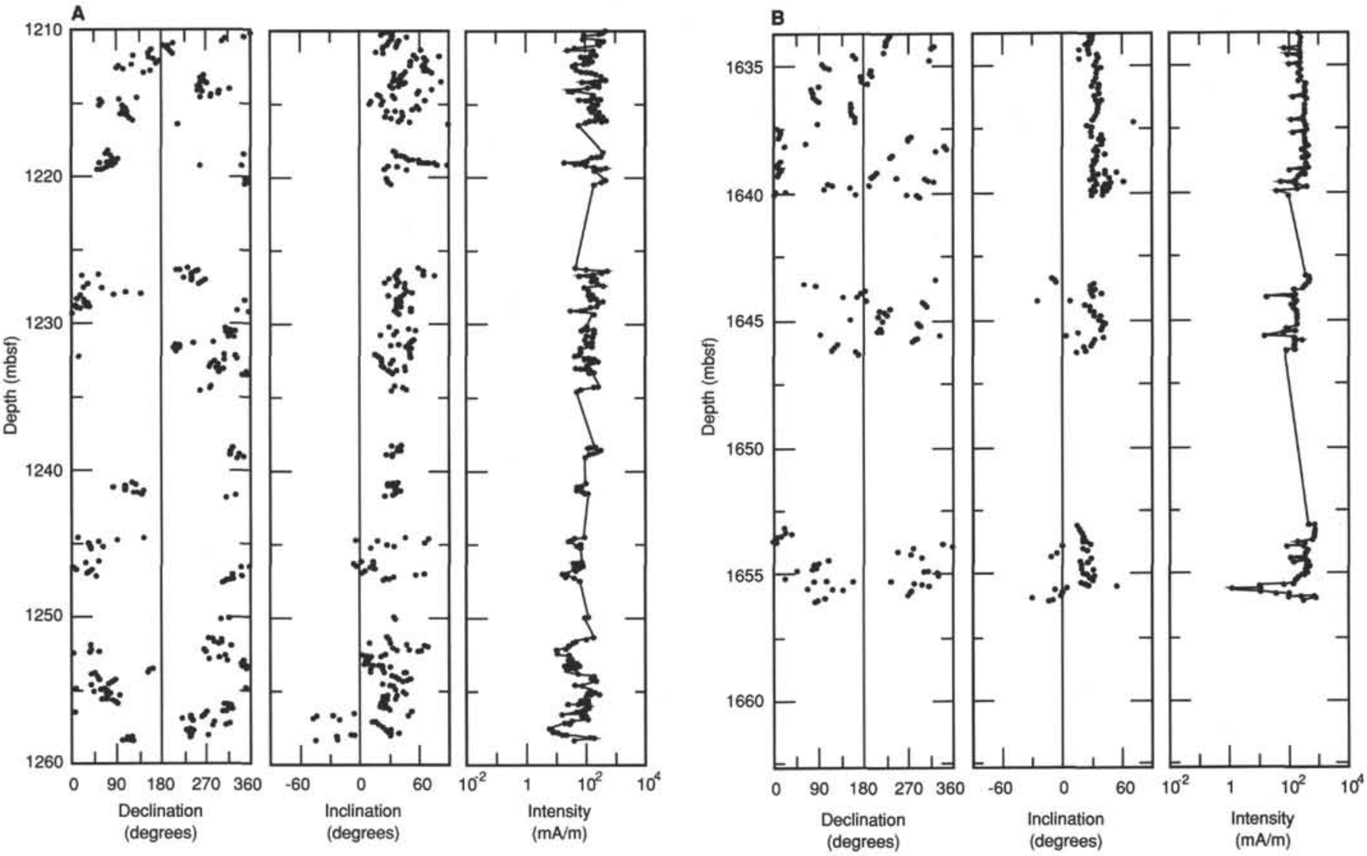

Figure 49. Paleomagnetic data vs. sub-bottom depth (mbsf). **A.** Cores 126-793B-66R through -70R. **B.** Cores 126-793B-110R through -112R.

Table 6. Results from paleomagnetic analysis of discrete samples, Site 793.

Core, section, interval (cm)	J(0)	Inc.(0) (degrees)	Optimum AF (mT)	J(AF)	Inc.(AF) (degrees)
126-793B-					
Sediments					
35R-3, 102	356	+47.0	90	15.6	+30.0
71R-2, 136	261	−24.1	35	109	−31.0
74R-1, 15	193	+20.0	50	45	−33.0
Igneous rocks					
92R-3, 11	1050	+30.6	25	259	+28.2
104R-1, 118	464	+29.8	50	42	−31.5
110R-2, 68	943	+46.7	35	93	+31.2

Note: Abbreviations are as follows: J(0) = intensity of natural remanent magnetization (NRM); Inc.(0) = inclination of NRM; Optimum AF = optimum field intensity of AF demagnetization; J(AF) = remanence intensity after optimum AF demagnetization; Inc.(AF) = inclination after optimum AF demagnetization. Demagnetization characteristics of these samples are plotted in Figure 44.

crystallizing phase and, hence, that the diabase has a tholeiitic differentiation trend. The absence of plagioclase phenocrysts in glomeroporphyritic clots, despite its presence as phenocrysts in the chilled margin as well as its abundance in the groundmass, is striking and indicates hydrous conditions.

Volcanic Clasts in Units III, V, and VI

One basaltic pebble (Sample 126-793B-3R-1, 92–98 cm) was recovered in the lower to middle Miocene section (lithologic Unit III), which consists of siltstones and claystones (see "Lithostratigraphy and Accumulation Rates" section, this chapter). This basalt displays porphyritic intersertal texture with clinopyroxene and plagioclase phenocrysts often in glomeroporphyritic clots, within a groundmass of trachytic plagioclase laths.

Lithologic Unit V, a 600-m-thick lower to mid-Oligocene section, consists of granule- to fine-pebble conglomerate, vitric and/or pumiceous sandstones, siltstones, and claystones. The volcanic clasts consist of plagioclase-clinopyroxene-orthopyroxene andesite, hornblende-clinopyroxene dacite, intersertal basalt, and pumice. Plagioclase-clinopyroxene-orthopyroxene andesite (Sample 126-793B-32R-3, 125–128 cm, and Samples 126-793-56R-3, 75–76 cm, and -56R-3, 85–86 cm) is the most common type. This andesite has a porphyritic and/or fluidal texture with abundant phenocrysts of plagioclase (up to 30%) and fresh clinopyroxene and orthopyroxene. Plagioclase and orthopyroxene are generally replaced by zeolite and smectites. Opaque minerals are included in the pyroxene phenocrysts and thus represent an early crystallization phase. The groundmass is often very altered, but the glass of some clasts (e.g., Sample 126-793B-56R-2, 75–76 cm) is surprisingly fresh. Uncommon hornblende-clinopyroxene-bearing crystal tuff is present in Sample 126-793B-37R-1, 68–69 cm. It contains perfectly fresh, green hornblende, clinopyroxene, and oscillatory-zoned plagioclase. The rare intersertal basalt clasts in Sample 126-793B-56R-2, 85–86 cm, show quenched clinopyroxene and plagioclase microlites in a highly vesicular groundmass.

Unit VI (lower[?] Oligocene) is a poorly sorted volcaniclastic breccia and microbreccia with a sandy matrix. Most clasts are angular. Porphyritic andesite with abundant plagioclase phenocrysts (20%–35%) represents the predominant type of clast (Samples 126-793B-83R-1, 120–121 cm, -84R-2, 39–40 cm, and -85R-2, 39–40 cm; Table 7). Clinopyroxene is always well pre-

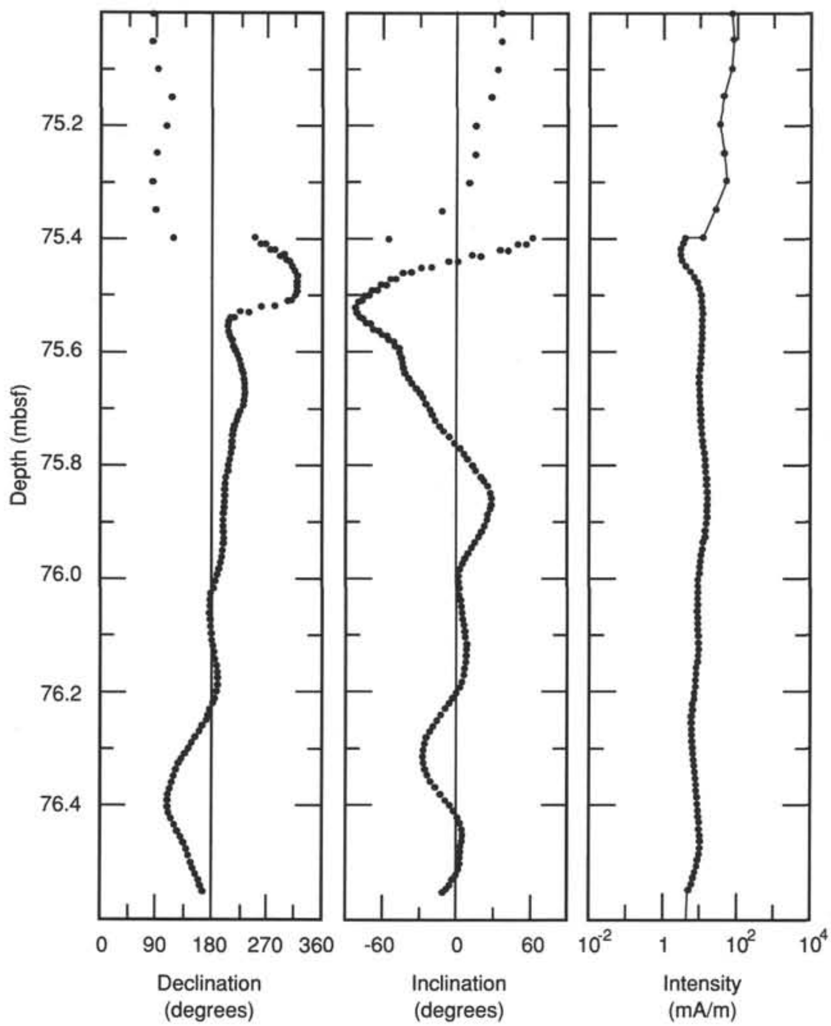

Figure 50. Downhole plot of azimuthally corrected declination, inclination, and intensity of remanent magnetization for the part of Core 126-793A-9H (archive half) that includes the Brunhes-Matuyama polarity transition.

served and forms glomeroporphyritic aggregates with orthopyroxene pseudomorphs. Plagioclase and orthopyroxene may be altered to smectites and zeolites (Sample 126-793B-84R-2, 39–40 cm; Table 7). Opaque minerals are included in these pyroxene phenocrysts, indicating their early crystallization. Sparse rounded quartz microphenocrysts may be present (e.g., Sample 126-793B-84R-2, 39–40 cm). The vesicles are lined by smectites and filled with zeolites. Where the phenocrysts display fluidal texture, the vesicles are flattened and lobate (Samples 126-793B-85R-1, 8–10 cm, and -85R-2, 39–40 cm).

Rare clinopyroxene phyric basic andesite with a few plagioclase phenocrysts (Sample 126-793B-84R-1, 16–18 cm) and intersertal basalt with quenched clinopyroxene and plagioclase microlites (Sample 126-793B-85R-1, 8–10 cm) are the two other types of clasts in this polymictic breccia. The former is similar to clasts in basement breccias.

The most common volcanic clast present in the conglomeratic volcaniclastic beds of Unit V as well as in the breccias of Unit VI is a plagioclase-clinopyroxene-orthopyroxene andesite that displays many similarities to the andesites recovered in the basement of Site 792 (i.e., abundance of plagioclase, presence of orthopyroxene and clinopyroxene that includes opaque minerals, and occasional occurrence of quartz) (see "Igneous Petrology" section, "Site 792" chapter, this volume).

The Basement

At Hole 793B, basement was reached at 1404 mbsf, and a further 278 m of penetration was achieved, reaching a total depth of 1682 mbsf. The rate of recovery for basement rocks was 33%. A lithostratigraphic column for Hole 793B basement is shown in Figure 55. We defined the upper contact of the basement with the overlying breccia (Unit VI, Core 126-793B-85R and above) on the basis of the lithology and diversity of the volcanic clasts, the type of the matrix, and the presence of a sheared zone in Core 126-793B-86R. The most common volcanic clast found in Unit VI is plagioclase-rich andesite with two pyroxenes, an early crystallizing opaque mineral, and minor quartz. In contrast, the andesitic clasts in the uppermost volcanic breccia of the basement (Unit 1, Core 126-793B-86R through Section 126-793E-92R-1) never have >10% plagioclase phenocrysts, and opaque minerals are absent (see the following discussion and Table 7). The Unit VI volcaniclastic breccia contains up to 40% sand-size matrix. In contrast, the matrix of the Unit 1 volcanic breccia is hyaloclastitic with a zeolitic cement.

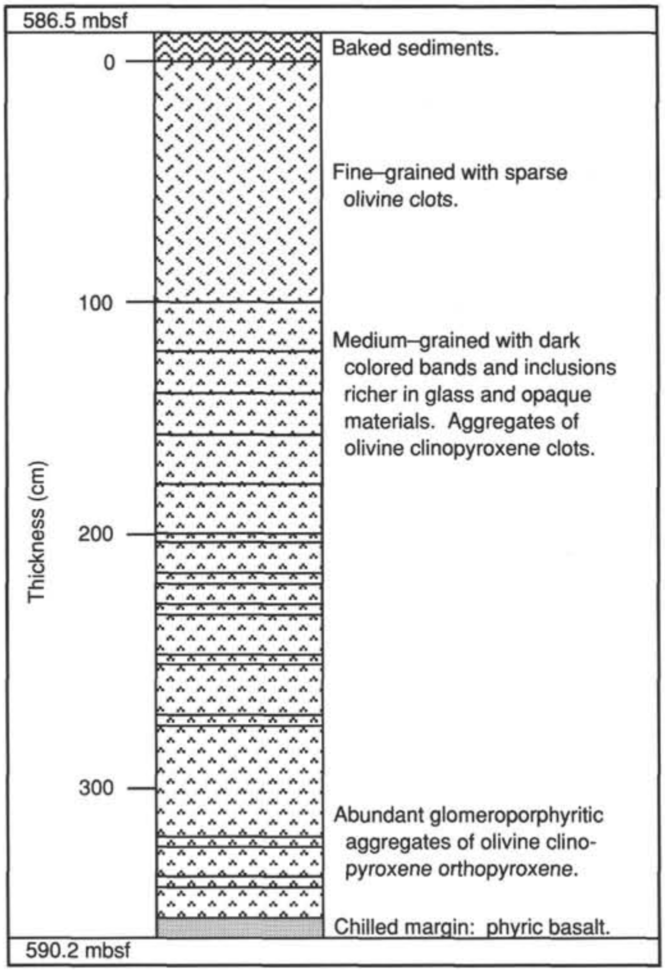

Figure 51. Schematic diagram of the diabase sill showing the textural differences between the upper, middle, and lower sections and the distribution of the dark-colored bands and inclusions.

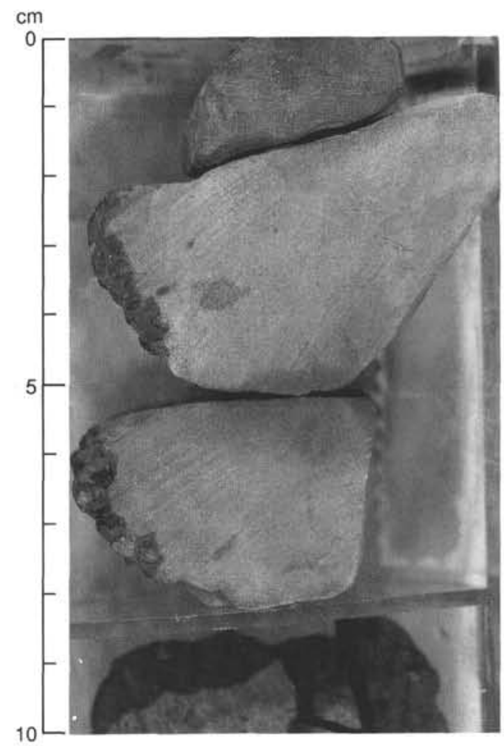

Figure 52. Photograph of the upper contact of the diabase sill with the baked sediments (Interval 126-793B-1R-1, 0–10.0 cm).

The top of the Unit 1 volcanic breccia is sheared, which could suggest a fault contact between the forearc sediments and the basement. Basement-like clasts are reworked in Unit VI breccias, but clasts similar to those of Unit VI are absent from the basement.

Pillowed and massive lava flows in the basement contain one reversal of magnetic polarity (see "Paleomagnetism" section, this chapter). The pillowed lava in Units 2 and 14 (Cores 126-793B-92R and -110R through -112R) are normally magnetized, whereas the massive flow in Unit 10 (Core 126-793B-104R) is reversed. The latter may represent the short reversal at about 31.6 Ma in the middle of Chron C11. Thus, the basement at Site 793 may have formed within as little as 0.1–0.9 m.y.

The basement consists of the following units:

Unit 1

Description: heterolithic andesitic breccia
Interval: 126-793B-86R to -92R-1 at 140 cm
Depth: 1404–1461 mbsf

This breccia is formed of 60% clasts, which range in size from 1 to 10 cm, in a hyaloclastitic matrix. The clasts have chilled margins on some surfaces and some are preshaped. They are interpreted as pillow fragments. They include clinopyroxene-rich porphyritic andesite or plagioclase-rich porphyritic andesite, and sparsely phyric andesite lithologic suites. The porphyritic clinopyroxene-rich andesite (Samples 126-793B-86R-2, 29–30 cm, -87R-4, 21–22 cm, -89R-2, 3–4 cm, and -89R-3, 111–113 cm; Table 7) displays porphyritic texture with an intersertal groundmass and includes large, abundant clinopyroxene and orthopyroxene phenocrysts (15%–23%) and variable amounts of smaller plagioclase crystals (5%–10%). The two pyroxenes are often clustered in glomeroporphyritic aggregates in which the orthopyroxene is frequently mantled by the clinopyroxene.

The porphyritic plagioclase-rich andesite (Sample 126-793B-86R-1, 117–119 cm; Table 7) differs mainly in having fewer pyroxene phenocrysts. The sparsely phyric andesite (Sample 126-793B-88R-1, 69–70 cm; Table 7) has a few (< 10%) plagioclase, orthopyroxene, and clinopyroxene phenocrysts in a trachytic groundmass that includes late-crystallizing opaque minerals. In all clasts, the vesicles (< 5%) are rounded or flattened and filled with smectites and/or zeolites, and the orthopyroxene is partly replaced by smectites. The hyaloclastitic matrix is formed of glass shards and clinopyroxene-orthopyroxene crystals. The cement is a mixture of heulandite-clinoptilolite containing small sheets of native copper.

Unit 2

Description: pyroxene-rich andesite pillow lava and an interlayer of monolithic breccia
Interval: 126-793B-92R-1 at 140 cm, through -93R-1 at 120 cm
Depth: 1461–1471 mbsf

The top of this unit was first regarded as representing the sediment/basement contact because of the occurrence of pillowed lavas. Beneath these, the hyaloclastitic breccia includes 1–6-cm pillow fragments in a matrix rich in glass shards and pyroxene crystals. More pillow lavas are present in Section 126-

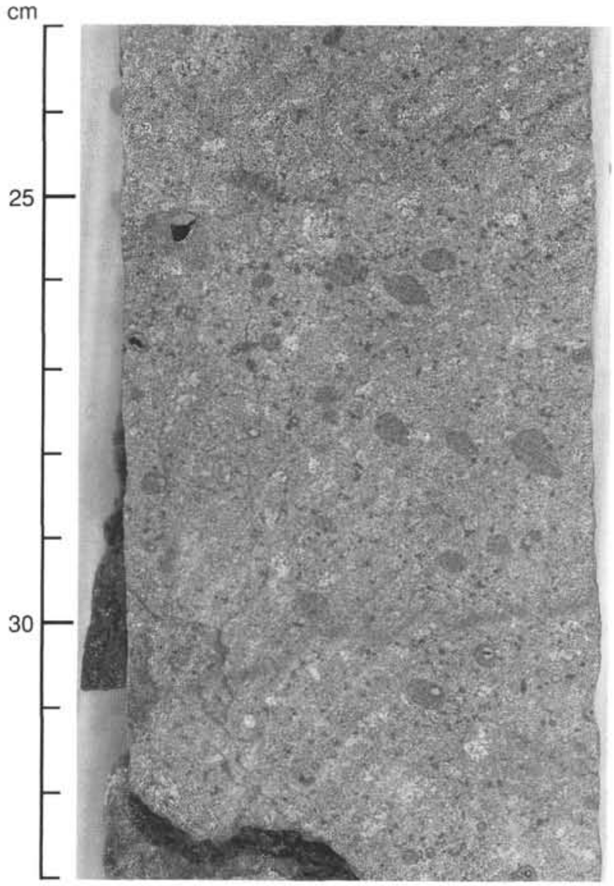

Figure 53. The glassy inclusions in the diabase with their rounded, empty, or smectite-filled vesicles are distinguished from the rest of the diabase sill by their black color and finer grain size. In contrast, the glomeroporphyritic clots are light colored and coarse grained (Interval 126-793B-1R-3, 23-33 cm).

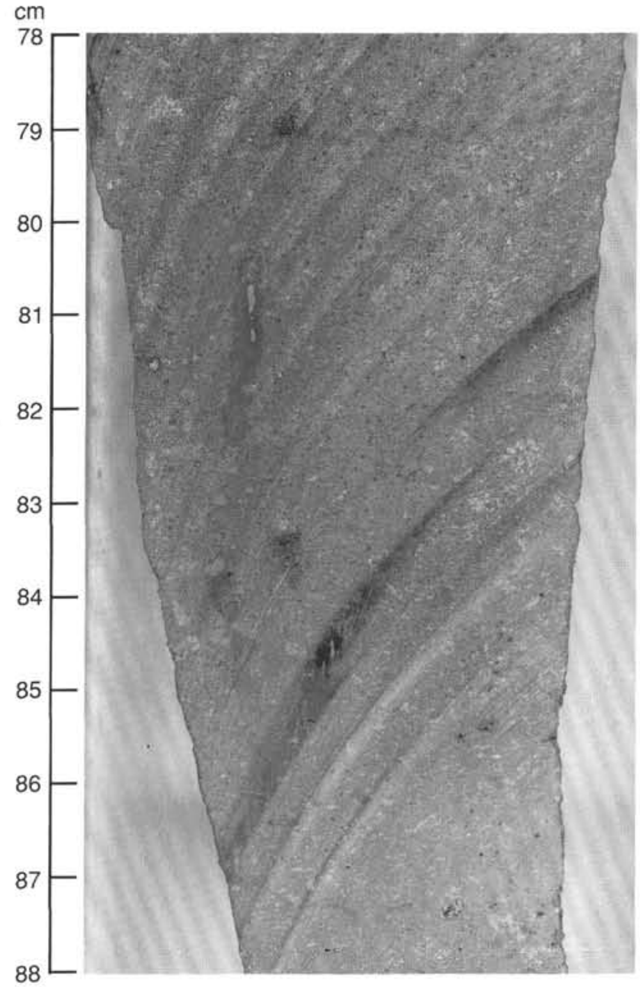

Figure 54. Photograph of the basal chilled margin of the diabase intrusion characterized by its larger and abundant glomeroporphyritic aggregates and its fine-grained groundmass. Just above the chilled margin, inclusions are sometimes tadpole-shaped, tapering downward with vesicles at the top (Interval 126-793B-1R-3, 78-88 cm).

793B-93R-1. The pillows and pillow fragments are formed of highly porphyritic andesite (Sample 126-793B-93R-1, 84-85 cm; Table 7) with orthopyroxene (up to 15%) and clinopyroxene (up to 10%) phenocrysts and rare plagioclase-lath phenocrysts (1%).

Unit 3

Description: monolithic sparsely phyric andesite breccia
Interval: 126-793B-93R-1 at 120 cm, through -96R-1 at 33 cm
Depth: 1471-1499 mbsf

The andesitic pillow fragments (0.5-10 cm) are included in a hyaloclastitic matrix formed of altered glass shards and pyroxene crystals cemented by zeolites and smectites. Sparsely phyric clasts predominate over coarsely porphyritic ones. The sparsely phyric andesite (Sample 126-793B-93R-2, 27-28 cm; Table 7) has an abundant felty groundmass that contains ~2% small, disseminated orthopyroxene and clinopyroxene phenocrysts.

Unit 4

Description: pyroxene-rich andesite pillow lava
Interval: 126-793B-96R-1, 33 cm, to -96R-CC
Depth: 1471-1499 mbsf

This unit is formed of porphyritic pyroxene-rich andesite pillow lava (Sample 126-793B-96R, 81-83 cm; Table 7) similar to the clinopyroxene-rich andesitic clasts present in Unit 1: predominant orthopyroxene phenocrysts (~12%), and clinopyroxene (~5%) approximately equal to plagioclase (~ 3%). The pillows show radial fractures. A thin breccia horizon formed of sparsely phyric and porphyritic andesitic pillow fragments is present between the pillows. The sparsely phyric andesitic fragments are similar to those of Unit 3.

Unit 5

Description: pyroxene-rich andesitic massive lava
Interval: Core 126-793B-97R
Depth: 1508-1518 mbsf

This andesite (Sample 126-793B-97R-1, 123-124 cm; Table 7) displays an intersertal trachytic groundmass with abundant (15%) orthopyroxene and clinopyroxene phenocrysts.

Unit 6

Description: monolithic, sparsely phyric andesite breccia
Interval: 126-793B-98R-1 through -99R-1 at 38 cm
Depth: 1518-1528 mbsf

This breccia is very similar to that of Unit 3 in containing mostly aphyric clasts (0.2-10 cm in diameter) in a hyaloclastitic matrix. The chilled fragments are characterized by elongate open-pipe vesicles that imply degassing processes. Their groundmass is

Table 7. Original percent of phenocrysts in thin sections of the basement at Site 793 as estimated without point counting.

Core, section, interval (cm)	Unit	Plagioclase (%)	Cpx (%)	Opx (%)	Olivine (%)	Opaques (%)	
126-793B-							
1R-1, 2–4	II	41	18	0	3	4	
1R-2, 115–116	II	37	20	1	7	5	
1R-3, 86–89	II	5	15	5	10	0	
3R-1, 95–96	III	5	3	0	0	0	
30R-3, 129–131	V	30	10	1	0	0	
32R-3, 125–128	V	10	2	1	0	0	
56R-2, 75–76	V	5–15	5	0–2	0	0	
82R-7, 80–82	VI	30	10	6	0	1	
83R-1, 120–121	VI	20	10	3	0	1	
84R-1, 76–78	VI	0	7	0	0	1	
84R-2, 39–40	VI	30	10	5	0	1	+ Qtz
85R-1, 8–10	VI	5	5	3	0	0	
85R-2, 39–40	VI	35	10	8	0	1	
86R-1, 117–119	1	10	6	2	0	0	
86R-2, 29–30	1	5	20	3	0	0	
87R-4, 21–22	1	10	20	10	0	0	
88R-1, 69–70	1	6	3	?	0	0	
89R-2, 3–4	1	1	15	5?	0	0	
89R-3, 111–113	1	1	15	10	0	0	
93R-1, 84–85	2	1	10	15	0	0	
93R-2, 27–28	3	2	1	1	0	0	
96R-1, 81–83	4	3	5	15	0	0	
97R-1, 123–124	5	0	7	8	0	0	
99R-1, 54–55	7	<1	5	4	1	0	
100R-1, 28–29	9	0.2	0.5	0.3	0	0	
104R-2, 48–49	10	8	8	1.5	0	0	
105R-1, 126–127	11	10	4	6	0	0	
107R-1, 17–18	12	7	5	1	0	0	
110R-1, 4–5	13	0	9	7	4	<1 Cr-Sp	
112R-1, 63–64	14	0	7	10	0	0	
113R-3, 136–137	16	1	0	0	0	0	

Note: Cpx = clinopyroxene; Opx = orthopyroxene; Qtz = quartz; Cr-Sp = chromium-spinel.

crossed by smectitic veinlets. Open cracks, filled with zeolites, crosscut the fragments and the matrix. Toward the base, in contact with the underlying porphyritic pillows, this breccia includes porphyritic and sparsely phyric andesitic clasts.

Unit 7

Description: boninitic pillow lava
Interval: 126-793B-99R-1, 38–150 cm
Depth: 1528-1529 mbsf

The pillows (Sample 126-793B-99R-1, 54–55 cm; Table 7) have rounded olivine (1%, 1 mm in size), euhedral clinopyroxene, and orthopyroxene phenocrysts. The chromium-spinels are included in the olivine. The groundmass contains up to 50% plagioclase laths and aligned vesicles (5%) partly filled with smectites and zeolites. This flow represents one of the two most mafic units of the basement.

Unit 8

Description: heterolithic andesitic breccia
Interval: 126-793B-99R-2 through -100R-1 at 132 cm
Depth: 1529–1539 mbsf

This breccia differs from the other heterolithic layers because differences are present between the top and base of the unit. The upper portion contains only small (< 3 cm) porphyritic and sparsely aphyric clasts enclosed in a matrix mainly formed of nonvesicular glassy shards and isolated pyroxene crystals. In contrast, the base includes larger clasts (up to 10 cm) and isolated aphyric pillows, and the zeolitic cement is more developed and forms larger crystals. The margins of the isolated pillows are chilled against the surrounding breccia. In thin section (Sample 126-793B-100R-1, 28–29 cm; Table 7), this pillow is characterized by a trachytic groundmass in which small amounts of clinopyroxene, orthopyroxene, and plagioclase euhedral microphenocrysts (0.1–0.3 mm) are present. The cores of the spherical vesicles are filled with smectites, whereas zeolites are in the rims and walls.

Unit 9

Description: monolithic sparsely-phyric andesite breccia
Interval: 126-793B-100R-1 at 132 cm, through -103R-CC
Depth: 1539–1576 mbsf

Compared to the later, sparsely phyric breccias (Units 3 and 4), this horizon differs in having a downward increase in the size and abundance of clasts.

Unit 10

Description: plagioclase-rich andesitic massive lava
Interval: Core 126-793B-104R
Depth: 1576–1586 mbsf

The top and base of the flow are clearly chilled against the overlying and underlying breccias. This andesite (Sample 126-793B-104R-2, 48–49 cm, through -104R-CC, 0–30 cm) differs from those above in that it contains equal proportions of plagioclase and clinopyroxene phenocrysts (~8%) and little orthopyroxene (<1.5%).

Unit 11

Description: monolithic plagioclase-rich andesitic breccia
Interval: 126-793B-105R-1 through -107R-1 at 53 cm
Depth: 1586–1615 mbsf

These porphyritic andesitic pillows (Sample 126-793B-105R-1, 126–127 cm; Table 7) and pillow fragments are very similar to the plagioclase-rich andesite of Unit 10. At the base of the unit, the chilled pillow rims in contact with the hyaloclastitic breccia are marked by abundant (30%) flattened vesicles filled with zeolites and smectites, and by the presence of vertical and radial fractures filled with vesicles.

Unit 12

Description: monolithic plagioclase-rich andesitic breccia in a tuffaceous matrix
Interval: 126-793B-107R-1 at 53 cm, through -109R-3 at 108 cm
Depth: 1615–1628 mbsf

The upper section of this unit is formed of large chilled clasts (~20 cm) similar to those in Unit 11, whereas the middle and lower sections contain smaller clasts (2–0.5 cm), decreasing in size downward. The tuffaceous matrix is a crystal tuff with entire or broken plagioclase and clinopyroxene crystals, and altered glass shards in a smectitic cement. The chilled andesitic fragments (Sample 126-793B-107R-1, 17–18 cm; Table 7) are very similar to the andesitic massive flow of Unit 11 in that phenocrysts of plagioclase outnumber those of clinopyroxene, in an intersertal to microphyric groundmass that includes late-crystallizing opaque minerals.

Unit 13

Description: boninitic massive lava, "orange spot lava"
Interval: 126-793B-110R-1 through -110R-5 at 74 cm
Depth: 1628–1650 mbsf

This flow (Sample 126-793B-110R-1, 4–5 cm; Table 7) best displays boninitic features, such as lack of plagioclase phenocrysts, presence of rounded olivine pseudomorphs, Cr-spinels in the olivine pseudomorphs and groundmass, and orthopyroxene rimmed by clinopyroxene. Moreover, there is an equal abundance of clinopyroxene and orthopyroxene phenocrysts. The groundmass includes abundant subhedral plagioclase laths and quenched clinopyroxene and orthopyroxene microphenocrysts (~0.02 mm). The interstitial glass is probably replaced by zeolites. The orange spots represent cumulate glomeroporphyritic aggregates of aligned, rounded, euhedral pseudomorphs after olivine, mantled by the two pyroxenes and associated with Cr-spinels and native copper. Olivine is replaced by calcite and

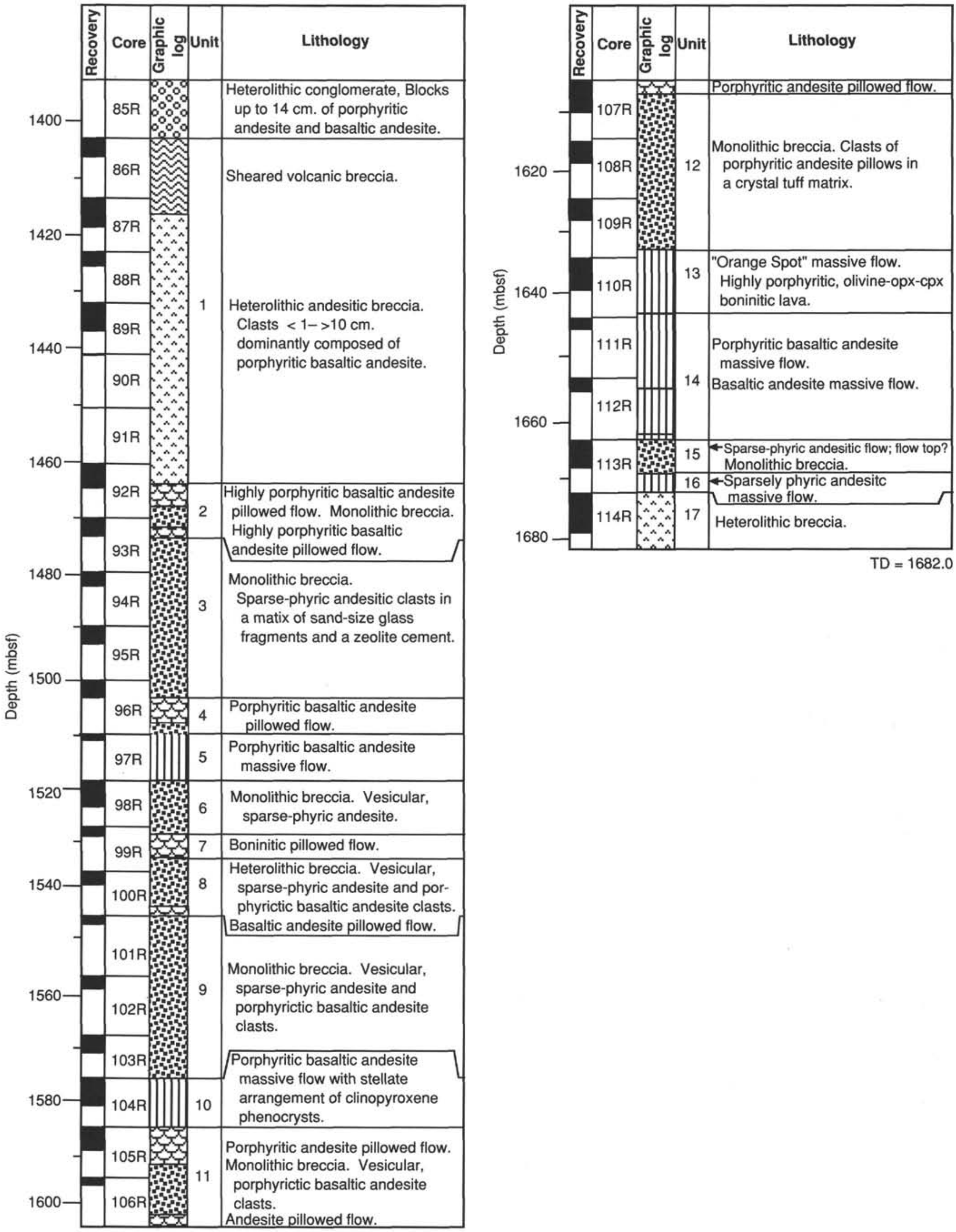

Figure 55. Lithostratigraphic column of the basement at Site 793.

smectites. Smectites are also present along fractures in orthopyroxenes.

Unit 14

Description: pyroxene-rich andesite massive lava
Interval: 126-793B-110R-5, 74 cm, through -112R-2 at 150 cm
Depth: 1650–1656 mbsf

The porphyritic andesite (Sample 126-793B-112R-1, 63–64 cm; Table 7) is characterized by clinopyroxene and orthopyroxene phenocrysts in an intersertal trachytic groundmass. Smectites replace glass and fill fractures. The vesicles are filled by zeolites and smectites.

Unit 15

Description: monolithic pyroxene-rich andesitic breccia
Interval: 126-793B-113R-1 through -113R-3 at 118 cm
Depth: 1656–1660 mbsf

The chilled andesitic clasts (1–10 cm) are set in a hyaloclastitic matrix formed of 1–10-mm glass shards and pyroxene crystals in a smectitic cement. The porphyritic andesite is similar to that of Unit 1.

Unit 16

Description: high-silica, sparsely phyric andesite massive lava
Interval: 126-793B-113R-3 at 118 cm, through -113R-4 at 35 cm
Depth: 1660–1661 mbsf

This aphyric andesite (Sample 126-793B-113R-3, 136–137 cm; Table 7) is characterized by uncommon clinopyroxene microphenocrysts, an abundant trachytic intersertal groundmass, and late-crystallizing magnetite.

Unit 17

Description: heterolithic plagioclase-rich andesitic breccia
Interval: Core 126-793B-114R
Depth: 1661–1682 mbsf

Most clasts in this heterolithic breccia are 1–10 cm in size, but we also recovered some 40-cm-diameter isolated pillows. The clasts contain less plagioclase than pyroxene, but clasts in the bottom of this unit are more typical of Units 10, 11, and 15 (i.e., with plagioclase < orthopyroxene < clinopyroxene).

Conclusions

The basement of Hole 793B is predominantly formed of andesitic massive or pillowed lavas, interbedded with monolithic and/or heterolithic hyaloclastitic breccias. Four main lithologic types can be distinguished using the following criteria: (1) porphyritic or aphyric, (2) olivine and Cr-spinels present, (3) relative abundance of plagioclase vs. pyroxenes, and (4) relative proportions of the two pyroxenes.

The first type consists of olivine and Cr-spinel-bearing basaltic andesite and is located in Units 7 and 13 (Samples 126-793B-99R-1, 54–55 cm and -110R-1, 4–5 cm). It is the most mafic lithology in the basement and displays some features in common with boninites. Plagioclase is present only as laths in the groundmass, which also includes two pyroxenes as microphenocrysts. Orthopyroxene phenocrysts are rimmed by clinopyroxene.

The porphyritic clinopyroxene-rich andesite in Units 2, 4, 5, and 14 (Samples 126-793B-86R-2, 29–30 cm; -89R-2, 3–4 cm; -89R-3, 111–112 cm; -93R-1, 81–85 cm; -96R-1, 81–83 cm; -97R-1, 123–124 cm; and -112R-1, 63–64 cm) is apparently the most common rock type in the basement and is present in breccias and as lavas. It contains a large amount of clinopyroxene and orthopyroxene phenocrysts (up to 30%). Clinopyroxene predominates over orthopyroxene, and plagioclase phenocrysts are very few (0%–3%).

The porphyritic plagioclase-rich andesite in Units 10 and 12 (Samples 126-793B-93R-2, 28–28 cm; -104R-2, 48–49 cm; -105R-1, 126–127 cm; and -105R-1, 17–18 cm) is present as pillow fragments in heterolithic and monolithic breccias, as well as massive and pillowed. It is characterized by an intersertal and felty groundmass and an equal proportion of plagioclase (2%–10%) and pyroxenes (5%–10%).

The last type is aphyric to sparsely phyric andesite and is present in Units 6, 9, and 16 (Samples 126-793B-100R-1, 28–29 cm and -113R-1, 136–137 cm; Table 7). It is present as pillow fragments and as massive flows. It is characterized by an intersertal trachytic groundmass (40% plagioclase laths), a few plagioclase, orthopyroxene, and clinopyroxene microphenocrysts (< 0.3 mm), and a late-crystallizing opaque mineral (magnetite?). It represents the most-differentiated rock type of the andesitic suite in the Hole 793B basement.

Overall, the basement of Hole 793B consists of an andesitic suite that ranges from olivine-Cr-spinel basaltic andesite (Mg rich) to more evolved siliceous andesite (Mg poor). All rock types have <2% vesicles, which are present in lavas and in hyaloclastitic breccia clasts. In all of the rock types, the plagioclase and pyroxene phenocrysts are euhedral and largely unzoned. The orthopyroxenes are nonpleochroic and are the most highly altered (to smectite) mineral. The cements vary in smectite/zeolite ratio, and native copper is prominent in Units 1 and 10–13.

IGNEOUS GEOCHEMISTRY

This section deals with the geochemistry of the three main occurrences of igneous rocks in Hole 793B: (1) an olivine diabase that intrudes middle Miocene sedimentary rocks, (2) volcanic clasts throughout the sedimentary sequence, and (3) the basement lava flows and breccias.

Olivine Diabase Intrusion

Hole 793B encountered an *in-situ* igneous unit at 586.5 mbsf. This unit appears to be a single diabase intrusion, 4.5 m thick (90% recovery), which is bound above and below by sediments. The age of the underlying sediments is late early to early middle Miocene (~14–17 Ma; see "Biostratigraphy" section, this chapter). The mineralogy of the diabase consists of olivine phenocrysts in a groundmass dominated by plagioclase, clinopyroxene, and opaque minerals. In the lowermost parts of the unit, including the chilled margin, clinopyroxene and orthopyroxene phenocrysts occur (see "Igneous Petrology" section, this chapter).

Three samples were analyzed by wavelength spectrometer X-ray fluorescence (XRF) for major and trace element abundances (Table 8). The samples come from the upper, middle, and lower sections of the intrusion.

The main geochemical features of this olivine diabase are its high concentrations of SiO_2 (~53.2%) and MgO (~9%; Table 8) and its low concentrations of Al_2O_3 (~15%), Na_2O (<1.7%), and K_2O (<0.28%). The high SiO_2 levels explain the presence of orthopyroxene phenocrysts. With a Mg number ranging between 64.8 and 67.9, this diabase intrusion is more mafic than any diabase drilled at Site 791 (see "Igneous Petrology" section, "Sites 790/791" chapter, this volume). The Fe_2O_3 values decrease slightly, whereas Cr and Ni contents, and to a lesser extent MgO, increase from the top to the base of the sill. This indicates a more differentiated upper section and more mafic middle and lower parts (the latter is a result of the presence of olivine-clinopyroxene-orthopyroxene glomeroporphyritic aggregates; see "Igneous Petrology" section, this chapter). This differentiation trend is probably related to the accumulation of the olivine and pyroxenes toward the base of the intrusion. The Fe

Table 8. Shipboard XRF analyses of rocks from Hole 793B.

Hole, core	126-793A-1H	126-793A-1H	126-793A-1H	126-793B-3R	126-793B-83R	126-793B-84R	126-793B-85R	126-793B-86R
Section, interval (cm)	1, 27–32	2, 59–62	3, 60–64	1, 95–98	1, 115–118	2, 35–40	2, 39–54	2, 26–30
Piece number	4A	5A	1D					
Depth (mbsf)	586.5	586.5						1409
Unit	II	II	II	III (sediments)	VI (sediments)	VI (sediments)	VI (sediments)	1 (basement)
Lithology	diabase	diabase	diabase	basalt				
SiO_2	53.25	52.36	52.28	52.81	55.55	51.46	53.2	55
TiO_2	0.59	0.55	0.54	0.66	0.45	0.45	0.47	0.33
Al_2O_3	15.14	14.59	14.33	17.07	17.96	19.52	20.01	15.94
Fe_2O_3	10.2	9.68	9.61	10.42	8.46	8.42	8.23	7.62
MnO	0.14	0.14	0.14	0.16	0.14	0.28	0.12	0.13
MgO	8.55	8.97	9.24	5.27	3.93	4.91	5.76	7.43
CaO	10.83	10.89	10.9	11.7	3.11	7.82	9.78	10.77
Na_2O	1.68	1.67	1.71	1.91	6.11	5.1	2.11	1.52
K_2	0.28	0.28	0.23	0.3	4.05	1.46	0.29	1.14
P_2O_5	0.03	0.03	0.03	0.04	0.09	0.36	0.03	0
LOI	0.96	1.32	1.13	0.33	12.23	6.95	2.5	2.23
Total	100.68	99.14	99	100.36	99.85	99.78	100.02	100.18
Zr	30	29.8	30.2		59.9	50.8	55.8	39.7
Y	16.6	15.6	15.5		33.9	53.7	13.8	9.6
Rb	2	2.6	2.9		31.5	13.8	1	10.1
Sr	115.5	111.2	110.4		89.5	107.9	180.3	124.5
Ba	44.1	23.6	39.9		173.5	246.5	20.7	—
V	295.2	269.6	285.7		223.7	203.7	261.4	201.9
Nb	0.7	0.5	0.9		1.1	1.2	1.1	1.1
Ni	88.9	104	109		31	29.8	29.7	50.4
Cr	266	344.1			87.2	40.1	51	377.9
Zn	91.1	92.4	85.2		104.7	107.4	103.2	87.2
Cu	73.6	97.7	75.2		33.5	53.7	119	16.8
Ce	7.4	2.3	0		12	5.1	—	—
Ti/Zr	118	110.7	107.2		45.07	53.14	50.53	52.89
Zr/Y	1.8	1.91	1.94		1.07	0.94	4.04	4.13
Ti/V	11.99	12.24	11.34		12.06	13.25	10.78	10.41

Note: Major elements are measured in wt% oxide, and trace elements are measured in parts per million (ppm); LOI = loss on ignition.

Table 8 (Continued).

Hole, core	126-793B-87R	126-793B-88R	126-793B-89R	126-793B-92R	126-793B-93R	126-793B-93R	126-793B-96R	126-793B-97R
Section, interval (cm)	4, 22–25	1, 65–68	2, 0–4	3, 25–28	1, 85–87	2, 27–29	1, 81–83	1, 124–127
Piece number								
Depth (mbsf)	1419.6	1424.4	1432.4	1468.7	1471.2	1475.4	1507.1	1516
Unit	1 (basement)	1 (basement)	1 (basement)	2 (basement)	2 (basement)	3 (basement)	4 (basement)	5 (basement)
Lithology								
SiO_2	54.89	54.73	55.65	54.58	52.89	53.71	53.48	53.28
TiO_2	0.32	0.35	0.26	0.28	0.28	0.37	0.29	0.28
Al_2O_3	15.14	18.85	13.74	13.97	13.08	17.9	14.46	13.78
Fe_2O_3	7.66	8	9.24	8.63	9.27	8.7	8.98	9.1
MnO	0.14	0.11	0.13	0.13	0.16	0.14	0.16	0.18
MgO	8.25	4.8	8.73	8.46	12.51	6.34	10.37	11.93
CaO	10.68	10.47	9.39	10.48	10.35	10.53	10.57	10.02
Na_2O	1.48	1.88	1.36	1.92	1.24	1.72	1.9	1.56
K_2	0.65	0.92	1.08	0.89	0.24	0.47	0.36	0.19
P_2O_5	0.01	0.03	0	0.32	0	0	0.01	0
LOI	2.42	2.66	2.19	1.4	1.56	1.84	1.68	2.14
Total	99.22	100.17	99.54	99.6	100.06	99.89	100.57	100.32
Zr	38.9	40.7	25.3	27.3	25.9	34.6	27.2	26
Y	8.9	15.5	18.5	19.6	8.8	9.8	10	7.8
Rb	3.7	13.5	18.5	15.9	3.2	3.9	6.4	1.4
Sr	123.1	154.7	145.1	161.7	141.5	184	149.3	141.3
Ba	—	12.4	—	18.2	15.1	13.1	21.6	8.6
V	204.8	204.5	193.6	224.2	225.5	260.3	235.8	196.6
Nb	0.6	0.6	0	0.6	0.5	0.5	0.6	0.3
Ni	56	38.4	102	110	172.5	55.2	140.2	124.7
Cr	335.5	133.4	627.9	437.3	589.6	144.1	599.9	513.1
Zn	86.8	95.3	87.3	79.3	83	88.4	100.7	82.2
Cu	65.7	26	16.4	16.1	18.2	75.5	19.4	24
Ce	3.3	—	3.2	—	—	—	—	—
Ti/Zr	53.98	57.49	68.77	65.93	71.8	65.02	66.17	69.23
Zr/Y	4.37	2.62	1.36	1.39	2.94	3.53	2.72	3.3
Ti/V	10.25	11.44	8.98	8.02	8.24	8.64	7.93	9.15

Table 8 (Continued).

Hole, core	126-793B-99R	126-793B-100R	126-793B-104R	126-793B-105R	126-793B-107R	126-793B-110R	126-793B-112R	126-793B-113R
Section, interval (cm)	1, 54–55	1, 28–30	2, 49–54	1, 127–131	1, 17–20	1, 1–3	1, 59–63	3, 137–141
Piece number								
Depth (mbsf)	1527.6	1537.58						
Unit	7 (basement)	9 (basement)	10 (basement)	11 (basement)	12 (basement)	13 (basement)	14 (basement)	16 (basement)
Lithology								
SiO_2	53.04	53.42	53.54	57	53.93	54.11	55.45	59.75
TiO_2	0.28	0.34	0.31	0.28	0.32	0.26	0.29	0.31
Al_2O_3	13.86	18.05	14.56	13.07	16.58	12.7	14.75	16.36
Fe_2O_3	9.75	9.13	9.37	9.26	9.43	9.06	8.11	7.58
MnO	0.14	0.11	0.15	0.15	0.12	0.13	0.11	0.07
MgO	9.33	5.68	7.91	8.53	7.08	10.14	7.04	3.76
CaO	11.07	10.28	11.93	10.43	10.38	9.9	9.44	8.26
Na_2O	1.64	2.11	2.09	1.82	2.24	2.23	2.7	2.74
K_2	0.78	0.7	0.53	0.44	0.48	0.66	1.16	1.66
P_2O_5	0.02	0	0.05	0.01	0	0.02	0.6	0.05
LOI	2	1.61	1.06	2.57	6.14	1.17	2.03	1.17
Total	99.9	99.84	100.45	100.99	100.05	99.2	99.64	100.51
Zr	23.3	32.4	31.6	28.8	34.2	24	29.5	33.5
Y	8.9	9.8	15.2	9.6	8.5	12.4	18.3	20.3
Rb	18.2	10.9	8.4	3.8	8.7	11.1	25.4	32.9
Sr	134.6	191	174.5	127	180.1	143.3	182.5	189.1
Ba	13.1	15.5	19.7	17.3	17.3	21.6	32.9	19.2
V	243.4	246	251.2	251.5	242.2	214.9	209.8	227
Nb	0.4	0.8	0.7	0.4	0.5	0.7	0.9	1
Ni	120.5	45.7	47.45	36.6	34.7	126.4	81.9	23.2
Cr	700	88.5	294.6	249.2	174.1	706.2	249.6	24.6
Zn	93.9	107.8	97.6	82.7	107.9	81.3	78.4	64.9
Cu	15.3	19.4	17.8	72	168.7	102.4	19.2	37.8
Ce	—	—	—	—	—	—	—	8.4
Ti/Zr	72.1	64.81	66.45	66.6	61.4	67.5	63.05	59.1
Zr/Y	2.61	3.3	2.07	3	4.02	1.93	1.61	1.65
Ti/V	6.9	8.5	8.35	7.63	8.67	6.69	8.86	8.72

enrichment in the upper part may be a result of the extraction of clinopyroxene and orthopyroxene, whereas Fe in the base may have been diluted by pyroxene. Thus, the analysis of the upper part of the sill is more representative of the diabase magma, whereas the analysis of the middle and lower parts shows the increasing effects of crystal accumulation. The low values of aluminum and total alkalis indicate that this diabase displays tholeiitic affinities, using the criteria of Kuno (1960).

The trace element geochemistry of the olivine diabase is characterized by the depletion in high-field-strength elements (e.g., TiO_2, P, Zr, Y, and Nb) relative to N-MORB (Table 8), which appears to be a constant feature of this arc-forearc system. Indeed, the basaltic andesites and andesites that form the basement in Hole 792E (see "Igneous Petrology" section, Site 792 chapter, this volume), as well as the Tori Shima basalts (Zhang et al., in press), display a depletion in high-field-strength elements similar to that in the diabase. However, the diabase also has low concentrations of Rb (2–3 ppm), Ba (~ 36 ppm), and Sr (~ 110 ppm) compared with most island-arc suites, including the Marianas (Stern and Ito, 1983).

Volcanic Pebbles in Unit VI

Unit VI is a poorly sorted volcaniclastic breccia with a sandy matrix. Porphyritic andesite with abundant plagioclase phenocrysts is the most common clast type. We analyzed three samples by XRF for major and trace elements to compare their geochemistry with the basement rocks of Sites 793 and 792. The high K_2O (4.50 wt%) and loss on ignition (or LOI, 12.23%; Table 8) contents of one of the analyzed samples show the high degree of alteration of some of these andesitic clasts. Nevertheless, the clasts display many similarities with the basement calc-alkaline andesites at Site 792 (i.e., they are Fe-poor and Ti-rich, their Al_2O_3 contents are high, and they are depleted in high-field-strength elements).

The Basement

The 278 m of basement in Hole 793B revealed a sequence of andesitic pillowed and massive lavas intercalated with monolithic and heterolithic breccias with hyaloclastitic and tuffaceous matrices. The lavas and clasts belong to both the high-Mg and low-Mg series (Fig. 56). Four main lithologic types were recognized, and are listed from the more mafic to the more acidic (see "Igneous Petrology" section, this chapter):

1. olivine and Cr-spinel-bearing basalt andesite, which displays some features in common with boninites;
2. clinopyroxene-rich andesite, which contains a fairly large amount of clinopyroxene and orthopyroxene phenocrysts;
3. plagioclase-rich andesite, which is characterized by a more equal proportion of plagioclase and pyroxenes; and
4. aphyric to sparsely phyric andesite, which differs from the other types by the lack of large phenocrysts, an abundant intersertal trachytic groundmass, and late-crystallizing opaque minerals.

To examine the magmatic affinities of the basement andesites, their fractionation history, and their geochemical analogies, 17 samples were analyzed by XRF for major and trace elements (see "Explanatory Notes" chapter, this volume).

Within the 17 basement samples, the SiO_2 content ranged from 53 to 60 wt%, corresponding to a range from basaltic to acidic andesites (Table 8). The K_2O contents are generally low, mostly 0.4–1.2 wt%, indicating unaltered compositions. The TiO_2 contents range from 0.26 to 0.37 wt% and are lower than in the andesites of the basement rocks at Site 792 and of most island arcs. In contrast, Fe_2O_3 contents are similar in all andesite types at Site 793 (7.56–9.75 wt%), but are higher than in the andesitic basement of Site 792 (Table 8). The difference between

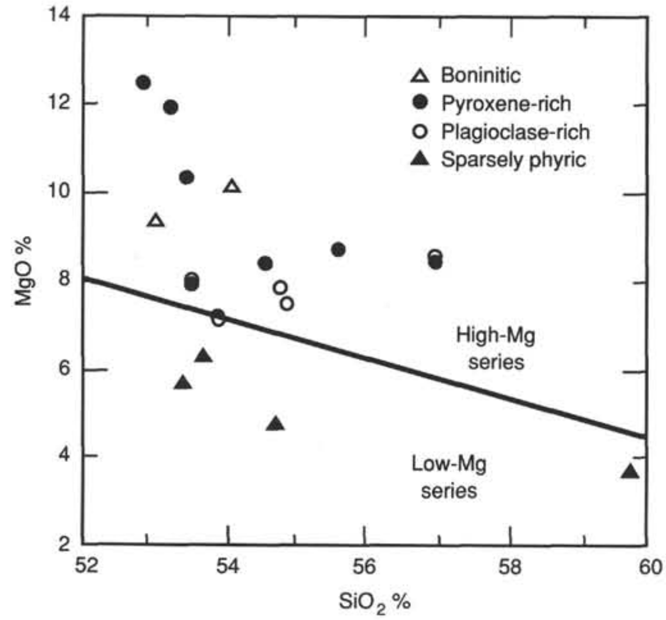

Figure 56. MgO wt% vs. SiO_2 wt% diagram. The boundary between the high-Mg and low-Mg series is discussed in the "Explanatory Notes" chapter (this volume) and is the same as for Leg 125.

the Fe-rich but Ti-poor andesites in the Site 793 basement rocks, and the Fe-poor but Ti-rich andesites in the Site 792 basement rocks, illustrates the tholeiitic affinity of the Site 793 andesitic suite vs. the calc-alkaline affinity of the Site 792 andesites. This contrast is also shown in the occurrence of opaque minerals, which are only present in the groundmass of the more differentiated andesites at Site 793, but which are included in the plagioclase and pyroxene phenocrysts of Site 792 basement andesites (see "Igneous Petrology" section, this chapter).

Another striking feature of the Site 793 basement suite is the relationship between MgO, Cr, and Ni contents. Chrome and nickel (and to a lesser extent, MgO) concentrations differ between the main petrographic types of andesite. The olivine-Cr-spinel-bearing basaltic andesites have the highest Cr (~700 ppm) and Ni (172.5–126.4 ppm) contents, whereas MgO contents are in the range of the clinopyroxene-rich andesite (9.33–10.14 wt%). The clinopyroxene-rich andesite shows a wider range of Cr (~249–628 ppm) and Ni (~50–140 ppm) contents, and the MgO contents of some samples (12.51%) are even higher than those of the olivine-Cr-spinel basaltic andesites. Even the plagioclase-rich andesites have rather high Cr (130–144 ppm), Ni (~38–55 ppm), and MgO (~8 wt%) contents compared with island-arc tholeiites. Only the sparsely to aphyric andesites display low Cr (<100 ppm), Ni (<50 ppm), and MgO (~3.78–5.68 wt%) contents. Thus, the first three types belong to a high-Mg series whereas the last type belongs to the more conventional low-Mg series (Fig. 56).

The Hole 793B andesites show the customary negative correlation between Al_2O_3 and MgO and can be subdivided into two groups on the basis of their Al_2O_3 contents. The olivine-Cr-spinel basaltic andesites and the clinopyroxene-rich andesites with MgO contents >7 wt% are Al_2O_3-poor (13–16 wt%). In contrast, the plagioclase-rich andesites and the sparsely phyric to aphyric andesites, with MgO ranging between 8 and 4 wt%, are Al_2O_3 rich (16–18 wt%).

In the MgO wt% vs. SiO_2 wt% diagram (Fig. 56), the Hole 793B andesitic suite fails to show a good negative correlation, implying that none of these rocks are linked by closed-system differentiation. In contrast, there is a very good positive correlation between TiO_2 and Al_2O_3 (Fig. 57), which indicates that these andesites are derived either from a similar mantle source through differing degrees of partial melting or from variably depleted sources.

Of the 17 trace elements analyzed, only Ce and (in some cases) Ba are considered unreliable, because their concentrations were close to the detection limits of the shipboard XRF.

The Site 793 andesites, compared with N-MORB, are enriched in the low-field-strength elements such as Rb, Sr, and Ba, features that are common to island-arc volcanic rocks. However, compared with many island-arc suites, including the Marianas, the Hole 793B basement andesites are depleted in Ba and Sr.

The Site 793 basement andesites also show rather low contents of high-field-strength elements (Fig. 58), especially Nb, which is always <1 ppm. However, they differ by a factor of 2 in Y contents in all four types of andesite; Y contents are either 8–10 ppm or 14–20 ppm (Table 8). Most Site 793 andesites have a Zr/Y ratio ranging between 1 and 5 (see Fig. 59), with the exception of some clinopyroxene-rich porphyritic andesites and the aphyric siliceous andesites that have Zr/Y ratios <1. The differences in the Y contents, like those in the Ti and Al contents of the Site 793 andesites, imply either variations in the degree of partial melting or differences in source compositions. The Cr vs. Y diagram (Fig. 60) shows that the andesites form three different groups on the basis of their Y contents. Within each group, the trend displayed by the andesites is consistent with crystal fractionation. Multiple lithologic suites constitute each group, with the most mafic members being boninitic, and the most differentiated being sparsely phyric.

Compared with the basement andesites of Site 792 that have the same ranges of SiO_2 and MgO values, those at Site 793 have lower Ti, P, and Zr contents. Andesites at both sites show twofold ranges in Y contents in otherwise similar rock types.

Finally, the basement volcanic rocks at Site 793 are exclusively andesitic, whereas the Eocene basement rocks of the outer-arc high at Site 786 are more diversified, being made up of basalts, dacites, and rhyolites, as well as andesites. The andesites of Site 793 are mostly high-Mg andesites, whereas the

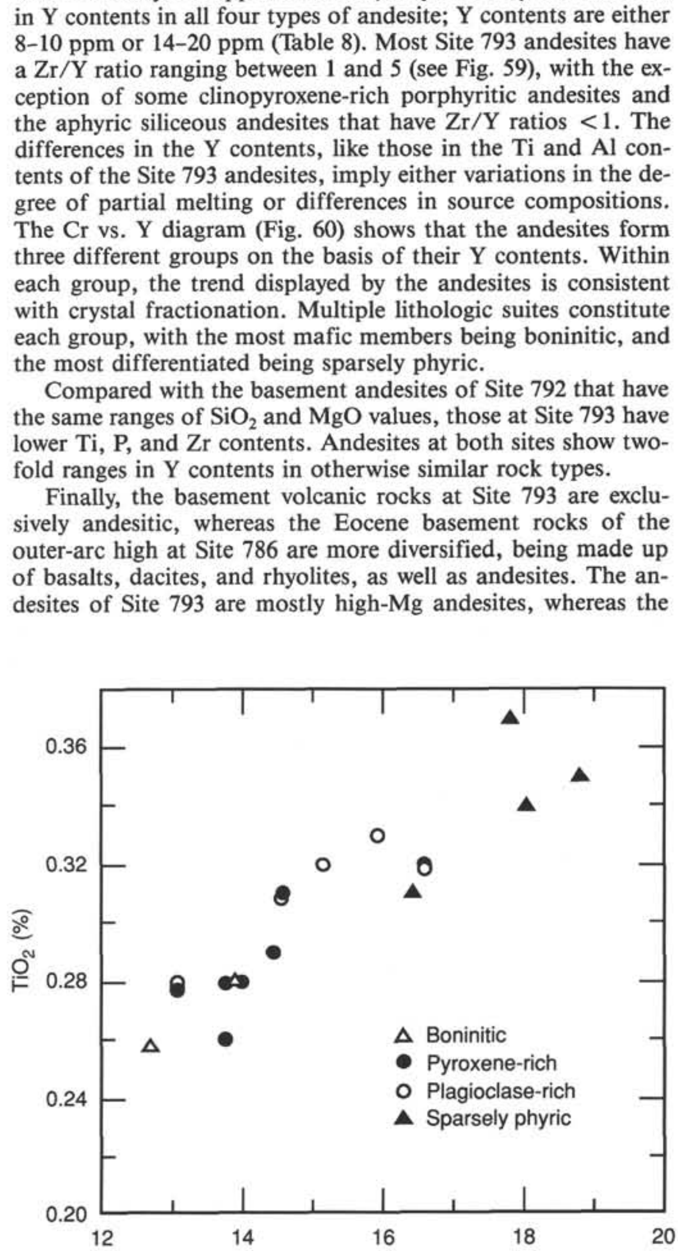

Figure 57. TiO_2 wt% vs. Al_2O_3 wt% diagram. There is a very good correlation between TiO_2 and Al_2O_3 in the basement andesites in Hole 793B.

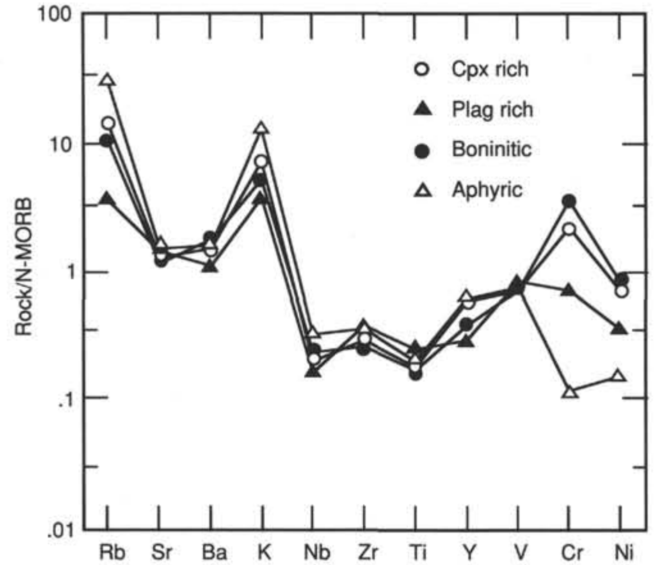

Figure 58. The four andesitic types are shown normalized to N-MORB. These patterns show a relative enrichment in the large-ion lithophile elements and depletion in the high-field-strength elements.

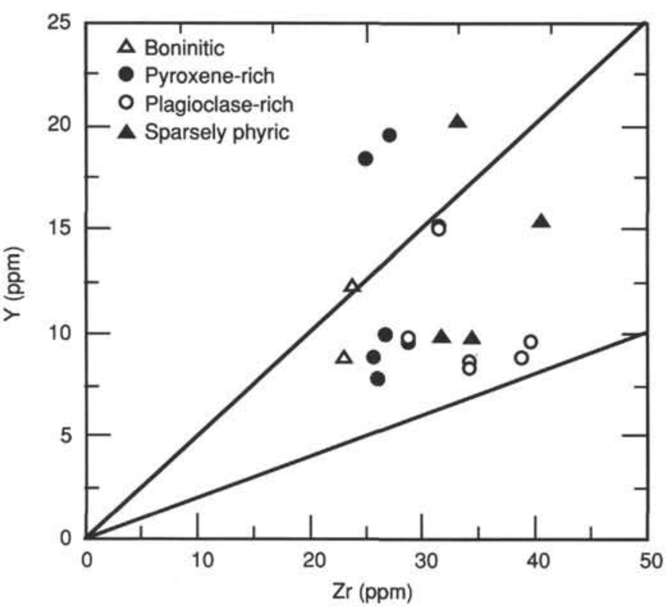

Figure 59. Y (ppm) vs. Zr (ppm) diagram showing the two-fold ranges in Y contents in the basement andesites in Hole 793B.

volcanic rocks of Site 786 are predominantly members of the low-Mg series. Finally, for the same range of SiO_2 contents, the basement volcanic rocks at Site 786 have lower TiO_2 contents and are more depleted in all the high-field-strength elements and Y. Thus, the temporal evolution noted above applies to the entire Cenozoic history of the Izu-Bonin Arc.

SEDIMENT/FLUID GEOCHEMISTRY

We obtained twelve 10-cm, six 25-cm, and thirteen 30-cm-long, whole-round samples from Holes 793A and 793B for electrical resistivity measurements, squeezing of pore water, and fluid and sediment analyses. Seven of the whole rounds did not yield any water.

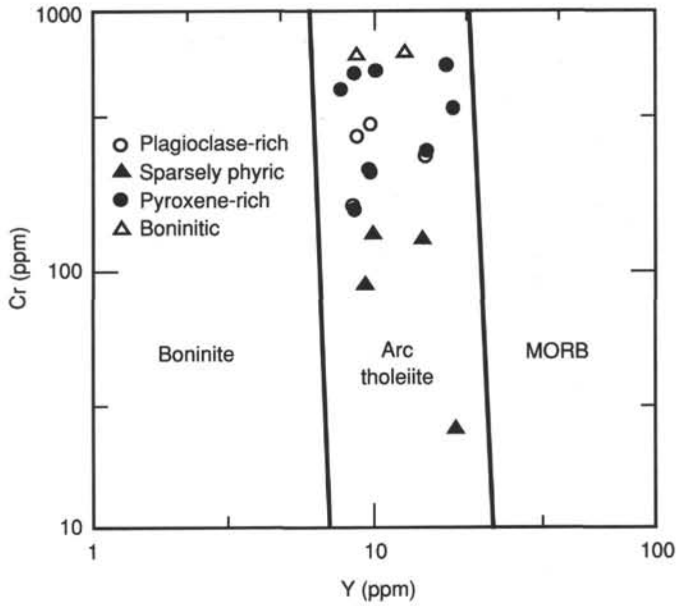

Figure 60. Y (ppm) vs. Cr (ppm). The boundaries between boninite, arc tholeiite, and MORB are those used during Leg 125 (J. Pearce, pers. comm.; see "Igneous Geochemistry" section, "Site 781" chapter [Fryer, Pearce, et al., 1990]) and are arbitrary. The failure to discriminate between the high-Mg and low-Mg series at Site 793 is unimportant, but the slope of the boundaries parallels typical crystal fractionation trends.

The deepest pore-water sample previously recovered by ODP was obtained from 1143.7 mbsf at Site 645. Here, we report data from samples down to 1258.95 mbsf.

Sediment Resistivity

Electric resistivity could only be measured on 20 of the whole rounds because of the geometry of some of the cores. For the samples below 1022 mbsf, resistivity was measured on slices cut from the whole rounds, and the electrode lengths were adjusted for each sample. The slices were cut <10 min after the core arrived on deck, holes for the electrodes were drilled, and the slices were submerged in 35 g/kg NaCl solution for 48 hr prior to measurement. The results are presented in Table 9.

The formation factors calculated from the resistivity measurements are fairly stable, at about 2.5, to a depth of 77 mbsf (Core 126-793A-9H). In Unit III of Hole 793B (Cores 126-793B-2R to -16R), the formation factors scatter about a mean value of 5.7 and then increase abruptly through Unit IV (Cores 126-793B-16R to -19R) to an average level of 22 in Unit V (Cores 126-793B-19R to -82R; Fig. 61). Much of the variation observed in Unit V can be attributed to varying particle size. In Units I and III, the magnitude of the formation factors is the same as determined by other investigators for similar sediments at the same stage of compaction (e.g., Manheim and Waterman, 1974). However, the formation factors measured in Unit V are exceptionally high for the given porosity (see "Physical Properties" section, this chapter).

The measured rock resistivities compare favorably with resistivity measurements performed with other electrode configurations aboard the ship and thus seem to be real and characteristic of vitric sand and siltstones. We are not aware of other published data on the resistivity of similar rock types.

Fluid Geochemistry

The headspace hydrocarbon analyses did not show any gases above background level and thus are not reported.

Table 9. Sediment resistivity (R_s), measurement temperature, pore-water resistivity (R_{pw}) at 25°C and formation factor (F) of sediments from Holes 793A and 793B.

Core, section, interval (cm)	Depth (mbsf)	Cell constant (m)	R_s (ohm-m)	Temp. (°C)	R_{pw} (ohm-m)	F
126-793A-						
3H-3, 140–150	17.95	0.0914	0.649	11.6	0.200	2.4
6H-1, 140–150	43.45	0.1040	0.721	12.7	0.198	2.7
9H-4, 140–150	76.85	0.0997	0.827	12.6	0.198	2.5
126-793B-						
3R-3, 130–140	608.65	0.1037	1.499	16.5	0.198	6.2
6R-3, 0–10	636.35	0.0989	1.133	18.2	0.198	4.8
9R-2, 132–142	664.97	0.0910	1.249	17.3	0.196	5.3
5R-3, 117–127	724.32	0.1018	1.611	15.3	0.197	6.5
8R-3, 115–125	753.00	0.0952	2.296	15.1	0.196	9.3
21R-6, 133–143	786.58	0.0994	2.456	17.4	0.190	10.8
33R-6, 0–25	900.93	0.1001	4.371	17.8	0.167	22.1
36R-3, 113–138	926.56	0.1003	4.593	15.6	0.168	21.9
40R-5, 96–121	968.09	0.0935	3.496	18.4	0.165	18.1
43R-5, 120–150	997.05	0.0991	5.206	16.4	0.162	26.3
46R-3, 116–141	1022.99	0.0937	4.213	22.3	0.159	24.9
58R-4, 76–106	1139.41	0.0540[a]	5.932	24.4	0.195[b]	30.1
61R-3, 56–86	1166.61	0.0505[a]	2.737	23.3	0.195[b]	13.5
64R-6, 117–147	1200.75	0.0921[a]	5.990	16.6	0.195[b]	24.9
70R-7, 0–30	1225.45	0.0565[a]	4.227	23.0	0.195[b]	20.5
73R-4, 120–150	1284.25	0.0565[a]	5.663	23.0	0.195[b]	27.6
80R-5, 0–30	1352.15	0.0587[a]	4.619	24.2	0.195[b]	22.8

[a] Rocks were saturated with 35 g/kg NaCl solution prior to measurements.
[b] Lengths of electrodes were adjusted to fit individual samples.

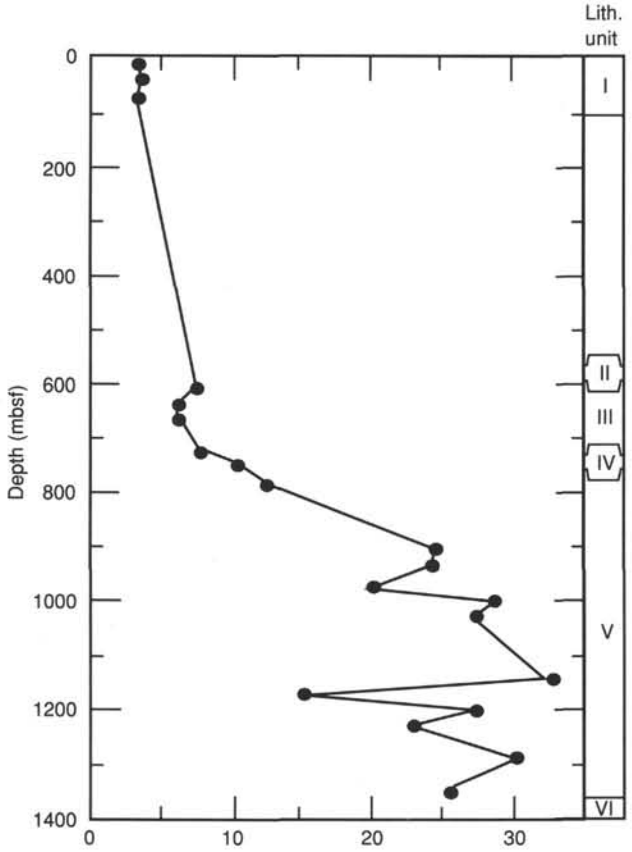

Figure 61. Formation factor, Holes 793A and 793B.

Because of a shortage of acetylene, the only cations that we could analyze were calcium and magnesium. To clean the hole, drilling mud was pumped between every second core. The drilling mud was the same as used at Site 792, and the composition of the drilling-mud filtrate is given in Table 10. There is no indication that any of the samples have been contaminated by drilling-mud filtrate. The distribution of calcium and magnesium (Fig. 62) follows the common evolution for marine sediments of decreasing magnesium and increasing calcium concentrations down to about 725 mbsf (Core 126-793B-15R). However, the continuous increase of calcium further down the hole is very unusual, and the pore waters below 786 mbsf (Core 126-793B-21R) are the most highly altered pore waters of marine origin ever recovered by DSDP/ODP, including the pore waters recovered at Site 792.

At Site 792, the highest calcium concentration was 169 mM at 600 mbsf (Core 126-792E-48R). At Site 793, we reached this level at 786 mbsf (Core 126-793B-21R), below which the calcium concentration continued to increase until it reached a stable level of about 300 mM at a depth of 1139 mbsf (Core 126-793B-58R). The pore waters below 850 mbsf are so highly altered that an isolated sample would have been difficult to recognize as altered seawater. Subsurface waters of similar composition are present in a few deep sedimentary basins and are classified as Ca-Cl-type waters, the origin of which has been disputed. The concentration of magnesium drops to about zero at 786 mbsf (Core 126-793B-21R). The sporadic occurrence of magnesium concentrations greater than the detection limit (about 0.2 mM) below this depth is probably a result of the precision of the methods. However, because of the limited sample volumes, other analyses were given priority above replicate magnesium analyses.

The data presented in Figure 62 show that even the concentration of chloride has been shifted relative to seawater. The concentration of chloride remains near seawater level through Unit III (Section 126-793B-15R-3) and then increases to a stable level of about 715 mM below 1023 mbsf (Core 126-793B-46R). Several processes leading to enhanced chloride concentrations in pore waters have been recognized. These are the dissolution of evaporites, gas hydrate formation, shale membrane filtration, and the uptake of water by authigenic mineral phases. Because of the absence of evaporites and the low concentration of organic carbon (Table 11), the first two of these may be excluded.

It has been observed that when shales become sufficiently compacted they may act as semipermeable membranes, which are more permeable to water than to ions (e.g., Kharaka and Berry, 1973). However, the efficiency of this process is dependent on the state of compaction, and none of the claystones at Site 793 have sufficiently low porosities to act as semipermeable membranes. Furthermore, if the elevated chloride concentrations were caused by shale-membrane filtration, one would expect to observe a corresponding chloride minimum on the low-pressure side (Unit III).

On the basis of this background, we concluded that the high chloride concentrations are caused during the uptake of water by the formation of authigenic mineral phases (smectites, gypsum, and zeolites). To our knowledge, this is the most extensive uptake of water ever reported for deep-sea sediments. This raises the question of the location of the reactions responsible for the dramatic changes in pore-water composition. The composition of pore waters is a dynamic equilibrium determined by the relative rates of reactions and processes (diffusion and advection) that remove or add a given component. At Site 792, the highly altered pore waters were attributed to low-temperature alteration of volcanogenic material. Because of the much higher formation factors at Site 793 (slower diffusion), the even more highly altered pore waters presumably could have been formed by the same reactions as at Site 792. The much slower diffusion

Table 10. Composition of pore water at Site 793.

Core, section,	Depth (mbsf)	pH	Alk (meq/l)	S (g/kg)	Cl^- (mM)	SO_4^{-2} (mM)	Mg^{+2} (mM)	Ca^{+2} (mM)	SiO_2 (μM)	NH_4 (μM)
126-793A-										
1H-2, 140–150	2.95	7.78	2.71	35.5	554	29.5	53.5	10.7	250	LD
3H-3, 140–150	17.95	7.74	2.71	36.0	555	29.5	52.8	10.4	589	11
6H-1, 140–150	43.45	7.77	3.32	36.5	561	28.2	52.8	9.5	623	282
9H-4, 140–150	76.85	7.85	3.36	ND	561	29.1	52.9	9.8	478	378
126-793B-										
3R-3, 130–140	608.65	7.69	2.07	35.0	560	29.1	51.4	19.2	725	LD
6R-3, 0–10	636.35	7.40	1.57	36.0	560	28.0	46.8	24.7	890	106
9R-2, 132–142	664.97	7.52	1.19	37.0	568	29.3	41.6	41.2	764	LD
12R-1, 100–110	692.15	7.65	1.40	37.5	566	29.0	37.4	52.3	905	104
15R-3, 117–127	724.32	7.64	0.88	37.5	569	29.5	25.4	80.2	914	58
18R-3, 115–125	753.00	7.63	0.62	38.5	588	22.5	14.8	108.6	158	33
21R-6, 133–143	786.58	ND	ND	ND	586	17.3	0.2	171.5	226	21
27R-7, 33–58	844.85	8.41	0.66	45.0	643	14.2	LD	213.2	172	LD
30R-4, 110–135	870.13	8.81	0.64	46.5	662	13.8	LD	237.3	143	LD
33R-6, 0–25	900.93	9.01	0.48	47.5	677	13.0	LD	255.2	196	LD
36R-3, 113–138	926.56	ND	ND	ND	671	11.9	LD	265.1	196	LD
40R-5, 96–121	968.09	ND	ND	ND	685	14.8	LD	276.3	196	ND
43R-5, 120–150	997.05	8.83	0.69	50.0	700	16.3	2.7	285.1	216	LD
46R-3, 116–141	1022.99	ND	ND	ND	715	16.6	LD	307.5	298	ND
58R-4, 76–106	1139.41	ND	ND	ND	710	15.7	LD	292.2	167	ND
61R-3, 56–86	1166.61	ND	ND	ND	724	14.4	1.1	298.7	197	LD
67R-4, 0–30	1225.45	ND	ND	ND	717	14.6	LD	293.9	138	ND
70R-7, 0–30	1258.95	ND	ND	ND	722	15.3	0.4	296.8	196	ND
Drilling mud filtrate		9.69	0.80	ND	215	12.0	2.7	7.0	19	58

Note: ND = not determined; LD = less than the detection limit.

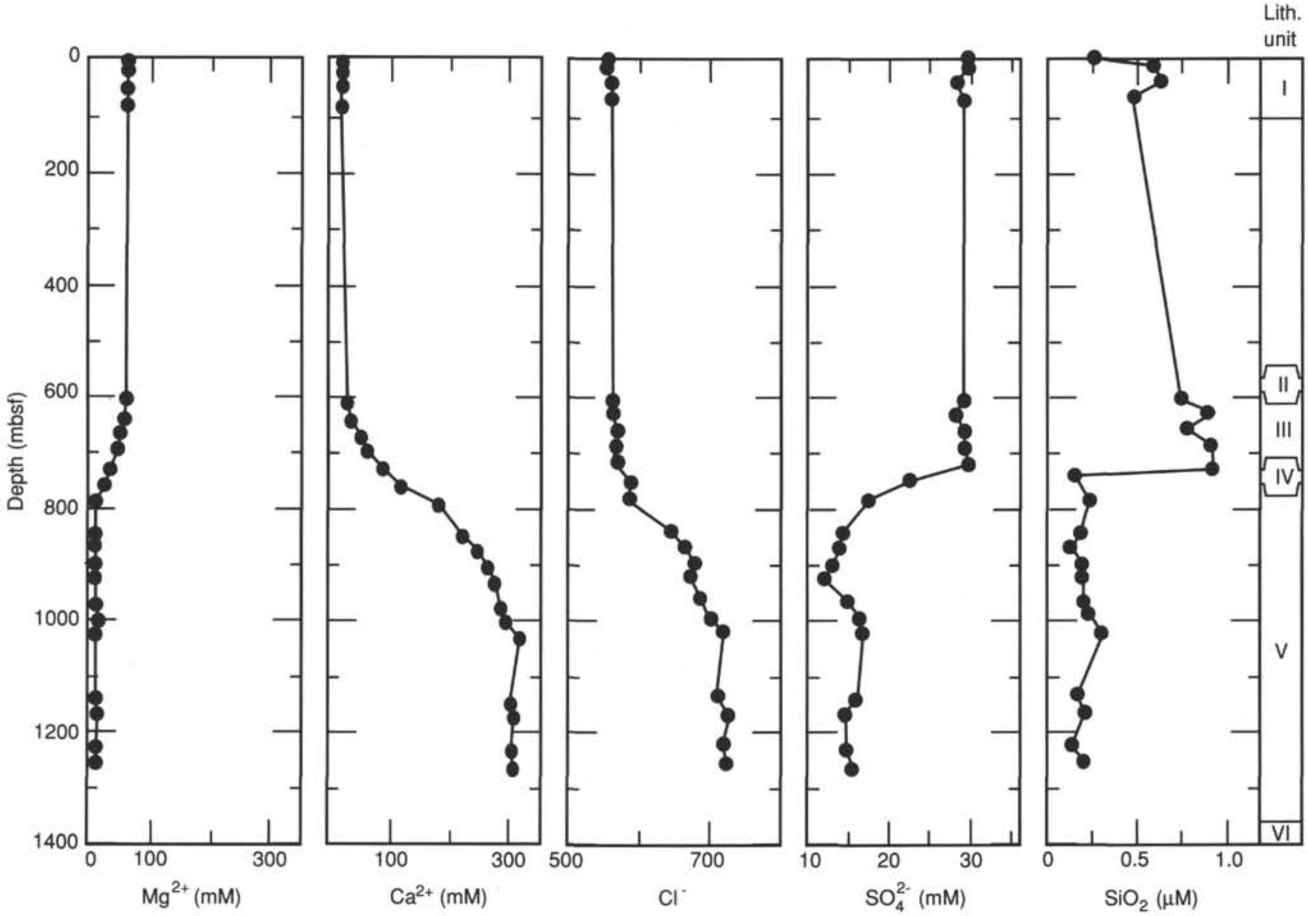

Figure 62. Pore-water characteristics, Holes 793A and 793B. Unit boundaries are shown at far right-hand side.

Table 11. Concentration of inorganic carbon, carbonate, total carbon, organic carbon, total nitrogen, and total sulfur in sediments from Site 793.

Core, section, interval (cm)	Depth (mbsf)	Inorg. C (%)	$CaCO_3$ (%)	Total C (%)	Org. C (%)	Total N (%)	Total S (%)
126-793A-							
1H-1, 68–70	0.68	0.97	8.1				
1H-2, 140–150	2.90	0.08	0.7	0.04	LD	LD	0.03
2H-2, 70–72	6.40	0.12	1				
3H-1, 115–118	14.65	2.71	22.6				
3H-2, 125–128	16.25	4.31	35.9				
3H-3, 46–47	16.96	5.88	49	6.16	0.28	0.03	0.02
3H-3, 83–86	17.33	5.39	44.9				
3H-3, 140–150	17.90	5.46	45.5	5.72	0.26	0.02	0.05
3H-4, 61–64	18.61	3.27	27.2				
4H-2, 40–42	24.90	3.56	29.7				
4H-6, 92–94	31.42	0.69	5.8	0.73	0.04	0.01	0.04
5H-1, 142–145	33.92	5.62	46.8				
5H-3, 21–25	34.32	2.95	24.6				
5H-4, 41–44	36.02	7.07	58.9				
5H-7, 118–120	41.29	3.45	28.7	3.83	0.38	0.05	0.06
6H-1, 77–79	42.77	3.72	31				
6H-1, 140–150	43.40	4.37	36.4	4.67	0.3	0.03	LD
6H-2, 114–116	44.64	5.69	47.4	5.91	0.22	0.03	LD
6H-3, 103–105	46.03	7.13	59.4				
6H-5, 64–66	48.64	5.75	47.9	6.08	0.33	0.04	0.01
7H-1, 119–121	52.79	4.31	35.9				
7H-2, 122–124	54.32	2.72	22.7				
7H-3, 93–95	55.53	4.05	33.7				
9H-1, 92–93	71.82	0.25	2.1	0.25	LD	0.01	0.01
9H-2, 76–79	73.16	0.56	4.7				
9H-3, 103–105	74.93	1.16	9.7	1.32	0.16	0.02	0.014
9H-4, 101–104	76.41	1.53	12.7				
9H-4, 140–150	76.80	0.97	8.1	1.11	0.14	0.02	0.1
9H-5, 75–78	77.65	1.34	11.2	1.49	0.15	0.02	0.1
10H-2, 136–137	82.27	1.66	13.8	1.7	0.04	0.02	0.07
11H-1, 81–82	90.91	5.72	47.7				
11H-2, 91–92	92.51	1.09	9.1				
11H-4, 34–37	94.94	0.33	2.8	0.33	LD	0.01	0.14
11H-7, 52–54	98.61	0.29	2.4				
126-793B-							
2R-1, 33–35	595.03	3.68	30.7	3.79	0.11	0.03	0.09
3R-1, 53–55	604.83	0.02	0.2				
3R-2, 19–21	605.79	0.04	0.3	0.07	0.03	0.01	0.1
3R-3, 5–7	607.09	1.34	11.2				
3R-3, 130–140	608.34	0.12	-1,	0.12	LD	LD	0.05
3R-4, 31–33	608.75	0.56	4.7				
4R-1, 62–64	614.62	0.14	1.2	0.17	0.03	0.01	0.05
4R-2, 9–11	615.59	3.26	27.2				
4R-3, 108–110	617.75	0.32	2.7				
4R-4, 70–72	618.90	0.24	2				
5R-1, 72–74	624.32	0.22	1.8				
5R-2, 118–120	626.18	0.39	3.3	0.43	0.04	0.01	0.09
5R-3, 128–130	627.63	0.44	3.7				
5R-4, 112–114	628.84	0.17	1.4				
5R-5, 44–46	629.57	1.28	10.7				
6R-1, 49–51	633.79	0.04	0.3	0.1	0.06	0.02	0.11
6R-2, 30–33	635.02	2.96	24.7	3.23	0.27	0.03	0.02
6R-3, 0–10	636.01	2.36	19.7	2.52	0.16	0.02	0.04
6R-CC, 3–5	636.54	0.69	5.8				
7R-1, 23–25	643.03	4.84	40.3	4.98	0.14	0.02	0.02
8R-1, 103–104	653.43	5.14	42.8				
8R-2, 17–18	653.98	0.75	6.3	0.8	0.05	0.01	0.03
9R-1, 29–31	662.39	0.63	5.3				
9R-1, 110–111	663.20	4.10	34.2	4.24	0.14	0.02	LD
9R-2, 45–46	664.01	2.47	20.6				
9R-2, 132–142	664.88	0.19	1.6	0.18	LD	LD	0.02
9R-3, 23–24	665.21	0.11	0.9				
10R-1, 40–42	672.20	0.07	0.6				
10R-1, 105–106	672.85	0.26	2.2	0.29	0.03	0.01	0.03
10R-2, 36–38	673.66	0.42	3.5				
10R-3, 109–111	675.86	1.34	11.2				
11R-1, 47–48	681.87	0.53	4.4				
11R-2, 86–87	683.65	0.69	5.8				
11R-3, 131–132	685.51	1.29	10.8				
11R-5, 134–135	688.38	0.34	2.8				
11R-6, 68–69	689.11	0.92	7.7				
12R-1, 33–35	691.43	1.19	9.9				

Table 11 (Continued).

Core, section, interval (cm)	Depth (mbsf)	Inorg. C (%)	$CaCO_3$ (%)	Total C (%)	Org. C (%)	Total N (%)	Total S (%)
126-793B-							
12R-1, 100–110	692.10	2.04	17	2.11	0.07	0.01	0.03
12R-2, 87–89	693.07	1.39	11.6				
13R-1, 43–45	701.23	3.68	30.7				
13R-2, 80–82	703.04	1.69	14.1				
13R-3, 33–34	704.01	0.22	1.8				
13R-4, 92–93	706.08	1.52	12.7				
14R-1, 120–121	711.60	0.17	1.4				
14R-2, 28–30	712.11	1.20	10				
15R-1, 45–47	720.55	0.55	4.6				
15R-2, 111–113	722.71	0.04	0.3				
15R-3, 75–77	723.67	0.04	0.3				
15R-3, 117–127	724.09	0.27	2.3	0.27	LD	LD	0.05
15R-4, 107–109	725.26	3.72	31				
16R-1, 29–31	729.99	0.47	3.9				
16R-2, 8–10	731.29	2.03	16.9	2.09	0.06	0.02	0.03
16R-3, 30–32	732.95	0.02	0.2				
16R-4, 21–23	734.28	2.68	22.3				
16R-5, 69–72	736.30	3.87	32.2				
16R-6, 107–109	738.18	4.66	38.8				
17R-1, 44–46	739.54	7.32	61	7.29	LD	0.02	0.06
17R-2, 41–43	740.36	4.73	39.4				
17R-3, 75–77	742.06	1.34	11.2				
17R-4, 75–77	743.50	4.81	40.1				
17R-5, 55–57	744.80	0.07	0.6	0.11	0.04	LD	LD
17R-6, 30–32	746.02	0.54	4.5				
17R-6, 92–93	746.64	0.74	6.2				
18R-1, 84–86	749.64	0.87	7.3				
18R-3, 38–40	752.18	0.87	7.3				
18R-3, 115–125	752.95	1.13	9.4				
18R-4, 22–24	753.52	1.29	10.8	1.31	0.02	LD	LD
19R-1, 123–125	759.63	0.08	0.7				
19R-2, 11–13	759.77	0.20	1.7				
19R-3, 54–56	761.63	0.04	0.3	0.08	0.04	LD	LD
19R-4, 81–83	763.36	0.04	0.3				
20R-1, 53–55	768.53	0.08	0.7				
20R-2, 120–122	770.63	0.11	0.9				
20R-3, 30–32	771.07	0.03	0.3	0.08	0.05	LD	LD
20R-4, 55–57	772.72	0.03	0.3				
20R-5, 123–125	774.85	0.03	0.3				
20R-7, 20–22	776.76	0.04	0.3				
21R-1, 77–78	778.47	0.03	0.3	0.06	0.03	LD	LD
21R-3, 94–96	781.64	0.07	0.6				
21R-5, 19–21	783.89	0.52	4.3				
21R-6, 133–143	786.53	0.41	3.4	0.45	0.04	LD	LD
22R-1, 81–82	788.11	0.66	5.5				
22R-3, 31–32	790.55	0.06	0.5				
23R-1, 58–60	797.58	0.15	1.3				
23R-3, 65–67	800.52	0.06	0.5	0.06	LD	LD	LD
23R-5, 40–41	803.13	0.05	0.4				
24R-2, 67–69	808.87	0.21	1.8				
24R-4, 7–9	811.16	0.03	0.3				
24R-4, 141–151	812.50	0.03	0.3	0.03	LD	LD	LD
24R-6, 55–57	814.67	0.29	2.4				
25R-1, 121–122	817.61	0.24	2				
25R-3, 29–30	819.58	0.08	0.7				
25R-5, 81–82	823.10	0.37	3.1	0.4	0.03	LD	LD
25R-6, 105–106	824.84	1.00	8.3				
26R-1, 45–47	826.15	0.27	2.3				
26R-3, 76–78	829.33	0.17	1.4				
26R-4, 18–20	830.25	0.13	1.1				
26R-5, 17–20	831.74	0.05	0.4	0.09	0.04	LD	LD
27R-2, 3–5	836.93	0.08	0.7				
27R-4, 21–23	839.91	0.23	1.9				
27R-6, 110–112	843.65	0.50	4.2				
27R-7, 33–58	844.38	0.21	1.8	0.23	0.02	LD	LD
28R-2, 85–87	846.62	0.05	0.4				
28R-4, 38–40	849.14	0.48	4				
28R-6, 100–102	852.63	0.06	0.5	0.08	0.02	LD	LD
28R-8, 37–39	854.81	0.12	1				
29R-1, 52–54	855.22	0.09	0.8				
29R-3, 22–24	857.58	0.06	0.5	0.1	0.04	LD	LD
29R-5, 90–92	860.90	0.13	1.1				
30R-1, 39–41	864.79	0.14	1.2				
30R-3, 56–58	867.96	0.14	1.2				
30R-4, 110–135	870.00	0.53	4.4	0.53	LD	LD	LD
30R-5, 40–42	870.65	0.30	2.5				
31R-1, 96–98	874.96	1.62	13.5				

Table 11 (Continued).

Core, section, interval (cm)	Depth (mbsf)	Inorg. C (%)	$CaCO_3$ (%)	Total C (%)	Org. C (%)	Total N (%)	Total S (%)
126-793B-							
31R-3, 62–63	877.27	0.83	6.9	0.86	0.03	LD	LD
31R-4, 14–16	877.99	2.37	19.7				
31R-6, 69–71	881.39	0.06	0.5	0.07	0.01	LD	LD
32R-1, 48–50	884.18	0.06	0.5	0.07	0.01	LD	LD
32R-3, 70–72	887.11	0.04	0.3				
32R-4, 128–130	889.19	0.05	0.4				
33R-1, 85–86	894.15	0.04	0.3				
33R-3, 87–89	897.02	1.03	8.6				
33R-5, 57–58	899.31	0.05	0.4				
33R-6, 0–25	900.09	0.08	0.7	0.08	LD	LD	LD
33R-7, 60–61	902.19	0.09	0.8				
34R-1, 31–32	903.31	1.35	11.3				
34R-3, 58–59	906.50	0.57	4.8				
34R-5, 88–89	909.16	0.03	0.3	0.04	0.01	LD	LD
34R-7, 27–28	911.06	0.05	0.4				
35R-1, 75–76	913.35	0.06	0.5				
35R-3, 53–54	916.01	1.26	10.5	1.37	0.11	LD	LD
35R-5, 125–126	919.51	0.19	1.6				
35R-6, 57–58	920.33	0.18	1.5				
36R-1, 115–117	923.45	0.94	7.8				
36R-3, 113–138	926.33	1.17	9.8	1.23	0.06	LD	LD
36R-5, 85–86	928.62	0.43	3.6				
37R-1, 33–34	932.33	0.17	1.4				
37R-5, 69–70	938.30	0.88	7.3	0.97	0.09	LD	LD
37R-7, 73–74	940.96	1.90	15.8				
38R-1, 138–140	942.98	3.47	28.9				
38R-3, 64–66	945.15	0.24	2.0	.28	0.04	LD	LD
38R-5, 143–145	948.37	0.67	5.6				
40R-2, 54–56	961.81	0.07	0.6				
40R-4, 106–108	965.14	0.39	3.3				
40R-5, 96–121	966.25	0.09	0.8	0.13	0.04	LD	LD
40R-6, 133–135	967.83	0.12	1				
40R-8, 109–111	970.48	0.14	1.2				
41R-2, 45–46	972.53	0.42	3.5				
41R-4, 59–61	975.32	0.05	0.4				
41R-6, 97–99	978.42	0.18	1.5				
42R-1, 43–45	980.73	0.32	2.7				
42R-3, 22–24	983.37	0.06	0.5				
43R-1, 17–19	989.87	0.08	0.7				
43R-3, 59–61	992.83	0.39	3.3				
43R-5, 68–70	995.62	0.09	0.8				
43R-5, 120–150	996.14	0.06	0.5				
43R-7, 5–7	997.87	0.41	3.4				
44R-1, 60–62	1000.00	0.42	3.5				
44R-3, 49–51	1002.77	0.15	1.3				
44R-5, 7–9	1005.21	0.10	0.8				
44R-7, 24–26	1008.27	0.09	0.8				
45R-1, 45–47	1009.55	0.13	1.1				
45R-1, 100–102	1010.10	0.37	3.1				
46R-1, 27–28	1018.97	0.08	0.7				
46R-3, 19–20	1020.83	0.14	1.2				
46R-3, 116–141	1021.80	0.18	1.5				
46R-5, 43–44	1024.00	0.08	0.7				
47R-1, 61–62	1028.61	0.06	0.5				
47R-3, 80–81	1031.34	0.06	0.5				
47R-4, 78–79	1032.82	0.44	3.7				
47R-5, 12–13	1033.52	0.11	0.9				
48R-1, 82–84	1038.42	0.18	1.5				
48R-3, 54–56	1041.14	0.07	0.6				
48R-5, 31–33	1043.91	0.23	1.9				
48R-6, 57–59	1045.46	0.06	0.5				
49R-1, 88–89	1048.18	0.13	1.1				
49R-2, 108–109	1049.88	0.19	1.6				
49R-3, 45–75	1050.52	0.18	1.5				
50R-1, 78–80	1057.78	0.06	0.5				
50R-3, 57–59	1060.57	0.57	4.8				
50R-5, 121–123	1064.13	0.18	1.5				
50R-6, 127–129	1065.69	0.05	0.4				
51R-2, 14–16	1067.28	0.27	2.3				
51R-4, 64–66	1070.78	0.13	1.1				
51R-6, 93–95	1073.92	0.51	4.3				
51R-8, 5–7	1075.83	0.18	1.5				
52R-1, 75–77	1077.15	0.07	0.6				
52R-1, 108–138	1077.48	0.06	0.5				
52R-3, 67–69	1079.95	0.05	0.4				
52R-5, 40–42	1082.07	0.15	1.3				
53R-1, 39–41	1086.49	0.13	1.1				

Table 11 (Continued).

Core, section, interval (cm)	Depth (mbsf)	Inorg. C (%)	$CaCO_3$ (%)	Total C (%)	Org. C (%)	Total N (%)	Total S (%)
126-793B-							
53R-3, 69–71	1089.66	0.07	0.6				
53R-CC, 8–10	1091.67	0.41	3.4				
54R-2, 35–37	1096.43	0.17	1.4				
54R-4, 32–34	1099.22	0.07	0.6				
55R-2, 0–30	1105.56	0.06	0.5				
55R-2, 134–136	1106.90	0.24	2				
55R-4, 103–105	1109.20	0.05	0.4				
56R-3, 70–74	1118.70	0.18	1.5				
57R-1, 48–50	1125.18	0.27	2.3				
57R-3, 15–17	1127.85	0.06	0.5				
58R-1, 37–39	1134.37	0.05	0.4				
58R-3, 94–96	1137.64	0.16	1.3				
58R-4, 76–106	1138.96	0.11	0.9				
58R-5, 122–124	1140.58	0.04	0.3				
58R-7, 87–89	1143.20	0.05	0.4				
59R-1, 45–46	1144.05	0.04	0.3				
59R-3, 75–77	1147.09	0.18	1.5				
59R-3, 132–133	1147.66	0.03	0.3	0.19	0.16	LD	LD
59R-5, 72–74	1149.89	0.04	0.3				
59R-7, 136–138	1153.26	0.04	0.3				
60R-1, 102–103	1154.22	0.06	0.5				
60R-3, 60–62	1156.80	0.05	0.4				
60R-5, 83–84	1159.84	0.03	0.3				
60R-7, 29–31	1161.90	0.05	0.4				
61R-1, 22–24	1163.12	0.04	0.3				
61R-3, 40–42	1166.05	0.10	0.8				
61R-3, 56–86	1166.21	0.09	0.8				
62R-1, 46–47	1173.06	0.05	0.4				
62R-2, 108–110	1174.89	0.05	0.4				
62R-4, 64–66	1177.14	0.04	0.3				
63R-1, 74–76	1182.94	0.05	0.4				
63R-4, 67–69	1187.34	0.06	0.5				
64R-1, 46–48	1192.36	0.06	0.5				
64R-3, 81–83	1195.33	0.05	0.4				
64R-5, 122–124	1198.56	0.07	0.6				
64R-6, 117–147	1200.01	0.13	1.1				
64R-7, 99–101	1201.30	0.74	6.2				
65R-1, 80–82	1202.30	0.03	0.2				
65R-5, 30–32	1207.64	0.04	0.3				
65R-6, 74–76	1209.58	0.23	1.9				
65R-7, 35–37	1210.69	0.04	0.3				
66R-1, 65–67	1211.75	0.03	0.2				
66R-3, 81–83	1214.81	0.03	0.2				
66R-4, 34–36	1215.84	0.04	0.3				
66R-4, 117–118	1216.67	0.21	1.8				
66R-6, 140–142	1219.69	0.37	3.1				
67R-1, 97–99	1221.77	0.05	0.4				
67R-3, 69–71	1224.35	0.20	1.7				
67R-4, 0–30	1225.11	0.04	0.3				
67R-5, 121–123	1227.82	0.05	0.4				
68R-1, 115–117	1231.65	0.26	2.2				
68R-3, 38–40	1233.78	0.11	0.9				
68R-4, 91–93	1235.67	0.10	0.8				
68R-6, 26–28	1237.95	0.10	0.8				
69R-1, 72–74	1240.92	0.60	5				
69R-3, 73–75	1243.85	0.07	0.6				
69R-5, 47–49	1246.38	0.77	6.4				
69R-7, 12–14	1248.99	0.06	0.5				
70R-1, 92–96	1250.72	0.26	2.2				
70R-3, 74–76	1253.49	0.14	1.2				
70R-5, 62–64	1255.93	0.35	2.9				
70R-7, 0–30	1258.31	0.11	0.9				
70R-7, 45–47	1258.76	0.13	1.1				
71R-1, 88–90	1260.28	0.27	2.2				
71R-7, 83–85	1268.11	0.12	1				
72R-1, 58–60	1269.28	0.32	2.7				
72R-3, 79–81	1272.49	0.09	0.7				
72R-5, 81–83	1275.51	0.33	2.7				
72R-7, 12–14	1277.54	0.06	0.5				
73R-1, 102–104	1279.42	0.14	1.2				
73R-3, 38–40	1281.54	0.08	0.7				
73R-4, 120–150	1283.71	0.37	3.1				
73R-5, 56–58	1284.57	0.31	2.6				
74R-5, 64–66	1294.17	0.32	2.7				
74R-7, 81–83	1296.83	0.59	4.9				
75R-1, 75–77	1298.45	0.45	3.7				
75R-5, 71–73	1304.34	0.65	5.4				

Table 11 (Continued).

Core, section, interval (cm)	Depth (mbsf)	Inorg. C (%)	$CaCO_3$ (%)	Total C (%)	Org. C (%)	Total N (%)	Total S (%)
126-793B-							
75R-7, 6-8	1306.69	0.13	1.1				
76R-1, 71-73	1308.01	0.08	0.7				
76R-5, 104-134	1314.25	0.06	0.5				
77R-1, 63-65	1317.63	0.11	0.9				
77R-3, 120-122	1321.13	0.57	4.7				
77R-5, 101-103	1323.88	0.09	0.7				
78R-1, 64-66	1327.34	0.21	1.7				
78R-3, 64-66	1330.31	0.09	0.7				
78R-5, 56-58	1332.68	0.26	2.2				
78R-7, 123-125	1336.11	0.24	2				
79R-1, 63-64	1337.03	0.24	2				
79R-5, 43-44	1342.15	0.54	4.5				
79R-6, 60-61	1343.77	0.22	1.8				
80R-1, 95-97	1346.95	0.21	1.7				
80R-3, 86-88	1349.86	0.24	2				
80R-5, 0-30	1351.63	0.10	0.8				
80R-5, 73-74	1352.36	0.81	6.7				
80R-7, 4-6	1354.49	0.55	4.6				
82R-1, 73-75	1366.03	0.05	0.4				
82R-3, 70-71	1368.80	0.05	0.4				
82R-5, 96-97	1371.78	0.04	0.3				
82R-7, 49-51	1374.18	0.03	0.2				
83R-1, 96-98	1375.86	0.06	0.5				
83R-2, 28-30	1376.68	0.05	0.4				
84R-1, 22-24	1384.72	0.03	0.2				
84R-2, 98-100	1386.98	0.04	0.3				
85R-1, 25-27	1394.45	0.04	0.3				
87R-3, 45-75	1416.91	0.05	0.4				
88R-1, 79-81	1423.69	0.07	0.6				
88R-2, 23-25	1424.55	0.07	0.6				
89R-1, 34-36	1431.74	0.07	0.6				
89R-3, 48-50	1434.80	0.05	0.4				

Note: LD = less than detection limit.

of dissolved constituents would sustain steeper concentration gradients and more prominent extremes. However, the possibility that the highly altered composition of the pore waters in Unit V is a result of reactions occurring in Unit VI must be considered.

At present, there are two lines of observations contradicting this hypothesis:

1. The concentration of magnesium drops to zero at the top of Unit V, which shows that reactions are taking place at the same rate that magnesium is diffusing from above.
2. None of the dissolved constituents show prominent gradients in the lower half of Unit V, indicating that exchange with the underlying unit is limited.

Most probably, any previous hydrothermal pore-water signal has now been overprinted by the prominent low-temperature alteration reactions and the growth of authigenic smectite at the expense of volcanic glass, which constitutes the major sink for magnesium. Calcium is probably derived from this reaction and from the alteration of plagioclase. Shipboard, semiquantitative XRD analyses show that smectites, gypsum, and zeolites are abundant constituents of Unit V and VI sediments (see "Lithostratigraphy and Accumulation Rates" section, this chapter). Although this cannot be confirmed by shipboard analyses, charge-balance calculations show that the pore waters are severely depleted in sodium. The most likely sink for sodium is the formation of zeolites.

The low alkalinities in Units IV and V (Table 10) are a result of the precipitation of carbonate in response to the release of calcium. The reason that alkalinities are not even lower is probably the formation of $CaHCO_3$ ion pairs, although this can only be confirmed by more detailed speciation studies. Note that the precipitation of this amount of carbonate would result in $<0.01\%$ calcite. Thus, this hypothesis does not conflict with the very low concentrations of sedimentary carbonate (Table 11).

Sulfate concentration profiles in marine sediments usually have a steep gradient close to the seafloor. At Site 793, the concentration of sulfate remains close to seawater levels down to 724 mbsf (Core 126-793B-15R) and then decreases to a minimum of 11.9 mM at 927 mbsf (Core 126-793B-36R; Fig. 62). As at Site 792, the concentration of sulfate appears to be controlled by the precipitation of gypsum, although saturation-state calculations show an apparent supersaturation with respect to this mineral below about 800 mbsf. This supersaturation probably is an artifact resulting from the use of constant-activity coefficients for calcium and sulfate similar to the activity constants in seawater. In these pore waters, the coefficients presumably are considerably smaller than in seawater as a result of the formation of $CaSO_4$ ion pairs.

The low concentrations of ammonia in Unit V substantiate the hypothesis that the removal of sulfate is a result of mineral precipitation rather than of bacterial consumption.

The concentration of dissolved silica increases from about 500 μM in Unit I to about 900 μM in Unit III, then decreases abruptly to about 200 μM in Units IV and V (Fig. 62). The steep gradient between Unit III and IV is another indication of high reaction rates.

Sediment Geochemistry

Sediments from Site 793 were analyzed on board ship for inorganic carbon, total carbon, nitrogen, and sulfur (see "Explanatory Notes" chapter, this volume). Analytical results are presented in Table 11. The concentration of organic carbon is very low, ranging from less than the detection limit to 0.38%, with an average of 0.07%. The concentration of total sedimentary sulfur varies from less than the detection limit to 0.14%.

PHYSICAL PROPERTIES

Introduction

Physical property measurements completed on APC cores in Hole 793A included multisensor track (MST) logging, thermal conductivity, vane shear strength, Hamilton Frame (HF) compressional sonic velocity, index properties, and carbonate analyses. Rotary-drilled cores from Hole 793B were measured for HF velocity, index properties, and calcium carbonate. Details of procedures are included in the "Explanatory Notes" chapter (this volume). As nearly 500 m of unrecovered section separates Holes 793A and 793B, and because significant differences in lithification exist between the sediments in the two holes, we will discuss the properties of each separately.

Index Properties

Hole 793A

Porosity and water content values decrease slightly with depth in Unit I, and correlate inversely with wet-bulk density (Table 12, Fig. 63). We did not observe any obvious changes at the Subunit IA/IB contact, but general downward trends are reflected in the average values of these index properties for the two subunits: porosity, 70.1% and 66.2%; water content, 79.4% and 66.4%; and wet-bulk density, 1.65 and 1.71 g/cm^3 in Subunits IA and IB, respectively. We note a tenuous correlation between porosity, water content, and carbonate content. High carbonate contents in this unit are associated with higher percentages of clay-size material and, therefore, higher porosities. The GRAPE and gravimetric wet-bulk density data from Hole 793A are shown in Figure 64. Similar density values are obtained by both methods. Higher variability in the GRAPE measurements, and intervals of noticeably lower GRAPE density values (e.g., between 40 and 50 mbsf), probably result from coring disturbance, which is generally avoided in gravimetric sampling.

Grain density values in Unit I are fairly high; the majority of values fall above 2.7 g/cm^3. In addition, grain density values correlate well with carbonate contents. One exception is the interval between 60 and 85 mbsf in which grain density is high, but carbonate contents are lower than average (Table 12). Grain density values increase slightly from Subunit IA (average 2.70 g/cm^3) to IB (average 2.77 g/cm^3).

Hole 793B

Unit II, a diabase sill, is characterized by very low porosity and high wet-bulk density values. Porosity and water content values from the diabases are the lowest measured at this site (averages of 10.4% and 4.0%, respectively), whereas wet-bulk density averages 2.76 g/cm^3 and grain density averages 2.79 g/cm^3.

With the exception of Unit II, correlation between the lithologic units and the index property measurements is marginal. Although fairly sharp changes in index properties were observed at several unit boundaries (e.g., Unit III/IV and Unit IV/V boundaries; see Fig. 63), similar changes were noted at numerous other depths within the section. Particularly interesting is the lack of a significant variation in the index property values from the base of the sediments into basement rock, probably the result of the gradual transition from the sediments to igneous breccias (see "Lithostratigraphy and Accumulation Rates" and "Igneous Petrology" sections, this chapter).

We recognized some general trends. Units III and IV have high porosity (means of 60.3% and 46.5%) and water content (means of 50.9% and 32%) values. A sharp change in these parameters is observed at the Unit III/IV boundary (e.g., porosity decreases from approximately 60% to 40%). Trends reverse within Unit IV and values comparable to those in Unit III are reached toward the base of Unit IV. Mean values of porosity and water content in lithologic Units VI and VII are lower: 31% and 27% (porosity) and 15% and 12% (water content), respectively. Fluctuations similar to those observed in Hole 792E are superimposed on these gross trends. Values of porosity and water content decrease from a maximum of 64% and 60%, respectively, at 600 mbsf, to a minimum of 25% and 10% at 900 mbsf, then increase to 40% and 30% at approximately 1000 mbsf. Another decrease occurs over the interval from 1000 to 1120 mbsf, below which values of both parameters remain essentially unchanged to a depth of 1280 mbsf. A fairly sharp decrease in porosity and water content follows. Minima at 1320 mbsf represent the lowest porosity and water content values in the hole, with the exception of the diabase of Unit II. This depth interval coincides with the occurrence of abundant opaque minerals.

No other obvious correlation between the lithology (in particular, grain size or mineralogy) is observed in this hole (see "Lithostratigraphy and Accumulation Rates" section, this chapter). Porosity and water content values increase to a depth of 1350 mbsf, then remain fairly stable to about 1480 mbsf, at which point both increase sharply. The volcanic breccia and lava flow units within the basement rocks are clearly differentiated by the index property measurements (Table 12). Samples from the flow units are characterized by generally low porosity and water content values, and high wet-bulk density values, compared with those in the breccia.

Wet-bulk density trends in Hole 793B mirror those observed in porosity and water content. Bulk density values increase from about 1.7 g/cm^3 at the top of the sediment (means of 1.86 and 2.05 g/cm^3 in Units III and IV, respectively) to 2.2 g/cm^3 at approximately 900 mbsf. The trend then reverses and values decrease sharply to a depth of 1000 mbsf, followed by a steady increase in wet-bulk density to the Unit VII boundary; the mean value in Unit VI is 2.5 g/cm^3. Values in basement rocks are quite stable, averaging 2.54 g/cm^3.

Grain density values display a high degree of variability throughout the sedimentary section in both Holes 793A and 793B. Values average 2.71 g/cm^3 within Unit III and 2.62 g/cm^3 in Unit IV. Average grain density values in Units V, VI, and VII are 2.57, 2.66, and 2.79 g/cm^3, respectively. In general, high values correspond to intervals of high carbonate content (Fig. 63). Grain density values above 2.8 g/cm^3 are probably associated with concentrations of heavy minerals.

Carbonate Content

Ranges and averages of carbonate contents in Units III (0.2%–43%; average 10%) and IV (1.0%–61%; mean 21%) are similar to those in the upper 100 mbsf (Unit I; Hole 793A). Much of the variability in carbonate is a result of the presence of nannofossil-rich layers. Except for a zone between 867 and 956 mbsf in which values reach 30%, carbonate contents are generally <4% in Units V and VI (averages are 2.0% and 0.4%, respectively). Lithologic Unit IV, which has the highest average carbonate content, has been interpreted as a pelagic unit deposited during a period of volcanic quiescence (see "Lithostratigraphy and Accumulation Rates" section, this chapter). This implies that much of the variation in $CaCO_3$ content is the result of dilution by volcanogenic input.

Vane Shear Strength

Hole 793A

Only 16 successful vane shear strength measurements were acquired in Hole 793A because of the short APC section. These values are shown in Table 13 and are plotted in Figure 65. Sev-

Table 12. Physical property (index properties, velocity, and calcium carbonate content) data from Holes 793A and 793B.

Core, section, interval (cm)	Depth (mbsf)	Wet-bulk density (g/cm^3)	Dry-bulk density (g/cm^3)	Porosity (%)	Water content (%)	Grain density (g/cm^3)	Void ratio	Carbonate content (%)	Velocity (km/s)
126-793A-									
1H-1, 69–71	0.69	1.59	0.88	72	86	2.81	2.55	8.1	
1H-2, 140–150	2.9							0.7	
2H-2, 67–71	6.39	1.10[a]	0.90	20[a]	23[a]	2.31[a]	0.25[a]	1.0	
3H-1, 114–116	14.64	1.67	0.98	70	75	2.71	2.31	22.6	1.52
3H-2, 125–128	16.25	1.73	1.04	71	72	2.89	2.39	35.9	1.53
3H-3, 46–47	16.96							49.0	
3H-3, 82–84	17.32	1.60	0.92	68	78	2.68	2.14	44.9	1.52
3H-3, 140	150							45.5	
3H-4, 61–64	18.61	1.67	0.97	70	76	2.79	2.37	27.2	
3H-5, 105–107	20.55	1.60[a]	0.73	88[a]	130[a]	1.62[a]	7.51[a]		
4H-2, 40–42	24.90	1.65	0.98	68	72	2.65	2.10	29.7	1.54
4H-4, 115–117	28.65	1.72	1.19	54	48	2.41	1.19		1.53
4H-6, 92–94	31.42							5.7	
5H-1, 142–145	33.92	1.57	0.87	71	87	2.81	2.50	46.8	1.53
5H-3, 21–25	34.32	1.81	1.22	59	51	2.66	1.46	24.6	1.58
5H-4, 41–45	36.02	1.71	1.03	68	69	2.75	2.16	58.9	1.53
5H-7, 118–121	41.29	1.75	1.12	64	60	2.83	1.77	28.7	1.55
6H-1, 76–79	42.76	1.73	1.03	70	71	3.24	2.35	31.0	1.52
6H-1, 140–150	43.4							36.4	
6H-2, 114–116	44.64	1.73	1.08	66	64	2.72	1.91	47.4	1.55
6H-3, 103–105	46.03	1.72	1.00	73	76	3.01	2.68	59.4	1.52
6H-5, 63–65	48.63	1.70	1.02	69	71	2.86	2.26	47.9	1.53
7H-1, 119–121	52.79	1.65	0.99	67	71	2.76	2.00	35.9	1.55
7H-2, 121–124	54.31	1.64	0.94	71	79	2.70	2.42	22.7	1.52
7H-3, 92–95	55.52	1.68	1.04	65	66	2.68	1.89	33.7	1.54
8H-1, 42–45	61.62	1.68	1.04	65	65	2.85	1.83		
8H-5, 140–141	68.08	1.73	1.20	53	46	2.82	1.12		
9H-1, 92–93	71.82	1.79	1.17	63	56	2.76	1.70	2.1	
9H-2, 76–78	73.16	1.91	1.26	66	54	2.87	1.90	4.7	1.58
9H-3, 107–110	74.97	1.74	1.05	70	71	2.82	2.37	9.7	1.58
9H-4, 103–107	76.43	1.79	1.16	64	58	2.82	1.78	12.7	1.61
9H-4, 140–150	76.8							8.1	
9H-5, 75–78	77.65	1.78	1.15	64	58	2.61	1.74	11.2	1.56
10H-1, 38–40	80.86	1.58	0.88	71	85	2.74	2.43		
10H-2, 135–138	82.26	1.78	1.14	64	59	2.86	1.81	13.8	
11H-1, 81–83	90.91							47.6	1.58
11H-1, 135–138	91.45	1.72	1.00	73	77	2.79	2.69		
11H-2, 90–92	92.50	1.63	0.98	65	70	2.49	1.88	9.1	1.61
11H-4, 34–37	94.94	1.62	0.99	64	67	2.44	1.76	2.7	1.65
11H-7, 52–53	98.61	1.64	1.02	63	64	2.56	1.68	2.4	1.65
126-793B-									
1R-1, 19–20	586.69	2.75	2.66	9	3	2.75*	0.10		5.14
1R-1, 66–68	587.16	2.88	2.77	12	4	2.93	0.13		4.66
1R-1, 123–125	587.73	3.13	3.00	13	4	3.13	0.15		5.06
1R-1, 101–103	589.01	3.07	2.94	13	5	3.21	0.15		4.66
1R-2, 113–115	589.13	2.76	2.66	10	4	2.79	0.11		5.00
1R-2, 18–20	589.53	3.27	3.17	10	3	3.14	0.12		4.63
1R-3, 70–73	590.05	2.77	2.65	12	5	2.82	0.14		4.99
2R-1, 32–34	595.02	1.63	0.94	70	78	2.63	2.29	30.7	1.86
3R-1, 54–57	604.84	1.69	1.08	61	59	2.65	1.57	0.2	2.10
3R-2, 20–22	605.80	1.97	1.43	55	40	2.70	1.20	0.3	1.97
3R-3, 6–8	607.10	1.78	1.13	66	61	2.68	1.91	11.2	1.94
3R-3, 130–140	608.34							1.0	
3R-4, 32–34	608.76	1.78	1.12	67	62	2.72	2.02	4.7	2.04
4R-1, 64–66	614.64	1.81	1.15	67	60	2.76	1.99	1.2	2.28
4R-2, 11–13	615.61	1.78	1.19	61	53	2.73	1.53	27.2	1.93
4R-2, 102–104	616.52	1.89	1.22	67	58	2.42	2.07		2.08
4R-3, 109–111	617.76	1.88	1.28	60	49	2.47	1.50	2.7	1.94
4R-4, 71–73	618.91	1.71	1.13	58	54	2.47	1.39	2.0	1.83
5R-1, 75–77	624.35	1.68	1.03	66	67	2.71	1.96	1.8	1.86
5R-2, 20–22	625.20	1.70	1.10	60	57	2.49	1.52		1.91
5R-2, 118–120	626.18							3.3	
5R-3, 129–131	627.64	1.84	1.24	60	51	2.57	1.51	3.7	2.01
5R-4, 111–113	628.83	1.77[a]	1.33	45[a]	35[a]	3.34[a]	0.82*	1.4	1.91
5R-5, 44–46	629.57	1.74	1.16	59	53	2.47	1.45	10.7	1.91
6R-1, 51–53	633.81	1.69	1.05	65	65	2.71	1.83	0.3	1.85
6R-2, 30–33	635.02	1.79	1.18	62	55	2.73	1.62	24.7	1.90
6R-3, 0–10	636.01							19.7	
6R-CC, 3–5	636.54	1.67	1.10	57	54	2.27	1.34	5.8	1.89
7R-1, 24–26	643.04	1.92	1.34	59	46	2.82	1.46	40.3	2.00
8R-1, 103–105	653.43	1.87	1.28	61	49	2.97	1.53	42.8	1.93
8R-2, 18–20	653.99	2.04	1.41	64	48	2.48	1.79	6.3	1.92

Table 12 (Continued).

Core, section, interval (cm)	Depth (mbsf)	Wet-bulk density (g/cm³)	Dry-bulk density (g/cm³)	Porosity (%)	Water content (%)	Grain density (g/cm³)	Void ratio	Carbonate content (%)	Velocity (km/s)
126-793B-									
9R-1, 29–30	662.39	1.90	1.24	66	56	2.66	1.97	5.3	1.92
9R-1, 110–112	663.20	2.01	1.38	64	48	2.89	1.76	34.2	1.97
9R-2, 44–46	664.00	1.93	1.29	65	52	3.08	1.85	20.6	2.06
9R-2, 132–142	664.88							1.6	
9R-3, 22–24	665.20	2.03	1.53	59	43	3.10	1.44	0.9	2.09
10R-1, 41–43	672.21	1.81	1.21	61	53	2.80	1.56	0.6	2.07
10R-1, 105–107	672.85	1.88	1.23	65	56	2.93	1.89	2.2	1.97
10R-2, 35–37	673.65	1.86	1.22	64	55	2.74	1.80	3.5	1.96
10R-2, 110–112	674.40	1.83	1.20	64	56	2.58	1.80		2.02
10R-3, 107–109	675.84	2.05	1.33	72	57	3.02	2.61	11.2	2.01
10R-3, 110–112	675.87	1.91	1.35	57	44	2.69	1.32		2.12
11R-1, 47–49	681.87	1.74	1.20	55	48	2.57	1.21	4.4	2.14
11R-2, 84–86	683.63	2.17	1.67	50	31	2.86	1.01	5.8	2.18
11R-3, 131–133	685.51	2.16	1.48	69	48	3.16	2.19	10.8	2.09
11R-4, 90–92	686.49	2.11	1.50	61	42	3.10	1.58		2.08
11R-5, 134–136	688.38	1.72	1.13	60	55	2.34[a]	1.50	2.8	1.92
11R-6, 68–70	689.11	1.95	1.37	58	44	2.98	1.38	7.7	2.19
12R-1, 33–35	691.43	1.79	1.18	62	54	2.66	1.60	9.9	2.07
12R-1, 100–110	692.10							17.0	
12R-2, 86–88	693.06	1.82	1.26	57	47	2.52	1.33	11.6	2.02
13R-1, 43–45	701.23	1.85	1.22	64	55	2.66	1.76	30.7	1.95
13R-2, 80–82	703.04	1.86	1.23	64	54	2.70	1.78	14.1	1.98
13R-3, 33–35	704.01	1.85	1.23	62	53	2.69	1.66	1.8	1.85
13R-4, 92–94	706.08	1.75	1.15	61	55	2.45	1.54	12.7	2.18
14R-1, 118–121	711.58	1.83		56	46	2.67	1.27	1.4	2.00
14R-2, 29–31	712.12	1.77	1.17	61	55	2.66	1.56	10.0	2.07
15R-1, 44–46	720.54	1.75	1.20	56	49	2.54	1.29	4.6	2.03
15R-2, 110–112	722.70	1.75	1.14	61	56	2.43	1.57	0.3	1.99
15R-3, 75–77	723.67	1.81	1.21	61	52	2.45	1.54	0.3	2.08
15R-3, 117–127	724.09							2.3	
15R-4, 106–108	725.25	1.97	1.42	56	41	2.87	1.27	31.0	2.09
16R-1, 29–31	729.99	1.80	1.22	59	50	2.69	1.41	3.9	2.00
16R-2, 7–10	731.28	1.81	1.25	57	47	2.56	1.31	16.9	2.05
16R-3, 30–32	732.95							0.2	
16R-3, 37–40	733.02	1.93	1.46	48	34	2.57	0.94		2.33
16R-4, 22–24	734.29	2.02	1.48	54	38	2.78	1.18	22.3	1.88
16R-5, 69–71	736.30	2.12	1.71	41	25	2.67	0.71	32.2	1.96
16R-6, 106–109	738.17	2.18	1.79	39	22	2.60	0.63	38.8	2.02
17R-1, 43–46	739.53	2.24	1.90	34	19	2.71	0.52	61.0	2.14
17R-2, 41–43	740.36	2.17	1.77	40	23	2.78	0.66	39.4	1.99
17R-3, 75–77	742.06	2.09	1.63	47	30	2.75	0.87	11.2	1.93
17R-4, 74–76	743.49	2.20	1.80	41	23	2.52	0.68	40.1	2.08
17R-5, 54–57	744.79	2.00	1.54	47	32	2.65	0.89	0.6	1.94
17R-6, 31–33	746.03	1.92	1.38	54	41	2.41	1.18	4.5	2.03
17R-6, 92–93	746.64							6.2	
18R-1, 85–87	749.65	2.12	1.64	49	31	2.59	0.97	7.3	1.92
19R-3, 39–41	752.19	1.78	1.25	53	45	2.49	1.15	7.3	1.97
18R-3, 115–125	752.95							9.4	
18R-4, 22–25	753.52	1.77	1.11	66	63	2.61	1.98	10.8	1.98
19R-1, 122–124	759.62	2.02	1.50	53	37	2.54	1.12	0.7	1.79
19R-2, 11–14	759.77	1.89	1.37	52	40	2.46	1.10	1.7	1.81
19R-3, 54–57	761.63	2.11	1.78	34	20	2.47	0.51	0.3	3.27
19R-4, 80–82	763.35	2.22	1.90	33	18	2.58	0.48	0.3	3.31
20R-1, 54–56	768.54	2.21	1.81	41	23	2.76	0.68	0.7	2.85
20R-2, 119–122	770.62	2.06	1.63	44	28	2.66	0.77	0.9	2.32
20R-3, 29–31	771.06	2.14	1.70	44	27	2.73	0.79	0.3	2.08
20R-4, 56–58	772.73	2.28	1.94	34	18	2.77	0.52	0.3	2.94
20R-5, 123–125	774.85	2.19	1.82	38	21	2.78	0.60	0.3	2.96
20R-7, 20–22	776.76	2.10	1.69	42	26	2.65	0.71	0.3	2.01
21R-1, 77–79	778.47	2.01	1.53	48	33	2.60	0.93	0.3	2.18
21R-2, 130–132	780.50	2.12	1.64	48	30	2.76	0.93		2.13
21R-3, 93–96	781.63	2.24	1.89	36	19	2.70	0.55	0.6	2.74
21R-4, 135–137	783.55	2.15	1.63	52	33	2.73	1.10		2.02
21R-5, 19–21	783.89	1.92		62	50	2.74	1.64	4.3	2.34
21R-6, 99–101	786.19	2.13	1.55	58	39	2.76	1.38		2.25
21R-6, 133–153	786.53							3.4	
22R-1, 81–83	788.11	2.09	1.64	46	29	2.68	0.84	5.5	2.16
22R-3, 32–34	790.56	2.20	1.87	34	19	2.34[a]	0.51	0.5	2.99
23R-1, 59–61	797.59	2.14	1.77	37	22	2.66	0.59	1.3	3.11
23R-3, 65–67	800.52	2.08	1.66	42	26	2.65	0.73	0.5	2.60
23R-5, 39–41	803.12	2.23	1.79	44	26	2.68	0.80	0.4	2.79
24R-2, 66–68	808.86	2.17	1.63	55	35	2.74	1.20	1.8	2.24
24R-4, 8–10	811.17	2.39	2.10	29	14	2.62	0.41	0.3	3.27
24R-4, 141–151	812.50							0.3	
24R-6, 54–56	814.66	1.96	1.38	58	44	2.92	1.38	2.4	2.05

Table 12 (Continued).

Core, section, interval (cm)	Depth (mbsf)	Wet-bulk density (g/cm^3)	Dry-bulk density (g/cm^3)	Porosity (%)	Water content (%)	Grain density (g/cm^3)	Void ratio	Carbonate content (%)	Velocity (km/s)
126-793B-									
25R-1, 121–123	817.61	2.00	1.57	43	29	2.64	0.76	2.0	2.30
25R-3, 29–31	819.58	2.15	1.69	47	29	2.64	0.88	0.7	2.55
25R-5, 80–82	823.09	2.06	1.60	47	30	2.60	0.88	3.1	2.32
25R-6, 105–106	824.84	2.22		54	33	3.02		8.3	2.14
26R-1, 45–47	826.15	1.98	1.46	53	38	2.55	1.13	2.3	2.18
26R-2, 61–63	827.67	1.94	1.56	39	26	2.45	0.64		2.73
26R-3, 75–77	829.32	2.11	1.74	38	23	2.51	0.61	1.4	2.79
26R-4, 18–20	830.25	2.21	1.73	48	29	2.50	0.92	1.1	2.74
26R-5, 3–5	831.60	2.27	1.88	40	22	6.32[a]	0.66		3.00
26R-5, 17–20	831.74							0.4	
26R-6, 63–65	833.70	2.19	1.81	38	22	2.58	0.62		2.96
26R-6, 139–141	834.46	2.22	1.82	40	23	2.30[a]	0.66		3.07
27R-2, 3–5	836.93	2.20	1.85	36	20	2.66	0.57	0.7	3.22
27R-4, 22–24	839.92	2.04	1.60	45	29	2.56	0.81	1.9	2.56
27R-6, 109–111	843.64	2.40	1.82	59	34	2.62	1.44	4.2	2.26
27R-7, 33–58	844.38							1.8	
28R-2, 85–88	846.62	2.05	1.68	38	23	2.50	0.61	0.4	2.74
28R-4, 38–40	849.14	1.97	1.47	50	35	2.65	1.00	4.0	2.27
28R-6, 99–101	852.62	1.93	1.50	44	30	2.32[a]	0.78	0.5	2.58
28R-8, 37–39	854.81	2.15	1.77	38	22	2.55	0.62	1.0	2.76
29R-1, 52–55	855.22	2.22	1.88	34	19	2.58	0.52	0.8	3.02
29R-3, 22–24	857.58	2.21	1.88	33	18	2.53	0.49	0.5	3.16
29R-5, 90–92	860.90	1.94	1.45	50	36	2.48	1.01	1.1	2.34
30R-1, 38–41	864.78	2.24	1.90	35	19	2.64	0.53	1.2	3.18
30R-3, 55–58	867.95	2.16	1.81	36	20	2.62	0.55	1.2	3.19
30R-4, 110–135	870.00							4.4	
30R-5, 40–42	870.65	1.94	1.38	57	43	2.96	1.32	2.5	2.28
31R-1, 95–97	874.95	2.13	1.72	42	25	2.86	0.72	13.5	2.43
31R-2, 128–131	879.56	1.92	1.44	48	35	2.48	0.93		2.53
31R-3, 10–12	879.75	1.86	1.37	50	38	2.56	0.98		2.43
31R-3, 25–28	876.90	1.97	1.46	51	36	2.45	1.04		2.49
31R-3, 62–63	877.27							6.9	
31R-4, 14–16	877.99	2.09	1.72	38	23	2.88	0.61	19.7	2.45
31R-6, 68–70	881.38	2.21	1.89	32	18	2.68	0.48	0.5	2.76
32R-1, 48–51	884.18	2.25	1.94	32	17	2.74	0.47	0.5	2.92
32R-3, 70–73	887.11	2.29	2.03	27	14	2.61	0.37	0.3	3.35
32R-4, 127–130	889.18	2.43	2.20	23	11	2.62	0.30	0.4	3.76
33R-1, 85–87	894.15	2.21	1.97	25	13	2.42	0.33	0.3	3.32
33R-3, 87–89	897.02	2.05	1.62	43	28	2.69	0.76	8.6	2.42
33R-5, 57–60	899.31	2.23	1.90	34	18	2.62	0.51	0.4	2.89
33R-6, 0–25	900.09							0.7	
33R-7, 60–63	902.19	2.01	1.62	39	25	2.43	0.63	0.8	2.73
34R-1, 31–33	903.31	2.28	1.86	42	23	2.80	0.71	11.3	2.39
34R-3, 57–59	906.49	2.28	1.95	33	18	2.68	0.50	4.8	2.75
34R-5, 87–89	909.15	2.44	2.23	21	10	2.58	0.26	0.3	3.59
34R-7, 25–27	911.04	2.27	1.91	37	20	2.56	0.59	0.4	2.95
35R-1, 75–77	913.35	2.28	1.99	30	16	2.53	0.43	0.5	3.19
35R-3, 55–57	916.03	2.26	1.92	35	19	2.60	0.53	10.5	2.87
35R-5, 125–127	919.51	2.11	1.67	45	28	2.39	0.82	1.6	2.62
35R-6, 57–59	920.33	2.29	1.85	44	25	2.70	0.79	1.5	2.54
36R-1, 66–68	922.96	2.25	1.78	48	28	2.80	0.91		2.29
36R-1, 116–118	923.46	2.10	1.64	46	29	2.68	0.86	7.8	
36R-3, 94–96	926.14	2.20	1.77	44	26	2.64	0.78		2.38
36R-3, 113–138	926.33							9.8	
36R-4, 12–14	926.70	2.32	1.90	43	23	2.71	0.75		
36R-5, 84–86	928.61	2.29	2.01	28	14	2.62	0.39	3.6	3.02
36R-6, 96–99	930.18	2.39	2.04	35	18	2.64	0.54		
37R-1, 32–34	932.32	2.15	1.81	35	20	2.60	0.53	1.4	2.77
37R-3, 58–61	935.54	2.23	1.90	34	19	2.64	0.51		2.85
37R-5, 69–71	938.30	2.12	1.70	42	26	2.51	0.74	7.3	2.49
37R-7, 73–75	940.96	2.25	1.83	43	24	2.70	0.74	15.8	2.47
38R-1, 138–140	942.98	2.32	2.01	32	16	2.62	0.46	28.9	2.82
38R-3, 64–66	945.15	2.23	1.80	44	25	0.82*	0.78	2.0	2.87
38R-5, 143–145	948.37	2.06	1.55	52	35	2.58	1.07	5.6	2.34
39R-1, 14–16	951.44	2.18	1.82	37	21	2.65	0.58		2.60
40R-2, 54–60	961.81	2.01	1.64	38	24	2.36*	0.61	0.6	2.75
40R-4, 106–108	965.14	1.95	1.54	41	28	2.33*	0.70	3.3	2.74
40R-5, 96–121	966.25							0.8	
40R-6, 133–135	967.83	2.30	1.95	34	18	2.64	0.53	1.0	2.92
40R-8, 109–111	970.48	2.02	1.61	42	27	2.21*	0.72	1.2	2.62
41R-2, 45–47	972.53	1.97	1.55	43	29	2.40	0.74	3.5	2.58
41R-4, 59–62	975.32	2.07	1.68	40	25	2.56	0.67	0.4	2.75
41R-6, 97–99	978.42	2.00	1.55	45	30	2.42	0.82	1.5	2.56
42R-1, 43–46	980.73	1.89	1.45	45	32	2.08*	0.81	2.7	2.61
42R-2, 4–6	981.77								2.60

Table 12 (Continued).

Core, section, interval (cm)	Depth (mbsf)	Wet-bulk density (g/cm³)	Dry-bulk density (g/cm³)	Porosity (%)	Water content (%)	Grain density (g/cm³)	Void ratio	Carbonate content (%)	Velocity (km/s)
126-793B-									
42R-3, 23–25	983.38	2.00	1.60	40	26	2.33*	0.66	0.5	2.77
42R-4, 59–61	985.14	2.09	1.64	46	29	2.71	0.84		2.60
42R-4, 133–135	985.88	2.12	1.63	49	31	2.51	0.96		2.48
42R-5, 76–78	986.71	2.02	1.60	42	27	2.29*	0.74		2.69
43R-1, 17–19	989.87	1.97	1.57	40	27	2.48	0.68	0.7	2.69
43R-3, 59–61	992.83	1.86	1.46	41	29	2.51	0.70	3.3	2.67
43R-5, 68–71	995.62	2.03	1.62	42	27	2.51	0.71	0.8	2.61
43R-5, 120–150	996.14							0.5	
43R-7, 4–7	997.86	2.02	1.60	42	27	2.45	0.73	3.4	2.56
44R-1, 60–62	1000.00	1.89	1.42	48	35	2.40	0.91	3.5	2.59
44R-3, 48–51	1002.76	2.02	1.58	44	29	2.54	0.78	1.3	2.67
44R-5, 7–9	1005.21	2.06	1.66	40	25	2.51	0.68	0.8	2.83
44R-7, 26–29	1008.29	1.98	1.57	41	27	2.46	0.70	0.8	3.04
45R-1, 45–47	1009.55	2.10	1.73	37	22	2.61	0.60	1.1	2.83
45R-1, 100–103	1010.10	1.90	1.48	42	30	2.37	0.73	3.1	2.61
46R-1, 26–29	1018.96	2.10	1.77	33	20	2.54	0.50	0.7	2.99
46R-2, 90–92	1020.04	2.00	1.55	46	31	2.49	0.84		2.00
46R-3, 21–23	1020.85	1.98	1.53	46	31	2.42	0.83	1.2	2.64
46R-3, 116–141	1021.80							1.5	
46R-4, 80–82	1022.85	1.88	1.47	41	29	2.41	0.71		1.98
46R-5, 42–44	1023.99	1.95	1.46	50	36	2.54	1.01	0.7	2.46
46R-6, 86–88	1025.93	2.04	1.57	47	31	2.59	0.89		2.03
46R-7, 119–121	1027.76	2.08	1.66	43	27	2.56	0.75		2.95
47R-1, 61–62	1028.61	2.01	1.65	36	23	2.46	0.56	0.5	3.19
47R-3, 80–81	1031.34	2.05	1.55	51	34	2.62	1.04	0.5	2.89
47R-4, 78–80	1032.82	1.97	1.46	51	36	2.45	1.05	3.7	2.28
47R-5, 12–14	1033.52	2.11	1.69	43	26	2.57	0.75	0.9	2.69
48R-1, 81–83	1038.41	1.96	1.53	44	30	2.40	0.78	1.5	2.63
48R-3, 54–56	1041.14							0.6	2.64
48R-5, 31–33	1043.91	1.98	1.54	44	30	2.38[a]	0.79	1.9	2.61
48R-6, 58–60	1045.47	2.35	1.98	38	20	2.84	0.61	0.5	2.89
49R-1, 87–89	1048.17	2.11	1.74	38	23	2.57	0.61	1.1	2.95
49R-2, 107–109	1049.87	1.98	1.54	45	30	2.33[a]	0.82	1.6	2.58
49R-3, 45–75	1050.52							1.5	
49R-4, 27–29	1051.09	1.62[a]	1.15[a]	48[a]	44[a]	1.88[a]	0.93[a]		2.56
50R-1, 80–82	1057.80	2.27	1.90	38	21	2.90	0.61	0.5	2.80
50R-3, 56–58	1060.56	2.09	1.58	51	33	2.73	1.03	4.8	2.37
50R-5, 120–122	1064.12	2.35	1.95	40	21	2.68	0.66	1.5	2.76
50R-6, 126–128	1065.68	2.38	2.11	28	14	2.63	0.38	0.4	3.20
51R-2, 14–16	1067.28	1.81[a]	1.18	64[a]	57[a]	2.41[a]	1.81[a]	2.3	2.29
51R-2, 78–80	1067.92	2.39	2.00	40	20	2.99	0.65		2.22
51R-4, 64–66	1070.78	2.36	2.10	26	13	2.51	0.36	1.1	3.58
51R-5, 61–63	1072.25	2.38	2.10	29	14	2.55	0.40		2.60
51R-6, 93–95	1073.92	2.19	1.75	45	27	2.51	0.83	4.3	3.14
51R-7, 72–74	1075.06	2.25	1.91	34	18	2.64	0.52		2.26
51R-8, 6–8	1075.84	1.98	1.56	42	28	2.38	0.73	1.5	2.63
52R-1, 76–78	1077.16	2.28	2.00	29	15	2.39	0.40	0.6	3.52
52R-1, 108–138	1077.48							0.5	
52R-3, 66–68	1079.94	2.31	2.04	28	14	2.49	0.38	0.4	3.57
52R-5, 40–42	1082.07	2.56[a]	2.01	56[a]	29[a]	2.29[a]	1.29[a]	1.3	3.73
53R-1, 39–42	1086.49	2.31	1.94	38	20	2.91	0.60	1.1	2.78
53R-3, 69–72	1089.66	2.10	1.67	44	27	2.70	0.78	0.6	2.53
53R-CC, 10–12	1091.69	2.06	1.55	52	35	2.54	1.06	3.4	2.43
54R-2, 36–38	1096.44	2.00	1.55	45	30	2.33[a]	0.83	1.4	2.67
54R-4, 31–33	1099.21	2.23	1.89	34	19	2.85	0.51	0.6	2.79
55R-2, 0–30	1105.56							0.5	
55R-2, 134–137	1106.90	2.17	1.77	40	23	2.62	0.66	2.0	1.85
55R-4, 104–107	1109.21	2.33	2.04	30	15	2.58	0.42	0.4	2.18
56R-1, 46–48	1115.46	2.36	2.11	25	12	2.64	0.34		2.44
56R-2, 47–50	1116.97	2.30	2.06	25	12	2.62	0.33		2.43
56R-3, 50–53	1118.50	1.92	1.50	43	30	2.26[a]	0.75		1.99
56R-3, 70–74	1118.70							1.5	
56R-3, 86–89	1118.86	1.90	1.49	41	28	2.30[a]	0.70		2.02
56R-4, 1–4	1119.51	2.23	1.86	37	21	2.71	0.59		2.00
56R-5, 60–62	1121.34	2.44	2.18	26	12	2.65	0.34		2.34
57R-1, 48–50	1125.18	2.01	1.88	13	7	2.93	0.15	2.3	1.93
57R-3, 14–17	1127.84	2.26	1.92	34	18	2.69	0.52	0.5	1.99
58R-1, 37–39	1134.37	2.26	1.97	30	16	2.64	0.42	0.4	2.20
58R-3, 94–97	1137.64	2.02	1.58	45	29	2.47	0.81	1.3	1.86
58R-4, 76–106	1138.96							0.9	
58R-5, 122–124	1140.58	2.21	1.89	32	17	2.60	0.46	0.3	2.13
58R-7, 87–89	1143.20	2.35	2.11	25	12	2.58	0.34	0.4	2.43
59R-1, 44–47	1144.04	2.31	2.08	24	12	2.52	0.31	0.3	2.46
59R-3, 74–77	1147.08	2.31	2.05	26	13	2.60	0.35	1.5	2.29
59R-3, 132–133	1147.66							0.3	

Table 12 (Continued).

Core, section, interval (cm)	Depth (mbsf)	Wet-bulk density (g/cm³)	Dry-bulk density (g/cm³)	Porosity (%)	Water content (%)	Grain density (g/cm³)	Void ratio	Carbonate content (%)	Velocity (km/s)
126-793B-									
59R-5, 72–75	1149.89	2.35	2.10	26	13	2.49	0.34	0.3	2.46
59R-7, 107–109	1152.97	2.37	2.10	27	14	2.58	0.38		
59R-7, 136–138	1153.27							0.3	2.37
60R-1, 102–104	1154.22	2.41	2.16	25	12	2.67	0.33	0.5	3.30
60R-3, 60–62	1156.80	2.31	2.03	28	14	2.43	0.40	0.4	2.98
60R-5, 82–84	1159.83	2.66	2.41	25	11	2.85	0.34	0.3	3.29
60R-7, 29–31	1161.90	2.53	2.31	22	10	2.92	0.28	0.4	3.54
61R-1, 22–24	1163.12	2.33[a]	1.68	66[a]	41[a]	2.22[a]	1.90	0.3	2.97
61R-1, 55–57	1163.45	2.62	2.42	20	9	2.73	0.25		3.65
61R-2, 69–71	1164.93	2.02	1.60	43	27	2.33[a]	0.74		2.69
61R-3, 41–43	1166.06	2.11	1.74	37	22	2.44	0.59	0.8	2.86
61R-4, 28–30	1166.79	2.40	2.07	34	17	2.83	0.52		2.79
62R-1, 45–47	1173.05	2.08	1.66	43	27	2.44	0.77	0.4	2.55
62R-2, 108–110	1174.89	2.24	1.91	34	18	2.55	0.51	0.4	2.78
62R-4, 64–66	1177.14	2.34	2.01	33	17	2.64	0.48	0.3	2.73
63R-1, 74–76	1182.94	2.22	1.84	39	22	2.70	0.65	0.4	2.41
63R-3, 33–35	1185.53	2.42	2.18	24	11	2.61	0.32		3.43
63R-4, 69–71	1187.36	2.26	1.86	40	22	2.63	0.68	0.5	2.64
64R-1, 46–48	1192.36	2.25	1.90	36	19	2.64	0.55	0.5	2.54
64R-3, 81–83	1195.33	2.20	1.81	40	23	2.61	0.66	0.4	2.44
64R-5, 122–124	1198.56	2.32	2.01	31	16	2.53	0.45	0.6	3.04
64R-6, 117–147	1200.01							1.1	
64R-7, 97–99	1201.28	2.58	2.33	25	11	2.68	0.34	6.2	3.44
65R-1, 78–81	1202.28	2.44	2.22	22	10	2.65	0.28		3.48
65R-3, 47–50	1204.89	2.50	2.32	18	8	2.66	0.23		4.23
65R-5, 31–33	1207.65	2.14	1.84	30	17	2.57	0.43		2.68
65R-6, 74–76	1209.58							1.9	
65R-7, 34–37	1210.68	2.12	1.71	42	25	2.44	0.72	0.3	2.51
66R-1, 65–68	1211.75	2.33	2.10	24	12	2.38	0.31	0.2	3.13
66R-3, 81–84	1214.81	2.23	1.92	32	17	2.53	0.46	0.2	2.99
66R-4, 33–36	1215.83	2.22	1.90	33	18	2.53	0.49	0.3	3.08
66R-4, 117–118	1216.67							1.8	
66R-5, 3–6	1216.88	1.75*	1.39	36[a]	26[a]	1.86[a]	0.55[a]		3.03
66R-6, 140–142	1219.69	2.03	1.67	36	23	2.33	0.57	3.1	2.94
67R-1, 97–99	1221.77	2.30	2.01	29	15	2.69	0.41	0.4	2.96
67R-3, 69–71	1224.35	2.46	2.18	29	14	2.84	0.40	1.7	3.14
67R-5, 121–123	1227.82	2.04	1.66	39	24	2.49	0.63	0.4	2.65
67R-6, 59–62	1228.56	2.26	2.07	19	10	2.75	0.24		
68R-1, 115–118	1231.65	2.21	1.83	38	22	2.69	0.62	2.2	2.58
68R-3, 38–40	1233.78	2.49	2.22	27	13	2.68	0.37	0.9	3.29
68R-4, 91–93	1235.67	2.09	1.66	43	27	2.36	0.76	0.8	2.70
68R-5, 26–28	1236.45	2.50	2.23	27	12	2.68	0.37		
68R-6, 26–28	1237.95							0.8	3.13
69R-1, 73–75	1240.93	2.04	1.66	38	24	2.42	0.62	5.0	2.71
69R-3, 73–75	1243.85	2.33	2.08	26	13	2.63	0.35	0.6	3.14
69R-5, 47–49	1246.38	2.04	1.64	40	25	2.39	0.67	6.4	2.69
69R-7, 12–14	1248.99	2.41	2.16	26	12	2.67	0.35	0.5	3.29
70R-1, 93–95	1250.73	2.40	2.14	26	12	2.68	0.35	2.2	3.28
70R-3, 74–76	1253.49	2.36	2.12	24	11	2.58	0.31	1.2	3.30
70R-5, 62–64	1255.93	2.33	1.95	39	20	2.71	0.63	2.9	2.60
70R-7, 0–30	1258.31							0.9	
70R-7, 45–47	1258.76	2.28	1.96	33	17	2.58	0.49	1.1	3.03
71R-1, 94–96	1260.34	2.37	2.10	27	13	2.64	0.37	2.2	3.23
71R-3, 12–14	1262.19	2.27	1.85	43	24	2.74	0.75		2.64
71R-4, 77–79	1264.02	2.02	1.65	37	23	2.36	0.59		2.97
71R-5, 83–85	1265.35								2.95
71R-7, 82–84	1268.10	2.33	2.04	30	15	2.59	0.43	1.0	3.06
72R-1, 60–62	1269.30	2.28	1.93	36	19	2.70	0.55	2.7	2.68
72R-3, 79–81	1272.49	2.02	1.58	44	29	2.36	0.80	0.7	2.70
72R-5, 80–82	1275.50	1.88[a]	1.49	39[a]	27[a]	2.13[a]	0.64[a]	2.7	2.84
72R-7, 12–14	1277.54	2.61	2.37	24	10	2.73	0.32	0.5	3.57
73R-1, 102–104	1279.42	2.29	1.95	35	18	2.63	0.53	1.2	2.91
73R-3, 37–39	1281.53	1.96[a]	1.58	39*	25[a]	2.25[a]	0.63[a]	0.7	3.05
73R-4, 120–150	1283.71							3.1	
73R-5, 56–58	1284.57	2.45	2.17	29	14	2.72	0.40	2.6	3.49
74R-1, 24–28	1288.24	2.34	2.06	28	14	2.57	0.40		3.35
74R-3, 118–121	1292.01	2.32	2.09	23	12	2.38	0.30		3.47
74R-5, 63–66	1294.16	2.47	2.19	28	13	2.60	0.39	2.7	3.26
74R-7, 81–84	1296.83	2.67	2.38	29	12	2.66	0.40	4.9	3.36
75R-1, 75–78	1298.45	2.44	2.16	28	13	2.70	0.38	3.7	3.45
75R-2, 86–89	1300.06	2.38	2.12	26	13	2.64	0.35		3.46
75R-5, 71–73	1304.34	2.41	2.10	31	15	2.70	0.46	5.4	2.84
75R-7, 6–9	1306.69	2.35	2.14	21	10	2.42	0.27	1.1	3.73
76R-1, 70–73	1308.00	2.39	2.18	20	10	2.47	0.26	0.7	3.70
76R-2, 44–47	1309.23	2.38	2.22	16	8	2.40	0.19		4.13

Table 12 (Continued).

Core, section, interval (cm)	Depth (mbsf)	Wet-bulk density (g/cm^3)	Dry-bulk density (g/cm^3)	Porosity (%)	Water content (%)	Grain density (g/cm^3)	Void ratio	Carbonate content (%)	Velocity (km/s)
126-793B-									
76R-3, 71–74	1311.01	2.38	2.20	19	9	2.48	0.23		4.03
76R-5, 6–9	1313.27	2.38	2.20	19	9	2.42	0.23		4.04
76R-5, 104–134	1314.25							0.5	
77R-1, 62–65	1317.62	2.42	2.29	13	6	2.39	0.15	0.9	4.32
77R-3, 120–123	1321.13	2.45	2.28	18	8	2.50	0.21	4.7	3.83
77R-5, 101–104	1323.88	2.41	2.30	11	5	2.54	0.13	0.7	4.40
78R-1, 64–66	1327.34	2.19	1.86	33	18	2.62	0.49	1.7	2.71
78R-3, 64–66	1330.31	2.59	2.46	13	6	2.61	0.15	0.7	4.29
78R-5, 56–59	1332.68	2.39	2.16	24	11	2.60	0.31	2.2	3.13
78R-7, 124–126	1336.12	2.34	2.06	28	14	2.59	0.39	2.0	3.13
79R-1, 63–65	1337.03	2.45	2.24	22	10	2.56	0.28	2.0	3.87
79R-3, 84–85	1339.78	2.35	2.08	27	13	2.52	0.36		3.57
79R-5, 43–44	1342.15	2.17	1.79	39	22	2.58	0.63	4.5	2.45
79R-6, 60–61	1343.77	2.38	2.28	10	4	2.56	0.11	1.8	3.88
80R-1, 95–97	1346.95	2.30	2.09	21	11	2.43	0.27	1.7	3.46
80R-3, 86–88	1349.86	2.20	1.90	31	17	2.40	0.45	2.0	3.25
80R-5, 0–30	1351.63							0.8	
80R-5, 72–74	1352.35	2.35	2.06	30	15	2.63	0.42	6.7	2.80
80R-7, 4–6	1354.49	2.36	2.05	32	16	2.68	0.48		2.84
81R-2, 126–128	1358.39	2.45	2.09	36	18	2.77	0.57		2.91
81R-3, 40–43	1359.03	2.27	1.92	36	19	2.62	0.55		2.87
81R-5, 43–46	1361.74	2.42	2.10	33	16	2.68	0.49		2.99
81R-5, 127–129	1362.58	2.32	2.01	32	17	2.59	0.47		2.94
81R-6, 37–39	1363.12	2.30	1.92	39	21	2.46	0.63		2.88
81R-6, 69–71	1363.44	2.27	1.95	33	18	2.67	0.49		2.88
82R-1, 75–77	1366.05	2.33	2.04	30	15	2.60	0.42		2.93
82R-3, 70–72	1368.80	2.30	2.06	24	12	2.69	0.32		3.12
82R-5, 85–87	1371.67	2.37	2.12	25	12	2.58	0.34		3.14
82R-6, 61–63	1372.93	2.21	2.02	20	10	2.50	0.25		3.60
82R-7, 49–51	1374.18	2.40	2.14	26	13	2.58	0.35		3.43
82R-CC, 20–22	1374.77	2.31	2.07	24	12	2.52	0.32		3.21
83R-1, 47–49	1375.37	2.89	2.40	51	22	2.49	1.02		2.70
83R-1, 48–50	1375.38	2.37	2.04	33	17	2.78	0.50		
83R-1, 98–100	1375.88	2.25	1.82	43	24	2.76	0.76		2.78
83R-2, 27–29	1376.67	2.45	2.16	29	14	2.33*	0.41		2.89
83R-2, 39–41	1376.79	2.51	2.24	27	12	2.53	0.37		2.91
84R-1, 21–23	1384.71	2.32	2.03	29	15	2.66	0.41		3.03
84R-2, 98–100	1386.98	2.48	2.25	23	11	2.58	0.30		3.11
85R-1, 24–27	1394.44	2.46	2.22	24	11	2.61	0.32		3.26
85R-1, 63–65	1394.93								3.53
85R-2, 34–36	1396.04								3.35
85R-2, 125–128	1396.95	2.55	2.27	29	13	2.78	0.40		2.96
86R-1, 29–32	1404.19	2.25	1.93	33	18	2.58	0.49		3.10
86R-2, 8–10	1405.48	2.61	2.42	19	8	2.78	0.23		4.30
87R-1, 84–87	1414.44	2.44	2.14	30	15	2.74	0.44		3.06
87R-2, 107–110	1416.16	2.42	2.13	29	14	2.73	0.41		3.30
87R-4, 82–84	1418.03	2.75	2.59	17	7	2.83	0.21		4.47
88R-1, 78–81	1423.68	2.43	2.14	30	14	2.79	0.42		3.27
88R-1, 121–124	1424.11								3.31
88R-2, 21–23	1424.53	2.42	2.11	31	15	2.73	0.45		3.18
89R-1, 34–36	1431.74	2.40	2.09	32	16	2.60	0.46		3.05
89R-3, 48–50	1434.80	2.43	2.12	31	15	2.67	0.45		3.08
89R-4, 25–27	1436.04	2.58	2.36	23	10	2.79	0.29		3.82
92R-1, 46–48	1460.56	2.57	2.33	25	11	2.95	0.33		3.75
92R-2, 137–139	1462.97	2.80	2.62	18	7	3.09	0.23		4.09
92R-3, 6–8	1463.13	2.84		18	7	3.02	0.23		4.04
93R-1, 137–140	1471.07	2.40		32	16	2.81	0.48		4.04
93R-2, 95–98	1472.15	2.63		24	10	3.13	0.31		3.57
94R-1, 54–57	1479.94	2.30		29	15	2.62	0.42		3.83
94R-2, 82–85	1481.54	2.56		19	8	2.62	0.23		3.47
95R-1, 78–80	1489.78	2.31		36	19	2.69	0.56		3.05
95R-1, 138–140	1490.38	2.40		32	16	2.64	0.47		3.10
95R-2, 64–66	1491.10	2.49		29	14	2.81	0.41		3.04
96R-1, 35–37	1499.05	2.52		53	28	2.57	1.14		3.32
96R-CC, 13–15	1500.06	2.21		38	22	2.63	0.62		3.15
97R-1, 89–93	1509.19	2.61		23	10	2.90	0.29		3.74
98R-1, 87–89	1518.87	2.37		31	16	2.55	0.46		3.41
98R-2, 67–69	1520.02	2.45		28	13	2.64	0.39		3.85
98R-2, 143–146	1520.78	2.37		27	13	2.61	0.36		3.41
98R-3, 73–75	1521.55	2.66		62	31	2.51	1.63		3.76
98R-4, 10–13	1522.33	2.34		26	13	2.55	0.35		3.51
98R-4, 44–46	1522.67	2.57		23	10	2.66	0.30		3.85
99R-1, 13–16	1527.73	2.44		25	12	2.57	0.34		3.96
99R-1, 88–91	1528.48	2.67		24	10	2.98	0.32		3.83
100R-1, 7–10	1537.37	2.49		24	11	2.50	0.32		3.61

Table 12 (Continued).

Core, section, interval (cm)	Depth (mbsf)	Wet-bulk density (g/cm^3)	Dry-bulk density (g/cm^3)	Porosity (%)	Water content (%)	Grain density (g/cm^3)	Void ratio	Carbonate content (%)	Velocity (km/s)
126-793B-									
100R-CC, 12–16	1539.24	2.57		27	12	2.90	0.37		3.62
101R-1, 44–48	1547.34	2.33		30	15	2.50	0.43		3.35
102R-1, 79–84	1557.39	2.55		25	11	2.88	0.33		3.37
102R-2, 27–30	1558.25	2.42		29	14	2.63	0.40		3.55
102R-CC, 6–9	1558.47	2.44		29	14	2.60	0.41		3.59
103R-1, 26–28	1566.56	2.36		35	18	2.57	0.54		3.50
103R-2, 43–45	1568.12	2.35		30	15	2.58	0.42		3.24
103R-3, 37–39	1569.46	2.37		66	40	3.68[a]	1.93		3.94
104R-1, 47–50	1576.37	2.67		25	11	2.93	0.34		3.45
104R-2, 26–28	1577.66	2.57		27	12	3.04	0.37		3.62
104R-3, 41–43	1579.21	3.40		29	9	3.64	0.40		3.32
104R-4, 35–37	1580.45	2.53		27	12	2.95	0.37		3.28
105R-1, 87–89	1586.37	2.68		17	7	2.78	0.21		4.30
105R-1, 123–125	1586.73	2.76		22	9	2.66	0.27		3.80
105R-3, 82–83	1589.15	2.67		28	12	3.00	0.39		3.39
105R-3, 115–117	1589.48	2.67		19	8	2.75	0.23		4.00
106R-1, 69–71	1595.89	2.71		20	8	2.86	0.25		4.24
106R-2, 24–26	1596.92	2.65		26	11	2.71	0.35		3.86
107R-1, 59–62	1605.39	2.54		27	12	2.77	0.37		3.52
107R-2, 38–40	1606.68	2.39		26	12	2.65	0.35		3.58
107R-3, 100–102	1608.64	2.45		29	14	2.56	0.41		3.56
107R-4, 128–132	1610.42	2.72		19	8	2.99	0.24		3.74
108R-1, 121–124	1615.61	2.48		28	13	2.69	0.38		3.90
108R-2, 115–117	1616.97	2.61		22	10	2.96	0.29		4.04
109R-1, 113–116	1625.23	2.45		28	13	2.68	0.38		3.55
109R-2, 144–147	1626.93	2.79		20	8	2.88	0.24		3.88
110R-1, 56–58	1634.36	2.64		24	10	2.90	0.32		3.73
110R-2, 39–41	1635.56	2.69		20	8	2.97	0.25		3.93
110R-4, 43–45	1638.23	2.71		21	9	2.96	0.26		3.81
111R-1, 23–25	1643.63	2.56		23	10	2.89	0.30		3.76
111R-2, 99–101	1645.89	2.92		19	7	2.94	0.24		3.97
112R-1, 25–27	1653.35	2.68		22	9	2.94	0.28		3.91
112R-2, 85–87	1655.45	2.63		23	10	2.90	0.31		3.81
113R-1, 100–102	1663.70	2.45		28	14	2.76	0.40		3.53
113R-4, 18–21	1667.21	2.90		13	5	2.77	0.15		4.57
114R-1, 40–42	1672.80	2.43		29	14	2.80	0.41		3.55
114R-4, 87–89	1677.57	2.43		29	14	2.76	0.40		3.66

[a] Data of uncertain quality.

eral trends were noted despite the wide sample spacing and paucity of data. The most obvious aspect of the shear strength curve is the peak at 40 mbsf, which is defined by four data points, and includes a maximum of 109 kPa. These high strength values do not correlate with either porosity or water content values, which are variable and display no consistent trends over this interval. The high strengths may be associated with intervals of interbedded nannofossil silty clays and nannofossil-rich silty clays.

A similar lithology (see "Lithostratigraphy and Accumulation Rates" section, this chapter) is reported at 90 mbsf where a secondary strength peak is located. Low shear strength values between 70 and 80 mbsf are associated with low $CaCO_3$ percentages. However, the primary cause of the low strengths between 70 and 80 mbsf is probably drilling disturbance (see "Lithostratigraphy and Accumulation Rates" section, this chapter).

Hole 793B

No vane shear strength measurements were made in Hole 793B because of the lithified state of the sediments.

Sonic Velocity

Hole 793A

Sonic velocity measurements were performed on discrete samples from Hole 793A using the HF method (Table 12, Fig. 66). In addition, all cores from Hole 793A were passed through the MST to obtain *P*-wave velocity data (Fig. 66). Although HF and MST methods exhibit the same general trends, the MST velocity values are higher. From the seafloor to 60 mbsf, HF velocity data remain fairly constant (~1.53–1.55 km/s; average = 1.54 km/s) and show little (if any) change across the Subunit IA/IB boundary. We observed a distinct downward increase (from 1.58 to 1.65 km/s; average = 1.60 km/s) from 70 mbsf to the bottom of Hole 793A.

Hole 793B

Sonic velocity measurements were performed on discrete samples from Holes 793B using the HF method (Fig. 63, Table 12). The first rocks recovered in Hole 793B, the Unit II diabase (Core 126-793B-1R; 586.5–591.0 mbsf), have the highest velocity values of the entire cored section at this site, averaging 4.88 km/s (range = 4.63–5.14 km/s).

The Unit II/III boundary is characterized by a decrease in velocity of more than 2.5 km/s. Velocity data exhibit the least variability (range = 1.85–2.33 km/s; average = 2.01 km/s) in Unit III (Cores 126-793B-2R through Section -16R-5; 591.0–735.7 mbsf), and do not show any significant downward trends. Velocity values across the Unit III/IV boundary and within Unit IV are fairly constant. The average velocity in Unit IV is 2.18 km/s, with little overall variation (range = 1.92–2.14 km/s).

At the Unit IV/V boundary (759.0 mbsf), velocity values increase by an average of 0.5 km/s. In contrast to Unit IV, Unit V

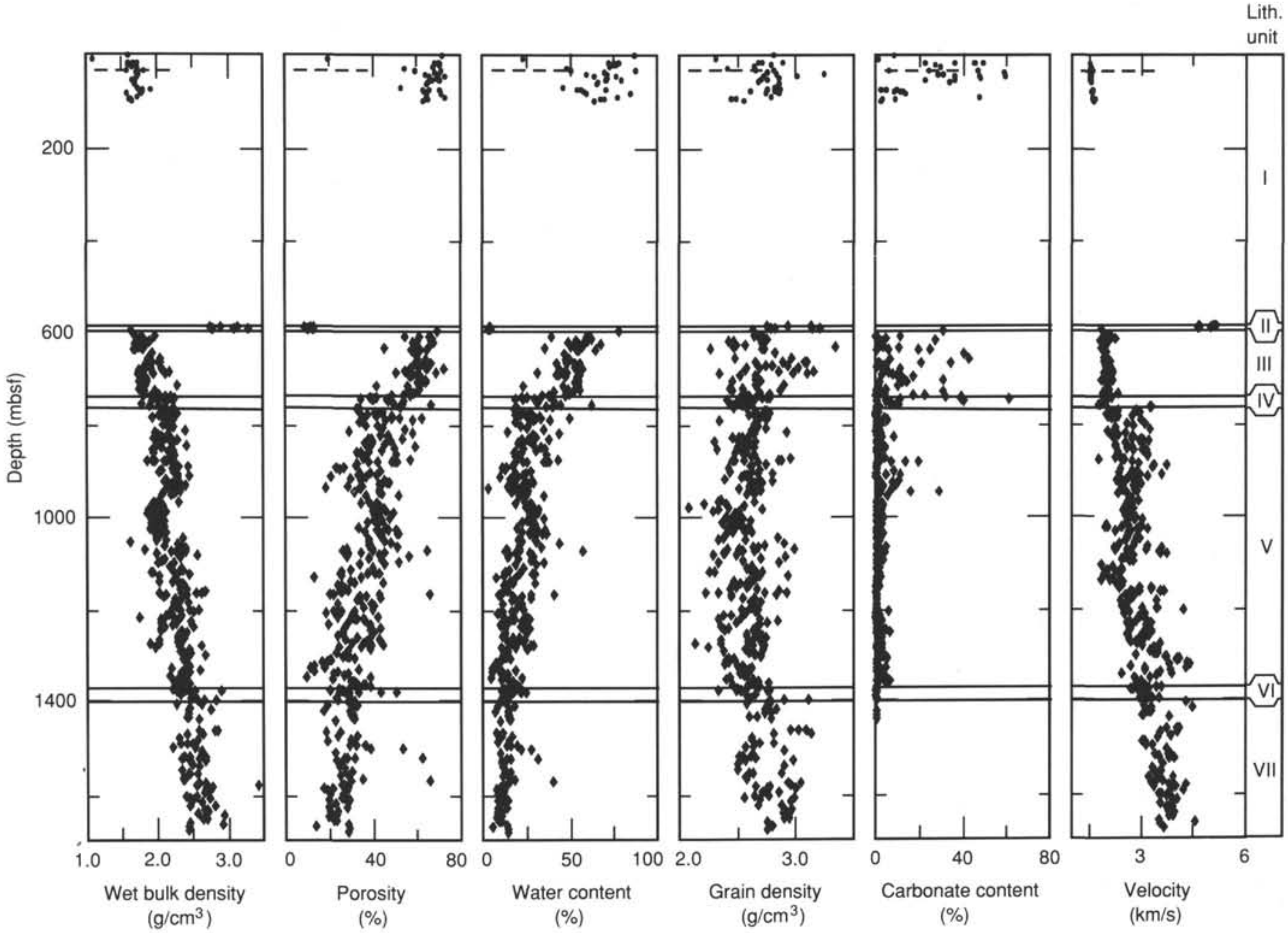

Figure 63. Physical properties, Holes 793A (circles) and 793B (diamonds). Horizontal solid lines indicate lithologic units. The dashed line indicates the Subunit IA/IB contact.

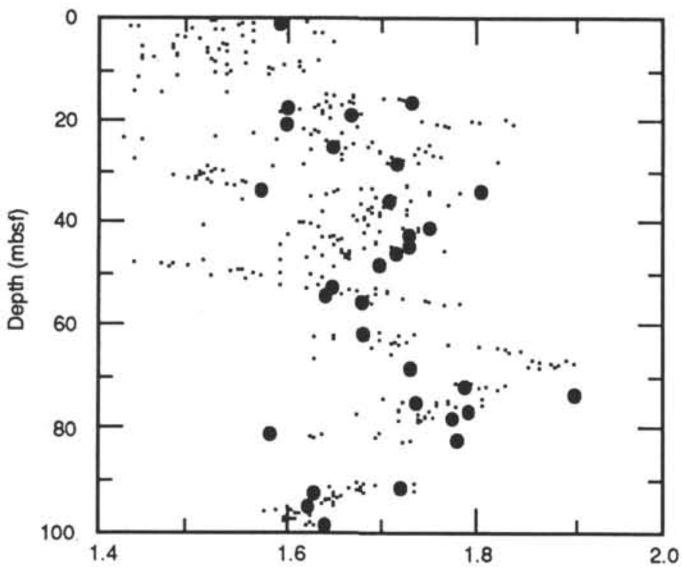

Figure 64. Comparison of gravimetric (large dots) and GRAPE wet-bulk density (small dots) for Hole 793A.

Table 13. Shear strength data from Site 793.

Core, section, interval (cm)	Depth (mbsf)	Shear strength (kPa)
126-793A-		
3H-1, 119	14.69	40.6
3H-2, 129	16.29	38.0
3H-3, 82	17.32	48.3
3H-4, 64	18.64	53.2
5H-4, 128	36.89	79.0
5H-7, 112	41.23	109.1
6H-1, 83	42.83	75.3
6H-3, 119	46.19	63.9
7H-1, 125	52.85	40.8
7H-2, 120	54.30	42.9
7H-3, 98	55.58	51.3
9H-3, 110	75.00	27.3
9H-5, 79	77.69	17.0
10H-2, 139	82.30	40.1
11H-1, 80	90.90	70.9
11H-2, 90	92.50	12.1

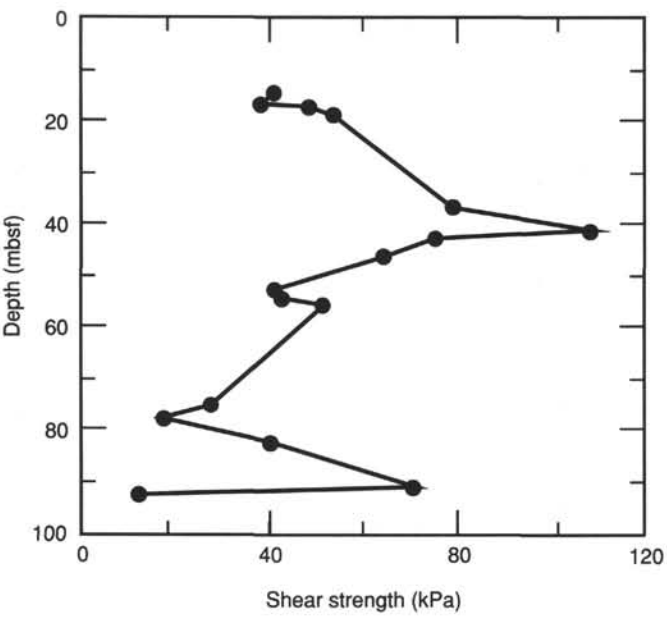

Figure 65. Plot of shear strength vs. depth for Hole 793A.

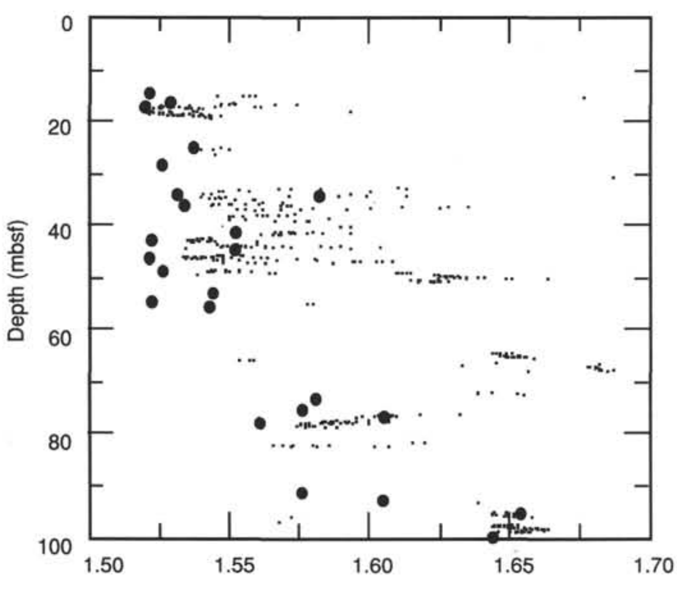

Figure 66. Comparison of sonic velocity determined by Hamilton Frame (HF; large circles) and multisensor track (MST; small dots) methods for Hole 793A.

is characterized by (1) rapidly fluctuating velocity values (total range >2.0 km/s); (2) a downward increase in velocity; (3) a distinct velocity minimum (1107–1150 mbsf); and (4) an average velocity of 2.81 km/s. We observed fluctuations of over 1.0 km/s between samples, which are related to the rapidly changing sediment types present in this unit (turbidites, debris flows; see "Lithostratigraphy and Accumulation Rates" section, this chapter). The downward velocity increase in this unit is illustrated by comparing the average velocity values in the upper part of Unit V (~759–1107 mbsf), which are 2.67 km/s, and those in the lower part of this unit (~1150–1373), which are 3.14 km/s. In the middle part of Unit V, a velocity minimum (average = 2.17 km/s) exists at 1107–1150 mbsf. This minimum has a velocity difference of 0.5 km/s with the overlying sediments and >1.0 km/s with those below.

Velocity values generally increase from 1200 to 1700 mbsf, but no significant increase marks the Unit VI/VII boundary, where we encountered igneous rocks. Within the igneous section, velocity data increase downward and are quite variable. The wide range of values (3.05–4.57 km/s) is likely related to alteration, changes in the relative proportion of clasts vs. matrix in the hyaloclastites, and the presence of interlayered high-velocity andesite flows and pillows. The uppermost part of the unit (1403–1440 mbsf) has an average velocity of 3.41 km/s, whereas the average is 3.84 km/s in the lowermost part (1560–1682 mbsf). Velocity values within Unit VI show no significant difference from the lower part of Unit V. Velocity values in this unit average 3.10 km/s (range = 2.78–3.55 km/s).

Thermal Conductivity

Hole 792A

Thermal conductivity measurements of samples from Hole 793A are shown in Figure 67 (Table 14). Subunit IA thermal conductivity values increase downward from 0.944 to 1.103 W/m · K (average = 1.007 W/m · K). Thermal conductivity values in Subunit IB decrease downward from 1.197 to ~0.900 (average 1.038 W/m · K).

Hole 792B

No thermal conductivity measurements were made on Hole 793B.

DOWNHOLE MEASUREMENTS

The drill pipe was pulled out of the hole on 14 June 1989, and the bit was removed in preparation for downhole measurements. The hole was reentered on 15 June, and the first downhole sensor was rigged up. Because the density tool failed to operate correctly at the surface, a reduced combination of geophysical sensors was deployed. Consequently, the first run consisted of resistivity, velocity, natural gamma, and temperature sensors. The assembly ran into an obstruction at 727.0 mbsf, and the short section located between that depth and the casing shoe (568.0 mbsf) was

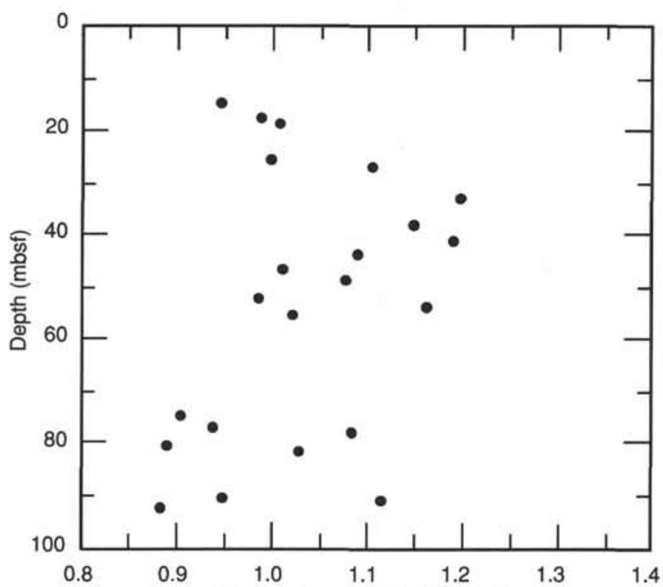

Figure 67. Plot of thermal conductivity vs. depth from Site 793.

Table 14. Thermal conductivity data from Site 793.

Core, section, interval (cm)	Depth (mbsf)	Thermal conductivity (W/m · K)
126-793A-		
1H-1, 12	0.12	0.738[a]
1H-3, 60	3.60	0.694[a]
3H-1, 119	14.69	0.944
3H-3, 107	17.57	0.986
3H-4, 55	18.55	1.006
4H-2, 92	25.42	0.997
4H-3, 108	27.08	1.103
5H-1, 36	32.86	1.197
5H-5, 82	37.93	1.148
5H-7, 106	41.17	1.191
6H-2, 41	43.91	1.088
6H-4, 12	46.62	1.009
6H-5, 55	48.55	1.075
7H-1, 67	52.27	0.983
7H-2, 75	53.85	1.161
7H-3, 71	55.31	1.019
9H-3, 44	74.34	0.902
9H-5, 24	77.14	0.937
9H-5, 104	77.94	1.081
10H-1, 22	80.72	0.887
10H-2, 84	81.75	1.027
11H-1, 29	90.39	0.945
11H-1, 78	90.88	1.114
11H-2, 35	91.95	0.881

[a] Data of uncertain quality.

logged. The drill pipe was lowered to clear the borehole, and the bit was set below the obstruction at 774.0 mbsf. The same combination of sensors encountered a second bridge at 965.0 mbsf. After logging this 191.0-m-long interval, the previous operation was repeated and the pipe set below the bridge at 1034.0 mbsf. The third run of the geophysical assembly was more successful, as the tool stopped at 1580 mbsf, allowing us to record data over a 546.0-m-long interval. Because this third interval was the longest open section of the borehole in which data could be recorded, we decided to keep the pipe at the depth of 1034.0 mbsf and to proceed with the rest of the measurements.

The second logging assembly consisted of the FMS, natural gamma, and temperature sensors. A depth of only 1539.0 mbsf was reached because the hole began filling up with debris as a result of clearing the two first bridges.

The geochemical (GLT), natural gamma (NGT), and temperature sensors were deployed as the third combination. The interval from 1532.0 to 1034.0 mbsf was logged in the open hole, and data were recorded through the drill pipe up to the casing shoe (568.0 mbsf). At this point we decided to run a reduced vertical seismic profile (VSP) because of time constraints. Poor clamping of the downhole sensor in the hole precluded the recording of good data, reducing the final dataset to only a few good shots at five discrete levels. The last run in Hole 793B consisted of the FMS, natural gamma, and temperature sensors deployed in the upper part of the open hole, from 762.0 mbsf to the casing shoe (568.0 mbsf), after pulling the drill pipe into the casing.

In the upper interval logged with the FMS (762.0–768.0 mbsf), the borehole was often measured to be larger than 15.5 in. in diameter. In the lower interval, the hole is generally cylindrical to slightly elliptical, with an average diameter of 12.0 in. Near the sediment/basement contact, the hole is caved and larger than 15.5 in. The deviation of the borehole axis from vertical is approximately 2.0°. The borehole conditions were favorable to downhole experiments because of the lithified nature of the sediments. As a consequence, the data recorded in Hole 793B are of excellent quality. The sampling distance of 2.52 mm for FMS data is the smallest of any presently available downhole sensor. Besides VSP checkshots, all the other records presented in this report have been sampled with a 0.152-m digitization interval. A detailed description of each of the sensors and measurement principles is provided in the "Explanatory Notes" chapter, this volume. Summary log figures appear as Figures 68 and 69. A summary of downhole measurements operations appears in Table 15.

Runs 1, 2, and 3

The first three runs (resistivity, sonic, natural gamma, and temperature) in Hole 793B consisted of a combination of two induction resistivity sensors (with deep and shallow radii of investigation for the deep-phasor induction measurement [IDPH] and the medium-phasor induction measurement [IMPH], respectively), a spherically focussed resistivity sensor (SFL), the long-spacing sonic sensor (LSS), a spectral natural gamma sensor (NGT), and the Lamont-Doherty Geological Observatory temperature tool (TLT). These last two sensors were included in each of the logging runs (the NGT for the purpose of depth correlation) and are discussed separately at the end of this section.

The SFL calibration sequence was found to be in error for Runs 1 and 2. Prior to Run 3, the cartridge of the resistivity sonde was changed and the problem disappeared. As a consequence, the SFL profiles provided for Runs 1 and 2 were normalized to the induction logs and should not be considered quantitative. They were kept because of the better vertical resolution of the SFL over the induction measurements. The resistivity data are otherwise of excellent quality, outlining, for example, numerous upward-fining sequences. The transition from sediments to basement is characterized at 1408.0 mbsf by the lowest resistivity value recorded in the lower part of the basement; this may correlate with a fault.

The main characteristic of the sonic data during acquisition was the high noise level that interfered with the signal from the formation. This noise is primarily the result of the absence of adequate centralization of the sonic tool, a consequence of the small diameter of the drill pipe, which does not allow for the use of centralizers. This lack of centralization resulted in asymmetrical arrivals at the receivers and "road-noise" caused by occasional direct contact between the tool and the formation. The final velocity profile was computed choosing mostly three of the four measured transit times (LTT1, LTT2, LTT3, and LTT4; see discussion of Site 645, Shipboard Scientific Party, 1987, for further details).

Runs 4 and 7

Runs 4 and 7 collected FMS images and natural gamma-ray and temperature data. The four continuous FMS images, which spanned the intervals 1539.0 to 1034.0 mbsf and 762.0 to 568 mbsf each covered about 10% of the internal surface of the borehole; the images will be produced after shore-based analysis. Shipboard image analysis showed the data to be of excellent quality. Features <1 cm in thickness are evident in the FMS results, and numerous turbidite sequences are visible.

The measurements pertaining to hole shape and direction (including two orthogonal measurements of drill hole diameter) were recorded over the same intervals. In basement, below the fault zone located at 1408.0 mbsf, the ellipticity of the drillhole tends to align in a N065°E direction. This constrains the maximum horizontal stress direction in the basement of Hole 793B to N155°E, significantly different from that observed in Hole 792E (N110°E).

Run 5

The geochemical data recorded during the fifth run (geochemical combination, natural gamma, and temperature) are of

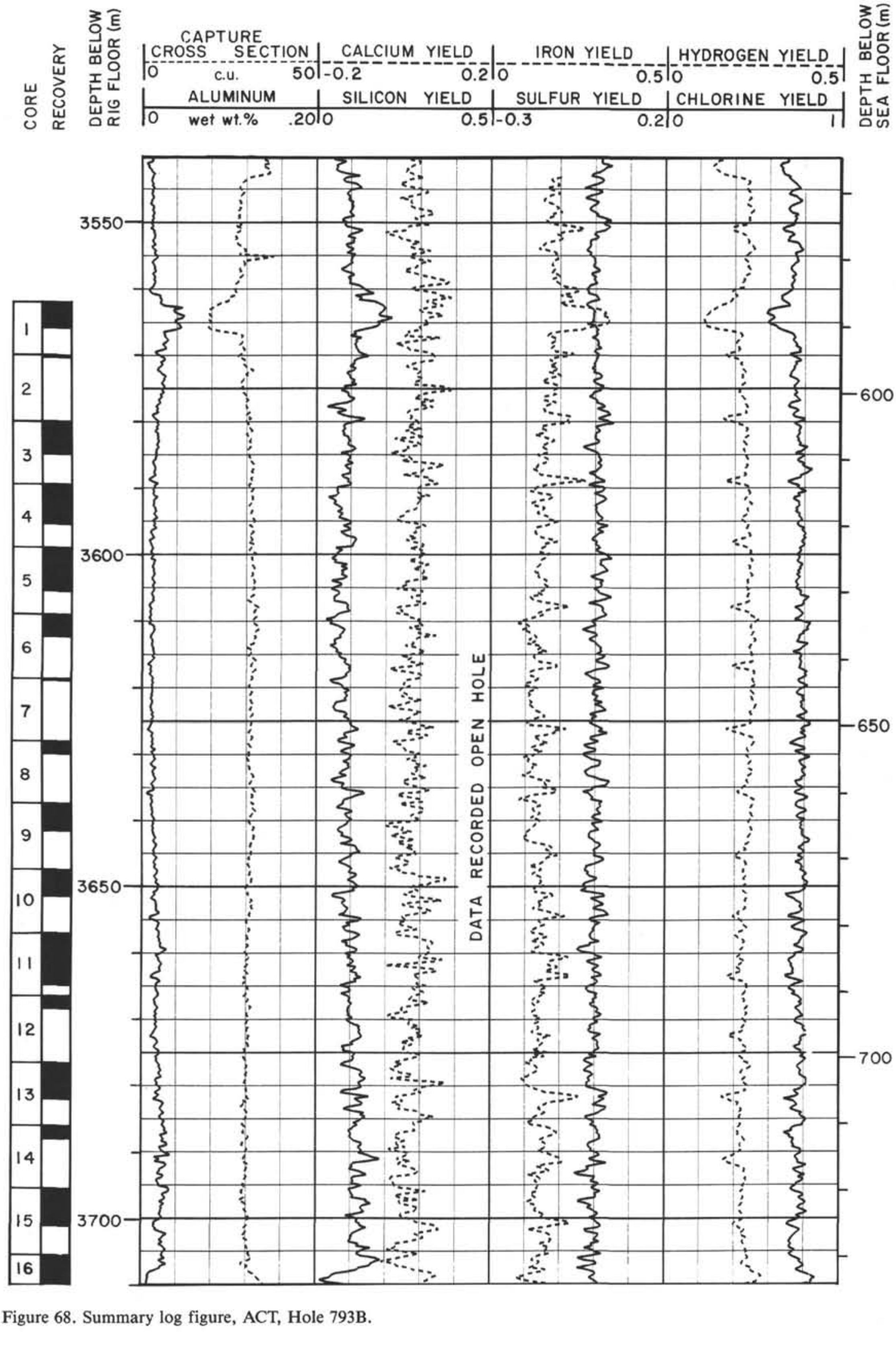

Figure 68. Summary log figure, ACT, Hole 793B.

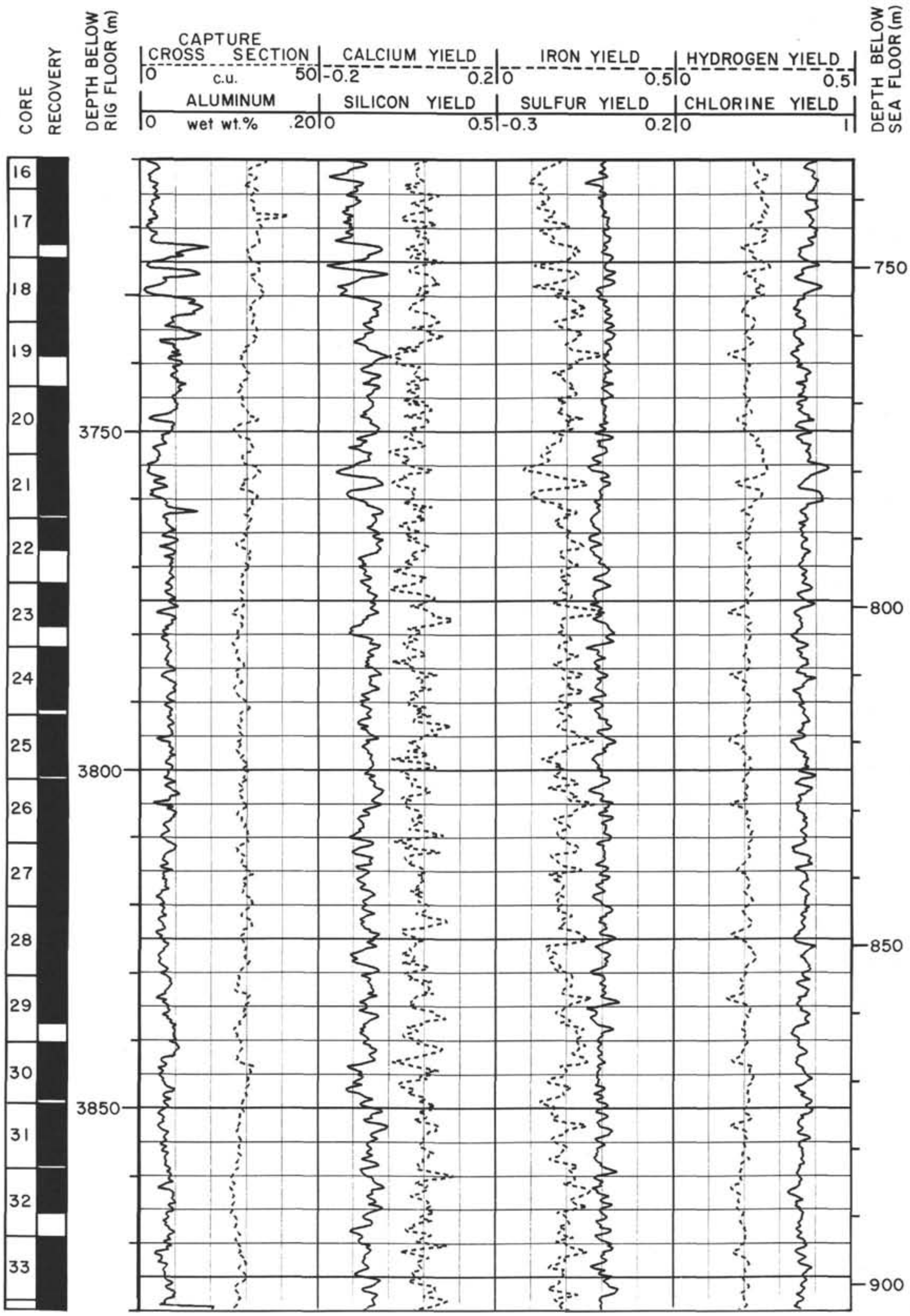

Figure 68 (continued).

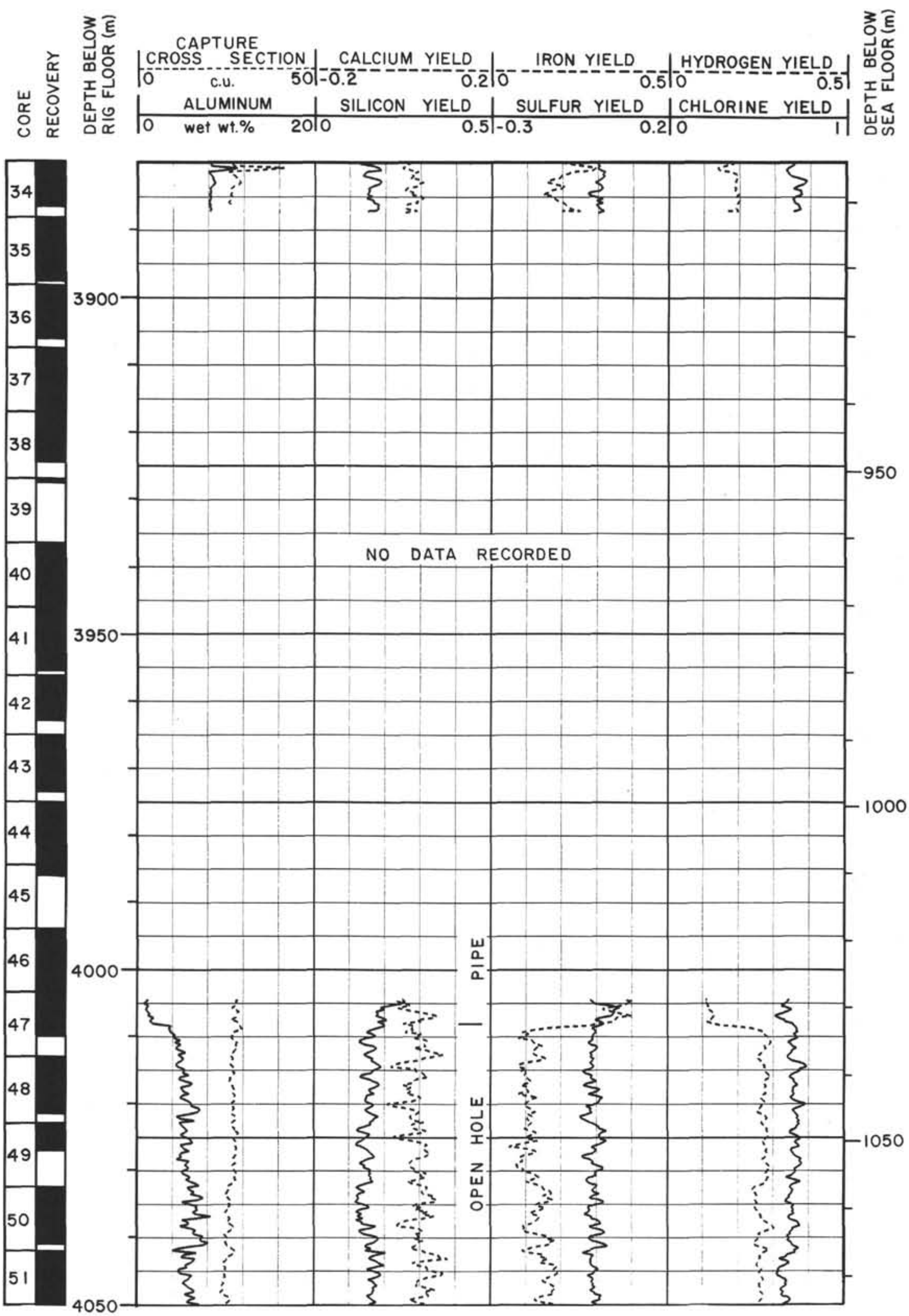

Figure 68 (continued).

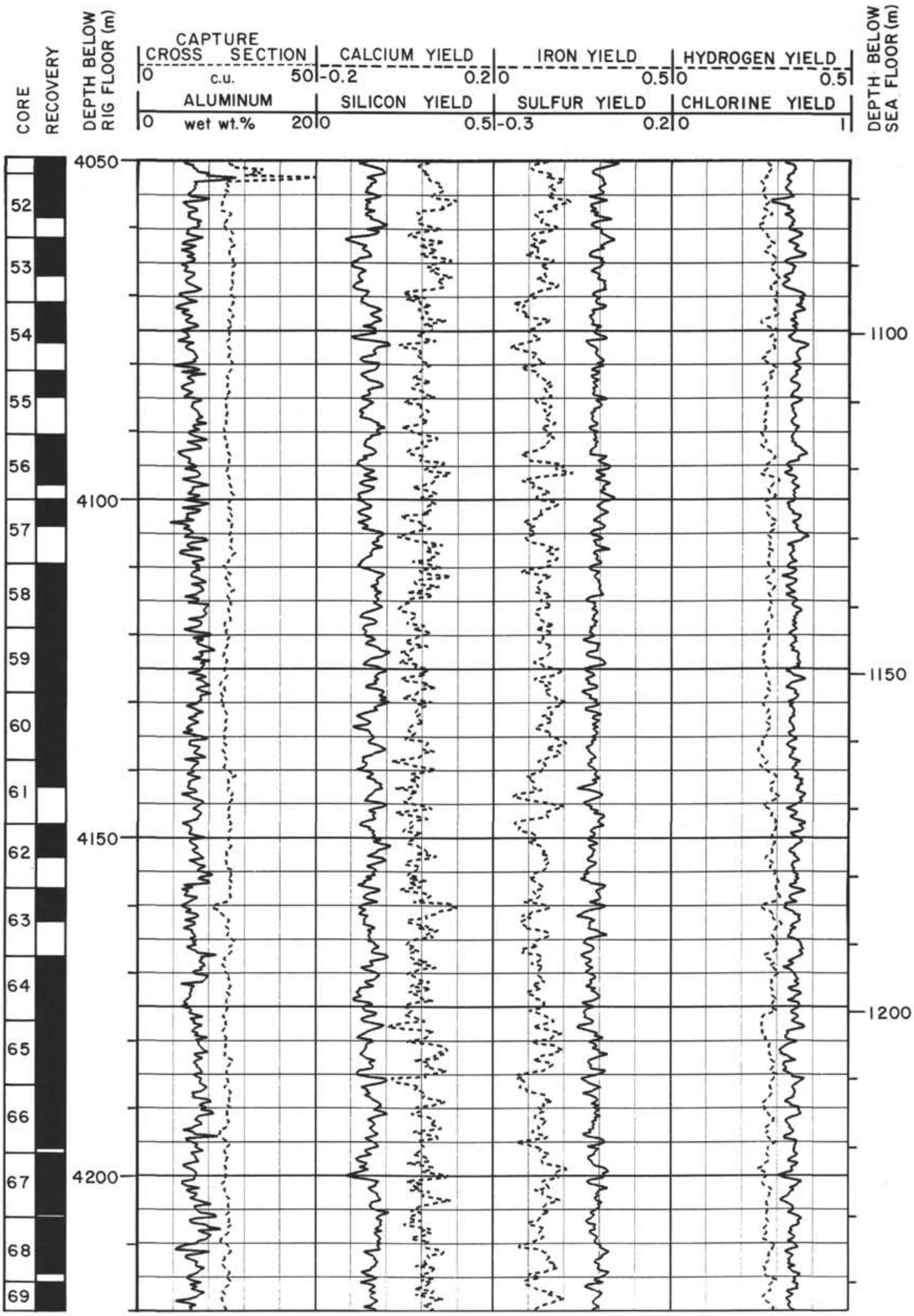

Figure 68 (continued).

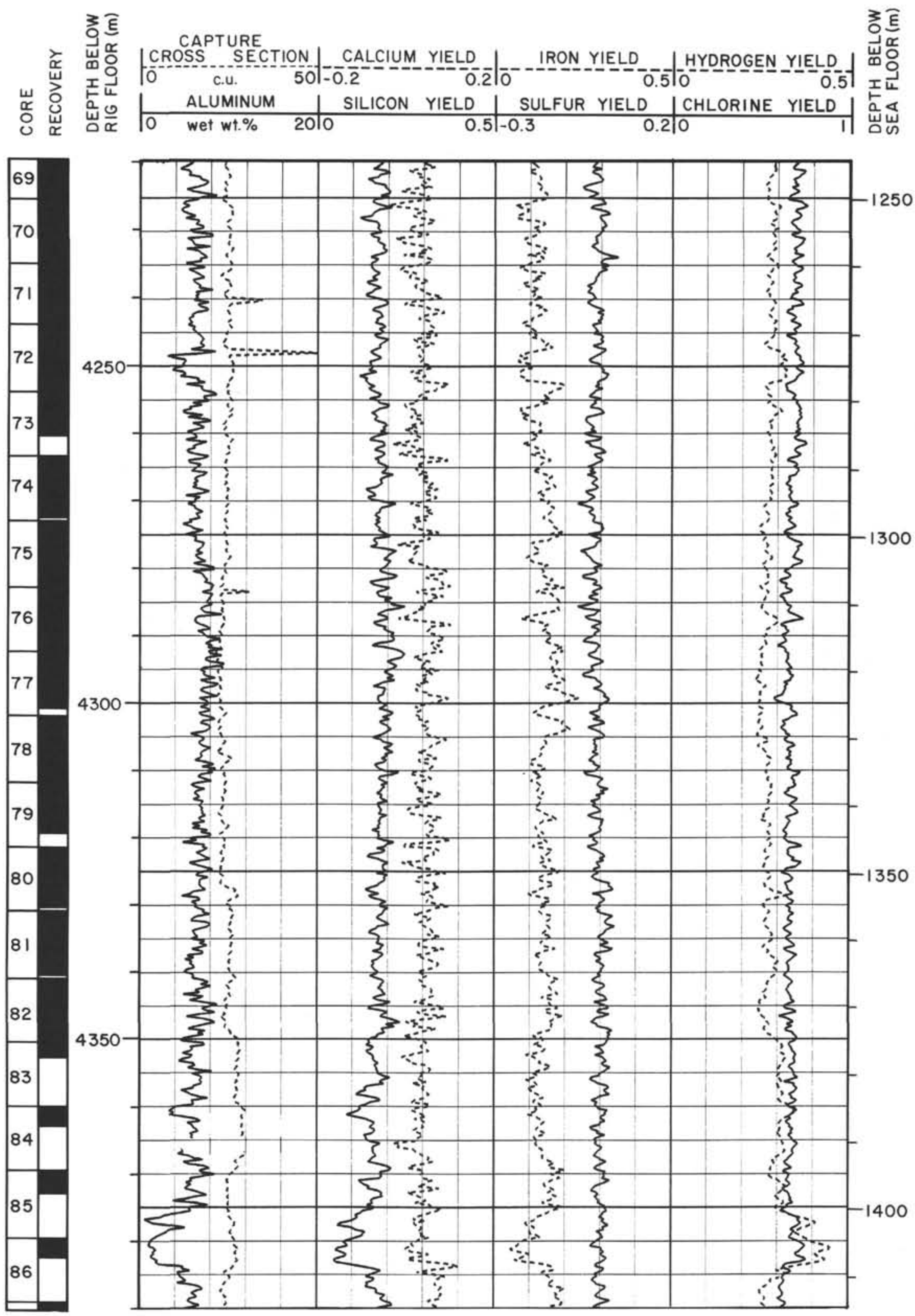

Figure 68 (continued).

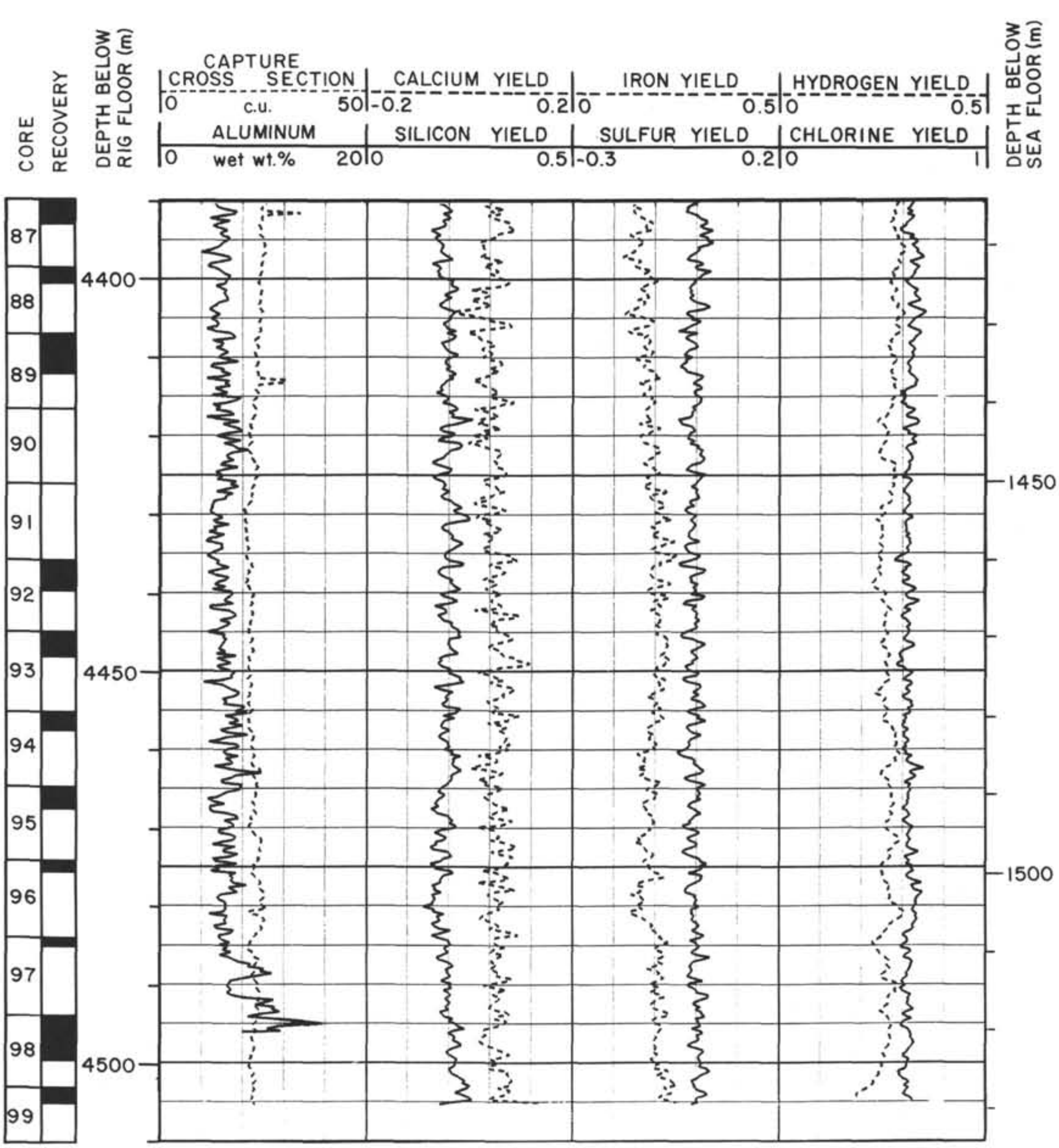

Figure 68 (continued).

excellent quality. The data were recorded over the entire length of the non-cased drillhole, both in the open hole for the lower section (from 1532.2 to 1034.0 mbsf), and in the pipe (from 1034.0 to 568.0 mbsf).

Run 6

The primary objectives of the vertical seismic experiment in Hole 793B were to enhance velocity analyses, identify and locate primary reflectors, correlate the lithostratigraphy with identified reflectors, and tie the surface multichannel seismics to well logs for regional-scale correlations. The data acquisition began near the bottom of the hole (1530 mbsf, 4505 mbsl).

Data Acquisition

The sound source used for the Hole 793B VSP experiment was the *JOIDES Resolution*'s large-volume (400 in.^{3}/16.0 L), high-pressure (2000 psi/140 bar) water gun (SSI H400). The gun was suspended 15 mbsl from a buoy, tethered from the drillship's aft port crane boom about 24 m abeam. The downhole seismic signals were received by a Schlumberger Well Seismic Tool (WST) single vertical component seismometer. The seismometer has four, series-connected, 10-Hz F_0 geophones (Geospace Model HS-1) mounted at its base. The water-gun acoustic signals were also detected by a separate calibrated hydrophone suspended directly from the crane boom at a depth 3 m below the water gun. This hydrophone configuration provided a stable, zero-time reference relative to the seafloor, allowing real-time summing of the seismic records observed for the several shots fired at each seismometer clamping level.

Unfortunately, repeated clamping problems were encountered because the tool slid downhole when the cable was slacked to allow for good coupling to the borehole wall. Only five acceptable shots were recorded at an average depth of 1300 mbsf. They may eventually provide reliable transit-time data to calibrate surface multichannel data. Transit time may also be recovered from six other noisy shots recorded at approximately the same depth.

Water-gun-generated signals received by the WST borehole seismometer are preamplified downhole, transmitted up the logging cable, and digitally recorded along the hydrophone signals by the PDP-11 minicomputer and A/D converter of the Schlumberger CSU logging data acquisition system. Timing information was logged with millisecond accuracy. First-break transit

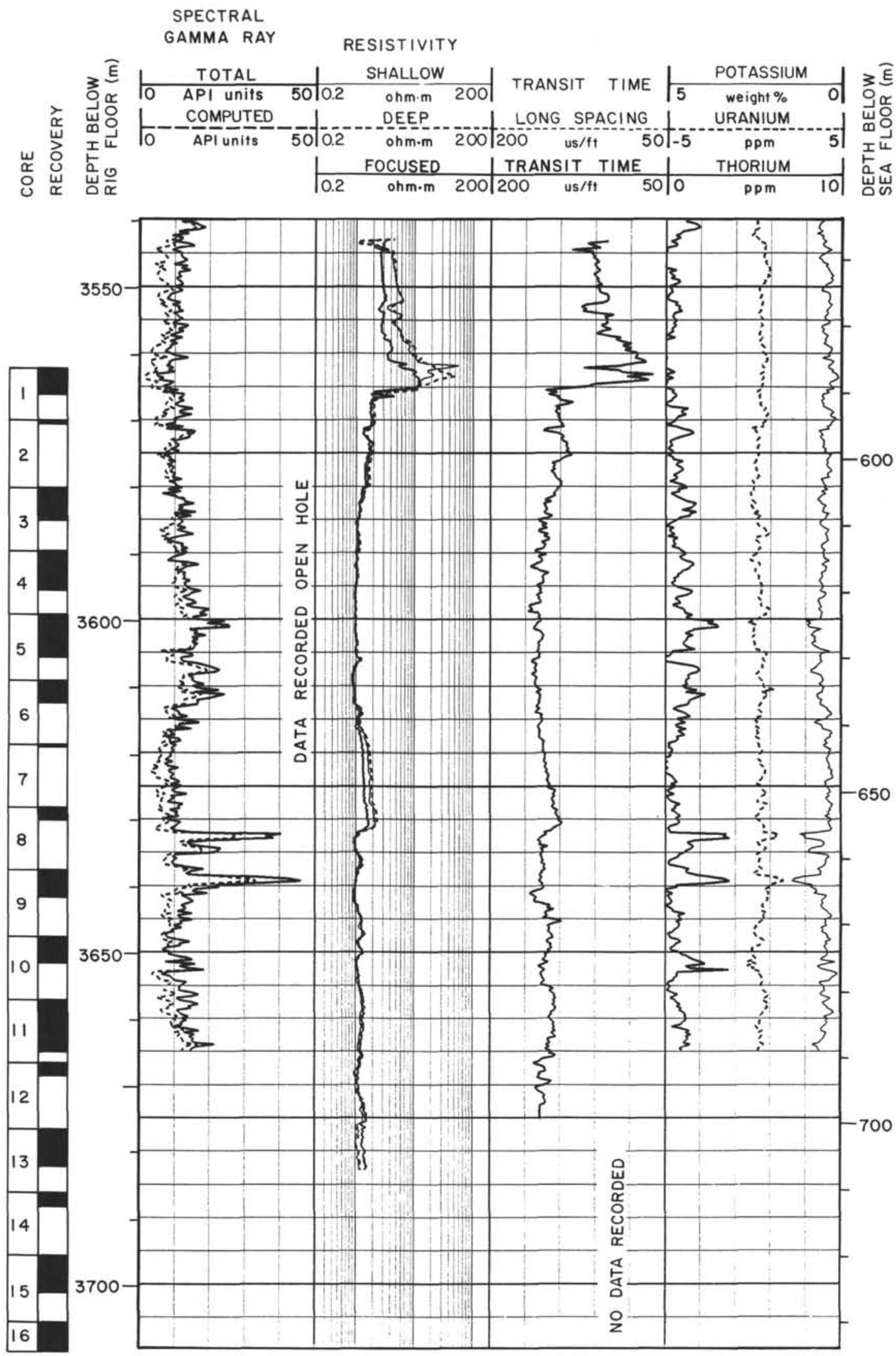

Figure 69. Summary log figure, DIT, Hole 793B.

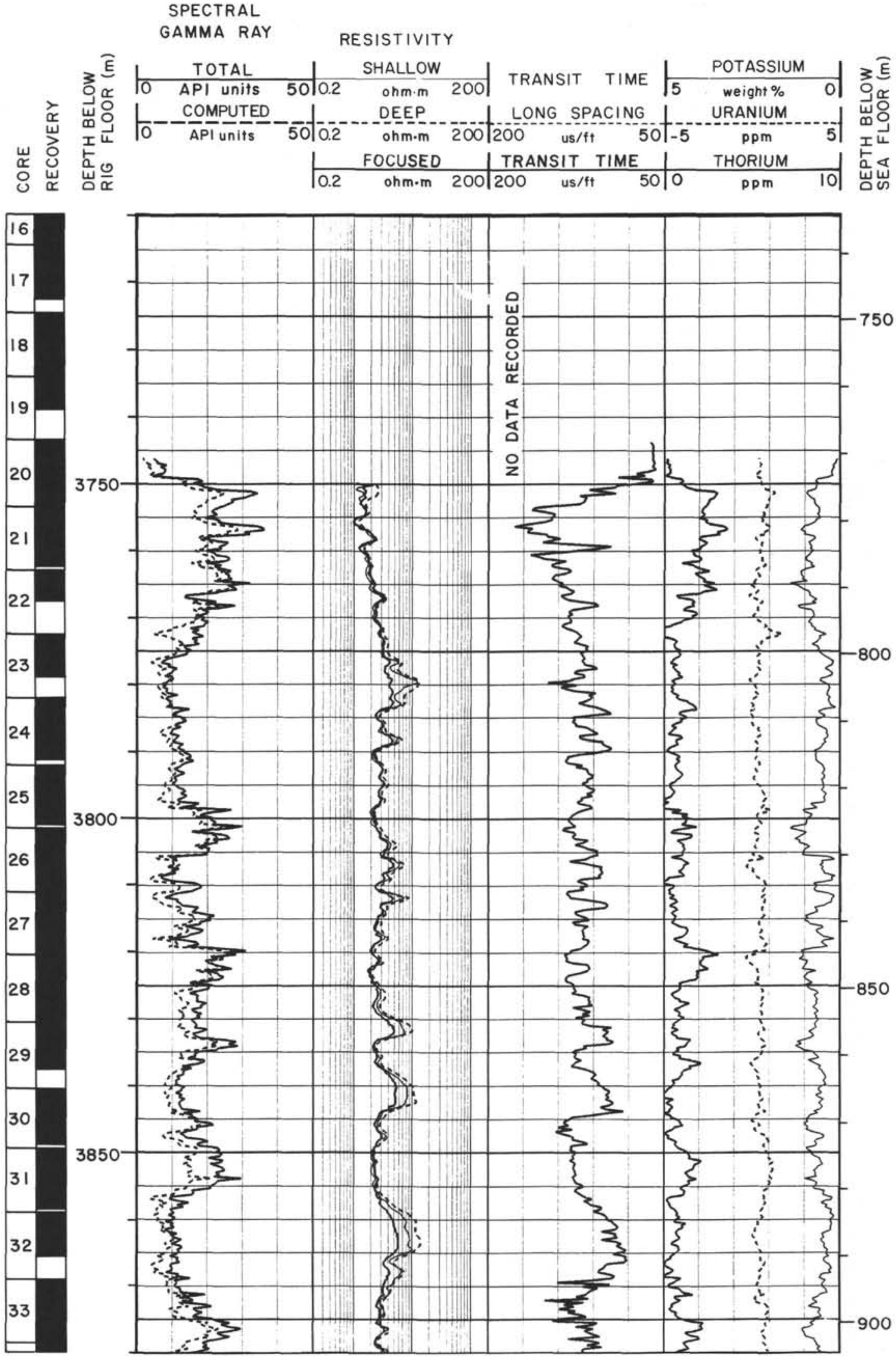

Figure 69 (continued).

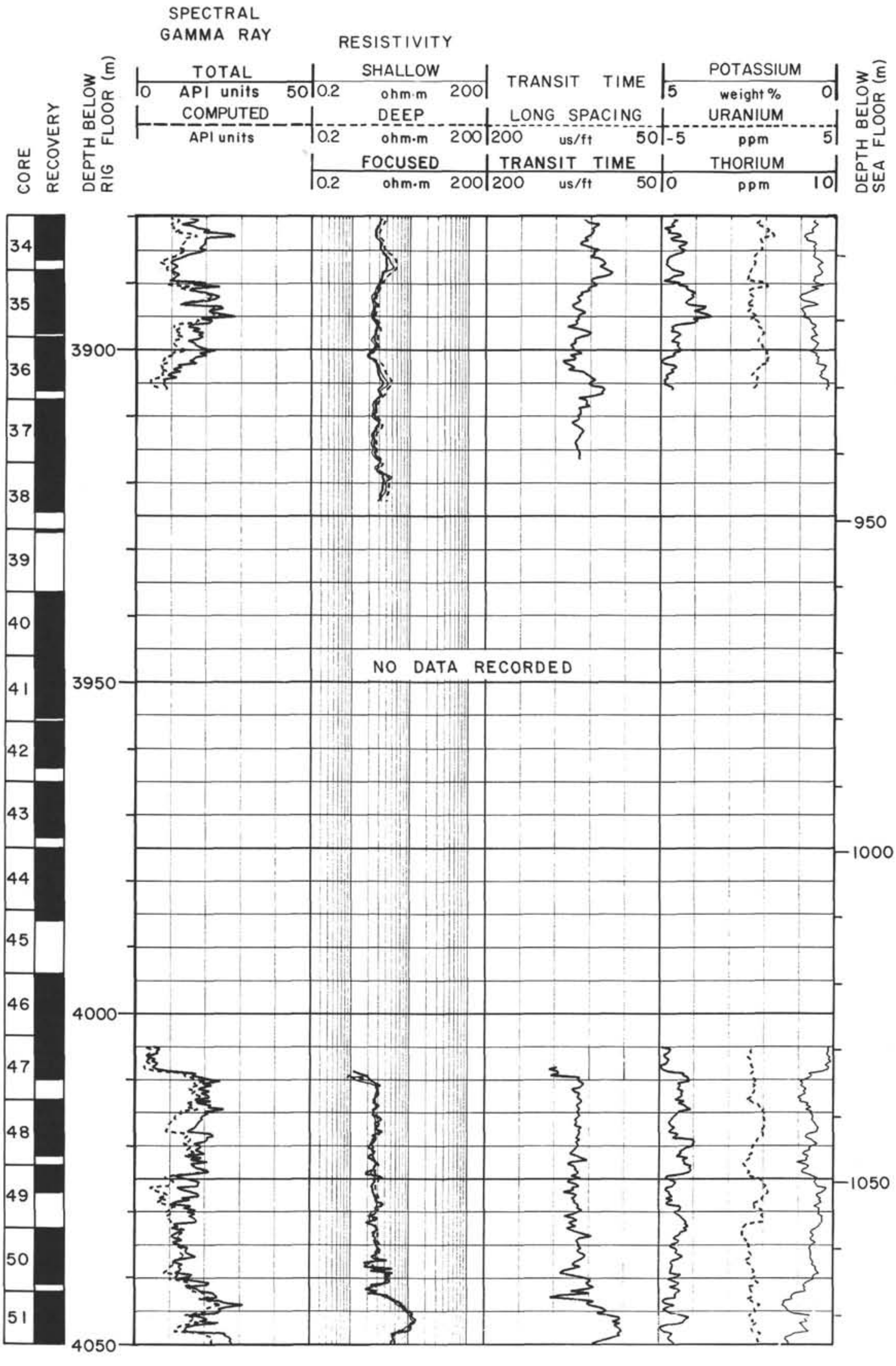

Figure 69 (continued).

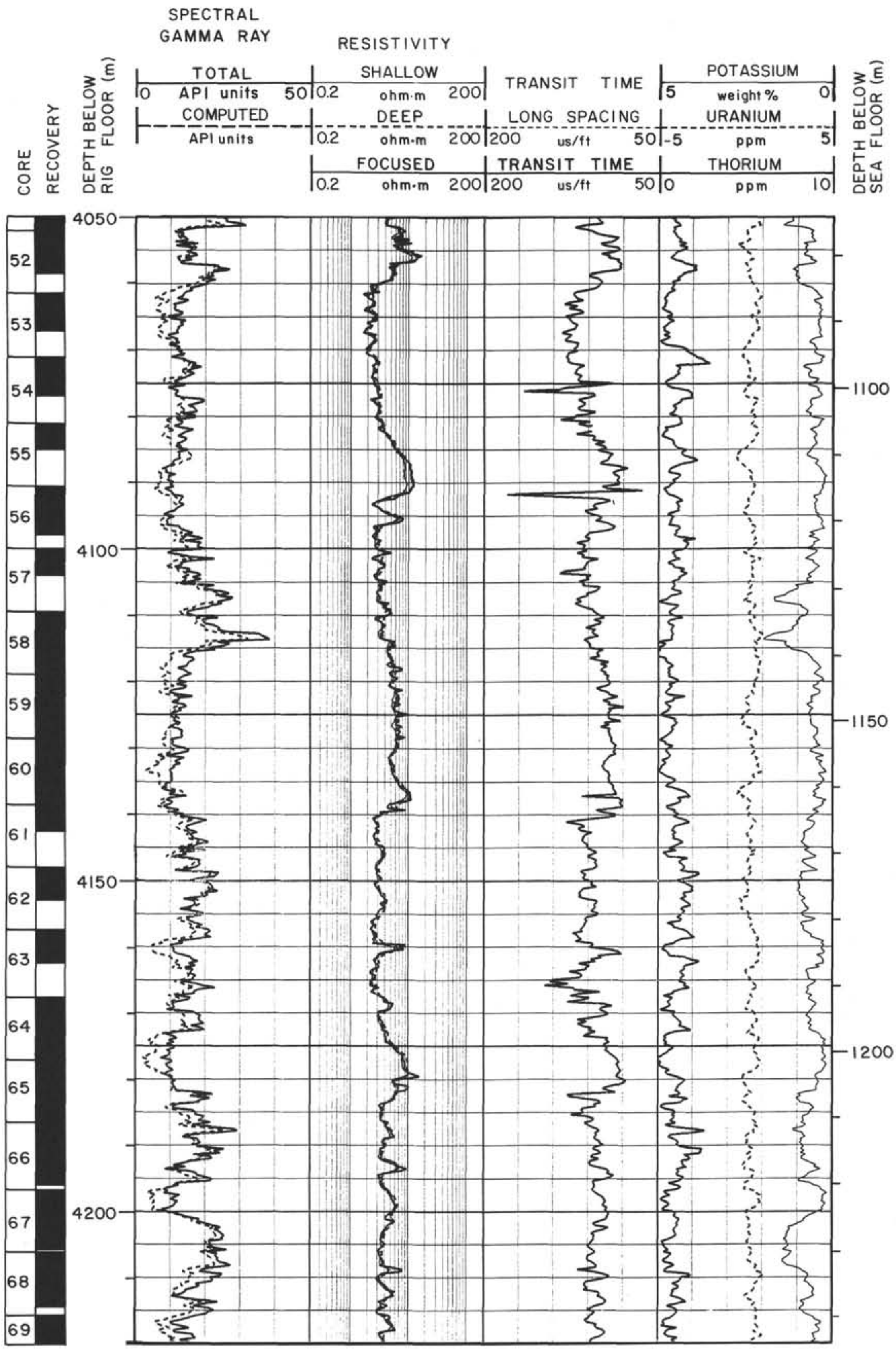

Figure 69 (continued).

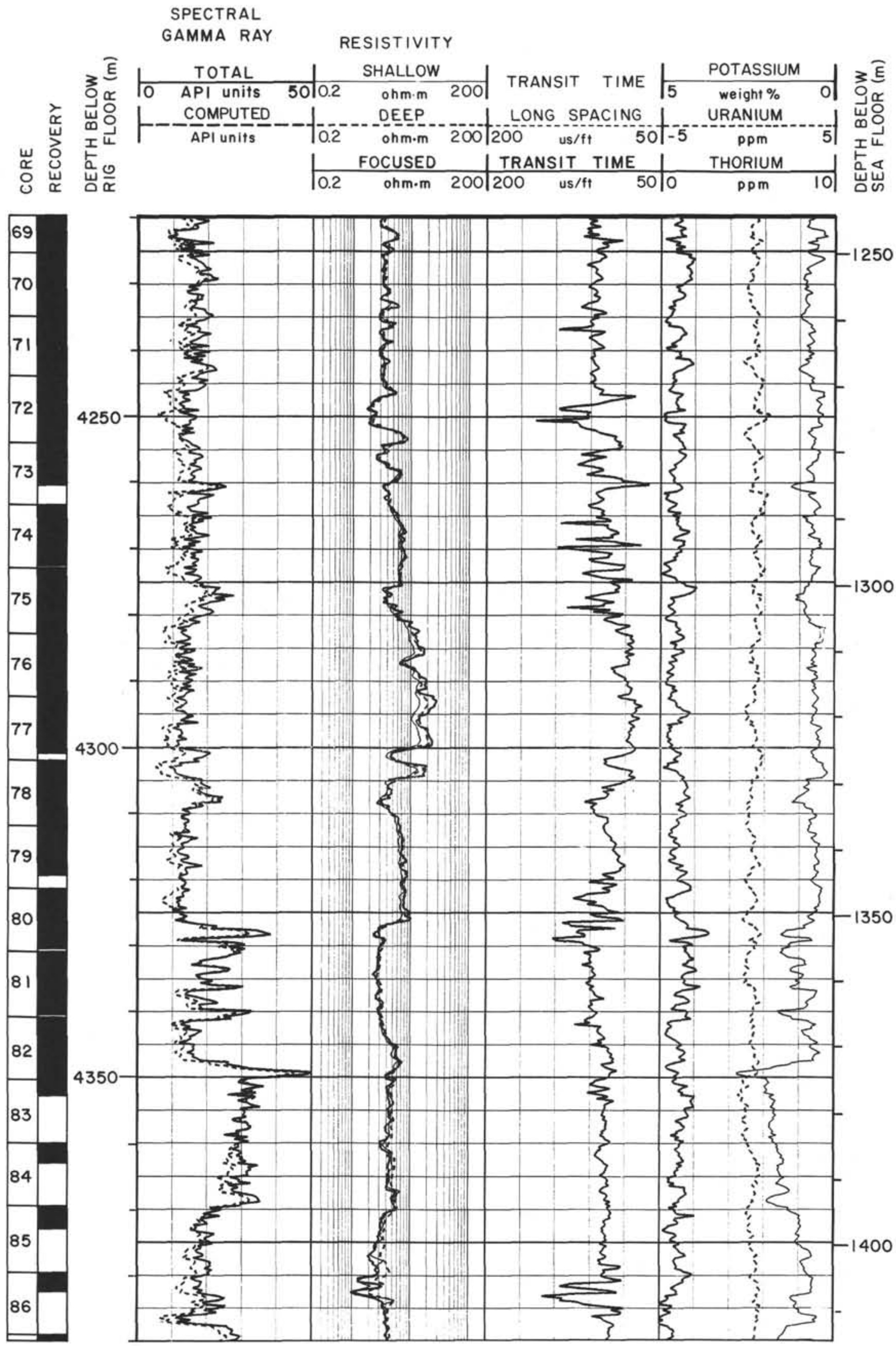

Figure 69 (continued).

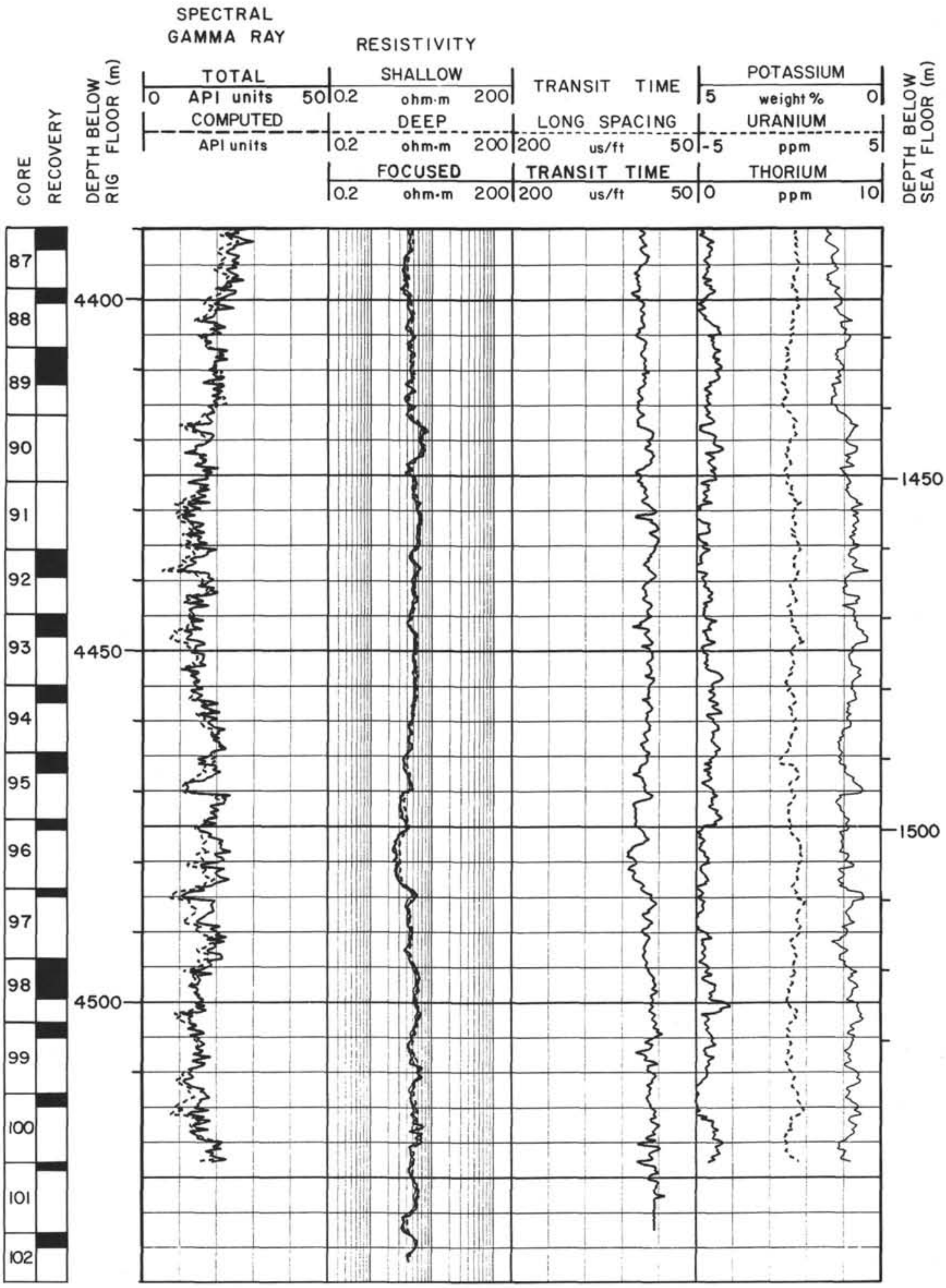

Figure 69 (continued).

traveltimes were calculated to 0.1 ms from the stacked shots at each clamping level.

Preliminary Stratigraphic Results from Downhole Measurements

The downhole measurements are analyzed here with respect to the stratigraphic column defined from cores. Because of the discontinuous nature of this dataset, we infer only limited results with respect to the stratigraphy.

As no data were recorded inside the 11-3/4-in. casing (from the seafloor to the casing shoe, located at 568.0 mbsf), Unit I is not represented by downhole measurements. Velocity and resistivity were measured in Units II (a diabase sill located from 586.0 to 591.0 mbsf) and III during Run 1. The FMS images re-

Table 15. Summary of downhole measurement operations, Site 793.

Date	Time (UTC)	Operation
June 15, 1989	0730	Rig-Up. Attempting DIL-LDT-LSS-NGT-TEMP HLDT failed with SS at surface—IMPH not working.
	1115	RIH with DIL-LSS-NGT-TEMP—Second DIL used.
	1315	Hit bridge at 12,090 ft. Log up to shoe at 11,624 ft. Good data.
	1600	Out of the hole with DIL (Run 1). Rig down to break through bridge with pipe.
	2000	Rig up DIL-LSS-NGT-TEMP.
	2215	Hit bridge at 12,886 ft. Log up to pipe at 12,301 ft. Good data.
June 16, 1989	0130	Out of the hole with DIL (Run 2). Rig down to break through bridge with pipe.
	0515	Rig up DIL-LSS-NGT-TEMP.
	0730	Hit bridge at 14,896 ft. Log up to pipe at 13,153 ft. (about 120 m off bottom). Good data. 77% of open hole covered.
	1015	Out of the hole with DIL (Run 3).
	1100	RIH with FMS-NGT-TEMP.
	1300	Hit bottom at 14,810 ft. Log up to pipe at 13,153 ft. Good data.
	1500	Out of the hole with FMS.
	1630	RIH with GST-ACT-NGT-TEMP.
	1900	Hit bottom at 14,785 ft. Log up to pipe at 13,153 ft. Good data.
	2200	Skip BHA. Logging through pipe from 12,770 ft. to casing shoe (11,624 ft.)
June 17, 1989	0100	Out of the hole with GLT.
	0130	RIH with WST.
Plan for the end of logging;		
	0300	Start recording about twelve levels from the bottom of the hole, and for a maximum of 90 min.
	0600	Out of the hole with WST. Rig down and trip pipe above casing shoe.
	0800	RIH with FMS-NGT-TEMP to log the upper part of the hole.
	1300	Rig down. Start pulling pipe out of the hole.
	2300	Sailing to Tokyo.

corded during the last run in the hole span approximately the same interval. Although Unit IV is not represented by downhole mesurements, Unit V is largely sampled. The base of Unit V (1374.5 mbsf) is the site of a large natural gamma peak, apparently the result of local potassium enrichment. The drill hole is generally oval in shape in Unit VI and caved at its base in what appears to be a faulted sediment/basement contact (from 1405.5 to 1408.2 mbsf). Basement (Unit VII) is characterized by uniform physical properties and generally featureless, mottled FMS images.

REFERENCES

Akimoto, K., 1989. Recent foraminifera from Enshunada. *In* Takayanagi, Y., and Ishizaki, K. (Eds.), *Collected Papers on Foraminifera from the Japanese Islands:* Sendai (Toko Press), 93–104.

Arthur, M. A., Carson, B., and von Huene, R. 1980. Initial tectonic deformation of hemipelagic sediment at the leading edge of the Japan convergent margin. *In* Langseth, M., Okada, H., et al., *Init. Repts. DSDP,* 56, 57, Pt. 1: Washington (U.S. Govt. Printing Office), 569–614.

Berggren, W. A., Kent, D. V., Flynn, J. J., and Van Couvering, J. A., 1985. Cenozoic geochronology. *Geol. Soc. Am. Bull.,* 96:1407–1418.

Blow, W. H., 1969. Late middle Eocene to Recent planktonic foraminiferal biostratigraphy. *In* Renz, H. H., and Brönniman, P. (Eds.), *Proc. 1st Intern. Conf. Planktonic Microfossils:* Leiden (E. J. Brill), 199–422.

Bolli, H. M., Saunders, J. B., and Perch-Nielsen, K. (Eds.), 1985. *Plankton Stratigraphy:* Cambridge (Cambridge Univ. Press).

Bouma, A. H., 1962. *Sedimentology of Some Flysch Deposits:* Amsterdam (Elsevier).

Champion, D. E., Lanphere, M. A., and Kuntz, M. A., 1988. Evidence for a new geomagnetic reversal from lava flows in Idaho: discussion of short polarity reversals in the Brunhes and late Matuyama polarity chrons. *J. Geophys. Res.,* 93:11,667–11,680.

Foreman, H. P., 1981. Radiolaria. *In* Emiliani, C. (Ed.), *The Sea* (Vol. 7): *The Oceanic Lithosphere:* New York (Wiley), 1121–1144.

Fryer, P., Pearce, J., et al., in press. *Proc. ODP, Init. Repts.,* 125: College Station, TX (Ocean Drilling Program).

Haq, B. U., Hardenbol, J., and Vail, P. R., 1987. Chronology of fluctuating sea levels since the Triassic. *Science,* 235:1156–1167.

Hiscott, R. N., and Middleton, G. V., 1979. Depositional mechanics of thick-bedded sandstones at the base of a submarine slope, Tourelle Formation (Lower Ordovician), Quebec, Canada. *In* Doyle, L. J., and Pilkey, O. H. (Eds.), *Geology of Continental Slopes.* Soc. Econ. Paleontol. Mineral. Spec. Publ., 27:307–326.

________, 1980. Fabric of coarse deep-water sandstones, Tourelle Formation, Quebec, Canada. *J. Sediment. Petrol.,* 50:703–722.

Ingle, J. C., Jr., 1980. Cenozoic paleobathymetry and depositional history of selected sequences within the southern California continental borderland. *Spec. Publ. Cushman Found. Foraminiferal Res.,* 19: 163–195.

Keller, G., 1979. Early Pliocene to Pleistocene planktonic foraminiferal datum levels in the North Pacific: DSDP Sites 173, 310, 296. *Mar. Micropaleontol.,* 4:281–294.

Kharaka, Y. K., and Berry, F.A.W., 1973. Simultaneous flow of water and solutes through geological membranes. *Geochim. Cosmochim. Acta,* 37:2577–2603.

Kuno, H., 1960. High-alumina basalt. *J. Petrol.,* 1:121–145.

Lowe, D. R., 1982. Sediment gravity flows: II. Depositional models with special reference to the deposits of high-density turbidity currents. *J. Sediment. Petrol.,* 52:279–297.

Lundberg, N., and Leggett, J. K., 1986. Structural features in cores from the slope landward of the Japan Trench, Deep Sea Drilling Project Leg 87B. *In* Kagami, H., Karig, D. E., Coulbourn, W. C., et al., *Init. Repts. DSDP,* 87: Washington (U.S. Govt. Printing Office), 809–826.

Manheim, F. T., and Waterman, L. S., 1974. Diffusimetry (diffusion constant estimation) on sediment cores by resistivity probe. *In* von der Borch, C. C., Sclater, J. G., et al., *Init. Repts. DSDP,* 22: Washington (U.S. Govt. Printing Office), 663–670.

Mutti, E., 1985. Turbidite systems and their relations to depositional sequences. *In* Zuffa, G. G. (Ed.), *Provenance of Arenites:* Dordrecht (D. Reidel), 65–93.

Nelson, C. H., and Maldonado, A., 1988. Factors controlling depositional patterns of the Ebro turbidite systems, Mediterranean Sea. *AAPG Bull.*, 72:698–716.
Ogawa, Y., and Miyata, Y., 1985. Vein structure and its deformation history in the sedimentary rocks of the Middle America Trench slope off Guatemala, Deep Sea Drilling Project Leg 84. *In* von Huene, R., Aubouin, J., et al., *Init. Repts. DSDP*, 84: Washington (U.S. Govt. Printing Office), 811–829.
Pierson, T. C., 1981. Dominant particle support mechanisms in debris flows at Mt. Thomas, New Zealand, and implications for flow mobility. *Sedimentology*, 28:49–60.
Seno, T., and Maruyama, S., 1984. Paleogeographic reconstruction and origin of the Philippine Sea. *Tectonophysics*, 102:53–84.
Shepard, F. P., 1963. Submarine canyons. *In* Hill, M. N. (Ed.), *The Sea* (Vol. 3): Huntington, NY (Krieger), 480–506.
Shipboard Scientific Party, 1987. Site 645. *In* Srivastava, S. P., Arthur, M., et al., *Proc. ODP, Init. Repts.*, 105: College Station, TX (Ocean Drilling Program), 61–418.
Stern, R. J., and Ito, E., 1983. Trace element and isotopic constraints on the source of magmas in active volcano and Mariana island arcs. *J. Volc. Geothermal. Res.*, 18:461–482.
Takayama, T., and Sato, T., 1987. Coccolith biostratigraphy of the North Atlantic Ocean, Deep Sea Drilling Project Leg 94. *In* Ruddiman, W. F., Kidd, R. B., Thomas, E., et al., *Init. Repts. DSDP*, 94, Pt. 2: Washington (U.S. Govt. Printing Office), 651–702.
Taylor, B., and Smoot, N. C., 1984. Morphology of Bonin fore-arc submarine canyons. *Geology*, 12:24–727.
Van Morkhoven, F.P.C.M., Berggren, W. A., and Edwards, A. S., 1986. Cenozoic cosmopolitan deep-water benthic foraminifera. *Bull. Cent. Rech. Explor.-Prod. Elf-Aquitaine*, No. 11.
Woodruff, F., 1985. Changes in Miocene deep-sea benthic foraminiferal distribution in the Pacific Ocean: relationship to paleoceanography. *In* Kennett, J. P. (Ed.), *The Miocene Ocean: Paleoceanography and Biogeography*. Mem. Geol. Soc. Am., 163:131–175.
Yasuda, H., 1989. Benthic foraminifera and sedimentary facies of the lower slope basin off Shikoku, Japan. *In* Takayanagi, Y., and Ishizaki, K. (Eds.), *Collected Papers on Foraminifera from the Japanese Islands:* Sendai (Toko Press), 83-92.
Zhang, Y., Langmuir, C. H., and Taylor, B., in press. Petrogenesis of Tori-shima and Sumisu-jima volcanoes of the Izu-Bonin arc. *Earth Planet. Sci. Lett.*

Ms 126A-110

NOTE: All core description forms ("barrel sheets") and core photographs have been printed on coated paper and bound as Section 3, near the back of the book, beginning on page 421.